Environment induced modifications of spontaneous quantum emission

Emmanuel Lassalle

AIX-MARSEILLE UNIVERSITÉ
ÉCOLE DOCTORALE 352
UFR SCIENCES
INSTITUT FRESNEL / ÉQUIPE CLARTÉ

Thèse présentée pour obtenir le grade universitaire de docteur

Discipline : Physique et Sciences de la Matière
Spécialité : Optique, Photonique et Traitement d'Image

Emmanuel LASSALLE

Émission quantique spontanée : modifications induites par l'environnement

Environment induced modifications of spontaneous quantum emission

Soutenue le 5 juillet 2019 devant le jury composé de :

Rémi CARMINATI	Institut Langevin	Rapporteur
Christophe SAUVAN	Laboratoire Charles Fabry	Rapporteur
Juan Jose SAENZ	Donostia International Physics Center	Examinateur
Patrice GENEVET	CRHEA	Examinateur
Anne SENTENAC	Institut Fresnel	Examinatrice
Brian STOUT	Institut Fresnel	Directeur de thèse
Thomas DURT	Institut Fresnel	Co-directeur de thèse

Remerciements

Cette thèse a été réalisée en partie au sein de l'Institut Fresnel, à l'Université d'Aix-Marseille à Marseille (France), de novembre 2015 à juin 2018, puis au « Centre for Disruptive Photonic Technologies » (CDPT), à Nanyang Technological University à Singapour, de juillet 2018 à juin 2019, dans le cadre d'une collaboration internationale. Pendant ces trois ans et huit mois, j'ai pu interagir avec beaucoup de personnes différentes, ce qui fut extrêmement enrichissant, et, sans leur aide et leur soutien, cette thèse n'aurait pas pu se dérouler ainsi. Je tiens à les remercier ici, en commençant tout d'abord par mes soutiens financiers.

Soutiens financiers : École Doctorale « Physique et Sciences de la Matière » (ED 352) pour son soutien financier de trois ans ; Institut Fresnel (Fonds de la Science 2017-2018) et Nanyang Technological University pour leur co-financement de mon séjour d'un an à Singapour.

Membres du jury : Je désire remercier chaque membre du jury d'avoir accepté d'investir de leur temps et de leur énergie pour lire, corriger et critiquer cette thèse, et de m'avoir permis d'améliorer ce travail de longue haleine. Je remercie ainsi Anne Sentenac, Rémi Carminati, Christophe Sauvan, Juan Jose Saenz et Patrice Genevet de m'avoir fait l'honneur d'être présents lors de ma défense de thèse.

Encadrants et collègues : Je veux exprimer ici toute ma reconnaissance envers Brian Stout et Thomas Durt, qui ont co-encadré cette thèse pendant presque quatre ans. J'ai énormément apprécié l'autonomie et la confiance qu'ils m'ont accordées, et ce dès le début, tout en étant toujours ouverts à des discussions ou des questions. J'ai vraiment eu beaucoup de chance d'avoir de tels encadrants qui ont pris soin de moi et m'ont traité de façon remarquable. Je tiens à remercier Nicolas Bonod, que j'ai considéré comme un mentor durant cette thèse, dont j'ai énormément apprécié le bon sens et les conseils, et qui a également su me motiver lorsque j'en avais besoin. Mon quatrième encadrant pendant cette thèse a été David Wilkowski qui m'a reçu pour un séjour d'un an dans son groupe à Singapour, et avec qui j'ai beaucoup apprécié d'interagir et de travailler. Je le remercie infiniment pour ce séjour, pour la confiance qu'il m'a donnée, et la qualité de son accompagnement. Je tiens à remercier chaleureusement Caroline Champenois avec qui j'ai bien collaboré, qui respire la motivation et la passion, et avec qui j'ai également énormément apprécié de travailler. Je remercie également Jérôme Wenger, que j'ai côtoyé durant cette thèse à l'Institut Fresnel ou bien en conférences, pour tous ses conseils et son investissement auprès des jeunes chercheurs que je trouve remarquable. Merci à Philippe Lalanne également qui m'a reçu pour un séjour de trois jours dans son laboratoire de Bordeaux pour me donner une véritable formation sur l'optique diffractive et les métasurfaces, ce

qui m'a fait gagner beaucoup de temps. Je suis ici reconnaissant pour les nombreuses discussions que l'on a eues, et pour sa générosité avec son temps et son énergie. Enfin, je remercie le reste de l'équipe CLARTÉ de l'Institut Fresnel qui regroupe de belles personnes, qui contribuent à faire de cette thèse un très bon souvenir.

Personnel administratif : Sans les personnes que je vais présenter ici, le laboratoire et la recherche ne pourraient pas fonctionner. La première à qui j'ai eu à faire pour mon installation administrative en tant que doctorant à l'Institut Fresnel a été Nelly Bardet, et je n'aurais pas pu espérer personne plus compétente, aidante, arrangeante et gentille qu'elle. Au sein de l'Institut Fresnel toujours, je suis extrêmement reconnaissant envers Évelyne Santacroce dont le soutien a permis que la collaboration internationale avec Singapour puisse avoir lieu. Dans la gestion de ce dossier délicat, j'ai eu l'aide et tout l'accompagnement d'une équipe très professionnelle et bienveillante : Fatima Kourourou, Cristina Pereira, Émilie Carlotti, ainsi qu'Aurore Piazzoli qui ont mené ce dossier avec brio. Concernant le déroulé de la thèse et la fin de thèse, je remercie Michèle Francia pour toute son aide au sujet de toutes les questions administratives de fin de thèse. À Singapour, j'ai reçu l'aide précieuse de Sruthi Varier, qui est le cœur et le sourire du laboratoire CDPT.

Amis : Parmi les amis rencontrés pendant ces années, il y a Vincent Debierre qui est la première personne avec qui j'ai réellement commencé à travailler, et avec qui j'ai presque tout le temps été sur la même longueur d'onde, ce qui fut un plaisir ; mon collègue de bureau pendant près de trois ans, Mahmoud Elsawy, avec qui j'ai partagé peines et joies ; Mauricio Garcia-Vergara, et les nombreuses et toujours intéressantes discussions pendant nos repas ; Nadège Rassem, son amitié et sa bienveillance envers « bébé Manu » ; Rémi Colom avec qui j'ai eu beaucoup d'affinité scientifique, et avec qui j'ai pu passer des heures à parler de science ; Mohamed Hatifi, avec qui j'ai partagé le même encadrant et passé de bons moments à parler et plaisanter. Je remercie également tous les gars de la « team foot » de l'Institut Fresnel, avec qui j'ai passé de merveilleux moments sportifs et de détente, ainsi que l'équipe « défi de Monte Cristo 2018 », composée de Marine Moussu et de Camille Scotté, pour tout son soutien pour relever ce défi. Je veux citer ici aussi mes colocataires, Alexis Devilez tout d'abord, pour nos nombreuses discussions enrichissantes et passionnantes, que ce soit sur la science, sur Dieu ou sur le monde, puis Alexandre Beaudier, copain de longue date de l'équipe de football de l'École Centrale Marseille puis de l'Institut Fresnel, et avec qui j'ai partagé les temps merveilleux à la « villa », entourée de piscine, de centraliens et de lapins... À Singapour, je suis très reconnaissant d'avoir eu un collègue comme Syed Aljunid, toujours disponible et pédagogue pour m'initier à la physique expérimentale, je n'aurais pas pu espérer mieux, et également Hubert Souquet-Basiège qui m'a initié à mes tous débuts à Singapour avec beaucoup de passion et d'enthousiasme.

Famille : Enfin, je remercie et honore ma chère famille sans qui je ne serais pas là et qui est la base qui me permet d'être où je suis aujourd'hui, et à qui je dédie cette thèse : mon père Michel Lassalle, ma mère Manolita Lassalle, mon frère Micaël Lassalle, et mon amour Meyi Ongsono. Merci enfin à mon Dieu, qui est l'ancre de ma foi.

Statement of contributions

This thesis, written in English, is composed of six chapters.

Chapter 1: The content of Chapter 1 corresponds to a large extent to the published research article mentionned in the publication list (listed number 3 in "List of publications"). In this work, Vincent Debierre and I have carried out all the derivations and calculations in Section 1.3. I did all the numerical calculations in Section 1.3. Caroline Champenois helped proposing the experiment in Section 1.4. This work was supervised by Vincent Debierre and Thomas Durt.

Chapter 2: The content of Chapter 2 corresponds to a large extent to the published research article mentionned in the publication list (listed number 1 in "List of publications"). In this work, the derivation of the multipole formula in Section 2.4 is mostly based on previous works of Brian Stout and co-workers about Mie theory and the T-Matrix formalism, which are cited in due form. I did all numerical computations presented in Section 2.5 using an in-house code developed by Alexis Devilez. I did the calculations in Section 2.6 on a system suggested by Jérôme Wenger. This work was supervised by Nicolas Bonod and Brian Stout.

Chapter 3: The content of Chapter 3 corresponds to a large extent to the published research article mentionned in the publication list (listed 2 in "List of publications"). I derived all the analytical formulas using the quasi-normal mode formalism and carried on all the numerical calculations (the comparison with Mie theory was done using the homemade code developped by Alexis Devilez). I also beneficiated from fruitful discussions with Rémi Colom and Xavier Zambrana-Puyalto. This work was supervised by Nicolas Bonod and Brian Stout.

Chapter 4: The Sections 4.2, 4.3 and 4.5 of Chapter 4 constitute a review of formalisms found in the literature which are cited in due form. The original part of Chapter 4 is the Section 4.4, where I use the formalism of the quasi-normal modes in a quantum framework. The numerical calculations in Appendix 4.C were carried out by Mohamed Hatifi. This work was supervised by Thomas Durt.

Chapter 5: In Chapter 5, I did all the derivations and calculations in Section 5.2 using a master-equation formalism. In Section 5.3, I carried out all the numerical computations using an open-source code RETICOLO developped by Philippe Lalanne and Jean-Paul Hugonin, and I beneficiated from three days training with Philippe Lalanne at the "Laboratoire de Photonique, Numérique et Nanosciences" (LP2N) in Talence, France. This

project was initiated by David Wilkowski. This work was supervised by Thomas Durt and David Wilkowski.

Chapter 6: Chapter 6 is the only experimental chapter of this thesis and was carried out entirely in Singapore, in the CDPT, in the group of David Wilkowski. I contributed to all the work presented in Sections 6.3 and 6.4 together with Syed Aljunid. The experimental work was supervised by Syed Aljunid and David Wilkowski.

List of publications

[1] E. Lassalle, A. Devilez, N. Bonod, T. Durt, and B. Stout, *Lamb shift multipolar analysis*, Journal of the Optical Society of America B **34**, 1348 (2017).
→ **Editors' Pick**

Open-access (arXiv version): https://arxiv.org/abs/1804.02005

[2] E. Lassalle, N. Bonod, T. Durt, and B. Stout, *Interplay between spontaneous decay rates and Lamb shifts in open photonic systems*, Optics Letters **43**, 1950 (2018).

Open-access (arXiv version): https://arxiv.org/abs/1804.08684

[3] E. Lassalle, C. Champenois, B. Stout, V. Debierre, and T. Durt, *Conditions for anti-Zeno-effect observation in free-space atomic radiative decay*, Physical Review A **97**, 062122 (2018).

Open-access (arXiv version): https://arxiv.org/abs/1804.01320

Résumé en français (long)

Le contrôle de l'émission spontanée d'émetteurs quantiques est d'une importance capitale dans le développement des futures technologies quantiques telles que la cryptographie ou l'ordinateur quantiques. La base de ces applications consiste en la manipulation d'atomes, de molécules ou d'atomes « artificiels » comme sources élémentaires de lumière, et en l'exploitation de la nature quantique de la lumière émise, constituée de photons uniques. Grâce au développement récent des techniques de nanofabrication et des nanotechnologies, la modification de l'émission spontanée par l'environnement est en train d'être explorée au niveau de quelques émetteurs seulement, ce qui ouvre la voie vers un contrôle et une manipulation de l'émission spontanée sans précédent. En parallèle des efforts expérimentaux, une compréhension théorique des mécanismes d'interaction fondamentaux entre émetteurs quantiques et leur environnement devient également indispensable.

Dans cette thèse, nous considérons l'émission spontanée dans trois paradigmes différents traitant de la modification de ce processus due à l'environnement. Dans le premier, nous considèrons le problème du « monitorage » de l'émission spontanée, c'est-à-dire le fait qu'un observateur extérieur puisse modifier le processus d'émission par des mesures fréquentes de l'état du système, ce qui est étroitement relié au problème de la mesure en mécanique quantique. Dans un deuxième temps, nous considèrons l'interaction d'émetteurs quantiques avec des résonances optiques supportées par des structures nanométriques placées à proximité. Enfin, nous traitons de l'interaction lointaine entre des émetteurs et des surfaces gravées avec des nanostructures fabriquées et positionnées selon un motif particulier, appelées métasurfaces.

Nous présentons et utilisons plusieurs formalismes pour modéliser ces différentes situations, qui interfacent divers domaines de la physique comme l'optique quantique et la nanophotonique. Nous illustrons chaque situation par des prédictions théoriques réalistes sur la manière dont l'émission spontanée est modifiée : dans le premier cas, par une altération de la durée de vie de l'émetteur, dans le second, par une altération de la fréquence du photon qui est émis, et, dans la dernière situation, comment l'environnement peut induire à longue distance une cohérence quantique chez l'émetteur. Pour chacune de ces prédictions, nous faisons des propositions expérimentales pour de futures confirmations de ces effets, afin d'améliorer notre compréhension et le contrôle de ces processus fondamentaux d'interaction lumière-matière.

Mots clés : émetteurs quantiques, émission spontanée, effet Zénon quantique, effet anti-Zénon quantique, théorie de Mie, modes quasi-normaux, plasmonique, métasurfaces

Partie I : Émission spontanée monitorée

Dans la première partie (correspondant au chapitre 1), nous étudions l'effet anti-Zénon quantique sur des atomes hydrogénoïdes couplés au champ dans l'espace libre. Une des prédictions de la mécanique quantique concernant l'émission spontanée est que des observations fréquentes de l'état du système — de notre émetteur quantique ici — peuvent conduire à une modification de la dynamique. Il s'agit d'un effet propre aux systèmes quantiques et fortement lié au problème de la mesure en mécanique quantique, puisqu'en physique classique on suppose en général que la mesure d'une grandeur physique ne modifie pas l'état ou la dynamique du système. La dynamique libre de l'émission spontanée peut être décrite par une décroissance exponentielle de la probabilité de survie dans l'état excité par[1] :

$$P_{\text{surv}}(t) = \mathrm{e}^{-\gamma t} \tag{1}$$

où γ est appelé *taux de décroissance* ou *taux d'émission* et peut-être calculé par la fameuse *règle d'or* de Fermi, selon laquelle :

$$\gamma = \frac{2\pi}{\hbar^2} \overline{|\langle \mathrm{e}, 0|\hat{H}_I|\mathrm{g}, 1_{k_0}\rangle|^2}\, \rho(\omega_0) \tag{2}$$

qui essentiellement signifie que γ est proportionnel à la densité d'états électromagnétiques ρ disponibles à la fréquences de l'atome ω_0. D'après la mécanique quantique, des observations fréquentes peuvent modifier cette dynamique : sous l'effet d'observations fréquentes, la probabilité de survie décroît toujours exponentiellement, mais à un taux de décroissance éventuellement modifié et donné par[2] :

$$P_{\text{obs}}(t) = \mathrm{e}^{-\gamma' t} \qquad \text{with} \qquad \gamma' = 2\pi \int \mathrm{d}\omega\, R(\omega) F_\tau(\omega - \omega_0) \tag{3}$$

où $R(\omega)$ est une fonction appelée *réservoir* et correspond essentiellement à la densité d'états électromagnétiques $\rho(\omega)$, et $F_\tau(\omega-\omega_0)$ est une fonction qui caractérise l'émetteur quantique centrée et symétrique en ω_0. Ces deux fonctions sont représentées graphiquement en Fig. 1. La largeur de la fonction $F_\tau(\omega-\omega_0)$ est $2\pi\nu$ où ν est le taux d'observations $\nu = 1/\tau$ et τ l'intervalle de temps entre deux observations successives. Plus le taux d'observation ν est grand, plus la fonction $F_\tau(\omega-\omega_0)$ est large et va donc explorer le réservoir $R(\omega)$, ce qui d'après l'Éq. (3) va pouvoir modifier le taux de décroissance γ. Comment γ est modifié va dépendre de la forme du réservoir autour de ω_0. Si γ est plus petit que celui donné par la règle d'or, l'émission de l'atome est moins rapide, et l'on parle de *l'effet Zénon quantique*, en référence au philosophe grec Zénon et son paradoxe de la flèche. Au contraire, si γ est plus grand, l'émission est accélérée, et l'on parle de *l'effet anti-Zénon quantique*.

Nous avons exploré dans cette thèse le cas d'atomes hydrogénoïdes, c'est-à-dire constitués d'un seul électron orbitant autour du noyau, et en espace libre, pour lesquels le

[1] V. Weisskopf and E. Wigner, Zeitschrift für Physik **63**, 54 (1930)
[2] A. Kofman and G. Kurizki, Nature **405**, 546 (2000)

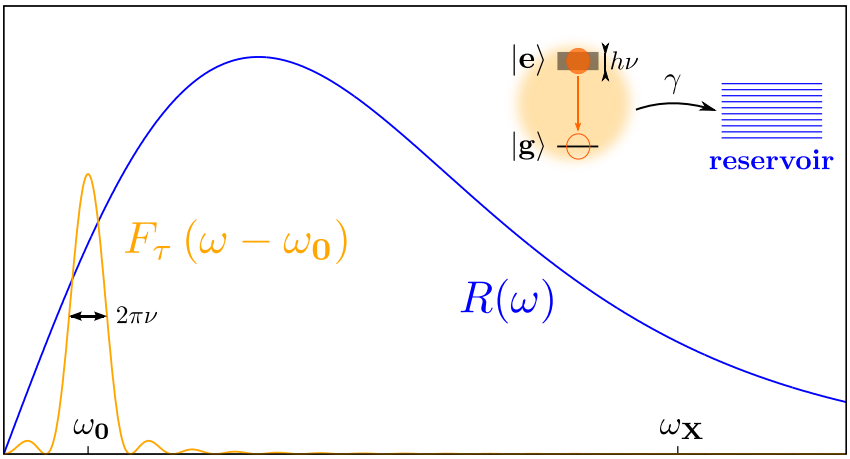

Figure 1 – Fonction réservoir $R(\omega)$ et $F_\tau(\omega-\omega_0)$ caractérisant la densité d'états électromagnétiques de l'environnement et les modes dans lesquels l'atome peut se désexciter, respectivement, et dont dépend le taux de décroissance par la formule $\gamma = 2\pi\int \mathrm{d}\omega\, R(\omega)F_\tau(\omega-\omega_0)$.

réservoir $R(\omega)$ est connu analytiquement. Son expression est la suivante[3] :

$$R(\omega) = \frac{D}{\omega_X^{\eta-1}} \frac{\omega^\eta}{\left[1+\left(\frac{\omega}{\omega_X}\right)^2\right]^\mu} \tag{4}$$

Dans cette expression, D est un coefficient sans unité, ω_X est une fréquence de coupure environ égale à $\omega_X \sim c/a_0$, où c est la vitesse de la lumière et a_0 le rayon de Bohr, et η et μ sont deux paramètres qui dépendent de la transition considérée. En particulier, η dépend du type de transition électronique : $\eta = 1$ pour une transition dipolaire électrique, et augmente ensuite pour les transitions multipolaires : $\eta = 3$ pour les transitions quadrupolaire électrique et dipolaire magnétique (cette dernière pouvant être vue comme un quadrupole électrique) et ainsi de suite... Nous avons voulu comprendre comment pour de tels systèmes l'émission est modifiée par des observations fréquentes, et pour cela, nous avons calculé l'intégrale de γ [Éq. (3)] en faisant certaines approximations. Nous avons obtenu la formule suivante pour le rapport entre le γ modifié et le γ donné par la règle d'or (et dénoté ci-après γ_{ROF}):

$$\frac{\gamma}{\gamma_{\mathrm{ROF}}} = 1 + A \times \left(\frac{\nu}{\omega_0}\right) \times \left(\frac{\omega_X}{\omega_0}\right)^{\eta-1} \tag{5}$$

où A est un pré-facteur de l'ordre de 1. Dans cette formule, le rapport entre le taux d'observation ν et la fréquence atomique ω_0 est très petit par rapport à 1, car ω_0 est une fréquence optique typiquement de l'ordre de la centaine de téra-hertz, et en pratique ν sera bien plus petit que cela (car limitée par l'électronique des instruments utilisés pour faire l'observation) ; tandis que le rapport entre la fréquence de coupure ω_X et ω_0 est de l'ordre de l'inverse de la constante de structure fine de l'électrodynamique, c'est-à-dire supérieur à 100.

De ce résultat analytique, on peut immédiatement faire les prédictions suivantes : lorsque $\eta = 1$, c'est-à-dire pour toutes les transitions *dipolaires électriques*, il n'y aura

[3] J. Seke, Physica A **203**, 269 (1994)

quasiment pas de modifications du taux d'émission, puisque le rapport ω_X/ω_0 disparaît et le reste est très petit devant 1, tandis que pour *tous les autres types de transitions*, pour lesquelles $\eta > 1$, on peut s'attendre à avoir une *accélération* de l'émission (effet anti-Zénon quantique) si le taux d'observation est suffisamment élevé.

Une telle prédiction permet d'expliquer pourquoi l'effet anti-Zénon quantique, qui avait été prédit pour le processus d'émission spontanée dès les années 2000, n'a encore jamais été observé expérimentalement, à notre connaissance, dans des expériences d'atomes froids ou d'ions piégés en espace libre. En effet, selon nos prédictions, cet effet n'est pas accessible pour toutes les transitions dipolaires électriques qui sont les plus largement étudiées et utilisées lors des expériences.

Dans un deuxième temps, nous avons essayé de proposer un candidat potentiel pour observer cet effet anti-Zénon quantique. Nous avons identifié une transition quadrupolaire électrique à 729 nm dans l'ion calcium Ca^+, qui peut être légitimement (mais pas strictement) considéré comme un atome hydrogénoïde puisqu'il ne possède qu'un électron de valence. Pour cela, nous proposons d'utiliser le processus STIRAP (pour Passage Adiabatic Raman Stimulé) afin de réaliser en pratique les *observations fréquentes*. Ce schéma d'observation consiste à illuminer l'atome avec deux lasers adressant les transitions à 850 nm et à 854 nm depuis l'état excité et légèrement hors-résonants (voir Fig. 2), afin de faire passer l'atome périodiquement de l'état excité $3D_{5/2}$ à l'état $3D_{3/2}$ et de le faire revenir à l'état $3D_{5/2}$. Un tel cycle marque la réalisation d'une observation sur l'état du système. Enfin, un schéma de *lecture* (read-out) permet avec des lasers de détecter lorsque l'atome est retombé dans l'état fondamental, et de reconstruire ainsi la statistique de la probabilité de survie dans l'état excité modifiée par les observations fréquentes. En appliquant notre formule analytique à cet ion, on estime qu'à partir d'un taux d'observation de 4 MHz, on atteint déjà une modification du taux de décroissance γ de 1%, ce qui est la meilleure précision actuelle. Une telle fréquence d'observation est a priori atteignable facilement, en jouant sur l'intensité des deux lasers utilisés pour le STIRAP.

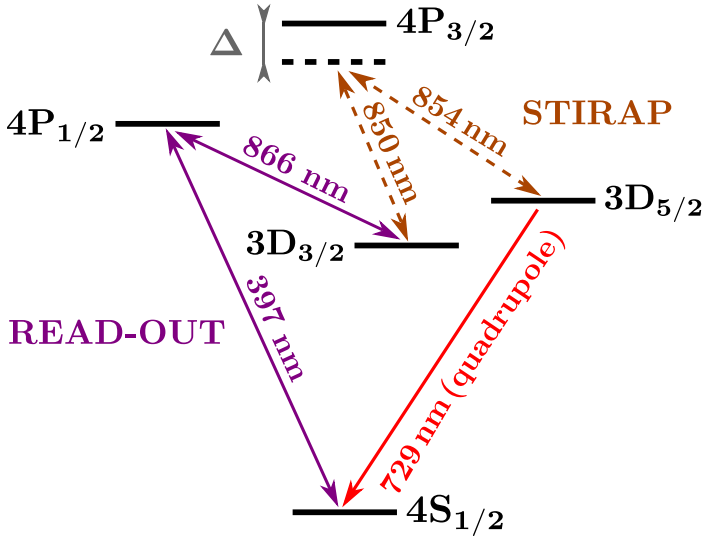

Figure 2 – Niveaux d'énergie pertinents dans l'ion Ca^+ pour pouvoir mettre en évidence l'effet anti-Zénon quantique sur la transition quadrupolaire électrique à 729 nm.

Partie II : Interactions en champs proche

Dans la deuxième partie (chapitres 2, 3 et 4), nous nous intéressons à l'émission spontanée d'un émetteur quantique couplé à une nanostructure en champ proche (voir schéma en Fig. 3).

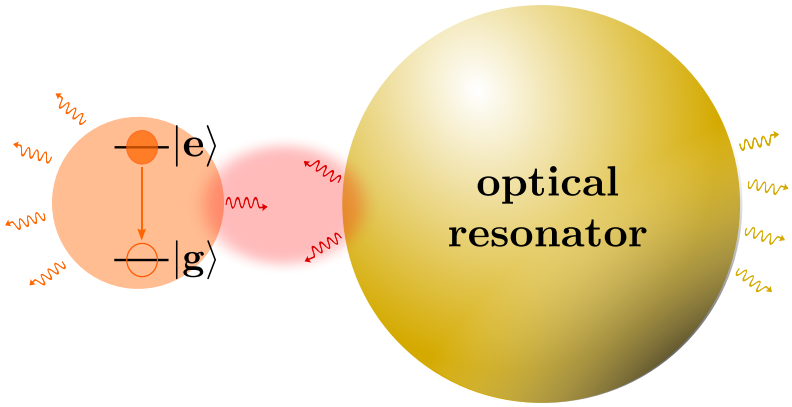

Figure 3 – Un émetteur quantique à deux niveaux couplé à une nanoparticule plasmonique.

Nous étudions tout d'abord (chapitre 2) le changement du taux d'émission et le décalage en fréquence (décalage de Lamb) en couplage faible, ce dernier ayant été peu étudié jusqu'à présent en nanophotonique. Une question que nous adressons tout particulièrement est si ce décalage en fréquence peut être plus grand que le taux de décroissance — lui aussi modifié par le couplage à la nanostructure — qui peut aussi être vu comme la largeur du spectre d'émission de l'atome. Une réponse favorable signifierait que le décalage de Lamb peut être conséquent.

En utilisant la théorie multipolaire, qui est particulièrement adaptée pour décrire la réponse optique de nanoparticules ayant une symétrie sphérique, nous établissons une expression générale du décalage en fréquence. Nous montrons son importance en prédisant un décalage observable dans une configuration réaliste qui pourrait être envisagée expérimentalement : une nanocavité formée par deux nanoparticules d'or. Nous prédisons pour une molécule *Alexa fluor 647* positionnée au centre de la cavité et émettant en l'absence de la cavité des photons avec une longeur d'onde de 670 nm, un décalage de la longeur d'onde d'émission de $\Delta\lambda = 2.5\,\mathrm{nm}$, ce qui est plus de deux fois supérieur à l'élargissement du spectre d'émission.

Dans le but d'obtenir des résultats plus généraux sur les situations dans lesquelles on peut espérer un décalage en fréquence supérieur au taux de décroissance, nous abordons ensuite (au chapitre 3) la description de l'interaction en utilisant le formalisme des modes quasi-normaux, qui sont les modes naturels de systèmes à pertes (pertes radiatives ou non-radiatives, *i.e* absorption), et permettent de décrire les résonances de ce type de systèmes [4]. Nous établissons des expressions générales du taux d'émission et du décalage de Lamb dans le cas du couplage faible avec un système ouvert et dissipatif. Un résultat majeur

[4] P. Lalanne, W. Yan, K. Vynck, C. Sauvan, and J.-P. Hugonin, Laser & Photonics Reviews **12**, 1700113 (2018)

de cette analyse est la démonstration que le décalage de Lamb peut être plus grand que la largeur de la raie d'émission pour un système dissipatif, alors que pour un système conservatif, ou ayant de faibles pertes comme une cavité fermée, ce décalage de Lamb reste inférieur à la largeur de raie.

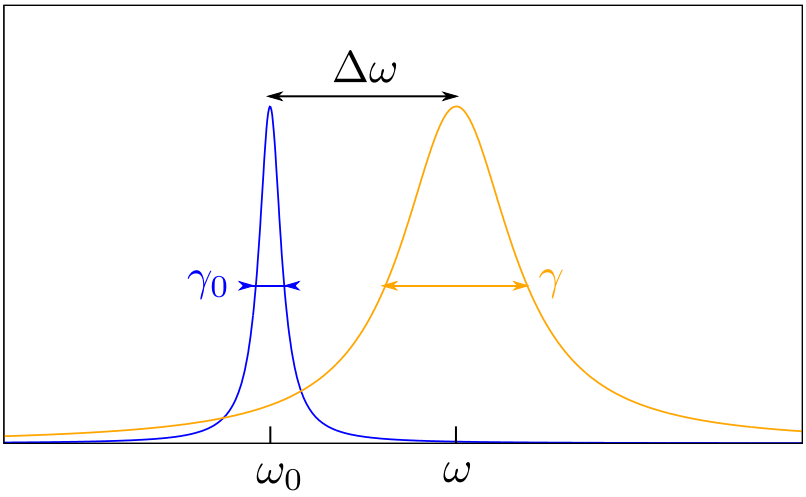

Figure 4 – Spectre d'émission modifié pour un émetteur quantique couplé à son environnement, de largeur de raie γ (γ_0 en espace libre) et centré sur la nouvelle fréquence d'émission $\omega = \omega_0 + \Delta\omega$, où $\Delta\omega$ est appelé *décalage de Lamb*.

Dans le chapitre 4, nous développons une description du couplage fort et faible d'un émetteur quantique avec un système résonant dissipatif. Le sujet est étudié en comparant différentes approches quantiques, rappelant le point de vue « standard » du couplage à une cavité à faibles pertes (système modèle de l'électrodynamique quantique en cavité ou cQED), jusqu'au développement de modèles valables pour des systèmes ouverts et/ou absorbants comme ceux rencontrés habituellement en nanophotonique, via l'utilisation des modes quasi-normaux. Un résultat concret de ce travail est l'extension des paramètres utilisés habituellement en cQED au cas de systèmes à forte dissipation.

Partie III : Interactions en champs lointain

Dans la troisième partie (chapitres 5 et 6), nous étudions la possibilité de modifier la dynamique d'émission spontanée en champ lointain, en utilisant une surface structurée réfléchissante (métasurface) permettant de modifier les fluctuations du vide même à grande distance (voir schéma en Fig. 5). Nous prédisons théoriquement (chapitre 5) que pour un atome dans une configuration Λ dite « lambda » (un état excité pouvant décroitre vers deux état fondamentaux différents via deux transitions dipolaires orthogonales), une cohérence à très longue durée de vie peut être créée lors de l'interaction avec une métasurface. Nous proposons également un design de métasurface permettant de produire une telle cohérence, montré en Fig. 6. Finalement, au chapitre 6, nous décrivons la mise en place d'une expérience dont l'objectif sera une première mesure de l'effet prédit, dans l'équipe de David Wilkowski à Singapour. Nous présentons la mise en place de la première

étape dans laquelle j'ai participé, consistant à refroidir un gaz d'atomes à une température de l'ordre de $20\,\mu$K, avec comme objectif ensuite d'en isoler un seul en utilisant un spot localisé généré par superoscillation optique.

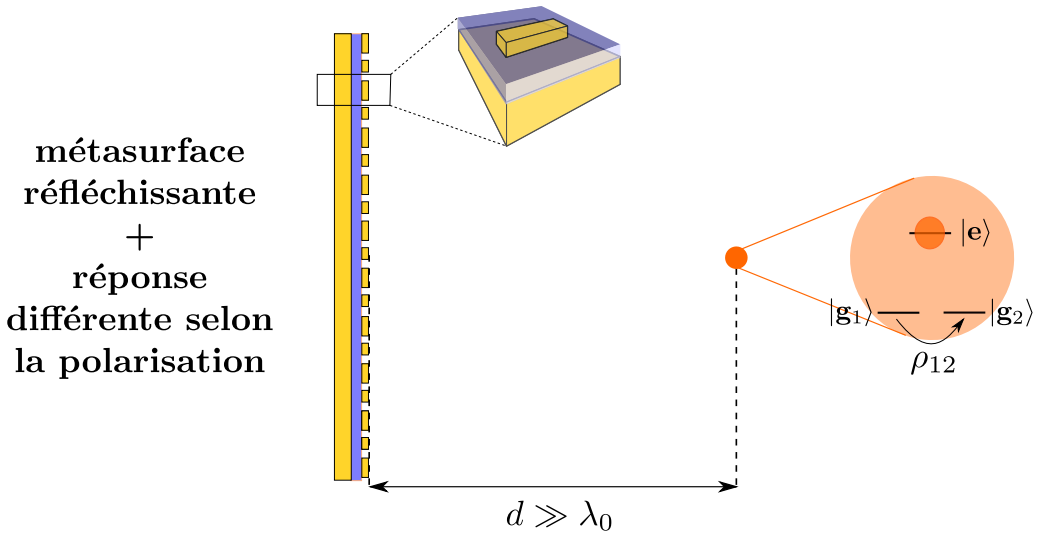

Figure 5 – Émetteur quantique dans une configuration Λ interagissant avec un métasurface placée à grande distance.

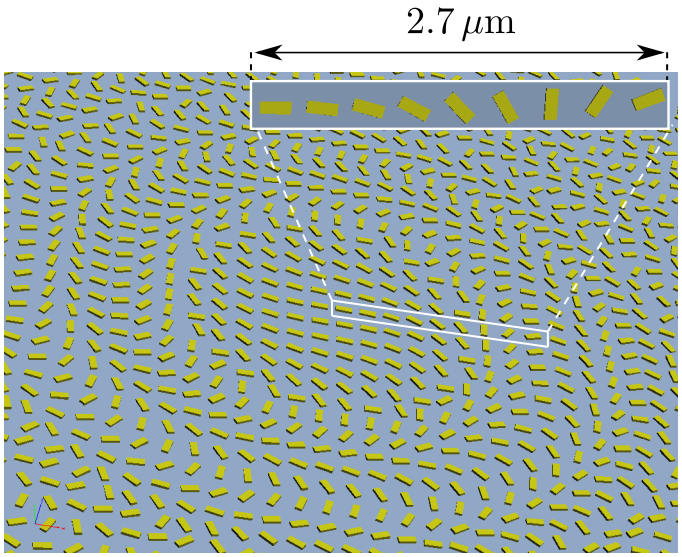

Figure 6 – Design de la métasurface.

Abstract in English (short)

The control of the spontaneous emission of quantum emitters is of fundamental importance for the development of future quantum technologies, like quantum cryptography or quantum computing. Such applications rely on the manipulation of atoms, molecules, or "artificial" atoms, as elementary sources of light, and on the exploitation of the quantum nature of the emitted light, single photons. With the recent developments in nanofabrication techniques and nanotechnologies, the modification of the dynamics of the spontaneous emission by the environment is being investigated at the level of a few emitters, allowing for unprecedented control and manipulation of the spontaneous emission. In parallel to the experimental efforts, theoretical understanding of the fundamental interaction mechanisms between quantum emitters and their environment also becomes more and more essential.

In this thesis, we tackle three different paradigms of the spontaneous emission phenomenon, all dealing with modifications of the spontaneous emission induced the environment. Firstly, we tackle the problem of monitored spontaneous emission, that is how the processus of emission is modified when the emitting system is being frequently monitored by an external observer, and which is closely related to the problem of measurement in quantum mechanics. Secondly, we consider the interaction between quantum emitters and optical resonances supported by nearby nanostructures. Finally, we study the remote interaction between quantum emitters and surfaces engraved with nanostructures which are designed and arranged in specific patterns, so-called metasurfaces.

We present and deal with different formalisms to model such different situations, interfacing different fields of physics like quantum optics and nanophotonics. In each of these situations, we illustrate with realistic theoretical predictions how the spontaneous emission is modified: in the first case, how the lifetime of the quantum emitter is altered, in the second case how the frequency of the emitted photon is altered, and in the last situation how the environment may induce quantum coherence in the emitter. For each case, for provide with experimental proposals for future confirmations of these predictions, to bring a better understanding and control over these fundamental processes.

Keywords: quantum emitters, spontaneous emission, quantum Zeno effect, anti-Zeno effect, Mie theory, quasi-normal modes, plasmonics, metasurfaces

Contents

Notations

- The unitary vectors are marked with an arrow. Example: $\vec{x}$.
- The other vectors are in bold. Example: $\mathbf{X}$.
- The operators are marked with a hat. Example: $\hat{X}$.
- The vectorial operators are in bold and marked with a hat. Example: $\hat{\mathbf{X}}$.

General introduction

Manipulating and controlling the spontaneous emission of quantum emitters is a fascinating domain of research. In a nutshell, it aims at using the most elementary source of light, an atom or a molecule, and how to exploit the quantum nature of the emitted light, a single photon, for future "quantum telecommunications", among them quantum cryptography or quantum computing.

A quantum emitter (QE), such as an atom, a molecule, or an "artificial atom" which generally refers to a solid-state emitter like a quantum dot or color-center, is system with discrete energy levels. Spontaneous emission occurs in a QE, when it is in a state of energy (an *excited* state) higher than its lowest energy state (the *ground* state), which decays to the ground state by emitting a photon, whose energy corresponds to the energy difference between the two states. Other "non-radiative" desexcitation channels exist, like vibrationnal relaxation in molecules, or dephasing processes in solid-state emitters (like phonon-assisted mechanisms), but they will not be studied in this thesis [1]. Moreover, we will interchangeably talk about quantum emitter or atom. The quantum emitters under interest in the present work typically emit light in the visible or near-infrared (transition frequency $\omega_0 \sim 2\pi \times 350\,\mathrm{THz}$ or emission wavelength $\lambda_0 = 2\pi c/\omega_0 \sim 800\,\mathrm{nm}$).

From a fundamental point of view, one cannot understand spontaneous emission if one does not consider the coupling of the QE with the *quantized* electromagnetic (EM) field in the vacuum. A first clarification: the term "vacuum" in this thesis refers to the *electromagnetic vacuum*, also called *quantum vacuum*, that is the absence of *light* (no photons), and *does not* refer to the absence of *matter* — one can have an EM vacuum in the presence of matter; to refer to the absence of matter, we will talk about "free space". Einstein, who knew thanks to Bohr that there are discrete levels of energy in molecules, developped in 1917 his theory of radiation in which he introduced three elementary processes of exchange of energy between light and matter: absorption, stimulated emission and spontaneous emission, characterized by the so-called Einstein's coefficients [2]. While the processes of absorption and stimulated emission could be explained in classical terms, he arrived at the conclusion that spontaneous emission cannot be explained by classical electromagnetism, showing the need for a quantum theory for radiation. The quantization of the EM field (refered to as the second quantization) is treated in the framework of Quantum ElectroDynamics (QED), the most successful theory of light-matter interaction. According to this theory, in the quantum vacuum, the EM field is not *null*: it is null *on average*, but presents *fluctuations*. Without taking into account the coupling between the atom and the quantized EM field in vacuum, one predicts that the atom would forever remain in the excited state and would never decay. Therefore, one can say that these vacuum fluctuations are responsible for the spontaneous emission, they "stimulate" or "trigger" the spontaneous decay of the QE.

One can study the dynamics of the spontaneous emission within the framework of quantum optics, the non-relativistic counterpart of QED. Of course, when one speaks about spontaneous emission, there are always two steps: the preparation of the atom in the excited state corresponds to a processus of *absorption*, and can be done for example using a laser whose frequency is resonant with the transition considered, and the processus of *emission* occurs through spontaneous decay. In this work, we assume that the absorption process is much faster than the emission process, so that the two processes can be considered as uncorrelated (for a treatment where both processes are taken into account, see *e.g.* Ref. [3]). Therefore, we will not consider the first step and we will always start the problem with an atom in the excited state at time $t = 0$. Consistently throughout this thesis, the quantity which is chosen to investigate the temporal behavior of the QE is the probability of the atom to remain in its excited state, called the survival probability and denoted by $P_{\text{surv}}(t)$ throughought this thesis. For a two-level atom in free-space, the Wigner-Weisskopf theory predicts that the survival probability decays exponentially in time at a rate γ_0 [4]:

$$P_{\text{surv}}(t) = \mathrm{e}^{-\gamma_0 t} \,, \tag{6}$$

where the "decay rate in free-space" γ_0, also called the Einstein A-coefficient, reads (introducing the electric dipole moment d of the atom):

$$\gamma_0 = \frac{\omega_0^3 d^2}{3\pi\epsilon_0 \hbar c^3} \,. \tag{7}$$

A second prediction of the theory is that the emitted spectrum has a Lorentzian distribution, of full-width at half maximum (FWHM), also called radiative linewidth, and equal to the decay rate γ_0. This can be seen as a time-energy uncertainty relation: by taking $\delta E = \hbar\gamma_0$ as a measure of the energy spread of the emitted photons, and defining $\tau = 1/\gamma_0$ the lifetime of the excited state, one has: $\delta E \tau = \hbar$. The meaning of the lifetime τ is that after a delay significantly longer than τ, one is nearly sure that one photon has been emitted. Typically for atoms or molecules $\tau \sim 10\,\text{ns}$.

The influence of the environment of the QE on its spontaneous decay was pointed out by Purcell as early as in 1946 in the context of microcavities [5], and also predictions were made about the spontaneous emission between mirrors in [6] and [7]: hence, this decay rate γ_0 appears not to be an intrinsic property of the atom, but could be modified by the environment. This is contained in the famous Fermi golden rule, which is derived within the framework of the time-dependent perturbation theory, and states that the decay rate in an arbitrary environment reads (such expression is derived in Chapter 4, Section 4.3):

$$\gamma = 2\pi R(\mathbf{r}_0, \omega_0) \,. \tag{8}$$

In this expression, we introduced a very important quantity used throughout this thesis, called the "reservoir coupling spectrum" $R(\mathbf{r}_0, \omega)$, where $\mathbf{r}_0$ emphasizes the dependence on the QE location, which is the density of states $\rho(\omega)$, corresponding to the number of EM states available per interval of frequency, weighted by the coupling strength $g(\mathbf{r}_0, \omega)$ (with the unit of a frequency), characterizing the coupling of the QE with the EM states of frequency ω [8]:

$$R(\mathbf{r}_0, \omega) = |g(\mathbf{r}_0, \omega)|^2 \rho(\omega) \,. \tag{9}$$

An important thing to note in the Fermi golden rule given by Eq. (8) is that the decay rate only depends on the density of states evaluated at the QE emission frequency ω_0. The first experimental demonstration of the alteration of the spontaneous emission in finite geometries was done by Drexhage in the early 1970s with fluorescent organic dyes deposited on top of a mirror, and whose distance from the mirror was precisely controlled using dielectric film spacers [9]. Later, in 1985, the inhibition of the spontaneous emission was demonstrated experimentally for excited atoms between two mirrors separated by less than half the atomic transition wavelength $\lambda_0/2$ [10].

In this thesis, we studied three facets of spontaneous emission. One of them is the problem of *monitored spontaneous emission*, that is how spontaneous emission can be modified when the QE is being frequently monitored in the excited state by an external observer. By "frequently monitored", I mean that an observer experimentally asks very frequently the question: "Is the atom still in the excited state?" as long as the answer is "Yes". This paradigm dates back to the work of Misra and Sudarshan in 1977 who raised the fact that in principle, frequent enough measurements of a quantum system in its excited state should "freeze" the dynamics. This prediction is known as the Quantum Zeno Effect [11]. This problem is related to the axioms of quantum mechanics about the measurement, according to which, in this case, a measurement of the atom in its excited state will project the atom onto this state. By repeating this measurement very frequently (before the atom has time to decay), it was shown that the frequent projections into the excited state are equivalent in effect to "dephasing" the excited state, which results in a broadening of its energy level [8]: if the time between each observation is $\delta t = 1/\nu$, with ν the rate of the observations, then the broadening of the energy level is $\delta E = \hbar\nu$, which leads, in agreement with the time-energy uncertainty relation, to $\delta E \delta t = \hbar$. Due to the broadening of its energy level, the atom will "see" a broader range of EM modes into which it can decay, which can modify its decay rate according to [8]:

$$\gamma = 2\pi \int_0^\infty \mathrm{d}\omega\, R(\mathbf{r}_0, \omega) F_\nu(\omega - \omega_0)\,, \tag{10}$$

where $R(\mathbf{r}_0, \omega)$ is the reservoir coupling spectrum, and $F_\nu(\omega - \omega_0)$ represents the broadening of the energy level of the excited state and is a function of width ν centered on ω_0. Therefore, depending on the range of $R(\mathbf{r}_0, \omega)$ (characterizing the environment) that is probed by the atom through $F_\nu(\omega - \omega_0)$ in the integral, spontaneous emission may be either frozen ($\gamma < \gamma_0$), this is the Quantum Zeno Effect, or accelerated ($\gamma > \gamma_0$), called the anti-Zeno effect (AZE). Note that in the limit where $\nu \to 0$, then $F_\nu(\omega - \omega_0) \to \delta(\omega - \omega_0)$ and one recovers the Fermi golden rule decay rate: $\gamma = 2\pi R(\mathbf{r}_0, \omega_0)$.

Another aspect of spontaneous emission is the coupling of the QE with resonances. One of the pioneering works is that of Purcell in 1946, who considered spontaneous emission in a microcavity and calculated the maximum enhancement of the decay rate due to an ideal coupling with the cavity resonance ω_c in the resonant case ($\omega_c = \omega_0$), introducing the so-called "Purcell factor" F_P which quantifies the *maximum* enhancement of the decay rate γ compared to γ_0 as [5]:

$$F_P = \frac{3}{4\pi^2} \lambda_0^3 \frac{Q}{V}\,. \tag{11}$$

In his equation, he introduced two figures-of-merit: the quality factor of the resonator $Q = \omega_c/\gamma_c$, with γ_c representing the bandwidth of the cavity resonance; and the mode volume V, which is the geometrical volume representing the spatial extent of the resonator. This Eq. (11) reveals two routes to increase the coupling: through increasing the quality factor Q of the resonator, or by decreasing the mode volume V. The first experiment of this type was performed in 1983 with atoms in a resonant microcavity [12], where the group of Haroche obtained an enhancement factor of approximately $F_P \approx 500$. For microcavities one usually has mode volumes limited by diffraction $V \sim \lambda_0^3$, such a milestone was possible because of the high quality factor $Q > 10^4$ obtained by using very high quality superconducting mirrors cooled to cryogenic temperatures. Such an experiment paved the way to the so-called cavity-Quantum ElectroDynamics (cQED), that is the study of the interaction between atoms and photons in resonant cavities at the single photon level. The physics of such systems can be modelled by considering the atom coupled to a single EM mode of the cavity: this is the Jaynes-Cummings model [13]. In this model, the reservoir coupling spectrum $R(\mathbf{r}_0, \omega)$ of Eq. (9) is obtained by using the expression of the coupling constant characterizing the coupling of the atom with the single mode in the case of a perfect matching in polarization and position (explained in Chapter 4, Section 4.2):

$$\hbar g = d\sqrt{\frac{\hbar\omega_c}{2\epsilon_0 V}}\,, \tag{12}$$

and the density of states is phenomenologically assumed to be Lorentzian with full-width at half maximum (FWHM) γ_c, so that at resonance ($\omega_0 = \omega_c$), it reads: $\rho(\omega_0) = 2/\pi\gamma_c$. The Purcell factor defined as $F_P = \gamma/\gamma_0$, reads: $F_P = 2\pi g^2\rho(\omega_0)/\gamma_0$ (using Eqs. (8) and (9) to express γ). By replacing $\rho(\omega_0)$ by $2/\pi\gamma_c$, g by its expression given by Eq. (12), and γ_0 by its expression given by Eq. (7), one can derive the Purcell factor originally given by Purcell [Eq. (11)]. This regime, where the irreversible decay of the excited QE happens like in free space but at a rate which is modified by the resonance and quantified by the Purcell factor F_P, is refered to as the *weak-coupling regime*, or also the low-Q cavity limit. In addition to this, the Jaynes-Cummings model [13] also predicts that when the coupling characterized by g is strong enough compared to the losses characterized by rate γ_c, spontaneous emission displays reversibility features: the survival probability does not decrease monotically anymore, and undergoes oscillations, called *vacuum Rabi oscillations*, revealing that the QE can exchange the emitted photon periodically with the resonator. Such a regime, called the *strong-coupling regime*, was later achieved by the cQED community (see [14] and references therein, and also [15, 16]). Such an ultimate control of the spontaneous emissiom of QE was remarkable, but however, these achievements require low temperatures, spectrally sharp QEs (such as atoms) and a fine tuning of the resonance of the cavity, rendering quantum applications difficult.

A more promising path towards applications began to be investigated in the 2000s by the nanophotonics community, which results from the convergence of several communities, notably by the near-field optics and plasmonics communities. One of the very first experiment coupling QEs (dye molecules) with surface plasmons was done in 1982 [17], where the authors already measured signatures of strong-coupling. In 2000, an experiment revealed that the presence of the so-called *plasmon resonances* in metallic nanos-

tructures could strongly modify the emission pattern of a fluorescent molecule [18]. Later in 2006, two studies quantify how the emission of QE are modified by resonant metallic nanoparticles [19, 20], quantifying the decay rate enhancement as well as the modification of the radiation pattern. Therefore, plasmonic resonances, which adopt the role of the resonant cavity, can also strongly modify the decay of QEs with huge advantages associated to the specificity of these systems *at room temperature* [21]. The first specificity is that plasmonic resonators present very broad resonances due to absorption in metals at optical wavelengths, which is good to couple broad QEs, but has the drawback of presenting very low quality factors $Q \sim 3-30$ which does not favor strong coupling *via* the Purcell formula in Eq. (11). However, to compensate for this, one can exploit the subwavelength confinement of plasmonic resonances, whenever the atom is placed in the near-field of the nanostructure. By simply extrapolating the Purcell factor formula to the case of nanophotonics, despite small quality factors, the interaction volume could reach up to $V \sim \lambda_0^3/10^4$, allowing, according to the Purcell formula, efficient coupling between the atom and the resonator.

A final feature of plasmonic resonators is the quenching of the spontaneous emission (absorption of the emitted photon by the metal) which one would like to avoid. Therefore, one must quantify not only the decay rate enhancement, but also the *radiative efficiency* which is the ratio between the radiative decay rate and the total decay rate made of radiative plus non-radiative contributions. Using essentially nanogap devices, where the QE is embedded in the gap between two metallic structures, decay rate enhancement above 1000 with a radiative efficiency above 50% have been demonstrated experimentally in the weak-coupling regime [22, 23]. Also, for these single-photon nanoantennas, which couple the emission of the QE with the far-field, to be interesting for applications, the direction of the emission should be controlled, which is possible, by using structures of size of the order of the wavelength, to induce constructive interferences in the desired direction. Moreover, the strong-coupling regime at the level of a few emitters at room temperature has been demonstrated and is underway [23, 24]. Even though, such coupling requires positioning the QE in very small volumes (which can be quite challenging due to surface-interactions like Casimir-Polders interactions), these systems are very promising in terms of practical implementation in quantum applications. One of the goals is to exploit the very high decay rate enhancement of the spontaneous decay to build ultra fast integrated light sources emitting streams of single photons [22], with promising applications in quantum information technology.

A last aspect of spontaneous emission that we will discuss is the *far-field* control of the spontaneous emission of an atom with optical devices acting as mirrors, for atom-mirror distances of many wavelengths typically $z \sim 10\lambda_0$. Firstly, it was demonstrated theoretically in [25] that a spherical mirror could literally suppress the vacuum fluctuations within a volume of λ_0^3 around the focus of the spherical mirror. Hence, the spontaneous emission of an excited atom located at this position can be fully suppressed, even if the mirror covers only half of the atomic emission solid angle. Such a remote interaction is an interferometric-like effect, in the sense that the QE must be located at a specific position (in this example in the focus of the spherical mirror), with a tolerance on the position of

about λ_0^3, and if one moves the atom along the atom-mirror axis from half a wavelength, one finds a two-fold increase of the decay rate [25]. In [26], the authors proposed to use instead of a simple spherical mirror a reflective surface engraved with subwavelength structures (nanoantennas), called a *metasurface*, to shape the quantum vacuum over remote distances. For instance, a metasurface that acts as a spherical mirror for a certain incident polarization, let us say linearly polarized along the x-axis, and as a planar mirror for the a polarization along the y-axis, would create an *anisotropic quantum vacuum* over remote distances. Such an anisotropic quantum vacuum is predicted to affect a multi-level atom: it would lead to the creation of a *coherence* between the two excited states of a three-level atom in a V-configuration [27], located at the focus of this spherical mirror and initially prepared in one of the excited states (coherence which does not exist in free-space). While no experimental demonstration have been made so far of the effect of a mirror or metasurface over macroscopic distances $z \gg \lambda_0/2\pi$ (experimental demonstrations exist in confined space, see *e.g.* [28]), this new paradigm could open the way towards the creation of entanglement between QEs over remote distances mediated by a metasurface [29].

Outline of the thesis: This thesis is divided into three Parts, and is organized as follows:

In the first Part of this thesis (Chapter 1), we study the problem of the monitored spontaneous emission. In a landmark article about monitored spontaneous emission [A. G. Kofman and G. Kurizki, Nature (London) **405**, 546 (2000)], Kofman and Kurizki concluded that acceleration of the decay by frequent measurements, called the quantum anti-Zeno effect (AZE), appears to be ubiquitous, while its counterpart, the quantum Zeno effect, is unattainable. However, up to now there have been no experimental observations of the AZE for atomic radiative decay (spontaneous emission) in free space. In Chapter 1, making use of the analytical results for the reservoir coupling spectrum $R(\mathbf{r}_0, \omega)$ available for hydrogen-like atoms [30, 31], we theoretically demonstrate that, in free-space, only non-electric-dipolar transitions should present an observable AZE, revealing that this effect is consequently much less ubiquitous than firstly predicted. We then propose an experimental scheme for AZE observation, involving the electric quadrupole transition in the alkali-earth ions like Ca^+ and Sr^+. The proposed protocol is based on the stimulated Raman adiabatic passage technique which acts like a dephasing quasi-measurement[5].

The second Part (Chapters 2, 3 and 4), is dedicated to the study of the *near-field interaction* between a single QE and resonant photonic nanostrutures. The near-field is defined as the region of space $z \ll \lambda_0/2\pi$, also called the non-retarded regime, which for optical QE, is typically $z \ll 100\,\text{nm}$; beyond this region, the coupling to the resonances is almost null. In the weak-coupling regime, this coupling not only changes the decay rate of the spontaneous emission, but can also induce energy shifts of the energy levels of the atom,

[5] E. Lassalle, C. Champenois, B. Stout, V. Debierre, and T. Durt, *Conditions for anti-Zeno-effect observation in free-space atomic radiative decay*, Physical Review A **97**, 062122 (2018)

resulting in a frequency-shift of the emitted photon frequency with respect to the bare transition frequency ω_0. Such an effect is called the photonic Lamb shift, or simply Lamb shift in this thesis. It is usually much less studied than the decay rate enhancement (Purcell effect) because the effect is considered as small. We start Chapter 2 by presenting in Section 2.2 the classical and quantum expressions of the decay rate and Lamb shift and showing their equivalence. After recalling the electric dipole approximation commonly use to describe the optical response of nanoparticles of sizes $a \ll \lambda_0$ in Section 2.3, we next study the photonic Lamb shift using the multipolar theory to describe the optical response of plasmonic nanostructures presented in Section 2.4. We show in Section 2.5 that this frequency-shift originates from the plasmon resonance coupling, illustrating this in the case of a QE coupled to a single silver plasmonic nanoparticle. We also compare the results obtained with the multipolar theory to the electric dipole approximation often used to describe nanoparticles of small size compared to the wavelength, and show that even in the case where the radius of the nanoparticle is $a \ll \lambda_0$, the electric dipole approximation can fail and several multipoles are necessary to describe the Lamb shift. We finally calculate in Section 2.6 the photonic Lamb shift in the case of an emitter embedded in the nanogap of a gold dimer, where we predict a significant shift of the emission frequency that could be observed at room temperature[6].

Next, in Chapter 3, we introduce the natural modes of photonic nanostructures, called "leaky modes", Quasi-Normal Modes (QNMs) or Resonant States, which take into account the *dissipative nature* of these systems that are open (radiation losses), can be absorbing (absorption losses) and also dispersive. These modes, presented in Section 3.2, can be used to describe the optical resonances supported by nanostructures, which can be of a different nature: Mie resonances in dielectric structures or surface plasmons in metallic ones. We use them to describe the Lamb shift and decay rate in Section 3.3, and we illustrate the obtained expressions in Section 3.4 for the canonical case of a sphere in two different cases: a dielectric nanoparticle (silicon) and a plasmonic nanoparticle (silver). Also, the analyticity provided by this tool allows us to address the question: "Can the induced shift of the emission frequency exceed the radiative linewidth?". In Section 3.5, we provide an answer to this question in the single-resonance case[7].

In Chapter 4, we make use of the previously introduced tools in a more general quantum treatment of the interaction between a single QE and resonant photonic or plasmonic nanostrutures, aiming at describing the weak and strong-coupling regimes. The usual cQED description considering the coupling to a resonant cavity, that we review in Section 4.2, most often deals with a single mode, and is valid for high-Q cavities, or in other words small losses. However, in nanophotonics, one deals with open and/or absorbing systems and there are usually several resonances involved as shown in Chapters 2 and 3, which goes well beyond the cQED description [32], and contains new physics beyond merely repeating cQED physics. As shown in Chapter 3, a remarkable advantage of the QNMs is that they allow us to generalize the usual cQED figures of merit characterizing

[6] E. Lassalle, A. Devilez, N. Bonod, T. Durt, and B. Stout, *Lamb shift multipolar analysis*, Journal of the Optical Society of America B **34**, 1348 (2017)

[7] E. Lassalle, N. Bonod, T. Durt, and B. Stout, *Interplay between spontaneous decay rates and Lamb shifts in open photonic systems*, Optics Letters **43**, 1950 (2018)

the interaction between a dipole source and a resonant cavity, such as the Purcell factor F_P or mode volume V, to the case of open and/or absorbing systems (that are almost always found in nanophotonics) and also taking into account material dispersion [33–35]. In Section 4.4, we incorporate this formalism into a fully quantum treatment of the interaction of a single QE with several resonances, which encompasses the weak and strong-coupling regime. A comparison with the figures-of-merit of cQED is also made in conclusion 4.6. Throughout this Part, we pay particular attention to the remarkable equivalence with a classical description of the atom as a damped harmonic oscillator, in this situation where only one photon is involved (decay rate and Lamb shift in the weak-coupling regime, and vacuum Rabi splitting in the strong-coupling regime). Such an equivalence is established via the Green tensor of the EM environment, and using the linear response theory and the quantum version of the fluctuation-dissipation theorem.

The third Part (Chapters 5 and 6) concerns the *far-field interaction* between a single three-level QE and a reflective metasurface. I present my theoretical work, and experimental work I am participating in, made in order to reach the following objective: to provide the first experimental evidence of the anisotropic quantum vacuum induced by a metasurface on a QE located at remote distance. I therefore present some recent theoretical work in Chapter 5 and experimental work in Chapter 6 realized in the group of David Wilkowski, at the *Centre for Disruptive Photonic Technologies*, in Singapore. We firstly noticed that, although interesting, the predictions made on a QE with a V-configuration (that is one ground state and two excited states) are difficult to realize experimentally, and the predicted coherence is lost once the atom has decayed by spontaneous emission. In Section 5.2, we studied a multilevel QE with a Λ-configuration (that is one excited level and two ground states). For such a configuration, our calculations predict a long-lifetime coherence induced by an anisotropic quantum vacuum, which is much more promising regarding experimental observations. We studied several designs for the metasurface in Section 5.3, in order to create this anisotropic quantum vacuum, using a *resonant-phase* approach and a *geometric phase* approach. Finally in in Chapter 6, we present the cold atom platform aimed at realizing this experiment with a cesium atom. The experiment is carried out in three stages: the first one is to trap and cool an ultra-cold atomic cloud of cesium atoms using a magneto-optical trap; the second step would be to design a *new* trap for a single atom, using a superoscillatory spot [36], and whose main advantage is the subwavelength size which is required to position the atom with a precision of about λ_0^3 which is required by this experiment; the third stage would be to interface the single trap atom with the metasurface, and to measure the predicted coherence between the two ground states using a tomography technique. We present the experimental set-up in Section 6.2, and we then provide technical details of the work done in the implementation of the set-up in Section 6.3, and finally we present the first measurements of the cold atomic cloud temperature in Section 6.4, which validates the first stage of the experiment.

Bibliography

[1] A. Auffèves, D. Gerace, J.-M. Gérard, M. F. Santos, L. Andreani, and J.-P. Poizat, Physical Review B **81**, 245419 (2010).

[2] A. Einstein, Physikalische Zeitschrift **18**, 121 (1917).

[3] D. Bouchet and R. Carminati, Journal of the Optical Society of America A **36**, 186 (2019).

[4] V. Weisskopf and E. Wigner, Zeitschrift für Physik **63**, 54 (1930).

[5] E. M. Purcell, Physical Review **69**, 681 (1946).

[6] P. W. Milonni and P. Knight, Optics Communications **9**, 119 (1973).

[7] D. Kleppner, Physical Review Letters **47**, 233 (1981).

[8] A. Kofman and G. Kurizki, Nature **405**, 546 (2000).

[9] K. Drexhage, Journal of luminescence **1**, 693 (1970).

[10] R. G. Hulet, E. S. Hilfer, and D. Kleppner, Physical Review Letters **55**, 2137 (1985).

[11] B. Misra and E. Sudarshan, Journal of Mathematical Physics **18**, 756 (1977).

[12] P. Goy, J. Raimond, M. Gross, and S. Haroche, Physical Review Letters **50**, 1903 (1983).

[13] E. T. Jaynes and F. W. Cummings, Proceedings of the IEEE **51**, 89 (1963).

[14] S. Haroche and D. Kleppner, Physics Today **42**, 24 (1989).

[15] R. Thompson, G. Rempe, and H. Kimble, Physical Review Letters **68**, 1132 (1992).

[16] Y. Zhu, D. J. Gauthier, S. Morin, Q. Wu, H. Carmichael, and T. Mossberg, Physical Review Letters **64**, 2499 (1990).

[17] I. Pockrand, A. Brillante, and D. Möbius, The Journal of Chemical Physics **77**, 6289 (1982).

[18] H. Gersen, M. F. García-Parajó, L. Novotny, J. Veerman, L. Kuipers, and N. F. van Hulst, Physical Review Letters **85**, 5312 (2000).

[19] P. Anger, P. Bharadwaj, and L. Novotny, Physical Review Letters **96**, 113002 (2006).

[20] S. Kühn, U. Håkanson, L. Rogobete, and V. Sandoghdar, Physical Review Letters **97**, 017402 (2006).

[21] B. Kolaric, B. Maes, K. Clays, T. Durt, and Y. Caudano, Advanced Quantum Technologies **1**, 1800001 (2018).

[22] A. F. Koenderink, ACS Photonics **4**, 710 (2017).

[23] F. Marquier, C. Sauvan, and J.-J. Greffet, ACS Photonics **4**, 2091 (2017).

[24] D. G. Baranov, M. Wersall, J. Cuadra, T. J. Antosiewicz, and T. Shegai, ACS Photonics **5**, 24 (2017).

[25] G. Hétet, L. Slodička, A. Glätzle, M. Hennrich, and R. Blatt, Physical Review A **82**, 063812 (2010).

[26] P. K. Jha, X. Ni, C. Wu, Y. Wang, and X. Zhang, Physical Review Letters **115**, 025501 (2015).

[27] G. Agarwal, Physical Review Letters **84**, 5500 (2000).

[28] W. Jhe, A. Anderson, E. Hinds, D. Meschede, L. Moi, and S. Haroche, Physical Review Letters **58**, 666 (1987).

[29] P. K. Jha, N. Shitrit, J. Kim, X. Ren, Y. Wang, and X. Zhang, ACS Photonics **5**, 971 (2017).

[30] H. Moses, Physical Review A **8**, 1710 (1973).

[31] J. Seke, Physica A **203**, 269 (1994).

[32] A. F. Koenderink, Optics Letters **35**, 4208 (2010).

[33] P. T. Kristensen, C. Van Vlack, and S. Hughes, Optics Letters **37**, 1649 (2012).

[34] C. Sauvan, J.-P. Hugonin, I. Maksymov, and P. Lalanne, Physical Review Letters **110**, 237401 (2013).

[35] E. Muljarov and W. Langbein, Physical Review B **94**, 235438 (2016).

[36] J. Baumgartl, S. Kosmeier, M. Mazilu, E. T. Rogers, N. I. Zheludev, and K. Dholakia, Applied Physics Letters **98**, 181109 (2011).

Part I

Monitored spontaneous emission

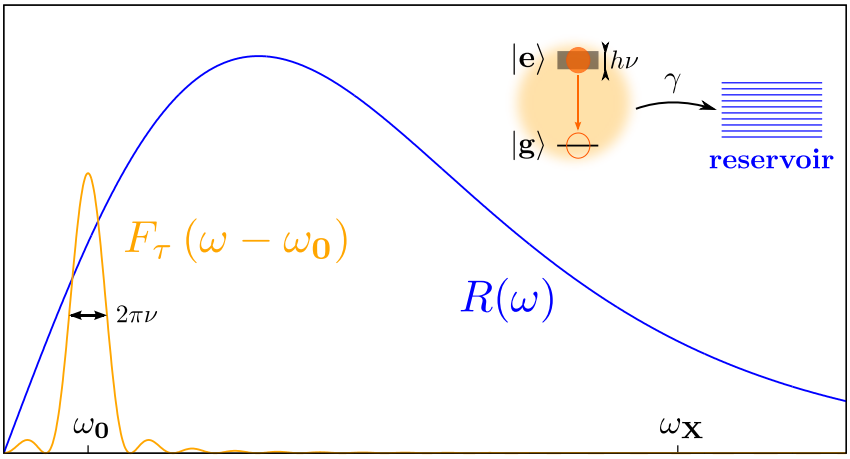

CHAPTER 1

Anti-Zeno Effect in hydrogen-like atoms

1.1 Introduction

One of the more peculiar features of quantum mechanics is that the measurement process can modify the evolution of a quantum system. The archetypes of this phenomenon are the quantum Zeno effect (QZE) and the quantum anti-Zeno effect (AZE) [1, 2]. The QZE refers to the inhibition of the decay of an unstable quantum system due to frequent measurements [3], and was observed experimentally for the first time with trapped ions [4, 5] and more recently in cold neutral atoms [6]. The opposite effect, where the decay is *accelerated* by frequent measurements, was first called the AZE in Ref. [7], and was discovered theoretically for spontaneous emission in cavities [8, 9], and first observed in a tunneling experiment with cold atoms (along with the QZE) [10], and recently with a single superconducting qubit coupled to a waveguide cavity [11]. However, despite predictions that the AZE should be much more ubiquitous than the QZE in radiative decay processes [1], it has never been observed to our knowledge for atomic radiative decay (spontaneous emission) in free space.

Here, we investigate the case of hydrogen-like atoms, for which the exact expression of the coupling between the atom and the free radiative field (*cf.* [12, 13]) allows us to derive an analytical expression for the measurement-modified decay rate. From this, we find that only non-electric-dipole transitions can exhibit the AZE in free space (*i.e.* non-dipole electric transitions *and* magnetic transitions of *any* multipolar order), which drastically limits the experimental possibilities to observe this effect. We start with a presentation of the general formal results about the measurement-modified decay rate in Section 1.2, and we then apply, in Section 1.3, this general framework to the case of electronic transitions in hydrogen-like atoms to derive an analytical expression of the measurement-modified decay rate in free space. Then, we discuss the experimental realizability of the described phenomenon in Section 1.4, and we identify a potential candidate: the electric quadrupole transition between $D_{5/2}$ and $S_{1/2}$ in Ca^+ or Sr^+.

1.2 Monitored spontaneous emission: general analysis

We consider a two-level atom in free space with a lower level (ground state) and a upper level (excited state), initially prepared in the excited state. The atom will eventually decay to the ground state with the emission of a photon whose energy is equal to the difference of energy between the two atomic levels. To understand this phenomenon, called ***spontaneous emission****, one must consider the coupling of the atom with the quantized radiation in the vacuum. We first briefly recall the formalism necessary to describe the interaction of an atom with the quantized radiation. Then, we examine how repeated observations (aimed at detecting whether the atom has decayed or not) can modify the decay, and we present the theory of monitored spontaneous emission.*

1.2.1 Hamiltonians

Atomic Hamiltonian

The Hamiltonian of the two-level atomic system reads, in the second-quantized form (see [14], chapter 4.9):

$$\hat{H}_A = \hbar\omega_g \left|g\right\rangle \left\langle g\right| + \hbar\omega_e \left|e\right\rangle \left\langle e\right| \tag{1.1}$$

where $|g\rangle$ (for ground state) and $|e\rangle$ (for excited state) are the eigen-states of $\hat{H}_A$ with associated eigen-energies $\hbar\omega_g$ and $\hbar\omega_e$, respectively. The transition (Bohr) frequency is defined as $\omega_0 \equiv \omega_e - \omega_g$.

Radiation field Hamiltonian

To get the Hamiltonian of the electromagnetic (EM) field (or radiation field), we follow the standard canonical quantization procedure introducing a fictitious[1] volume V. In this procedure, one expands the EM field onto EM modes (which are the most elementary solution of the Maxwell's equations), that we choose to be *polarized travelling plane monochromatic wave* (but other types of modes exist). Such a mode, labelled by j, is characterized by its frequency ω_j, its wavevector $\mathbf{k}_j$ whose modulus verifies $|\mathbf{k}_j| = \omega_j/c$, and its polarization vector $\vec{\varepsilon}_j$ such that $\vec{\varepsilon}_j \cdot \mathbf{k}_j = 0$. The energy of a mode in the quantization volume V, taking periodic boundary conditions, has the same form as the one of a *harmonic oscillator* (see [15]). The total energy of the EM field is the sum of the energies of all modes without any cross-terms (this result is not trivial). This decoupling allows to easily perform the canonical quantization (a procedure elaborated by Dirac in his thesis in 1925) of the total EM field, whose quantum Hamiltonian reads (see [16], chapter 4.5):

$$\hat{H}_R = \sum_j \hbar\omega_j \left(\hat{a}_j^\dagger \hat{a}_j + \frac{1}{2}\right) \quad \text{where} \quad \left[\hat{a}_j, \hat{a}_k^\dagger\right] = \delta_{jk} \tag{1.2}$$

[1] The introduction of a finite quantization volume is not absolutely necessary for quantizing the EM field, but it is convenient because it simplifies the mathematics as we will see.

where $\hat{a}_j$ and $\hat{a}_j^\dagger$ are, respectively, the photon annihilation and creation operators for the mode j with frequency ω_j, and δ_{jk} is the Kronecker delta. The subscript R stands for "radiation". This remarkable result suggests that the quantized EM field, in the absence of charges, can be considered as a set of quantum harmonic oscillators independent of each other, as shown by the fact that the radiation Hamiltonian is the sum of each individual Hamiltonians $\hat{H}_j = \hbar\omega_j(\hat{a}_j^\dagger\hat{a}_j + \frac{1}{2})$, and that the ladder operators $\hat{a}_j$ and $\hat{a}_k^\dagger$ for different oscillators *do* commute.

Interaction Hamiltonian

The interaction Hamiltonian which accounts for the coupling of the atom with the quantized EM field is given in the Coulomb gauge (and in SI units) by (see [16], chapter 6):

$$\hat{H}_I = \frac{e}{m_e}\hat{\mathbf{A}}(\hat{\mathbf{r}})\cdot\hat{\mathbf{p}}\,, \tag{1.3}$$

with e the elementary electric charge, m_e the electron mass, $\hat{\mathbf{r}}$ and $\hat{\mathbf{p}}$ are the position and linear momentum operators of the electron, respectively, and $\hat{\mathbf{A}}$ the vector potential operator of the quantized EM field. In writing Eq. (1.3), we consider only one-electron hydrogen-like atoms (in the sense that they have a *single* atomic electron orbiting around the atomic nucleus). We also neglect the term relative to the nucleus (smaller by a factor m_e/M, where M is the mass of the nucleus), and finally we neglect the term $\propto \hat{\mathbf{A}}^2$ (see Eq. (6.69) in [16]). The interaction Hamiltonian (1.3) derives from the so-called *minimal-coupling* form of the total Hamiltonian, and is known as the $\mathbf{A}\cdot\mathbf{p}$ form (see [14], chapter 4.8). There exist other forms for the interaction Hamiltonian, and our choice is dictated by the fact that (1.3) is more convenient for the multipolar treatment that will follow.

1.2.2 Time-dependent perturbation theory

General result

To study the interaction between the atom and the quantized EM field, one must consider the whole system {atom + EM field}. In particular, in order to describe the spontaneous emission phenomenon, we restrict the Hilbert space of the atom and EM field states to the subspace consisting of the atomic ground and excited states, and of the EM field vacuum state and one-photon states. In addition to this, we will make the rotating wave approximation (RWA), which consists in dropping the terms in the interaction Hamiltonian that couple the {atomic excited state + one-photon state} with the {atomic ground state + vacuum state}. Mathematically, this means that the system is described by the state:

$$|\psi(t)\rangle = \alpha(t)\,\mathrm{e}^{-\mathrm{i}\omega_0 t}\,|\mathrm{e},0\rangle + \sum_j \beta_j(t)\,\mathrm{e}^{-\mathrm{i}\omega_j t}\,|\mathrm{g},1_j\rangle \tag{1.4}$$

where $|\mathrm{g},1_j\rangle \equiv |\mathrm{g}\rangle\otimes|1_j\rangle$ is the tensor product between the atomic state $|\mathrm{g}\rangle$ and the state of the EM field $|1_j\rangle$ containing one photon in the mode j and the vacuum in all other modes (this is called a *one-photon state*) and $|\mathrm{e},0\rangle \equiv |\mathrm{e}\rangle\otimes|0\rangle$ is the tensor product between the

atomic state $|\mathrm{e}\rangle$ and the vacuum state of the EM field $|0\rangle$. In writing the state of the system in this form, the zero of energy is taken at the level of the ground state $|\mathrm{g}\rangle$ ($\hbar\omega_g = 0$), and we considered the energy associated to a one-photon state $\hbar\omega_\mathrm{j}$ by taking the *infinite* energy of the vacuum $E_v = \sum_\mathrm{j} \hbar\omega_\mathrm{j}/2$ as a reference (this is called *renormalization*). Therefore, $\hat{H}_A$ reduces to $\hat{H}_A = \hbar\omega_0 |\mathrm{e}\rangle\langle\mathrm{e}|$ and $\hat{H}_R$ is recast in the form $\hat{H}_R = \sum_\mathrm{j} \hbar\omega_\mathrm{j} \hat{a}_\mathrm{j}^\dagger \hat{a}_\mathrm{j}$. To know the dynamics, one must get the coefficients $\alpha(t)$ and $\beta_\mathrm{j}(t)$ by solving the Schrödinger equation

$$\mathrm{i}\hbar \frac{\mathrm{d}|\psi(t)\rangle}{\mathrm{d}t} = \hat{H}|\psi(t)\rangle \tag{1.5}$$

with $\hat{H} = \hat{H}_A + \hat{H}_R + \hat{H}_I$ and with the initial condition $|\psi(0)\rangle = |\mathrm{e},0\rangle$ (*i.e.*, $\alpha(0) = 1$ and $\forall \mathrm{j}$ $\beta_\mathrm{j}(0) = 0$) corresponding to the atom initially in the excited state $|\mathrm{e}\rangle$ and no photons in the EM field. One then obtains the following differential equations fullfilled by the coefficients $\alpha(t)$ and $\beta_\mathrm{j}(t)$ (taking into account the fact that as $\{|0\rangle, |1_\mathrm{j}\rangle\}$ are eigen-states of $\hat{H}_R$ — often called Fock states, $\{|\mathrm{e},0\rangle, |\mathrm{g},1_\mathrm{j}\rangle\}$ are eigen-states of the Hamiltonian $\hat{H}_A + \hat{H}_R$):

$$\mathrm{i}\dot{\alpha}(t) = \sum_\mathrm{j} g_\mathrm{j}^* \beta_\mathrm{j}(t)\, \mathrm{e}^{\mathrm{i}(\omega_0 - \omega_\mathrm{j})t}, \tag{1.6}$$

$$\mathrm{i}\dot{\beta}_\mathrm{j}(t) = g_\mathrm{j}\alpha(t)\, \mathrm{e}^{-\mathrm{i}(\omega_0 - \omega_\mathrm{j})t} \tag{1.7}$$

where we introduced the **coupling constant** g_j defined by:

$$\hbar g_\mathrm{j} \equiv \langle \mathrm{g}, 1_\mathrm{j}|\hat{H}_I|\mathrm{e},0\rangle \qquad \text{Unit:} \quad \left[g_\mathrm{j}\right] = \mathrm{s}^{-1}. \tag{1.8}$$

By formally integrating Eq. (1.7) together with the initial condition $\beta_\mathrm{j}(0) = 0$, one gets:

$$\mathrm{i}\beta_\mathrm{j}(t) = g_\mathrm{j} \int_0^t \mathrm{d}t'\, \alpha(t') \mathrm{e}^{-\mathrm{i}(\omega_0 - \omega_\mathrm{j})t'} \tag{1.9}$$

and inserting this expression into Eq. (1.6) gives:

$$\boxed{\dot{\alpha}(t) = -\sum_\mathrm{j} |g_\mathrm{j}|^2 \int_0^t \mathrm{d}t'\, \alpha(t') \mathrm{e}^{\mathrm{i}(\omega_0 - \omega_\mathrm{j})(t-t')}}. \tag{1.10}$$

Up to now, no approximations have been made, and Eq. (1.10) is exact. We proceed now by using perturbation theory, which is motivated by the double fact that (i) we are interested in the short-time behavior of the system (when $\alpha(t) \simeq \alpha(0) = 1$) and moreover (ii) we suppose that the coupling between the atom and the quantized EM field is weak (*i.e.*, the coupling constants g_j are small compared to the matrix elements of the non-interacting Hamiltonian $\hat{H}_0 = \hat{H}_A + \hat{H}_R$, with $\hat{H}_A$ and $\hat{H}_R$ given by Eqs. (1.1) and (1.2), respectively) (see [17], chapter 5.2). To get the first-order perturbative solution, we set $\alpha(t') = 1$ in the right-hand side of Eq. (1.10) and get

$$\begin{aligned} \dot{\alpha}(t) &\simeq -\sum_\mathrm{j} |g_\mathrm{j}|^2 \int_0^t \mathrm{d}t'\, \mathrm{e}^{\mathrm{i}(\omega_0 - \omega_\mathrm{j})(t-t')} \\ &= -\sum_\mathrm{j} |g_\mathrm{j}|^2 \times \frac{\mathrm{e}^{\mathrm{i}(\omega_0 - \omega_\mathrm{j})t} - 1}{\mathrm{i}(\omega_0 - \omega_\mathrm{j})} \\ &= -\sum_\mathrm{j} |g_\mathrm{j}|^2 \times h\left(\omega_0 - \omega_\mathrm{j}, t\right) \times t \end{aligned} \tag{1.11}$$

where we introduced the function $h(\omega,t)$ defined by:

$$h(\omega,t)\equiv\frac{1}{\mathrm{i}\omega t}(\mathrm{e}^{\mathrm{i}\omega t}-1)\,. \tag{1.12}$$

We proceed as previously by formally integrating Eq. (1.11) together with the initial condition $\alpha(0)=1$, to get:

$$\begin{aligned}\alpha(t)&\simeq 1-\sum_{\mathrm{j}}|g_{\mathrm{j}}|^2\int_0^t \mathrm{d}t'\,h\left(\omega_0-\omega_{\mathrm{j}},t'\right)\times t'\\&=1-\sum_{\mathrm{j}}|g_{\mathrm{j}}|^2\times\mathrm{i}\times\frac{1-h(\omega_0-\omega_{\mathrm{j}},t)}{\omega_0-\omega_{\mathrm{j}}}\times t\,.\end{aligned} \tag{1.13}$$

To compute the survival probability $P_{\mathrm{surv}}(t)$ defined as

$$\begin{aligned}P_{\mathrm{surv}}(t)&\equiv|\,\langle \mathrm{e},0|\psi(t)\rangle\,|^2\\&=|\alpha(t)|^2\,,\end{aligned} \tag{1.14}$$

we will ignore the second-order contributions (*i.e.*, the term $\propto\left[\sum_{\mathrm{j}}|g_{\mathrm{j}}|^2\right]^2$) because we already neglected contributions of this order in obtaining Eq. (1.13) for $\alpha(t)$. Then the first order perturbative solution for the probability $P_{\mathrm{surv}}(t)$ is:

$$\begin{aligned}P_{\mathrm{surv}}(t)&=|\alpha(t)|^2\\&\simeq 1-2\times\mathrm{Re}\left(\sum_{\mathrm{j}}|g_{\mathrm{j}}|^2\times\mathrm{i}\times\frac{1-h(\omega_0-\omega_{\mathrm{j}},t)}{\omega_0-\omega_{\mathrm{j}}}\times t\right)\\&=1-2\times\sum_{\mathrm{j}}|g_{\mathrm{j}}|^2\times\mathrm{Re}\left(\mathrm{i}\times\frac{1-h(\omega_0-\omega_{\mathrm{j}},t)}{\omega_0-\omega_{\mathrm{j}}}\right)\times t\\&=1-2\times\sum_{\mathrm{j}}|g_{\mathrm{j}}|^2\times\mathrm{Im}\left(\frac{h(\omega_0-\omega_{\mathrm{j}},t)}{\omega_0-\omega_{\mathrm{j}}}\right)\times t\end{aligned} \tag{1.15}$$

Moreover, one can easily show that

$$\mathrm{Im}\left(\frac{h(\omega_0-\omega_{\mathrm{j}},t)}{\omega_0-\omega_{\mathrm{j}}}\right)=\frac{1}{2}\,t\,\mathrm{sinc}^2\left(\frac{(\omega_0-\omega_{\mathrm{j}})t}{2}\right) \tag{1.16}$$

with $\mathrm{sinc}(x)\equiv\sin(x)/x$ and thus:

$$P_{\mathrm{surv}}(t)=1-\sum_{\mathrm{j}}|g_{\mathrm{j}}|^2\times t\,\mathrm{sinc}^2\left(\frac{(\omega_0-\omega_{\mathrm{j}})t}{2}\right)\times t\,. \tag{1.17}$$

Finally, Eq. (1.17) can be recast in the form

$$\boxed{P_{\mathrm{surv}}(t)=1-2\pi\int_0^\infty \mathrm{d}\omega\,R(\omega)\,F_t(\omega-\omega_0)\times t} \tag{1.18}$$

where

$$\boxed{R(\omega)\equiv\sum_{\mathrm{j}}|g_{\mathrm{j}}|^2\,\delta(\omega-\omega_{\mathrm{j}})} \qquad \text{Unit:}\quad [R(\omega)]=\mathrm{s}^{-1} \tag{1.19}$$

and

$$\boxed{F_t(\omega-\omega_0)\equiv\frac{t}{2\pi}\mathrm{sinc}^2\left(\frac{(\omega-\omega_0)\,t}{2}\right)} \qquad \text{Unit:}\quad [F_t(\omega-\omega_0)]=\mathrm{s}\,. \tag{1.20}$$

Quasi-continuum and density of states The one-photon states $|1_j\rangle$ in the fictitious box of volume V (which is assumed to be large compared to λ_0^3 where $\lambda_0 = 2\pi c/\omega_0$) represent a *quasi-continuum*, *i.e.* they form an ensemble of discrete states very close in frequency (and a real continuum when one allows the dimensions of the box to tend to infinity). Moreover, they form a *degenerate* quasi-continuum, which means that for a given frequency ω_j, there are many one-photon states. Indeed, for a given frequency ω_j, there are many modes differing only by their polarization and propagation direction. It is convenient to introduce the concept of **density of states** $\rho(\omega)$, which is equal to the number of quasi-continuum states in the frequency range from ω to $\omega + d\omega$ divided by the frequency width of this interval $d\omega$, and to replace the discrete sum in Eq. (1.19) by

$$\boxed{R(\omega) \longrightarrow \overline{|g(\omega)|^2}\,\rho(\omega)} \qquad \text{Unit:} \quad [\rho(\omega)] = \text{s} \tag{1.21}$$

where $\overline{|g(\omega)|^2}$ corresponds to $|g_j|^2 = \hbar^{-2}|\langle g, 1_j|\hat{H}_I|e, 0\rangle|^2$ *averaged over all one-photon states with* $\omega_j = \omega$ (*i.e.* averaged over all emission directions and polarizations).

Therefore, the function $R(\omega)$, which is a property of the interaction Hamiltonian $\hat{H}_I$, represents the density of states $\rho(\omega)$ weighted by the coupling strengths $\overline{|g(\omega)|^2}$, and will be called the **reservoir coupling spectrum**. The function $F_t(\omega - \omega_0)$ shows the broadening of ω_0 at very short times. In a sense, it represents the range of frequencies "seen" by the atom in which it can decay. We will call it the **atomic spectral profile**.

First limiting case: the Zeno regime

Even if Eq. (1.18) has been derived for a two-level atom coupled to the EM field in *free space*, it holds for any type of environment provided that the perturbation treatment still holds. In practice, the reservoir $R(\omega)$ of the environment has a center of weight ω_c and a bandwidth $\Delta\omega_c$ which determines the effective range of integration in Eq. (1.18), and is most conveniently described by the quality factor $Q_c \equiv \omega_c/\Delta\omega_c$. For very short times for which

$$\omega_c\, t \ll Q_c \quad \text{and} \quad \omega_c\, t \ll \frac{\omega_c}{|\omega_c - \omega_0|} \tag{1.22}$$

the argument in the $\text{sinc}(x)$ appearing in the function $F_t(\omega - \omega_0)$ is close to zero and $\text{sinc}(x)$ can be approximated by 1. Thus, $F_t(\omega - \omega_0) \sim t/(2\pi)$ and Eq. (1.18) reduces to

$$P_{\text{surv}}(t) \simeq 1 - C \times t^2 \quad \text{where} \quad C \equiv \int_0^\infty R(\omega)\, d\omega\,. \tag{1.23}$$

This t^2 dependence is characteristic of what is known as the *quantum Zeno regime* for a reason that will be explained later. The condition (1.22) can be easily met for a very peaked and narrow reservoir centered on ω_0 ($Q_c \to \infty$, $\omega_c = \omega_0$) like a resonant cavity for instance, whereas for the limit of an unbounded flat continuum ($Q_c \to 0$), this time interval shrinks to zero.

Second limiting case: the Fermi golden rule regime

Very quickly, for

$$\omega_c\, t \gg Q_c \quad \text{and} \quad \omega_c\, t \gg \frac{\omega_c}{|\omega_c - \omega_0|} \tag{1.24}$$

(but not for too long times so that the perturbative treatment still holds), one has:

$$F_t\,(\omega - \omega_0) = \frac{t}{2\pi}\mathrm{sinc}^2\left(\frac{(\omega-\omega_0)\,t}{2}\right) \longrightarrow \delta\,(\omega - \omega_0) \tag{1.25}$$

and therefore Eq. (1.18) becomes

$$P_{\mathrm{surv}}\,(t) \simeq 1 - \gamma_0 t \tag{1.26}$$

where the decay rate γ_0 reads

$$\gamma_0 \equiv 2\pi R(\omega_0) = 2\pi\,\overline{|g(\omega_0)|^2}\,\rho\,(\omega_0) \qquad \text{Unit:} \quad [\gamma_0] = \mathrm{s}^{-1} \tag{1.27}$$

This is the **Fermi golden rule (FGR)**. Note that according to the FGR, only the one-photon states of frequency ω_0 contribute to the decay. In Appendix 1.A, we explicitely calculate $\overline{|g(\omega_0)|^2}$ and recover the well-known expression for the decay rate in vacuum. Moreover, when one goes beyond a perturbative treatment, the survival probability $P_{\mathrm{surv}}(t)$ decays exponentially at a rate given by the FGR, and the present perturbative solution is simply the short-time expansion of the exponential behavior $P_{\mathrm{surv}}(t) = \mathrm{e}^{-\gamma_0 t}$. The exponential decay is known as the **Wigner-Weisskopf decay** (see [17], chapter 5.3), in reference to the method developped by Wigner and Weisskopf to calculate the non-perturbative long-time solution in 1930 [18]. Note that a secondary result of the calculation of Wigner and Weisskopf is that the atom emission spectrum is a Lorentzian curve of width γ_0.

1.2.3 Monitored spontaneous emission: quantum Zeno and anti-Zeno effects

In this section, we want to know what happens when the unstable atom is being continuously observed (monitored). According to one of the axioms of quantum mechanics, an observation (measurement) corresponds to an ideal instantaneous projection onto an eigenstate of the system. We therefore study how the evolution of the system is modified if n frequent projections onto the state $|\mathrm{e}\rangle$ are performed every time τ during a period $t = n\tau$. The probability that no decay occurs during a period $t = n\tau$ is then defined as:

$$P_{\mathrm{moni}}\,(t = n\tau) \equiv \underbrace{P_{\mathrm{surv}}\,(\tau) \times \ldots \times P_{\mathrm{surv}}\,(\tau)}_{n\,\text{times}} = [P_{\mathrm{surv}}\,(\tau)]^n \ . \tag{1.28}$$

In the Zeno regime

In the Zeno regime for which the survival probability is given by Eq. (1.23), when n frequent projections onto the state $|\mathrm{e}\rangle$ are performed every time τ during a period $t = n\tau$,

the probability (1.28) reads:

$$\begin{aligned} P_{\text{moni}}(t=n\tau) &= \left(1-C\times\tau^2\right)^n \\ &= \left[1-C\times\left(\frac{t}{n}\right)^2\right]^n \qquad (\tau=\frac{t}{n}) \\ &\simeq 1-C\times\frac{t^2}{n} \qquad \text{(Taylor expansion to first order)} \end{aligned} \tag{1.29}$$

and in the limit of "continuous measurements" ($\lim_{n\to\infty}$),

$$\lim_{n\to\infty} P_{\text{moni}}(t=n\tau) = 1\,. \tag{1.30}$$

This result means, according to Misra and Sudarshan [3] that: "[...] an unstable particle which is continuously observed to see whether it decays will never be found to decay!". They called this phenomenon the "Zeno's paradox in quantum theory", also known as the **quantum Zeno effect**, in reference to the Greek philosopher Zeno and his arrow paradox.

In the Fermi regime

Contrary to the quantum Zeno effect, in the Fermi regime, where the survival probability is given by Eq. (1.26), if n frequent projections onto the state $|e\rangle$ are performed at every time τ during a period $t=n\tau$, then the probability (1.28) reads:

$$\begin{aligned} P_{\text{moni}}(t=n\tau) &= (1-\gamma_0\tau)^n \\ &= \left(1-\gamma_0\frac{t}{n}\right)^n \qquad (\tau=\frac{t}{n}) \\ &= \exp\left[n\log\left(1-\gamma_0\frac{t}{n}\right)\right] \\ &\simeq \exp\left[n\left(-\gamma_0\frac{t}{n}\right)\right] \qquad (n\to+\infty) \\ &= \exp(-\gamma_0 t) \end{aligned} \tag{1.31}$$

and one can see that there is no modification of the decay under frequent measurements.

In the general case

We now come back to the more general result for the survival probability given by Eq. (1.18) and we want to see what happens when the atom in the excited state is being frequently monitored at a rate $\nu=1/\tau$ (n measurements during the interval $t=n\tau$). The probability (1.28) reads:

$$\begin{aligned} P_{\text{moni}}(t=n\tau) &= \left(1-2\pi\int_0^\infty \mathrm{d}\omega\, R(\omega)\, F_\tau(\omega-\omega_0)\times\tau\right)^n \\ &= \left(1-2\pi\int_0^\infty \mathrm{d}\omega\, R(\omega)\, F_\tau(\omega-\omega_0)\times\frac{t}{n}\right)^n \qquad (\tau=\frac{t}{n}) \\ &\simeq \exp(-\gamma t) \end{aligned} \tag{1.32}$$

where γ is the **measurement-modified decay rate** and reads [1]:

$$\boxed{\gamma \equiv 2\pi \int_0^\infty \mathrm{d}\omega\, R(\omega) F_\tau(\omega - \omega_0)}\,. \tag{1.33}$$

Eq. (1.33) represents a universal result: the decay rate of a frequently monitored two-level atom is simply the overlap of the reservoir coupling spectrum and the *broadened* spectral profile

$$F_\tau(\omega - \omega_0) = \frac{\tau}{2\pi}\mathrm{sinc}^2\left((\omega - \omega_0)\frac{\tau}{2}\right) \tag{1.34}$$

due to the frequent measurements at a rate $\nu = 1/\tau$, and whose frequency broadening is about ν. A graph of $F_\tau(\omega - \omega_0)$ is shown on Fig. 1.1 (orange line).

The broadening of the atomic spectral profile (1.34) can be interpreted as the fact that frequent measurements on an excited two-level atom, *i.e.* repeated instantaneous projections onto the state $|\mathrm{e}\rangle$, lead to a broadening of its energy level. This is analogous to collision broadening which induces a linewidth equal to the collision rate ν (see [14], chapter 2.9). Therefore, the atom probes a larger range of EM modes in the reservoir spectrum, and these new decay channels might modify the dynamics. Indeed, depending on the profile of $R(\omega)$ in the bandwidth $2\pi\nu$ around ω_0, the system may experience an acceleration ($\gamma > \gamma_0$), called the **quantum anti-Zeno effect (AZE)**, or a deceleration ($\gamma < \gamma_0$) called the **quantum Zeno effect (QZE)**, of the decay compared to the measurement-free decay whose rate is given by the FGR decay rate γ_0.

Note that the result of Eq. (1.29) for the probability in the Zeno regime will be valid at all times for a reservoir of the type $R(\omega) \approx C\delta(\omega - \omega_0)$, and the FGR result of Eq. (1.31) for a spectrally flat and unbounded reservoir $R(\omega) = R(\omega_0)$ for $-\infty < \omega < +\infty$.

The integral (1.33) can in principle be evaluated once the function $R(\omega)$ is specified. In the following, we aim at investigating the case of hydrogen-like atoms coupled to the free space EM field, for which the function $R(\omega)$ can be calculated analytically. This will allow us to highlight the conditions for an AZE observation in such systems. Before doing so, however, it is worth mentioning that in the perturbative treatment that we use, Eqs. (1.33) and (1.19) are valid to the first order (*i.e.* only one-photon processes are considered), and do not include higher-order contributions (*i.e.* two-photon and many-photon processes). For this approximation to be valid, we need to ensure that, compared to the spontaneous single-photon emission of the $|\mathrm{e}\rangle \to |\mathrm{g}\rangle$ transition considered, two-photon processes, which involve other atomic levels, are negligible. This can only be checked on a case-by-case basis for specific atoms. In Sec. 1.4, we consider the specific case of the electric quadrupole transition of Ca^+, and we check that the single-photon emission is the dominant decay channel from the relevant excited state (in Sec. 1.4.1).

1.3 Quantum anti-Zeno effect in hydrogen-like atoms

In a landmark article about the QZE and the AZE [1], Kofman and Kurizki demonstrated unambiguously that the QZE, i.e., the deceleration of the decay by frequent measurements,

is unattainable for atomic radiative decay (spontaneous emission) in free space. Moreover, they concluded that its counterpart, the AZE, appears to be ubiquitous: "By contrast, the condition [...] for the accelerated decay (AZE) trend is in principle realizable for decay into any reservoir, whether spectrally broad or narrow, and is therefore far more ubiquitous than the QZE". Here, making use of analytical results available for hydrogen-like atoms, we find that in free space, only non-electric-dipolar transitions should present an observable AZE, revealing that this effect is consequently much less ubiquitous than first predicted.

1.3.1 Reservoir coupling spectrum for hydrogen-like atoms

For hydrogen-like atoms in free space, it is useful to write the states of the (non-relativistic, spinless) atom in terms of the multipolar modes $|g\rangle = |n_g, l_g, m_g\rangle$ and $|e\rangle = |n_e, l_e, m_e\rangle$ where each atomic state is described by three discrete quantum numbers n_i, l_i and m_i which are respectively the principal, total angular momentum and magnetic quantum numbers. Similarly, it is useful to write the one-photon states in the energy-angular-momentum basis [12, 13] $|1_j\rangle = |J, M, \lambda, \omega\rangle$ where a photon is characterized by its angular momentum J, its magnetic quantum number M, its helicity λ and its frequency ω.

By making use of the interaction Hamiltonian in the minimal-coupling form [Eq. (1.3)] together with the **rotating-wave approximation**[2], one can obtain an analytic expression for the reservoir coupling spectrum (1.21) for hydrogen-like atoms in free space (the effects of the RWA on the QZE and AZE have been discussed in Refs. [19, 20], showing no essential differences between the predictions made with and without the RWA). Based on the exact calculations (in the non-relativistic approximation) of the matrix elements initiated by Moses [12] and completed by Seke [13], the reservoir coupling spectrum

[2] But we do NOT make the electric dipole approximation.

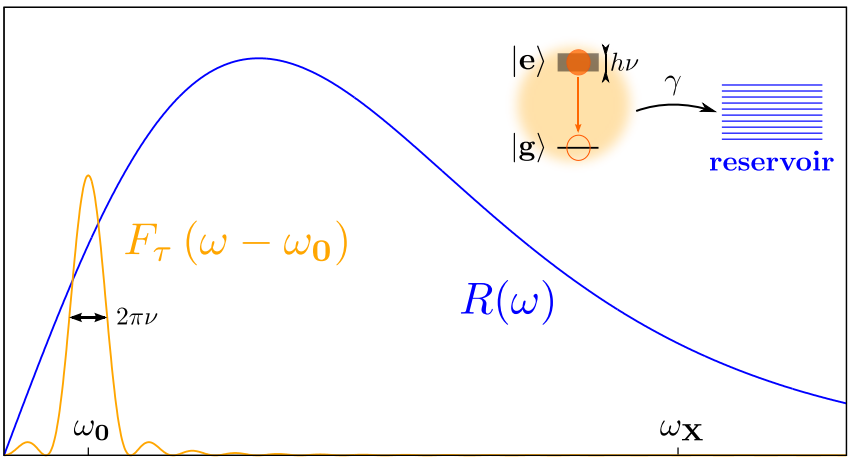

Figure 1.1 – Scheme of the broadened spectral profile $F_\tau(\omega - \omega_0)$ (orange line) of an atom with transition frequency ω_0 due to repeated measurements at a rate $\nu = 1/\tau$ with τ the interval between each measurement, and reservoir coupling spectrum $R(\omega)$ (blue line) of the form of Eq. (1.38) with a cutoff frequency $\omega_X \gg \omega_0$. The inset shows that the energy broadening of $|e\rangle$, induced by the frequent measurements at rate ν, changes its decay into the EM reservoir.

Transitions	$2P$-$1S$	$3D$-$1S$	$4F$-$1S$
η	1	3	5
μ	4	6	8
ω_X/ω_0	548.1	411.1	365.4

Table 1.1 – Parameters of the reservoir spectrum given by Eq. (1.38) for the electric transitions $2P$-$1S$ (dipole), $3D$-$1S$ (quadrupole) or $4F$-$1S$ (octupole) in the hydrogen atom.

reads (see Appendix 1.B for details)

$$\boxed{R(\omega)=\sum_{J=|l_\mathrm{e}-l_\mathrm{g}|}^{l_\mathrm{e}+l_\mathrm{g}}\sum_{r=0}^{N_J}\frac{D_{Jr}}{\omega_\mathrm{X}^{\eta_J+2r-1}}\frac{\omega^{\eta_J+2r}}{\left[1+\left(\frac{\omega}{\omega_\mathrm{X}}\right)^2\right]^\mu}} \tag{1.35}$$

where $\eta_J=1+2J$ for magnetic transitions, and $\eta_J=-1+2J$ for electric transitions with J starting at 1 for a dipole transition ($|l_\mathrm{e}-l_\mathrm{g}|=1$), 2 for a quadrupole transition ($|l_\mathrm{e}-l_\mathrm{g}|=2$) and so on; $\mu=2\big(n_\mathrm{g}+n_\mathrm{e}-1\big)$; D_{Jr} are dimensionless constants involving the Clebsch-Gordan coefficients of the transition under consideration; and ω_X is the non-relativistic cutoff frequency that emerges naturally from calculations [21, 22] and reads [13]:

$$\boxed{\omega_\mathrm{X}=Z\left(\frac{1}{n_\mathrm{g}}+\frac{1}{n_\mathrm{e}}\right)\frac{c}{a_0}} \tag{1.36}$$

where Z the atomic number and a_0 is the Bohr radius whose expression is

$$a_0=\frac{4\pi\epsilon_0\hbar^2}{m_e e^2}\qquad\text{Unit:}\quad[a_0]=\mathrm{m}\,. \tag{1.37}$$

Finally, the index at which the sum is terminated is $N_J=2\big(n_\mathrm{e}+n_\mathrm{g}\big)-4-J-l_\mathrm{e}-l_\mathrm{g}-\epsilon$ with $\epsilon=0$ for electric transitions and $\epsilon=1$ for magnetic transitions.

For simplicity, we first consider the case of electric transitions ($\epsilon=0$) between a state of maximal angular momentum ($l_\mathrm{e}=n_\mathrm{e}-1$) and the ground state $1S$ ($n_\mathrm{g}=1$, $l_\mathrm{g}=0$). Indeed, in this, case, one has $N_J=0$, and therefore the two sums disappear in Eq. (1.35) which reduces to

$$\boxed{R(\omega)=\frac{D}{\omega_\mathrm{X}^{\eta-1}}\frac{\omega^\eta}{\left[1+\left(\frac{\omega}{\omega_X}\right)^2\right]^\mu}} \tag{1.38}$$

where we defined $D\equiv D_{J0}$ and $\eta\equiv\eta_J$. This reservoir coupling spectrum is sketched on Fig. 1.1. The parameters η, μ and ω_X corresponding to the electric transitions $2P$-$1S$ (dipole), $3D$-$1S$ (quadrupole) or $4F$-$1S$ (octupole) whose reservoir coupling spectrum is of the form (1.38) are given in Table 1.1.

1.3.2 Analytical results for $\omega_0 \ll \omega_X$

Approximation

In this section, we want to derive an analytical expression of the measurement-modified decay rate (1.33) to see how it scales with the measurement rate ν when the reservoir coupling spectrum is of the form of Eq. (1.38). In order to derive analytical results, we will consider the case $\omega_0 \ll \omega_X$, which is always respected for low-Z atoms. Indeed, the Bohr formula for ω_0 is (valid for hydrogen-like atoms):

$$\hbar\omega_0 \equiv \hbar(\omega_\mathrm{e} - \omega_\mathrm{g}) = -Z^2 \mathrm{R_y}\left(\frac{1}{n_\mathrm{e}^2} - \frac{1}{n_\mathrm{g}^2}\right). \tag{1.39}$$

The Rydberg constant $\mathrm{R_y}$ is defined as (in unit of energy):

$$\mathrm{R_y} = \frac{m_e e^4}{32\pi^2\epsilon_0^2\hbar^2} = \frac{1}{2}\hbar\alpha\frac{c}{a_0} \qquad \text{Unit:} \quad [\mathrm{R_y}] = \mathrm{kg}\cdot\mathrm{m}^2\cdot\mathrm{s}^{-2}. \tag{1.40}$$

This constant corresponds to the energy necessary to ionize a hydrogen-like atom with a nucleus mass considered as infinite. In the right-hand-side, we introduced the fine structure constant of electrodynamics α which reads

$$\alpha = \frac{e^2}{4\pi\epsilon_0\hbar c} \tag{1.41}$$

such that ω_0 reads

$$\boxed{\omega_0 = -\frac{1}{2}Z^2\alpha\left(\frac{1}{n_\mathrm{e}^2} - \frac{1}{n_\mathrm{g}^2}\right)\frac{c}{a_0}}. \tag{1.42}$$

Thus, the ratio between ω_0 [Eq. (1.42)] and ω_X [Eq. (1.36)] can then be computed easily to give

$$\boxed{\frac{\omega_0}{\omega_\mathrm{X}} = \frac{1}{2}(Z\alpha)\left(\frac{1}{n_\mathrm{g}} - \frac{1}{n_\mathrm{e}}\right)}. \tag{1.43}$$

Since α is of approximate value $\alpha \simeq 1/137$, one can see from Eq. (1.43) that the assumption $\omega_0 \ll \omega_X$ makes sense for atoms with Z moderately small.

The derivation that follows is simply based on the following observation: taking a look on Fig. 1.1, one can reasonably consider that the total decay rate in Eq. (1.33) essentially results from two contributions:

(i) one from the central peak of the function $F_\tau(\omega-\omega_0)$ that probes the reservoir $R(\omega)$ in a frequency range of width $\sim 2\pi\nu$ around ω_0 and that we call the *resonant* contribution;

(ii) one from the tail $\propto 1/(\omega-\omega_0)^2$ of the function $F_\tau(\omega-\omega_0)$ that probes the rest of the reservoir for $\omega \gg \omega_0$ and that we call the *tail* contribution (the other tail contribution that probes the reservoir for $\omega \ll \omega_0$ will be negligible compared to the tail contibution for $\omega \gg \omega_0$).

Resonant contribution

To get an analytical scaling with ν of the *resonant* contribution, we make the following approximation of the sinc square function in $F_\tau(\omega-\omega_0)$ [Eq. (1.34)]:

$$\mathrm{sinc}^2\left((\omega-\omega_0)\frac{1}{2\nu}\right) \simeq \begin{cases} 1 & \text{for} \quad \omega_0-\pi\nu<\omega<\omega_0+\pi\nu \\ 0 & \text{otherwise} \end{cases} \tag{1.44}$$

which gives

$$F_\tau^{\mathrm{res}}(\omega-\omega_0) = \begin{cases} 1/(2\pi\nu) & \text{for} \quad \omega_0-\pi\nu<\omega<\omega_0+\pi\nu \\ 0 & \text{otherwise} \end{cases} \tag{1.45}$$

and is illustrated in Fig. 1.2. This approximation might seem coarse but it will be shown to be excellent, because the "door function" (green dashed curve in Fig. 1.2) is also centered on ω_0 with a similar width and it has the same area $\mathcal{A}=1$ as the $F_\tau(\omega-\omega_0)$ function [Eq. (1.34)]. In addition to this, in the frequency range of interest here (small range of width $\sim 2\pi\nu$ centered on ω_0), we only stand in the rising part of $R(\omega)$ (see Fig. 1.1), and therefore we can consider that $R(\omega) \underset{\omega_0}{\sim} D\omega^\eta/\omega_X^{\eta-1}$ (as $\omega_0 \ll \omega_X$). Using these approximations, one can write the resonant contribution of the decay rate

$$\begin{aligned} \gamma^{\mathrm{res}} &= 2\pi\int_0^\infty \mathrm{d}\omega\, R(\omega)\, F_\tau^{\mathrm{res}}(\omega-\omega_0) \\ &\simeq 2\pi\int_{\omega_0-\pi\nu}^{\omega_0+\pi\nu} \mathrm{d}\omega\, \frac{D}{\omega_X^{\eta-1}}\omega^\eta\frac{1}{2\pi\nu} \\ &= \frac{D}{\omega_X^{\eta-1}}\frac{1}{\nu}\frac{1}{\eta+1}\omega_0^{\eta+1}\left[\left(1+\frac{\pi\nu}{\omega_0}\right)^{\eta+1}-\left(1-\frac{\pi\nu}{\omega_0}\right)^{\eta+1}\right] \end{aligned} \tag{1.46}$$

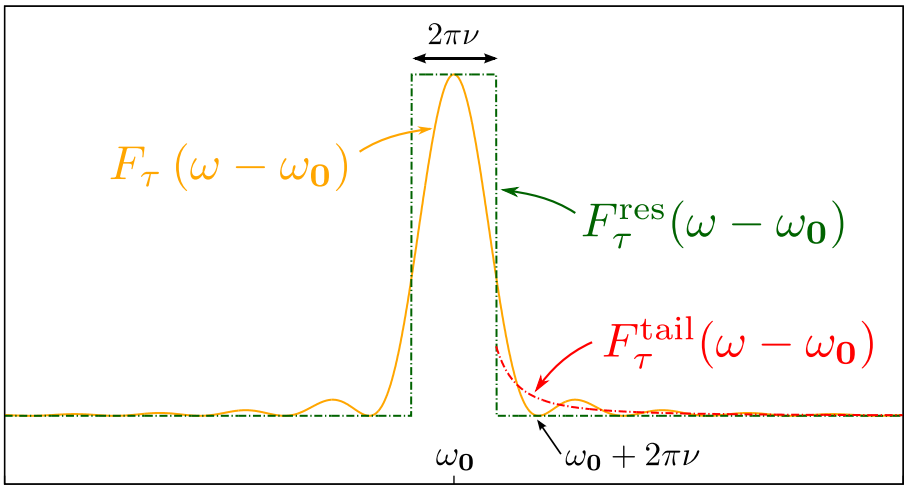

Figure 1.2 – Scheme of the broadened spectral profile $F_\tau(\omega-\omega_0)$ (orange line) and its resonant [$F_\tau^{\mathrm{res}}(\omega-\omega_0)=1/(2\pi\nu)$ for $-\pi\nu<\omega-\omega_0<\pi\nu$ (green dashed line)] and tail [$F_\tau^{\mathrm{tail}}(\omega-\omega_0)=\nu/[\pi(\omega-\omega_0)^2]$ for $\omega-\omega_0>\pi\nu$ (red dashed line)] approximations.

Furthermore, if we consider $\nu \ll \omega_0$ (this will be justified later), we can expand the two terms in the bracket to third order in $\pi\nu/\omega_0$ to get

$$\boxed{\gamma^{\text{res}} \simeq 2\pi \frac{D}{\omega_X^{\eta-1}} \omega_0^{\eta}} \tag{1.47}$$

which is nothing else than the FGR decay rate $\gamma_0 = 2\pi R(\omega_0) \simeq 2\pi D\omega_0^{\eta}/\omega_X^{\eta-1}$ (as $\omega_0 \ll \omega_X$). Therefore the resonant contribution contains the FGR decay rate and nothing else: the effect of the frequent measurements will be contained in the second contribution: the tail contribution which will give the scaling of the measurement-modified decay rate in terms of the measurement rate ν. Therefore:

$$\boxed{\gamma^{\text{res}} \simeq \gamma_0} \tag{1.48}$$

Tail contribution

Now, we are interested in the contribution of the tail of $F_\tau(\omega-\omega_0)$ far from ω_0 ($\omega \gg \omega_0$) which behaves as $\propto 1/(\omega-\omega_0)^2$ and probes the rest of the reservoir $R(\omega)$. To get an analytical expression of this contribution, we replace the $\sin^2$ in $F_\tau(\omega-\omega_0)$ by its mean value $1/2$:

$$\text{sinc}^2\left((\omega-\omega_0)\frac{1}{2\nu}\right) \simeq \frac{2\nu^2}{(\omega-\omega_0)^2} \tag{1.49}$$

which gives

$$F_\tau^{\text{tail}}(\omega-\omega_0) = \frac{\nu}{\pi(\omega-\omega_0)^2} \tag{1.50}$$

and is illustrated in Fig. 1.2. Therefore the tail contribution reads:

$$\begin{aligned}
\gamma^{\text{tail}} &= 2\pi\left[\int_0^{\omega_0-\pi\nu} \mathrm{d}\omega\, R(\omega) F_\tau^{\text{tail}}(\omega-\omega_0) + \int_{\omega_0+\pi\nu}^{\infty} \mathrm{d}\omega\, R(\omega) F_\tau^{\text{tail}}(\omega-\omega_0)\right] \\
&\simeq 2\pi \int_{\omega_0\ll\omega\ll\omega_X}^{\infty} \mathrm{d}\omega\, \frac{D}{\omega_X^{\eta-1}} \frac{\omega^\eta}{\left[1+\left(\frac{\omega}{\omega_X}\right)^2\right]^\mu} \frac{\nu}{\pi(\omega-\omega_0)^2} \\
&\simeq 2\pi \int_{\omega_0\ll\omega\ll\omega_X}^{\infty} \mathrm{d}\omega\, \frac{D}{\omega_X^{\eta-1}} \frac{\omega^\eta}{\left[1+\left(\frac{\omega}{\omega_X}\right)^2\right]^\mu} \frac{\nu}{\pi\omega^2} \\
&\simeq \frac{D}{\omega_X^{\eta-1}} \times \nu \times I_{\eta\mu}
\end{aligned} \tag{1.51}$$

where

$$I_{\eta\mu} \equiv 2\int_{\omega_0\ll\omega\ll\omega_X}^{\infty} \mathrm{d}\omega\, \frac{\omega^{\eta-2}}{\left[1+\left(\frac{\omega}{\omega_X}\right)^2\right]^\mu} \tag{1.52}$$

To calculate the integral $I_{\eta\mu}$, one can make the change of variable $X = (\omega/\omega_X)^2$. This leads to:

$$I_{\eta\mu} = \omega_X^{\eta-1} \int_\varepsilon^{\infty} \mathrm{d}X\, \frac{X^{\frac{\eta}{2}-\frac{3}{2}}}{(1+X)^\mu} \tag{1.53}$$

where $(\omega_0/\omega_X)^2 \ll \varepsilon \ll 1$. One must now distinguish two cases.

Case $\eta = 1$: electric dipole transitions In this case,

$$I_{1\mu}(\varepsilon) = \int_{\varepsilon}^{\infty} \mathrm{d}X \, \frac{1}{X(1+X)^{\mu}} \, . \tag{1.54}$$

This integral is defined only if $\varepsilon > 0$, and we write $I_{1\mu}(\varepsilon)$ to show the ε dependence, as the numerical result will depend on the value of ε chosen. There is no analytical result for this integral which must be computed numerically, and the most general result which one can give for $\eta = 1$ is:

$$\boxed{\gamma^{\mathrm{tail}} = D \times I_{1\mu}(\varepsilon) \times \nu \qquad (\text{for } \eta = 1)} \tag{1.55}$$

Case $\eta > 1$: non-electric-dipole transitions For $\eta > 1$, replacing ε by 0 is not problematic as the integral is still well-defined when $\varepsilon = 0$ and moreover has an analytical expression in terms of the special "Euler's Beta function":

$$\begin{aligned} I_{\eta\mu} &= \omega_X^{\eta-1} \int_{\varepsilon}^{\infty} \mathrm{d}X \, \frac{X^{\frac{\eta}{2}-\frac{3}{2}}}{(1+X)^{\mu}} \\ &\simeq \omega_X^{\eta-1} \int_{0}^{\infty} \mathrm{d}X \, \frac{X^{\frac{\eta}{2}-\frac{3}{2}}}{(1+X)^{\mu}} \qquad (\text{as } \varepsilon \ll 1) \\ &= \omega_{\mathrm{X}}^{\eta-1} \, B\left(\frac{\eta}{2}-\frac{1}{2}, \mu-\frac{\eta}{2}+\frac{1}{2}\right) \end{aligned} \tag{1.56}$$

where B refers to Euler's Beta function (well-defined for $\eta > 1$ and $\mu > (1/2)(\eta-1)$). This yields the scaling (partially obtained in [1]):

$$\boxed{\gamma^{\mathrm{tail}} \simeq D \times B\left(\frac{\eta}{2}-\frac{1}{2}, \mu-\frac{\eta}{2}+\frac{1}{2}\right) \times \nu \qquad (\text{for } \eta > 1)} \, . \tag{1.57}$$

Therefore, one can see that the tail contribution gives a scaling of the measurement-modified decay rate as $\propto \nu$.

Final result and generalization

To sum up, the analytical expression of the decay rate $\gamma = \gamma^{\mathrm{res}} + \gamma^{\mathrm{tail}}$ normalized by the FGR decay rate $\gamma_0 = 2\pi R(\omega_0) \simeq 2\pi D \omega_0^{\eta} / \omega_X^{\eta-1}$, reads [Eqs. (1.47), (1.55) and (1.57)]:

$$\boxed{\frac{\gamma}{\gamma_0} = 1 + A \frac{\nu}{\omega_0} \left(\frac{\omega_{\mathrm{X}}}{\omega_0}\right)^{\eta-1}} \quad \text{where} \quad A = \begin{cases} (2\pi)^{-1} \, I_{1\mu}(\varepsilon) & \text{for} \quad \eta = 1 \\ (2\pi)^{-1} \, B\left(\frac{\eta}{2}-\frac{1}{2}, \mu-\frac{\eta}{2}+\frac{1}{2}\right) & \text{for} \quad \eta > 1 \end{cases} \, . \tag{1.58}$$

Note that when the measurement rate $\nu \to 0$, we recover the FGR decay rate γ_0.

Now, we extend the previous result found for a reservoir of the simple form (1.38) to the general form (1.35). We must sum over r, and then over J. In the general case, the FGR decay rate γ_0 will be, for the reservoir coupling spectrum (1.35), given by

$$\gamma_0 = 2\pi R(\omega_0) \simeq 2\pi \sum_{J=|l_{\mathrm{e}}-l_{\mathrm{g}}|}^{l_{\mathrm{e}}+l_{\mathrm{g}}} \sum_{r=0}^{N_J} \frac{D_{Jr}}{\omega_{\mathrm{X}}^{\eta_J+2r-1}} \omega_0^{\eta_J+2r} \, . \tag{1.59}$$

The hierarchy $\omega_0 \ll \omega_X$ ensures that the contribution from the smallest possible value $\{\eta_J + 2r\}$ is dominant, that is for $r = 0$ and $J = \left|l_e - l_g\right| \equiv J_{\min}$. By writing $\eta_{\min} \equiv \eta_{J_{\min}}$, the FGR decay rate reduces to:

$$\gamma_0 \simeq 2\pi \frac{D_{J_{\min}0}}{\omega_X^{\eta_{\min}-1}} \omega_0^{\eta_{\min}} . \tag{1.60}$$

This is true if we assume that the coefficients D_{Jr} have the same order of magnitude and that $D_{J_{\min}0}$ does not vanish, which can occur for instance in the case of the electric dipole transitions ($\epsilon = 0$, $J = 1$) between levels sharing the same principal quantum number (see Table 1.1 in Ref. [13]). However, we do not focus on this special case here.

The measurement-modified decay rate will be obtained as before as the sum of two contributions $\gamma = \gamma^{\text{res}} + \gamma^{\text{tail}}$ by separating two cases.

Case $\eta_{\min} > 1$: non-electric-dipole transitions For $\eta_{\min} > 1$, we just have to sum over r and over J:

$$\gamma \simeq \gamma_0 + \sum_{J=|l_e-l_g|}^{l_e+l_g} \sum_{r=0}^{N_J} D_{Jr} \times B\left(\frac{\eta_J}{2} + r - \frac{1}{2}, \mu - \frac{\eta_J}{2} - r + \frac{1}{2}\right) \times \nu \tag{1.61}$$

Case $\eta_{\min} = 1$: electric dipole transitions For $\eta_{\min} = 1$ (and $J_{\min} = 1$), the term in the double sum $\{r = 0; J = 1\}$ must be treated separately as previously

$$\gamma \simeq \gamma_0 + \underbrace{D_{10} \times I_{1\mu}(\varepsilon) \times \nu}_{\text{term } r=0;J=1} + \underbrace{\sum_{J=2}^{l_e+l_g} D_{J0} \times B\left(\frac{\eta_J}{2} - \frac{1}{2}, \mu - \frac{\eta_J}{2} + \frac{1}{2}\right) \times \nu}_{\text{terms } r=0;J=2,\ldots,l_e+l_g} + \underbrace{\sum_{J=1}^{l_e+l_g} \sum_{r=1}^{N_J} D_{Jr} \times B\left(\frac{\eta_J}{2} + r - \frac{1}{2}, \mu - \frac{\eta_J}{2} - r + \frac{1}{2}\right) \times \nu}_{\text{terms } r=1,\ldots,N_J;J=1,\ldots,l_e+l_g} \tag{1.62}$$

Finally, by dividing by the FGR decay rate (1.60) one gets

$$\boxed{\frac{\gamma}{\gamma_0} \simeq 1 + A \frac{\nu}{\omega_0} \left(\frac{\omega_X}{\omega_0}\right)^{\eta_{\min}-1}} \tag{1.63}$$

where the coefficient A now reads:

$$A = (2\pi)^{-1} I_{1\mu}(\varepsilon) + (2\pi)^{-1} \sum_{J=2}^{l_e+l_g} \frac{D_{J0}}{D_{10}} \times B\left(\frac{\eta_J}{2} - \frac{1}{2}, \mu - \frac{\eta_J}{2} + \frac{1}{2}\right) + (2\pi)^{-1} \sum_{J=1}^{l_e+l_g} \sum_{r=1}^{N_J} \frac{D_{Jr}}{D_{10}} \times B\left(\frac{\eta_J}{2} + r - \frac{1}{2}, \mu - \frac{\eta_J}{2} - r + \frac{1}{2}\right) \quad \text{for} \quad \eta_{\min} = 1 \tag{1.64}$$

and

$$A = (2\pi)^{-1} \sum_{J=|l_e-l_g|}^{l_e+l_g} \sum_{r=0}^{N_J} \frac{D_{Jr}}{D_{J_{\min}0}} \times B\left(\frac{\eta_J}{2} + r - \frac{1}{2}, \mu - \frac{\eta_J}{2} - r + \frac{1}{2}\right) \quad \text{for} \quad \eta_{\min} > 1 \tag{1.65}$$

1.3.3 Comparison analytical/numerical calculations and discussion

From Eq (1.63), and despite the more complicated form of the expression of the coefficient A, we see that the parametric dependence of the ratio of the decay rates is the same as previously: the important parameter is $\eta_{\min}-1$. This means that the AZE is very dependent on the type of transition. There is a competition between $\nu/\omega_0 \ll 1$ and $\omega_X/\omega_0 \gg 1$ but, for transitions where $\eta_{\min} = |l_e - l_g| = 1$ (called "electric dipole transitions"), the factor $(\omega_X/\omega_0)^0 = 1$ fails to play a role, whereas for other type of electronic transitions, $\eta_{\min} \geq 3$, and one can expect that the second factor will dominate, and this second factor becomes all the more dominant for higher values of $\eta_{\min}$, that is, for transitions with high difference between the orbital angular momenta of the initial and final levels.

Before commenting on the scope of this result, we first compare in Fig. 1.3 the analytical approximation of γ given by Eq. (1.58) to the numerical computation γ^{num} of Eq. (1.33) (using (1.34) and (1.38)) for three different reservoir coupling spectra $R(\omega)$ corresponding to the electric dipole ($\eta = 1$, in green), quadrupole ($\eta = 3$, in red) and octupole ($\eta = 5$, in blue) transitions whose parameters are given in Table 1.1. For the quadrupole and octupole transitions, the value of the cœfficient A are calculated to be 0.032 and 0.004, respectively. About the dipole case ($\eta = 1$), this cœfficient is taken to be equal to 1.500. We can see a very good agreement for the quadrupole and octupole transitions up to $\nu \lesssim 100\,\omega_0$, and for the dipolar transition up to $\nu \lesssim 10\,\omega_0$. Note that in practice, it may not be feasible to reach such high measurement rates as $\nu \sim \omega_0$ (particularly for optical transitions, *cf.* Sec. 1.4), and moreover, for $\nu \gtrsim \omega_0$, the RWA is not valid anymore. Therefore, the analytical results are revealed to be excellent in the regime of interest $\nu \ll \omega_0$ with a relative error $(\gamma^{\text{num}} - \gamma)/\gamma^{\text{num}}$ up to 3% for the dipolar case, up to 2% for the quadrupolar case and about 1% for the octupolar case.

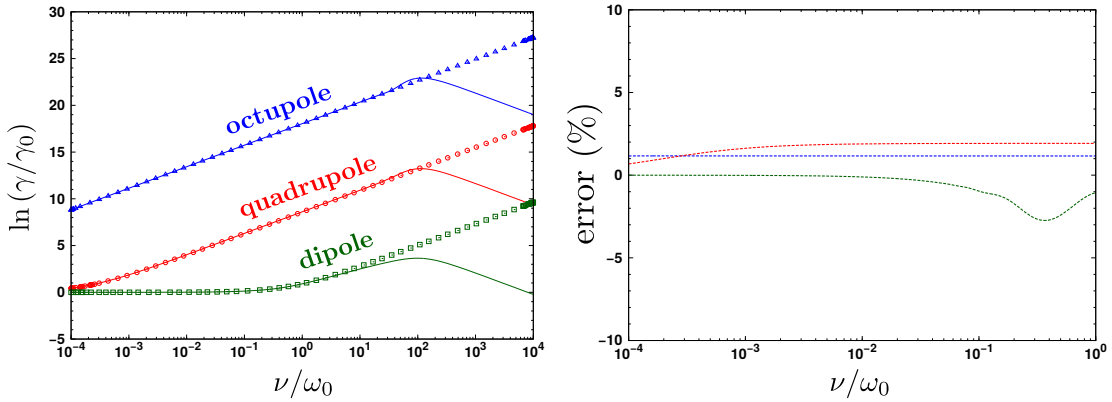

Figure 1.3 – Left: comparison between numerical (full lines) and analytical (dotted lines) calculations of $\ln(\gamma/\gamma_0)$ as a function of the normalized measurement rate ν/ω_0 for three different electric transitions: dipole ($\eta = 1$, in green), quadrupole ($\eta = 3$, in red) and octupole ($\eta = 5$, in blue). The associated parameters used for the function $R(\omega)$ corresponding to these transitions are displayed in Table 1.1. Right: Relative error $= (\gamma^{\text{num}} - \gamma^{\text{ana}})/\gamma^{\text{num}}$ as a function of the normalized measurement rate ν/ω_0 with γ^{num} the decay rate computed numerically from Eqs. (1.33), (1.34) and (1.38), and γ^{ana} the decay rate calculated from Eq. (1.58). Note that the horizontal axis is in logscale and spans from 10^{-4} to 10^{+4} in the graph on the left and from 10^{-4} to 1 in the graph on the right.

Concerning the AZE, we can see that in the case of the electric dipole transition, the AZE trend ($\gamma > \gamma_0$) appears only for $\nu \gtrsim \omega_0$ (green curve) — which is not interesting for experimental observations as just discussed, whereas for the other transitions (red and blue curves), the AZE is obtained already for $\nu \ll \omega_0$ and can be very strong. This has been overlooked in the past and constitutes our main result: within the natural hierarchy $\omega_0 \ll \omega_X$, we predict from our general Eq. (1.58) that electric dipole transitions ($\eta = 1$) will *not* exhibit the AZE, whereas the AZE can be expected for all other types of electronic transitions ($\eta > 1$). Indeed, we see from Eq. (1.58) that for all transitions except electric-dipolar ones, the ratio $\omega_X/\omega_0 \gg 1$ may give rise, despite the ratio $\nu/\omega_0 \ll 1$, to a strong anti-Zeno effect $\gamma \gg \gamma_0$, particularly for high-order multipolar transitions. Thus, as electric dipole transitions are arguably the most standard and studied type of electronic transitions in atoms, these predictions make the AZE much less ubiquitous than what had been stated in Ref. [1]. The goal of the next section is to identify realistic systems suitable for an AZE observation.

1.4 Experimental proposal

Here, we propose an experimental scheme for AZE observation, involving the electric quadrupole transition between $D_{5/2}$ and $S_{1/2}$ in the alkali-earth ions Ca^+ and Sr^+. The proposed protocol is based on the stimulated Raman adiabatic passage technique which acts like a dephasing quasi-measurement.

1.4.1 Transition choice

The search for a possible candidate to observe the AZE is framed by experimental constraints. Even if the AZE is expected to be observable on magnetic dipolar transitions and even more effective on electric octupolar transitions, the very long natural lifetime (of the order of one year or more) of the excited states involved in these transitions makes them very inappropriate to lifetime measurement. Therefore, in what follows, we focus on demonstrating the AZE on an electric quadrupolar transition.

The first choice candidate to confirm the predictions derived for hydrogenic atoms is the hydrogen atom itself, by transferring the atomic population to the lowest D-state (the $3D$-state would play the role of the excited state $|e\rangle$), and frequently monitoring the excited state. A major limit lies in the level scheme of hydrogen which allows an atom in the $3D$-state to decay to the $2P$-states by a strong dipolar transition (see Fig. 1.4(a)). The lifetime of the $3D$-state is then conditioned by its dipolar coupling to $2P$ and is not limited by its quadrupolar coupling to $1S$. Therefore, no measurable reduction of the lifetime due to the AZE is expected. The same problem arises with Rydberg states, which were originally proposed as promising candidates [1] for AZE observation due to their transitions in the microwave domain that favor the scaling in $(1/\omega_0)^\eta$ of Eq. (1.58) compared to optical frequencies.

To circumvent this problem of unwanted transitions, it is then essential to identify a metastable D-state, which has no other decay route to the ground state than the quadrupo-

lar transition. This can be found in the alkali-earth ions like Ca^+ or Sr^+, where the lowest D-level is lower in energy than any P-level (see Fig. 1.4(b)). The order of magnitude of the lifetime of these D-levels ranges from 1 ms to 1 s. The contribution to the D-level spontaneous emission rate of *two-photon* decay, allowed by second-order perturbation theory based on non-resonant electric-dipole transitions, has been calculated in [23, 24] for Ca^+ and Sr^+. The results show that the two-photon decay channel contributes to 0.01% to the lifetime of the lowest D-states of Ca^+ and Sr^+. As a consequence, the spontaneous emission from the lowest D-level in Ca^+ and Sr^+ can be considered to be due only to electric quadrupolar transition and we then focus on these two atomic systems in the following.

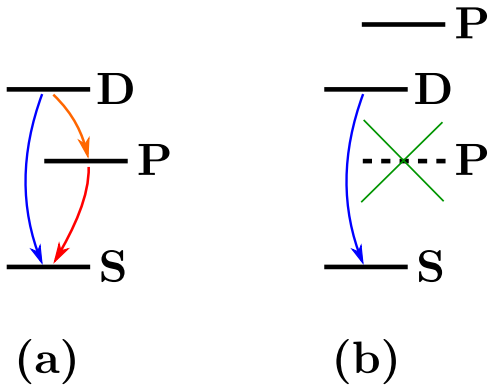

Figure 1.4 – Energy levels scheme (a) in hydrogen and Rydberg atoms and (b) alkali-earth ions like Ca^+ or Sr^+. For hydrogen atoms, the electric quadrupole transition $D \rightarrow S$ is in competition with the strong dipole transition $D \rightarrow P$, whereas for the alkali-earth ions represented, there is only one route towards the S state from the D state.

1.4.2 Measurement scheme and read-out

Concerning the measurements of the frequently monitored excited state, ideal instantaneous projections on $|e\rangle$ are not strictly required. Indeed, they amount in effect to dephasing the level $|e\rangle$, that is, to making the phase of state $|e\rangle$ completely random [1]. Different schemes were proposed to emulate projective measurements in Refs. [1, 25, 26] and performed in Ref. [11], for which Eq. (1.33) still holds. Here, we propose an alternative protocol in the same spirit of the "dephasing-only measurement" of Ref. [11]. In this scheme, state $|e\rangle$ is the metastable state $D_{5/2}$ and the dephasing measurement is driven by the transition from $D_{5/2}$ to $D_{3/2}$, by two lasers through the strong electric dipolar transitions to the common excited state $P_{3/2}$ (see Fig. 1.5) using a stimulated Raman adiabatic passage (STIRAP) process [27]. If the two-photon Raman condition is fulfilled (identical detuning for the two transitions), the intermediate $P_{3/2}$-state is not populated and the population is trapped in a coherent superposition of the two states $D_{5/2}$ and $D_{3/2}$. By changing the laser power on each transition with appropriate time profile and time delay, the atomic population can be transferred between the two metastable D-states, as demonstrated in Ref. [28]. After one transfer and return, state $|e\rangle$ thus acquires a phase related to the phase of the two lasers. By applying a random phase jump on one laser between each completed STIRAP transfer, the phase coherence of the excited state $|e\rangle$ is

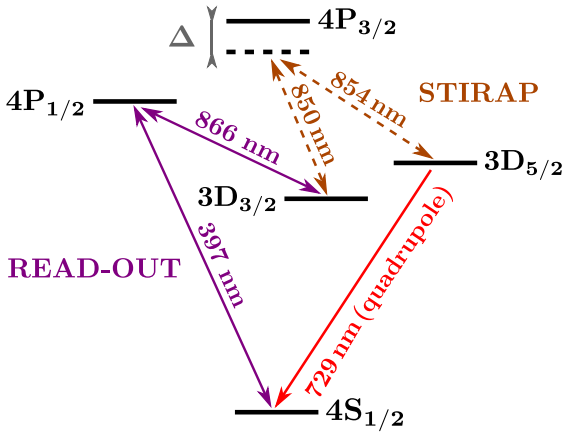

Figure 1.5 – Dephasing measurement and read-out schemes for AZE observation in $^{40}Ca^{+}$. The transition used for the AZE is the electric quadrupole transition at 729 nm (red solid arrow). The dephasing measurement can be performed using a STIRAP process between the $D_{5/2}$ and $D_{3/2}$ states *via* two strong electric dipole transitions $D_{5/2} \rightarrow P_{3/2}$ at 854 nm and $D_{3/2} \rightarrow P_{3/2}$ at 850 nm, both detuned from resonance (brown dashed arrows) [28]. The read-out consists in observation of laser induced fluorescence if the atom has decayed to the ground state [29] (purple solid arrows).

washed out, and a "dephasing" measurement of the level $|e\rangle$ is performed.

To measure the effective lifetime of the $D_{5/2}$-state, the read-out of the internal state must be based on electronic states which do not interfere with $D_{5/2}$. For that purpose, the electron-shelving scheme first proposed by Dehmelt can be used [29]. It requires two other lasers, coupling to the $S_{1/2} \rightarrow P_{1/2}$ and to the $D_{3/2} \rightarrow P_{1/2}$ transitions (see Fig. 1.5). When shining these two lasers simultaneously, the observation of scattered photons at the $S_{1/2} \rightarrow P_{1/2}$ transition frequency is the signature of the decay of the atom to the ground state [30]. This read-out scheme is switched on during a short time compared to the lifetime of the $D_{5/2}$-state, at a time when the STIRAP process has brought back the electron to $D_{5/2}$.

1.4.3 Calculation for $^{40}Ca^{+}$

We now try to see whether the AZE might be observable in Ca^{+}, which is not strictly speaking hydrogenic, but is alkali-like in a sense that it has a single valence electron, and can be seen as a single electron orbiting around a core with a net charge $+2e$. Ca^{+} is the lightest of the alkali-earth ions having the appropriate level-scheme required for the proposed experimental protocol (see Fig. 1.5). Therefore, we assume that it still makes sense to use Eq. (1.58) (derived for hydrogen-like atoms) and we apply it to the electric quadrupole ($\eta = 3$) transition $3D_{5/2} \rightarrow 4S_{1/2}$ to find

$$\frac{\gamma - \gamma_0}{\gamma_0} = A \frac{\nu}{\omega_0} \left(\frac{\omega_X}{\omega_0} \right)^2 \tag{1.66}$$

where the numerical pre-factor A cannot be computed for such an electronic system (see Eq. (1.65) for the general expression of A in the simpler case of hydrogen-like atoms).

To be observable, the AZE must induce a lifetime reduction larger than 1%, the best precision reached in recent $3D_{5/2}$-lifetime measurements in Ca^+ [30]. We evaluate ω_X using Eq. (1.36) with $n_g = 4$ and $n_e = 3$ and by replacing the atomic number Z by the effective number of charges $Z_{eff} = 2$. Using the frequency of this transition $\omega_0 = 2\pi \times$ 411 THz, this gives a ratio $(\omega_X/\omega_0)^2 \simeq 6.6\times10^6$. If the unknown pre-factor A is assumed to be of the order of unity, one would need $\nu \sim 4$ MHz to meet the observation requirement.

The transfer between the states $D_{5/2}$ and $D_{3/2}$ has been demonstrated in $^{40}Ca^+$ with a STIRAP process [28], where a complete one-way transfer duration of 5 μs was observed for 420 mW/mm^2 on the 850 nm $3D_{3/2} \rightarrow 4P_{3/2}$ transition and 640 mW/mm^2 on the 854 nm $3D_{5/2} \rightarrow 4P_{3/2}$ transition, with both lasers detuned by $\Delta = 600$ MHz from resonance (see Fig. 1.5). To reduce the duration of the dephasing measurement to time scales smaller than 1 μs, one can increase the laser intensity by stronger focusing and/or larger power, but we can also consider that a complete STIRAP transfer is not required to achieve a dephasing of the excited state. Furthermore, a close inspection of Tables I and II in Ref. [13] suggests that the pre-factor A could be much larger than unity, making the constraint on a high measurement rate less stringent for AZE observation.

Even if the experimental requirements for AZE observation on quadrupole transition in Ca^+ are more demanding than today's best achievements, realistic arguments show that they can be met in a dedicated experimental set-up. This experimental challenge would benefit from theoretical insight concerning the still unknown pre-factor scaling the lifetime reduction.

1.5 Conclusion

Based on well-established results for hydrogen-like atoms, we derived in Section 1.3 an analytical expression of the decay rate modified by frequent measurements which allows us to highlight the main condition for an observable AZE in atomic radiative decay in free space: all transitions except electric-dipole transitions will exhibit an AZE under sufficiently rapid repeated measurements. This analytical formula also indicates how the AZE scales with the measurement rate.

We then identified in Section 1.4 a suitable level scheme in the alkali-earth ions Ca^+ and Sr^+ for AZE observation, involving the electric quadrupole transition between $D_{5/2}$ and $S_{1/2}$, and using a new "dephasing" measurement protocol based on the STIRAP technique. Other suitable experimental schemes might exist, and we encourage further proposals in this sense.

1.A Decay rate in free space

In this appendix, we follow more or less the chapter 6.4 in [16] to derive an analytical expression for the decay rate given by the FGR in Eq. (1.27) for a two-level atom in free space. We recall here its expression:

$$\gamma_0 = 2\pi \overline{|g(\omega_0)|^2}\, \rho(\omega_0) \tag{1.67}$$

Two things must be calculated: (i) the density of one-photon states $|1_j\rangle$, which corresponds to the density of modes j *in the fictitious volume V and (ii) the coupling constant $|g_j|^2$ averaged over all emission directions and polarizations.*

1.A.1 Density of states in the volume V

The density of states $\rho(\omega)$ is equal to the number of quasi-continuum modes in the frequency range from ω to $\omega + \mathrm{d}\omega$, divided by the frequency width of this interval $\mathrm{d}\omega$: $\rho(\omega) \equiv \mathrm{d}N/\mathrm{d}\omega$. One must then find a way to count the number of modes $\mathrm{d}N$ in the width $\mathrm{d}\omega$. In vacuum and within the quantization volume V, the number of modes is easy to count. First, we recall that here a mode j is referred to as a polarized travelling plane monochromatic wave, characterized by its frequency ω_j, its wavevector $\mathbf{k}_j$ whose modulus verifies $|\mathbf{k}_j| = \omega_j/c$ and its polarization vector $\vec{\varepsilon}_j$.

Moreover, we use periodic boundary conditions because they are well adapted for the quantization of freely propagating fields. They impose the quantization of the wavevectors of the modes $\mathbf{k}_j$: $\mathbf{k}_j = (2\pi/L)(n_x\vec{x} + n_y\vec{y} + n_z\vec{z})$ where L is the side of the cubic volume, and $\{n_x, n_y, n_z\}$ are integers. This has the advantage to make them countable, because each wavevector can be represented by a point in the reciprocal space, and they constitute a cubic lattice with unit cell volume $(2\pi/L)^3$. We now can count the number of points $\mathrm{d}N$ lying between spheres of radii k and $k + \mathrm{d}k$ in the reciprocal space. This is equal to the elementary volume between the two spheres $4\pi k^2 \mathrm{d}k$ divided by the volume of a unit cell $(2\pi/L)^3$. Moreover, taking into account that two modes are associated with each wavevector, corresponding to two polarizations, the number of modes in this elementary volume is therefore:

$$\begin{aligned} \mathrm{d}N &= 2\frac{4\pi k^2}{(2\pi/L)^3}\mathrm{d}k \\ &= V\frac{k^2}{\pi^2}\mathrm{d}k \end{aligned} \tag{1.68}$$

Finally, because we want the number of modes in the bandwidth $\mathrm{d}\omega$, we make the change of variable $k = \omega/c$ to get

$$\mathrm{d}N = V\frac{\omega^2}{\pi^2 c^3}\mathrm{d}\omega \tag{1.69}$$

and one get the density of states $\rho(\omega)$ by dividing $\mathrm{d}N$ by $\mathrm{d}\omega$:

$$\boxed{\rho(\omega) = V\frac{\omega^2}{\pi^2 c^3}} \tag{1.70}$$

1.A.2 Coupling constant

We proceed by averaging the coupling constant $|g_j|^2$ over all emission directions and polarizations. By noting $\overline{|g(\omega)|^2}$ the quantity $|g_j|^2$ averaged over all modes with $\omega_j = \omega$, that is over all polarizations and emission directions, one has:

$$\overline{|g(\omega)|^2} = \frac{1}{2}\frac{1}{4\pi}\sum_{p=1}^{2}\int \mathrm{d}\Omega_{\mathbf{k}_j}|g_j|^2 \quad \text{where} \quad \hbar g_j \equiv \langle g, 1_j|\hat{H}_I|e, 0\rangle \tag{1.71}$$

where the sum is over the two orthogonal polarizations $\vec{\varepsilon}_1$ and $\vec{\varepsilon}_2$ forming a basis for the polarization vector $\vec{\varepsilon}_j$ (and are chosen to form a direct triad with $\mathbf{k}_j$, see Fig. 1.6), and $\mathrm{d}\Omega_{\mathbf{k}_j}$ is the element of solid angle corresponding to the direction of $\mathbf{k}_j$. We want to calculate this quantity. For that, we must express the coupling constant $|g_j|^2$. To get an expression for $|g_j|^2$, we first simplify the form of the interaction Hamiltonian $\hat{H}_I$ of Eq. (1.3) by making the **dipole approximation** (also called **long-wavelength approximation**). This consists in replacing the vector potential $\hat{\mathbf{A}}(\mathbf{r})$ by its value at the position of the nucleus $\mathbf{r} = 0$. The vector potential operator $\hat{\mathbf{A}}$ can be expanded into travelling plane wave modes and expressed in terms of the operators $\hat{a}_j$ and $\hat{a}_j^\dagger$ according to (see [16], chapter 4):

$$\hat{\mathbf{A}}(\mathbf{r}) = \sum_j \vec{\varepsilon}_j \frac{\mathcal{E}_j^{(1)}}{\omega_j}\left(\hat{a}_j e^{i\mathbf{k}_j\cdot\mathbf{r}} + \hat{a}_j^\dagger e^{-i\mathbf{k}_j\cdot\mathbf{r}}\right) \tag{1.72}$$

with

$$\mathcal{E}_j^{(1)} = \sqrt{\frac{\hbar\omega_j}{2\epsilon_0 V}} \qquad \text{Unit:} \quad [\mathcal{E}_j^{(1)}] = \mathrm{V.m^{-1}} \tag{1.73}$$

where the volume V appearing in the expression of $\mathcal{E}_j^{(1)}$ is the quantization volume, and we take $\mathbf{r}$ as a classical quantity. $\mathcal{E}_j^{(1)}$ is called the "one-photon amplitude of the mode j" and comes from a freedom of choice of constant. It is chosen to be the amplitude of the classical field with energy $\hbar\omega_j$ corresponding to the energy of a single photon in the mode j (see [16], chapter 4). By making the dipole approximation, the interaction Hamiltonian becomes

$$\hat{H}_I = \frac{e}{m_e}\sum_j \sqrt{\frac{\hbar}{2\epsilon_0\omega_j V}}\vec{\varepsilon}_j\cdot\hat{\mathbf{p}}\left(\hat{a}_j + \hat{a}_j^\dagger\right) \tag{1.74}$$

Therefore, the coupling constant to the mode j reads:

$$\begin{aligned}\hbar^2|g_j|^2 &= |\langle g, 1_j|\hat{H}_I|e, 0\rangle|^2 \\ &= \frac{e^2}{m_e^2}\frac{\hbar}{2\epsilon_0\omega_j V}|\langle g|\vec{\varepsilon}_j\cdot\hat{\mathbf{p}}|e\rangle|^2\end{aligned} \tag{1.75}$$

Now, we proceed to the calculation of the term $\langle g|\vec{\varepsilon}_j\cdot\hat{\mathbf{p}}|e\rangle$. To make a complete calculation, we will consider the particular case of an *electric dipole transition* $P \to S$ between an excited state $|e\rangle$ with orbital angular momentum $\{l_e = 1, m_e = 0\}$ and a ground state $|g\rangle$ with zero orbital angular momentum $\{l_g = 0, m_g = 0\}$. For a quantization axis taken along $\vec{z}$, one gets:

$$\langle g|\vec{\varepsilon}_j\cdot\hat{\mathbf{p}}|e\rangle = \langle g|\hat{p}_z|e\rangle\left(\vec{\varepsilon}_j\cdot\vec{z}\right) \tag{1.76}$$

Moreover, if we choose one polarization $\vec{\varepsilon}_1$ to be in the plane $(\vec{z}, \mathbf{k}_j)$, one has $\vec{\varepsilon}_1 \cdot \vec{z} = \sin\theta$ (see Fig. 1.6) and

$$\langle g|\, \vec{\varepsilon}_1 \cdot \hat{\mathbf{p}}\, |e\rangle = \langle g|\, \hat{p}_z\, |e\rangle \sin\theta \tag{1.77}$$

and then the other polarization $\vec{\varepsilon}_2$ is perpendicular to $\vec{z}$: $\vec{\varepsilon}_2 \cdot \vec{z} = 0$ (see Fig. 1.6), and therefore the matrix element is zero for this polarization. Thus, one gets

$$\hbar^2 |g_j|^2 = \frac{e^2}{m_e^2} \frac{\hbar}{2\epsilon_0 \omega_j V} |\, \langle g|\, \hat{p}_z\, |e\rangle\, |^2 \sin^2\theta \tag{1.78}$$

Note: Note that this term $\propto \sin^2\theta$ gives the pattern of spontaneous emission for this particular transition, which is zero in the $\vec{z}$ direction ($\theta = 0$) and maximal in the directions perpendicular to $\vec{z}$ ($\theta = \pi/2$). One can notice that it is the same pattern as the radiation diagram obtained by a classical calculation of radiation from an electric dipole oscillating in the $\vec{z}$ direction.

Therefore, by writing the element of solid angle as $\mathrm{d}\Omega = \sin\theta\, \mathrm{d}\theta\, \mathrm{d}\varphi$, in the integral, one gets for $\overline{|g(\omega)|^2}$:

$$\hbar^2 \overline{|g(\omega)|^2} = \frac{1}{2} \frac{1}{4\pi} \frac{e^2}{m_e^2} \frac{\hbar}{2\epsilon_0 \omega V} |\, \langle g|\, \hat{p}_z\, |e\rangle\, |^2 \int_0^{2\pi} \mathrm{d}\varphi \int_0^{\pi} \mathrm{d}\theta \sin^3\theta \tag{1.79}$$

Moreover, taking into account that

$$\int_0^{2\pi} \mathrm{d}\varphi \int_0^{\pi} \mathrm{d}\theta \sin^3\theta = \frac{8\pi}{3} \tag{1.80}$$

one gets

$$\boxed{\hbar^2 \overline{|g(\omega)|^2} = \frac{1}{3} \frac{e^2}{m_e^2} \frac{\hbar}{2\epsilon_0 \omega V} |\, \langle g|\, \hat{p}_z\, |e\rangle\, |^2} \tag{1.81}$$

Finally, together with the density of states, one gets for the decay rate defined in Eq. (1.67):

$$\boxed{\gamma_0 = \frac{1}{3\pi\epsilon_0} \frac{e^2}{m_e^2} \frac{\omega_0}{\hbar c^3} |\, \langle g|\, \hat{p}_z\, |e\rangle\, |^2} \tag{1.82}$$

Note 1: The decay rate is independent of the quantization volume V.

Note 2: This matrix element is also related to the matrix element with the atomic dipole operator $\hat{\mathbf{d}} = -e\hat{\mathbf{r}}$, that is[3]: $\langle g|\, \vec{\varepsilon}_j \cdot \hat{\mathbf{p}}\, |e\rangle = \mathrm{i}(m_e/e)\omega_0 \langle g|\, \vec{\varepsilon}_j \cdot \hat{\mathbf{d}}\, |e\rangle$, so that the decay rate also takes the form:

$$\boxed{\gamma_0 = \frac{1}{3\pi\epsilon_0} \frac{\omega_0^3}{\hbar c^3} |\, \langle g|\, \hat{d}_z\, |e\rangle\, |^2} \tag{1.83}$$

[3] This identity directly results from $\hat{\mathbf{p}} = -(\mathrm{i}m_e/\hbar)[\hat{\mathbf{r}}, \hat{H}_A]$.

Note 3: With classical calculation, within the model of the elastically bound electron, the radiative damping reads:

$$\gamma_{\mathrm{cl}} = \frac{e^2}{6\pi\epsilon_0}\frac{\omega_0^2}{m_e c^3} \tag{1.84}$$

Thus, one can see that the quantum decay rate is related to the classical damping rate by $\gamma_0 = f_{\mathrm{ge}}\gamma_{\mathrm{cl}}$ where the dimensionless constant f_{ge} reads $f_{\mathrm{ge}} = (2m_e\omega_0/\hbar)|\langle \mathrm{g}|\hat{z}|\mathrm{e}\rangle|^2$ and is called the **oscillator strength** of the transition.

Example: decay rate for the $2P-1S$ transition in hydrogen atom Using the Bohr formula [Eq. (1.42)] for ω_0: $\omega_0 = (3/8)\alpha c/a_0$, and the fact that $|\langle \mathrm{g}|\hat{d}_z|\mathrm{e}\rangle|^2$ can be calculated analytically for the transition $2P-1S$ in H and reads $-0.745\, e\, a_0$ where a_0 is the Bohr radius given in Eq. (1.37), one gets from Eq. (1.83):

$$\begin{aligned}\gamma_0 &= \frac{(0.745\times 3)^2}{2^7}\alpha^4\frac{c}{a_0}\\ &\simeq 0.039\,\alpha^4\frac{c}{a_0}\end{aligned} \tag{1.85}$$

Finally, one finds the lifetime for this excited state to be: $\gamma_0^{-1} = 1.6$ ns.

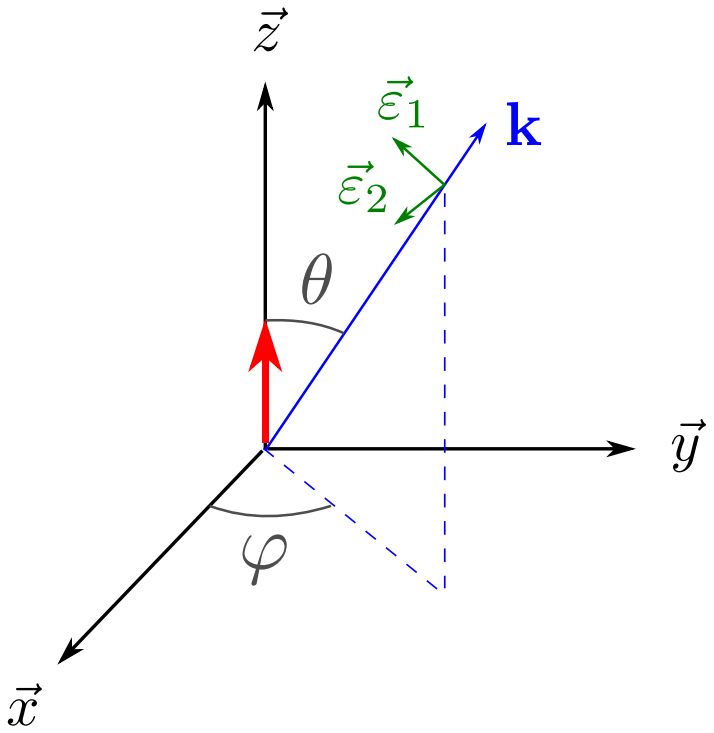

Figure 1.6 – Spherical coordinate system. The wavevector **k** of a mode emitted by the atom centered at the origin (in red the direction of its dipole moment) is shown, together with the polarization basis ($\tilde{\varepsilon}_1$,$\tilde{\varepsilon}_2$) that form a direct triad with **k**.

1.B Reservoir for hydrogen-like atoms in free space

In this Appendix, we sum up the results obtained by Moses [12] and Seke [13] and link them to our notations of the reservoirs Eqs. (1.35) and (1.38).

For hydrogen-like atoms in free space, it is useful to write the states of the (non-relativistic, spinless) atom in terms of the multipolar modes $|\mathrm{g}\rangle = |n_\mathrm{g}, l_\mathrm{g}, m_\mathrm{g}\rangle$ and $|\mathrm{e}\rangle = |n_\mathrm{e}, l_\mathrm{e}, m_\mathrm{e}\rangle$ where each atomic state is described by three discrete quantum numbers n_i, l_i and m_i which are respectively the principal, total angular momentum and magnetic quantum numbers. Similarly, it is useful to write the one-photon states in the energy-angular-momentum basis $|1_\mathrm{j}\rangle = |J, M, \lambda, \omega\rangle$ where a photon is characterized by its angular momentum J, its magnetic quantum number M, its helicity λ and its frequency ω, and the normalization is such that (note that unfortunately the normalizations used in [12] and [13] are different and we follow here the one of Seke defined (not given explicitely)):

$$\langle J, M, \lambda, \omega \,|\, J', M', \lambda', \omega' \rangle = \delta_{JJ'}\delta_{MM'}\delta_{\lambda\lambda'}\delta\left(\omega - \omega'\right) \tag{1.86}$$

The reservoir coupling spectrum (1.19) for given photon quantum numbers $\{J, M, \lambda, \omega\}$ is then given by

$$R(\omega) = \sum_{J,M,\lambda} \hbar^{-2} |\, \langle n_\mathrm{g}, l_\mathrm{g}, m_\mathrm{g}; J, M, \lambda, \omega | \hat{H}_I \,| n_\mathrm{e}, l_\mathrm{e}, m_\mathrm{e}; 0 \rangle \,|^2 \tag{1.87}$$

because of the normalization in Eq. (1.86). Moreover, as a consequence of the conservation of the angular momentum, the values of J and M must verify

$$\begin{cases} J = |l_\mathrm{e} - l_\mathrm{g}|, |l_\mathrm{e} - l_\mathrm{g}| + 1, ..., l_\mathrm{e} + l_\mathrm{g} \\ M = m_\mathrm{e} - m_\mathrm{g} \equiv \overline{M} \end{cases} \tag{1.88}$$

which are the *exact* selection rules. Therefore, the full reservoir takes the form

$$R(\omega) = \sum_{J=|l_\mathrm{e}-l_\mathrm{g}|}^{l_\mathrm{e}+l_\mathrm{g}} \sum_{M=-J}^{+J} \sum_{\lambda=0}^{1} \hbar^{-2} |\, \langle n_\mathrm{g}, l_\mathrm{g}, m_\mathrm{g}; J, M, \lambda, \omega | \hat{H}_I \,| n_\mathrm{e}, l_\mathrm{e}, m_\mathrm{e}; 0 \rangle \,|^2 \delta_{M\overline{M}} \tag{1.89}$$

In the non-relativistic approximation, Seke calculated in [13] the exact matrix elements $\langle n_\mathrm{g}, l_\mathrm{g}, m_\mathrm{g}; J, M, \lambda, \omega | \hat{H}_I \,| n_\mathrm{e}, l_\mathrm{e}, m_\mathrm{e}; 0 \rangle$ for hydrogen-like atoms in free space, using the interaction Hamiltonian in the minimal-coupling form [Eq. (1.3)], by writing the vector potential operator $\hat{\mathbf{A}}$ in the energy-angular-momentum representation (Eqs. (33a) and (33b) in [12]), and the linear momentum operator $\hat{\mathbf{p}}$ in the position representation $\hat{\mathbf{p}} = -\mathrm{i}\hbar\nabla$, he found that [Eqs. (17-19) in [13]]:

$$\begin{aligned} \langle n_\mathrm{g}, l_\mathrm{g}, m_\mathrm{g}; J, M, \lambda, \omega | \hat{H}_I \,| n_\mathrm{e}, l_\mathrm{e}, m_\mathrm{e}; 0 \rangle \;\propto\; & \lambda \, \langle l_\mathrm{g}, J, m_\mathrm{g}, M | l_\mathrm{g}, J, l_\mathrm{e}, m_e \rangle \\ & \times \frac{\left(\frac{\omega}{\omega_X}\right)^{J+\epsilon-1/2}}{\left[1 + \left(\frac{\omega}{\omega_X}\right)^2\right]^{n_\mathrm{g}+n_\mathrm{e}-1}} \sum_{r=0}^{N'_J} d'_{Jr} \left(\frac{\omega}{\omega_X}\right)^{2r} \end{aligned} \tag{1.90}$$

where $\langle l_g, J, m_g, M | l_g, J, l_e, m_e \rangle$ are the Clebsch-Gordan coefficients of the transition of interest, and ω_X is the non-relativistic cutoff frequency given by Eq. (1.36). The coefficients d'_{Jr} are numerical coefficients that have been calculated for certain transitions in [13] (note that the coefficients d'_{Jr} here correspond to the coefficients $d_{00}d_r$ in Eq. (18) in Ref. [13]). The index at which the sum is terminated is $N'_J = n_e + n_g - 2 - (1/2)(J - l_e - l_g - \epsilon)$ with $\epsilon = 0$ for electric transitions and $\epsilon = 1$ for magnetic transitions. The square of this expression that appears in Eq. (1.89) gives

$$|\langle n_g, l_g, m_g; J, M, \lambda, \omega | \hat{H}_I | n_e, l_e, m_e; 0 \rangle|^2 \propto \lambda^2 \langle l_g, J, m_g, M | l_g, J, l_e, m_e \rangle^2 \times \frac{\left(\frac{\omega}{\omega_X}\right)^{2J+2\epsilon-1}}{\left[1+\left(\frac{\omega}{\omega_X}\right)^2\right]^{2(n_g+n_e-1)}} \left(\sum_{r=0}^{N'_J} d'_{Jr} \left(\frac{\omega}{\omega_X}\right)^{2r} \right)^2 \tag{1.91}$$

which can be recast in the form

$$|\langle n_g, l_g, m_g; J, M, \lambda, \omega | \hat{H}_I | n_e, l_e, m_e; 0 \rangle|^2 \propto \lambda^2 \langle l_g, J, m_g, M | l_g, J, l_e, m_e \rangle^2 \times \sum_{r=0}^{N_J} d_{Jr} \frac{\left(\frac{\omega}{\omega_X}\right)^{2J+2\epsilon-1+2r}}{\left[1+\left(\frac{\omega}{\omega_X}\right)^2\right]^{2(n_g+n_e-1)}} \tag{1.92}$$

where $N_J = 2\left(n_e + n_g\right) - 4 - J - l_e - l_g - \epsilon$ and d_{Jr} are combinations of the previous d'_{Jr} coefficients.

Finally, by plugging this expression into Eq. (1.89) one gets the reservoir shown in Eq. (1.35), that is

$$R(\omega) = \sum_{J=|l_e-l_g|}^{l_e+l_g} \sum_{r=0}^{N_J} \frac{D_{Jr}}{\omega_X^{\eta_J+2r-1}} \frac{\omega^{\eta_J+2r}}{\left[1+\left(\frac{\omega}{\omega_X}\right)^2\right]^{\mu}} \tag{1.93}$$

where $\eta_J = 1 + 2J$ for magnetic transitions, and $\eta_J = -1 + 2J$ for electric transitions with $J = 1$ for a dipole transition, $J = 2$ for a quadrupole transition and so on; $\mu = 2\left(n_g + n_e - 1\right)$ and where the D_{Jr} are dimensionless constants involving the previous d_{Jr} coefficients and the Clebsch-Gordan coefficients of the transition under consideration $\langle l_g, J, m_g, \overline{M} | l_g, J, l_e, m_e \rangle$.

Note that this reservoir can take a much simpler form in the case of electric transitions ($\epsilon = 0$) between a state of maximal angular momentum ($l_e = n_e - 1$) and the ground state $1S$ ($n_g = 1$, $l_g = 0$). Indeed, in this, case, one has $N_J = 0$, and therefore the two sums disappear in the previous expression which reduces to the Eq. (1.38)

$$R(\omega) = \frac{D}{\omega_X^{\eta-1}} \frac{\omega^{\eta}}{\left[1+\left(\frac{\omega}{\omega_X}\right)^2\right]^{\mu}} \tag{1.94}$$

where we defined $D \equiv D_{J0}$ and $\eta \equiv \eta_J$.

Example: decay rate for the $2P-1S$ transition in hydrogen atom For example, for the $2P-1S$ transition in hydrogen atom, $\eta = 1$ and $\mu = 4$ and one has:

$$R(\omega) = D \frac{\omega}{\left[1+\left(\frac{\omega}{\omega_X}\right)^2\right]^4} \tag{1.95}$$

with $D = (2/\pi)(2/3)^9\alpha^3$ (see [21] and [31], chapter 6). Taking into account that for the transition $2P-1S$ of H atom ($n_g = 1$, $n_e = 2$, $Z = 1$), $\omega_0 = (3/8)\alpha c/a_0$ [Eq. (1.42)] and $\omega_X = (3/2)(c/a_0)$ [Eq. (1.36)] which gives a ratio $\omega_0/\omega_X = \alpha/4$ [Eq. (1.43)], the decay rate reads:

$$\begin{aligned}\gamma_0 &= 2\pi R(\omega_0) \\ &= \left(\frac{2}{3}\right)^8 \alpha^4 \frac{c}{a_0}\left[1+\left(\frac{\alpha}{4}\right)^2\right]^{-4}\end{aligned} \tag{1.96}$$

Now, if one neglects the term $[1+(\alpha/4)^2]^{-4}$, the decay rate becomes

$$\begin{aligned}\gamma_0 &\simeq \left(\frac{2}{3}\right)^8 \alpha^4 \frac{c}{a_0} \\ &\simeq 0.039\,\alpha^4 \frac{c}{a_0}\end{aligned} \tag{1.97}$$

which is fortunately the same result as the one found in the Appendix 1.A, Eq. (1.85). Therefore, as pointed out by Moses in [12], the dipole approximation used in Appendix 1.A to calculate the decay rate is equivalent to neglect the "retardation term" $[1+(\alpha/4)^2]^{-4}$. The prediction for the lifetime doing the dipole approximation is quite good, but one can increase the precision by keeping the retardation term.

Bibliography

[1] A. Kofman and G. Kurizki, Nature **405**, 546 (2000).

[2] P. Facchi, H. Nakazato, and S. Pascazio, Physical Review Letters **86**, 2699 (2001).

[3] B. Misra and E. Sudarshan, Journal of Mathematical Physics **18**, 756 (1977).

[4] R. Cook, Physica Scripta **1988**, 49 (1988).

[5] W. M. Itano, D. J. Heinzen, J. Bollinger, and D. Wineland, Physical Review A **41**, 2295 (1990).

[6] Y. Patil, S. Chakram, and M. Vengalattore, Physical Review Letters **115**, 140402 (2015).

[7] B. Kaulakys and V. Gontis, Physical Review A **56**, 1131 (1997).

[8] A. Kofman and G. Kurizki, Physical Review A **54**, R3750 (1996).

[9] M. Lewenstein and K. Rzazewski, Physical Review A **61**, 022105 (2000).

[10] M. Fischer, B. Gutiérrez-Medina, and M. Raizen, Physical Review Letters **87**, 040402 (2001).

[11] P. Harrington, J. Monroe, and K. Murch, Physical Review Letters **118**, 240401 (2017).

[12] H. Moses, Physical Review A **8**, 1710 (1973).

[13] J. Seke, Physica A **203**, 269 (1994).

[14] R. Loudon, *The quantum theory of light* (Oxford University Press, 2000).

[15] L. Rayleigh, The London, Edinburgh, and Dublin Philosophical Magazine and Journal of Science **49**, 539 (1900).

[16] G. Grynberg, A. Aspect, and C. Fabre, *Introduction to quantum optics: from the semi-classical approach to quantized light* (Cambridge University Press, 2010).

[17] S. M. Barnett and P. M. Radmore, *Methods in theoretical quantum optics*, Vol. 15 (Oxford University Press, 2002).

[18] V. Weisskopf and E. Wigner, Zeitschrift für Physik **63**, 54 (1930).

[19] H. Zheng, S. Zhu, and M. Zubairy, Physical Review Letters **101**, 200404 (2008).

[20] Q. Ai, Y. Li, H. Zheng, and C. Sun, Physical Review A **81**, 042116 (2010).

[21] P. Facchi and S. Pascazio, Physics Letters A **241**, 139 (1998).

[22] V. Debierre, T. Durt, A. Nicolet, and F. Zolla, Physics Letters A **379**, 2577 (2015).

[23] M. S. Safronova, W. R. Johnson, and U. I. Safronova, Journal of Physics B: Atomic, Molecular and Optical Physics **43**, 074014 (2010).

[24] M. S. Safronova, W. R. Johnson, and U. I. Safronova, Journal of Physics B: Atomic, Molecular and Optical Physics **50**, 189501 (2017).

[25] A. Kofman and G. Kurizki, Physical Review Letters **87**, 270405 (2001).

[26] Q. Ai, D. Xu, S. Yi, A. G. Kofman, C. P. Sun, and F. Nori, Scientific Reports **3** (2013).

[27] J. R. Kuklinski, U. Gaubatz, F. T. Hioe, and K. Bergmann, Physical Review A **40**, 6741 (1989).

[28] J. L. Sørensen, D. Møller, T. Iversen, J. B. Thomsen, F. Jensen, P. Staanum, D. Voigt, and M. Drewsen, New Journal of Physics **8**, 261 (2006).

[29] H. Dehmelt, in *Bulletin of the American Physical Society*, Vol. 20 (1975) p. 60.

[30] A. Kreuter, C. Becher, G. P. T. Lancaster, A. B. Mundt, C. Russo, H. Häffner, C. Roos, W. Hänsel, F. Schmidt-Kaler, R. Blatt, and M. S. Safronova, Physical Review A **71**, 032504 (2005).

[31] V. Debierre, *La fonction d'onde du photon en principe et en pratique*, Ph.D. thesis, Ecole Centrale de Marseille (2015).

Part II

Near-field interactions

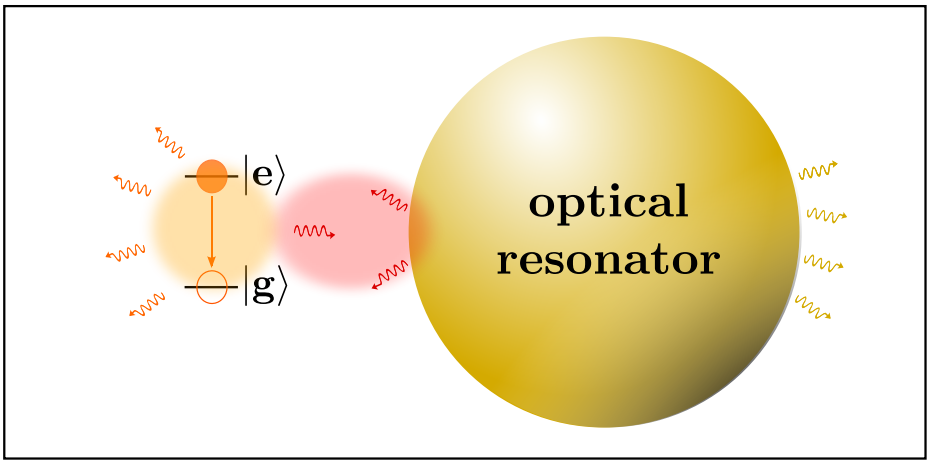

CHAPTER 2

Lamb shift multipolar analysis

2.1 Introduction

The coupling between quantum emitters (QEs) and optically resonant nanostructures is at the heart of nanophotonics [1]. In the weak-coupling regime, the exponential decay in time of the excited state of the QE is characterized by the decay rate, which can be either enhanced [2] or inhibited [3] by the local electromagnetic (EM) environment: this is known as the *Purcell effect*. A less often discussed effect of spontaneous emission is that the surrounding environment also induces level shifts of the excited atomic states, resulting in a frequency-shift for the emitted photons, in comparison with the bare resonance frequency. This is the photonic *Lamb shift*, also called radiative frequency-shift or Casimir-Polder frequency-shift (historically it was called Lamb shift and referred to level shifts of atoms in free space [4, 5]). In this Chapter, we will refer to it as photonic Lamb shift or simply Lamb shift, and sometimes frequency-shift. This effect has been theoretically studied in the case of perfect reflectors [6], partially reflecting surfaces [7, 8], photonic crystals [9–11], in the case of a dielectric microsphere without [12, 13] and with [14] absorption, dielectric or metallic prolate spheroids [15], and in the case of two-dimensional photonic crystals [16]. However, there is a lack of experimental demonstration of such an effect in quantum emitters.

In the present Chapter, we study the *weak-coupling* between a QE and its environment. We firstly start this Chapter with the Section 2.2, where we will justify the use of a classical formalism to study the photonic Lamb shift and modified decay rate induced by the presence of the environment by showing, in the weak-coupling regime, its equivalence to the quantum result. We focus on the study of the *photonic Lamb shift* of a QE *weakly*[1] coupled to optically resonant nanostructures, characterized by dielectric constants. We do not consider the extreme near-field (*i.e.* distances QE-object of $z \sim 1\,\mathrm{nm}$), where on must take into account non-local effects in the nanostructure [17]. The resonances of a given nanostructure characterize its optical response to an excitation electromagnetic (EM) field, and can be of different nature: for example Mie resonances in Mie resonators [18], or localized surface plasmon resonances in metallic nanoparticles [19]. After recalling in Section 2.3 a model commonly used to describe the optical response of a plasmonic nanoparticle, which consists in treating the particle as an electric dipole (known as the

[1] We refer here to the weak-coupling by opposition to the strong-coupling that will be studied in Chapter 4.

electric dipole approximation), we present a more general treatment within the multipolar theory and the T-Matrix formalism in Section 2.4. Such a framework can describe the optical response of an arbitrary set of resonant scatterers, either dielectric and/or metallic, and can take into account multiple scattering. Based on this formulation, we derive, still in Section 2.4, a general multipole expression of the Lamb shift in terms of the T-Matrix, valid for an arbitrary set of scatterers. This formula is then illustrated in Section 2.5 in the case of an emitter coupled to a silver nanosphere, and where we also study the influence of the nanoparticle's size on the induced Lamb shift. We predict a displacement (*blue*-shift) of the emitter's Lamb shift resonance as the size of the nanoparticle changes, which cannot be explained by a simple description of the nanoparticle in the electric dipole approximation (which predicts a *red*-shift). Finally, we present a practical calculation in Section 2.6, where we compute the Lamb shift in the case of a dimer nanoantenna, and we predict an observable shift of the emission wavelength.

2.2 Lamb shift and decay rate expressions

We consider a two-level atom prepared in the excited state in the presence of a non-homogeneous environment composed of dielectric matter. We show how to calculate the modified decay rate (inverse of the lifetime in the excited state) and the modified frequency of the emitted photon due to the environment, first in a classical way, and then in a more quantum fashion. We then demonstrate the equivalence between the two approaches.

2.2.1 Classical approach

Classically, an excited two-level atom with transition frequency ω_0 and natural linewidth γ_0 can be modeled by a harmonically oscillating *point dipole*, whose electric dipole moment $\mathbf{p}(\mathbf{r}_0, t)$ obeys, in the case of *small damping* ($\gamma_0 \ll \omega_0$) (see [20] Chapter 8 or [21] Chapter 16):

$$\frac{d^2\mathbf{p}(\mathbf{r}_0,t)}{dt^2} + \gamma_0 \frac{d\mathbf{p}(\mathbf{r}_0,t)}{dt} + \omega_0^2 \mathbf{p}(\mathbf{r}_0,t) = \frac{q^2}{m}\mathbf{E}_s(\mathbf{r}_0,t) \qquad \text{with} \quad \gamma_0 = \frac{1}{4\pi\epsilon_0\varepsilon_b}\frac{2n_b^3 q^2}{3c^3}\frac{\omega_0^2}{m} \tag{2.1}$$

where $\{\omega_0, \gamma_0, q, m\}$ are the characteristics of the classical dipole (the natural frequency of the oscillator, the damping constant in the nonabsorbing *homogeneous* background of refractive index n_b and permittivity ε_b, the charge and the mass respectively). $\mathbf{E}_s(\mathbf{r}_0, t)$ is the part of the field emitted by the oscillating point dipole which is scattered by the environment back to the dipole position $\mathbf{r}_0$. Adopting the following *ansatz*:

$$\begin{cases} \mathbf{p}(\mathbf{r},t) = \mathbf{p}_0 e^{-i\omega t} e^{-\gamma t/2} \\ \mathbf{E}_s(\mathbf{r}_0,t) = \mathbf{E}_s(\mathbf{r}_0,\omega_0) e^{-i\omega t} e^{-\gamma t/2} \end{cases} \tag{2.2}$$

with γ and ω respectively indicating the *new decay rate and resonance frequency*, together with the *weak-coupling approximation* in a classical context: $q^2/m|\mathbf{E}_s| \ll \omega_0^2|\mathbf{p}|$, one finds the following expression for the frequency-shift defined as $\Delta\omega \equiv \omega - \omega_0$ of the light

emitted by the dipole and decay rate modifications due to the environment [20]:

$$\frac{\Delta\omega}{\gamma_0} = -\frac{3\pi\epsilon_0\varepsilon_b}{k^3} \times \frac{1}{|\mathbf{p}_0|^2} \times \mathrm{Re}(\mathbf{p}_0^* \cdot \mathbf{E}_s(\mathbf{r}_0, \omega_0)) \,, \tag{2.3}$$

$$\frac{\gamma}{\gamma_0} = 1 + \frac{6\pi\epsilon_0\varepsilon_b}{k^3} \times \frac{1}{|\mathbf{p}_0|^2} \times \mathrm{Im}(\mathbf{p}_0^* \cdot \mathbf{E}_s(\mathbf{r}_0, \omega_0)) \,, \tag{2.4}$$

where $k = n_b(\omega_0/c)$ is the wave-number in the nonabsorbing homogeneous background medium. In this classical picture, one can see from Eqs. (2.3) and (2.4) that the environment contribution to the frequency-shift and decay rate is due to the dipole interacting with its own electric field scattered back by the environment.

To link this expression with the quantum one, one can derive the dipole fields using the *Green-function* formalism (for the sake of simplicity, we consider the dipole emitter to be in vacuum: $\varepsilon_b = 1$). The field produced at $\mathbf{r}$ by a *point* dipole located at $\mathbf{r}_0$ and with natural frequency ω_0 is [20]:

$$\mathbf{E}(\mathbf{r}, \omega_0) = \omega_0^2 \mu(\mathbf{r}, \omega_0) \mu_0 \hat{\mathbf{G}}(\mathbf{r}, \mathbf{r}_0, \omega_0) \cdot \mathbf{p}_0 \,, \tag{2.5}$$

with $\mu(\mathbf{r}, \omega)$ the relative permeability and where $\hat{\mathbf{G}}(\mathbf{r}, \mathbf{r}', \omega)$ is defined as the solution of the classical Maxwell equations with a δ function source term [20]

$$\nabla \times \frac{1}{\mu(\mathbf{r}, \omega)} \nabla \times \hat{\mathbf{G}}(\mathbf{r}, \mathbf{r}', \omega) - \frac{\omega^2}{c^2} \varepsilon(\mathbf{r}, \omega) \hat{\mathbf{G}}(\mathbf{r}, \mathbf{r}', \omega) = \hat{\mathbf{I}} \delta(\mathbf{r} - \mathbf{r}') \quad \text{Unit:} \quad [\hat{\mathbf{G}}] = \mathrm{m}^{-1} \tag{2.6}$$

with the proper boundary conditions. $\hat{\mathbf{I}}$ is the unit tensor and $\varepsilon(\mathbf{r}, \omega)$ is the relative permittivity. Because of the linearity of Maxwell equations, one can decompose the Green tensor into two parts:

$$\hat{\mathbf{G}}(\mathbf{r}, \mathbf{r}', \omega) = \hat{\mathbf{G}}_0(\mathbf{r}, \mathbf{r}', \omega) + \hat{\mathbf{G}}_s(\mathbf{r}, \mathbf{r}', \omega) \tag{2.7}$$

where $\hat{\mathbf{G}}_0(\mathbf{r}, \mathbf{r}', \omega)$ is the "free-space" contribution to the Green tensor, solution of the Maxwell equations in free space, and $\hat{\mathbf{G}}_s(\mathbf{r}, \mathbf{r}', \omega)$ is the "scattered" contribution. The free-space Green function is given by [20]:

$$\hat{\mathbf{G}}_0(\mathbf{r}, \mathbf{r}', \omega) = \mathcal{P} \left\{ \hat{\mathbf{I}} + \frac{1}{k^2 \varepsilon_b} \nabla\nabla \right\} \frac{\mathrm{e}^{\mathrm{i}k\sqrt{\varepsilon_b}R}}{4\pi\varepsilon_b R} - \frac{\hat{\mathbf{I}}}{3k^2\varepsilon_b} \delta(\mathbf{r} - \mathbf{r}') \tag{2.8}$$

where $\mathcal{P}$ denotes the "principal value" of the integral, and R denotes the distance $R = |\mathbf{r} - \mathbf{r}'|$.

Assuming a constant permeability $\mu = 1$, Eq. (2.3) can then be cast in terms of the scattering Green tensor as:

$$\frac{\Delta\omega}{\gamma_0} = -\frac{3\pi c}{\omega_0} \times \vec{u}_p \cdot \mathrm{Re}(\hat{\mathbf{G}}_s(\mathbf{r}_0, \mathbf{r}_0, \omega_0)) \cdot \vec{u}_p \,, \tag{2.9}$$

and similarly for the decay rate:

$$\frac{\gamma}{\gamma_0} = 1 + \frac{6\pi c}{\omega_0} \times \vec{u}_p \cdot \mathrm{Im}(\hat{\mathbf{G}}_s(\mathbf{r}_0, \mathbf{r}_0, \omega_0)) \cdot \vec{u}_p \,, \tag{2.10}$$

with $\vec{u}_p$ being the unit vector in the direction of the dipole moment: $\mathbf{p}_0 = p_0 \vec{u}_p$.

2.2.2 Quantum approach

Quantum mechanically, there is no way to understand the phenomenon of spontaneous emission, *i.e.* the fact that an atom in an excited state eventually decays to a lower lying state (to the ground state), if one does not consider the coupling of the atom with the *quantized EM field*. Indeed, if one does not consider this coupling, an atom prepared in the excited state, which is an eigen-state of the atomic Hamiltonian, should be stable, and therefore the atom should not decay. There is another phenomenon that cannot be explained without refering to the quantized nature of the EM field: the shift of the energy levels of the atom. Historically, in the 1940s, it was demonstrated experimentally by Lamb and Retherford that the levels $2S_{1/2}$ and $2P_{1/2}$ of the hydrogen atom in free space do not have the same energy [4], contrary to what is predicted in the absence of coupling with the quantized EM field (by the Dirac equation). This small shift of the energy levels, named the *Lamb shift* after its discoverer, has stimulated theorists to calculate the exact value of the Lamb shift for these levels and led to the most successful theory of light-matter interactions: Quantum ElectroDynamics (QED).

According to QED, the *quantized* EM field in the *vacuum* state (no light, no photon, no excitation) is not *null*: it is null *on average*, but it has fluctuations. These "vacuum fluctuations" can be invoked to explain the phenomenon of spontaneous emission and energy level shifts as we are going to see.

The decay rate, *i.e.* the transition probability per unit time to the ground state, is calculated from the time-dependent perturbation theory to first order in the atom - quantized EM field coupling; this is the so-called Fermi golden rule. The shift of energy levels of the atom are calculated to second order in the atom - quantized EM field coupling from time-independent perturbation theory.

The details of these quantum calculations are given in Appendix 2.A, and we summarize here the different steps leading to the quantum expressions of the decay rate and energy level shifts. We start from the second-order perturbation result of the energy level shifts for the ground and excited states and the Fermi golden rule for the decay rate, given in Appendix 2.A by Eqs. (2.56) and (2.59), respectively, and we use following interaction Hamiltonian, for the atom - quantized EM field coupling, taken in the electric dipole approximation:

$$\hat{H}_I(\mathbf{r}_0) = -\hat{\mathbf{d}} \cdot \hat{\mathbf{E}}_v(\mathbf{r}_0) \tag{2.11}$$

where $\hat{\mathbf{d}}$ is the atomic electric dipole operator and $\hat{\mathbf{E}}_v(\mathbf{r}_0)$ is the transverse electric field operator evaluated at the position of the atom $\mathbf{r}_0$. From this, the energy level shift and decay rate can be expressed in terms of a *correlation function* of the vacuum field [see Eqs. (2.67) and (2.68) in Appendix 2.A]:

$$\Delta E_e = \frac{1}{2\pi\hbar} \mathcal{P} \left\{ \int_0^{+\infty} \mathrm{d}\omega \, \frac{\mathbf{d}^* \cdot \hat{\mathbf{C}}(\mathbf{r}_0, \mathbf{r}_0, \omega) \cdot \mathbf{d})}{(\omega_0 - \omega)} \right\} \tag{2.12}$$

where here again $\mathcal{P}$ denotes the "principal value" of the integral, and

$$\gamma = \frac{1}{\hbar^2} \mathbf{d}^* \cdot \hat{\mathbf{C}}(\mathbf{r}_0, \mathbf{r}_0, \omega_0) \cdot \mathbf{d} \tag{2.13}$$

where $\mathbf{d} = \langle \mathrm{e}|\,\hat{\mathbf{d}}\,|\mathrm{g}\rangle$. The correlation function $\hat{\mathbf{C}}$ appearing in Eqs. (2.12) and (2.13) is given (see Eq. (2.65) in Appendix 2.A):

$$\hat{\mathbf{C}}(\mathbf{r},\mathbf{r}',\omega) \equiv \int_{-\infty}^{+\infty} \mathrm{d}t\, \left\langle \hat{\mathbf{E}}_v(\mathbf{r},t)\hat{\mathbf{E}}_v(\mathbf{r}',0)\right\rangle \mathrm{e}^{\mathrm{i}\omega t} \tag{2.14}$$

where $\hat{\mathbf{E}}_v(\mathbf{r},t)$ is now in the interaction picture and the braket indicates an ensemble average:

$$\left\langle \hat{\mathbf{E}}_v(\mathbf{r},t)\hat{\mathbf{E}}_v(\mathbf{r},0)\right\rangle = \sum_{I,F} p(I)|\,\langle F|\,\hat{\mathbf{E}}_v(\mathbf{r})\,|I\rangle\,|^2\,\mathrm{e}^{-\mathrm{i}(\omega_F-\omega_I)t} \tag{2.15}$$

where the capital letters I and F refer to the states of the EM field in the presence of the medium, and $p(I)$ is the probability that the field is in the state I with energy E_I (assuming that the field is in thermodynamic equilibrium with the environment at temperature T) given by:

$$p(I) = \frac{\exp(-\beta E_I)}{\sum_k \exp(-\beta E_k)} \qquad \text{with} \quad \beta \equiv (k_B T)^{-1} \tag{2.16}$$

This function characterizes mathematically the temporal fluctuations of the vacuum EM. This is why the vacuum fluctuations are said to be responsible of the spontaneous decay and the energy level shift; indeed, if one sets this correlation function to zero in Eqs. (2.67) and (2.68), one can see that there is no longer a decay ($\gamma = 0$) neither energy shifts ($\Delta E_i = 0$).

This correlation function can be calculated by giving an explicit quantization of the field $\hat{\mathbf{E}}_v(\mathbf{r},t)$, expressing it in terms of annihilation and creation operators (like the ones introduced in the previous Chapter), and by using the properties of these operators to carry on the calculation. However, it is complicated to give an explicit quantization of the field for an arbitrary environment[2]. Here, we use a different method. According to Eqs. (2.67) and (2.68), *the temporal fluctuations of the EM vacuum contains all the information about the dynamics of an atom initially prepared in the excited state*. From linear-response theory, we know how to relate these fluctuations to the linear-response function of the system, which is for this problem the classical Green tensor of Maxwell equations introduced in Section 2.2.1: the relation is given by the *fluctuation-dissipation theorem* for a system in thermodynamic equilibrium at temperature T [22–24]:

$$\boxed{\hat{\mathbf{C}}(\mathbf{r},\mathbf{r}',\omega) = \left(1-\mathrm{e}^{-\hbar\omega/k_B T}\right)\frac{2\hbar\omega^2}{\epsilon_0 c^2}\mathrm{Im}(\hat{\mathbf{G}}(\mathbf{r},\mathbf{r}',\omega))} \tag{2.17}$$

The temperature dependence will only be important for $k_B T > \hbar\omega$, and since we are dealing with optical frequencies, $k_B T \ll \hbar\omega$ at room temperature, so we will set $T = 0\,\mathrm{K}$ in the following. This powerful theorem connects the fluctuations of the vacuum to the dielectric constants via the Green tensor. In other words, it tells us how the vacuum fluctuations are modified by the presence of an environment (characterized by the Green tensor). Thanks

[2] Some procedures exist to quantize the EM field in an arbitrary environment, by giving an explicit representation of the quantized EM field in terms of the Green tensor and bosonic field operators $\hat{\mathbf{f}}$ and $\hat{\mathbf{f}}^\dagger$ that depend of both the position $\mathbf{r}$ and the frequency ω, but the formalism is rather involved. The presentation of this quantization scheme is given in the next Chapter.

to this theorem, one can avoid the explicit quantization of the EM field, and it is instead the Green tensor of the environment that is used in the quantum treatment.

From the Appendix 2.A, one eventually finds the expressions in terms of the Green tensor of the energy level shifts ΔE_e and ΔE_g of the ground and excited states, respectively, defined as $\Delta E_i \equiv E_i^* - E_i$, with E_i the eigen-energy and E_i^* the new shifted energy [see Eqs. (2.71) and (2.72)]:

$$\Delta E_\mathrm{e} = -\mathcal{P}\left\{\int_0^{+\infty} \mathrm{d}\omega\, \frac{1}{\pi}\frac{1}{\epsilon_0}\frac{\omega^2}{c^2}\,\frac{\mathbf{d}^*\cdot\mathrm{Im}(\hat{\mathbf{G}}(\mathbf{r}_0,\mathbf{r}_0,\omega))\cdot\mathbf{d}}{(\omega-\omega_0)}\right\} \tag{2.18}$$

$$\Delta E_g = -\int_0^{+\infty} \mathrm{d}\omega\, \frac{1}{\pi}\frac{1}{\epsilon_0}\frac{\omega^2}{c^2}\,\frac{\mathbf{d}^*\cdot\mathrm{Im}(\hat{\mathbf{G}}(\mathbf{r}_0,\mathbf{r}_0,\omega))\cdot\mathbf{d}}{(\omega+\omega_0)} \tag{2.19}$$

and decay rate [see Eq. (2.73)]:

$$\gamma = \frac{2\omega_0^2}{\hbar\epsilon_0 c^2}\mathbf{d}^*\cdot\mathrm{Im}(\hat{\mathbf{G}}(\mathbf{r}_0,\mathbf{r}_0,\omega_0))\cdot\mathbf{d} \tag{2.20}$$

Eq. (2.18) can be cast in the following form (see [25] for a direct calculation, or by invoking the Kramers–Kronig relations for the Green tensor see [26])

$$\Delta E_\mathrm{e} = -\frac{\omega_0^2}{\epsilon_0 c^2}\,\mathbf{d}^*\cdot\mathrm{Re}\left(\hat{\mathbf{G}}(\mathbf{r}_0,\mathbf{r}_0,\omega_0)\right)\cdot\mathbf{d} \underbrace{-\int_0^{+\infty} \mathrm{d}\omega\, \frac{1}{\pi}\frac{1}{\epsilon_0}\frac{\omega^2}{c^2}\,\frac{\mathbf{d}^*\cdot\mathrm{Im}(\hat{\mathbf{G}}(\mathbf{r}_0,\mathbf{r}_0,\omega))\cdot\mathbf{d}}{(\omega+\omega_0)}}_{\Delta E_\mathrm{e}^\mathrm{vdW}} \tag{2.21}$$

where the super-script "vdW" means "van der Waals" as called in [25].

Comment: One can note that the second term in the right hand side (r.h.s.) of Eq. (2.21) corresponds exactly to the expression of ΔE_g. This fortuitous cancellation happens because we considered here a two-level atom, but for a model of the atom more realistic than a two-level atom, $\Delta E_\mathrm{e}^\mathrm{vdW}$ and ΔE_g will not in general be the same [6, 25, 27]. For general expressions of the energy shifts and decay rate in a multilevel atom, see [8, 25].

The frequency-shift of the photon emitted by spontaneous emission $\Delta\omega \equiv \hbar^{-1}(\Delta E_\mathrm{e} - \Delta E_g)$, called photonic Lamb shift, simply Lamb shift or frequency-shift in this thesis, is therefore for a two-level atom:

$$\Delta\omega = -\frac{\omega_0^2}{\hbar\epsilon_0 c^2}\,\mathbf{d}^*\cdot\mathrm{Re}\left(\hat{\mathbf{G}}(\mathbf{r}_0,\mathbf{r}_0,\omega_0)\right)\cdot\mathbf{d} \tag{2.22}$$

As previously, we separate the Green tensor into a "free-space" $\hat{\mathbf{G}}_0$ plus a "scattering" $\hat{\mathbf{G}}_s$ contributions [20], so that the Lamb shift and decay rate of Eqs. (2.22) and (2.20) read:

$$\Delta\omega = -\frac{\omega_0^2}{\hbar\epsilon_0 c^2}\,\mathbf{d}^*\cdot\mathrm{Re}\left(\hat{\mathbf{G}}_0(\mathbf{r}_0,\mathbf{r}_0,\omega_0)\right)\cdot\mathbf{d} - \frac{\omega_0^2}{\hbar\epsilon_0 c^2}\,\mathbf{d}^*\cdot\mathrm{Re}\left(\hat{\mathbf{G}}_s(\mathbf{r}_0,\mathbf{r}_0,\omega_0)\right)\cdot\mathbf{d} \tag{2.23}$$

$$\gamma = \frac{2\omega_0^2}{\hbar\epsilon_0 c^2}\mathbf{d}^*\cdot\mathrm{Im}(\hat{\mathbf{G}}_0(\mathbf{r}_0,\mathbf{r}_0,\omega_0))\cdot\mathbf{d} + \frac{2\omega_0^2}{\hbar\epsilon_0 c^2}\mathbf{d}^*\cdot\mathrm{Im}(\hat{\mathbf{G}}_s(\mathbf{r}_0,\mathbf{r}_0,\omega_0))\cdot\mathbf{d} \tag{2.24}$$

Comment: In the expression of the Lamb shift Eq. (2.23), $\mathrm{Re}[\hat{\mathbf{G}}_0(\mathbf{r}_0,\mathbf{r}_0,\omega_0)]$ diverges. It is well-known since the work of Bethe [5] that a non-relativistic treatment of the atom-field coupling leads to a vacuum level shift that is incorrect, and that the correct way is provided by QED theory. However, as we are not interested in this effect of the vacuum (which is small), but by the frequency-shift produced by the presence of a medium, the vacuum shift will be considered as already included in the energy levels of the atom, and we will only keep the part containing the scattered part in Eq. (2.23) (see also [25, 26]).

Finally, using the fact in Eq. (2.24) that $\vec{u}_d \cdot \mathrm{Im}(\hat{\mathbf{G}}_0(\mathbf{r}_0,\mathbf{r}_0,\omega_0)) \cdot \vec{u}_d = \omega_0/6\pi c$ where $\vec{u}_d$ is the unit vector defining the direction of the dipole moment $\mathbf{d}$ (see [20] Chapter 8), the previous equations are written as:

$$\Delta\omega = -\frac{\omega_0^2}{\hbar\epsilon_0 c^2}\,\mathbf{d}^* \cdot \mathrm{Re}\left(\hat{\mathbf{G}}_s(\mathbf{r}_0,\mathbf{r}_0,\omega_0)\right) \cdot \mathbf{d} \tag{2.25}$$

$$\gamma = \gamma_0 + \frac{2\omega_0^2}{\hbar\epsilon_0 c^2}\mathbf{d}^* \cdot \mathrm{Im}(\hat{\mathbf{G}}_s(\mathbf{r}_0,\mathbf{r}_0,\omega_0)) \cdot \mathbf{d} \tag{2.26}$$

where in Eq. (2.26) the quantum decay rate in free space appears:

$$\gamma_0 = \frac{\omega_0^3 |\mathbf{d}|^2}{3\pi\epsilon_0\hbar c^3} \tag{2.27}$$

The expressions of the Lamb shift and decay rate, given by Eqs. (2.25) and (2.26), respectively, are exactly equal to the classical expressions given in Eqs. (2.9) and (2.10) once *normalized by the decay rate in free-space* given by Eq. (2.27). Normalizing the decay rate by the classical/quantum expressions in free space eliminates the dependencies on $\mathbf{d}/\mathbf{p}$ and provides a safe link between quantum and classical formalisms.

Thus, in the *weak-coupling regime*, or in other words within the framework of the lower-order perturbation theory, the quantum treatment of a two-level atom gives the same result as the classical treatment when considering the *normalized* Lamb shift and the *normalized* decay rate.

2.3 Nanoparticle in the electric dipole approximation

In the Section 2.2, we showed that, for a two-level atom, the quantum and classical expressions of the Lamb shift (and decay rate) are the same provided these quantities are normalized with respect to the decay rate in free space γ_0 *(the classical one for the classical expressions and the quantum mechanical one for the quantum ones). Therefore, one can use the classical expressions, which lead to another interpretation of the problem: according to Eqs. (2.3) and (2.4), one can see that the Lamb shift and decay rate induced by the surrounding environment are caused by the field* $\mathbf{E}_s$ *scattered back at the position of the QE* $\mathbf{r}_0$*. The determination of* $\mathbf{E}_s$ *is thus the chief obstacle to the calculation of the Lamb shift. The problem can be therefore reformulated as a scattering problem: given an excitation field — in this case the one produced by an oscillating point dipole (in a classical picture),*

find the electric field scattered by the environment $\mathbf{E}_s$*. In this Section, we analyse the Lamb shift of a quantum emitter near plasmonic nanoparticles, using a multipolar formulation of the scattered field. But before diving into the multipolar formalism, we first present a simple description of the optical response of a plasmonic nanoparticle, modeled as an electric dipole, which allows to compute the field scattered by a sphere, and explain why a multipole description of the scattered field is often necessary in the nanoantenna problems in general. Next, we briefly sketch the multipolar theory and the T-Matrix formalism within which an analysis of the Lamb shift will be carried on. We then analyse the Lamb shift calculated within this formulation with a in-house code, in the case of an emitter coupled to a silver nanoparticle, to illustrate the multipolar origin of the plasmon resonance enhanced Lamb shift. We next show some physical effects due to the response of several multipoles, and finally end the section with a calculation of the Lamb shift of a QE in the gap of a gold dimer, predicting a shift of the emission wavelength of* 2.5 *nm.*

2.3.1 Scattered field in the electric dipole approximation

We first consider the case of an electric dipole source near a plasmonic nanoparticle. The parameters of the problem are shown in Fig. 2.1.

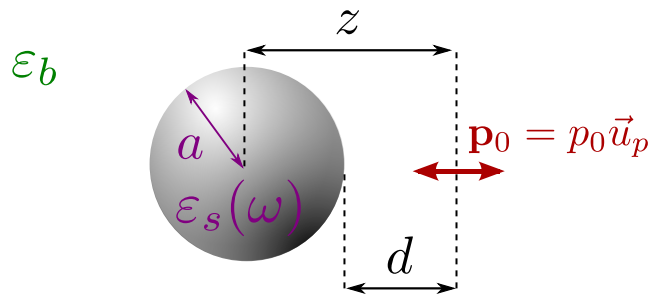

Figure 2.1 – Parameters of the problem: a sphere of relative permittivity $\varepsilon_s(\omega)$ and radius a at the position $\mathbf{r}_s$, and a point dipole source of electric dipole moment $\mathbf{p}_0 = p_0\tilde{u}_p$ (red arrow) at the position $\mathbf{r}_0$, all embedded in a homogeneous environment of relative permittivity ε_b. $z = |\mathbf{r}_s - \mathbf{r}_0|$ denotes the distance between the center of the sphere and the point emitter, and $d = z - a$ denotes the distance between the emitter and the surface of the sphere.

The optical response of a plasmonic nanoparticle to an excitation field $\mathbf{E}_{\text{exc}}$, in a homogeneous background of permittivity ε_b, is often calculated by modeling the nanoparticle as an induced electric dipole $\mathbf{p}_s$:

$$\mathbf{p}_s = \epsilon_0\varepsilon_b\alpha(\omega)\mathbf{E}_{\text{exc}}(\mathbf{r}_s,\omega) \tag{2.28}$$

which oscillates at the frequency of the excitation field $\mathbf{E}_{\text{exc}}(\mathbf{r}_s,\omega)$, where $\mathbf{r}_s$ is the position of the sphere.

This approximation called the *electric dipole approximation* which models the nanoparticle as an electric dipole is valid if the excitation field is uniform (homogeneous) within the nanoparticle (this is the case for example of a plane wave of wavelength $\lambda \gg a$ with a the radius of the nanoparticle) [28], so that the response of the nanoparticle is due to a collective excitation of the electrons, and the particle behaves as a "giant" electric dipole

(the magnetic dipole is negligible for metallic nanoparticles [28], but must be taken into account for dielectric nanoparticles [29]).

Caveat: This *electric dipole approximation* used to model the optical response of a nanoparticle should not be confused with the approximation of the same name used to write the interaction Hamiltonian between a two-level atom and the electric field as in Eq. (2.55) for instance.

The proportionnality coefficient $\alpha(\omega)$ in Eq. (2.28) is the called the *polarizability* of the sphere. It is given, accounting for radiation damping, and in the *quasi-static approximation* which considers that $2\pi a/\lambda \to 0$ [28, 30, 31]:

$$\alpha(\omega) = \frac{\alpha_0(\omega)}{1 - \mathrm{i}(k^3/6\pi)\alpha_0(\omega)} \tag{2.29}$$

and $\alpha_0(\omega)$ is the *quasi-static* polarizability and is given by:

$$\alpha_0(\omega) = 4\pi a^3 \frac{\varepsilon_s(\omega) - \varepsilon_b}{\varepsilon_s(\omega) + 2\varepsilon_b} \tag{2.30}$$

We introduce in this example the notion of *localized surface plasmon resonance*. The plasmon resonance is the frequency at which $\varepsilon_s(\omega) \simeq -2\varepsilon_b$. It is at this frequency that the response of the nanoparticle to an excitation field will be the largest. For example, for a silver nanoparticle in air ($\varepsilon_b = 1$), this resonance occurs at (in terms of wavelength): $\lambda \simeq 364\,\mathrm{nm}$. [3]

From these expressions, one can then calculate the field scattered by the nanoparticle in any point $\mathbf{r}$ of space outside the particle as ([20], Chapter 8):

$$\mathbf{E}_s(\mathbf{r}, \omega) = \omega^2 \mu\mu_0 \hat{\mathbf{G}}_0(\mathbf{r}, \mathbf{r}_s, \omega) \cdot \mathbf{p}_s \tag{2.31}$$

where $\hat{\mathbf{G}}_0(\mathbf{r}, \mathbf{r}', \omega)$ is the free-space Green function given by Eq. (2.8).

2.3.2 Lamb shift and decay rate in the electric dipole approximation

We now want to calculate the decay rate and Lamb shift modifications on a dipole emitter located at the $\mathbf{r}_0$ due to the presence of the plasmonic nanoparticle, where the later is treated within the electric dipole approximation. According to Eqs. (2.3) and (2.4), one simply has to evaluate the field scattered by the nanoparticle at the position of the emitter $\mathbf{r}_0$ and at the excitation frequency corresponding to the emitter frequency ω_0 $\mathbf{E}_s(\mathbf{r}_0, \omega_0)$, by using Eq. (2.31) [with $\mathbf{p}_s$ calculated by Eqs. (2.28), (2.29), (2.30)], and

[3] In order to know the dependence of the plasmon resonance with the radius of the sphere, one must go beyond the quasi-static approximation where the dipolar polarizability of the sphere is related to the electric dipolar Mie coefficient a_1 by $\alpha = \mathrm{i}6\pi/k^3 a_1$. By denoting $x \equiv 2\pi a/\lambda$, one can then Taylor expand the Mie coefficient considering $x \ll 1$ and $n_s x \ll 1$ with $n_s = \sqrt{\varepsilon_s}$, and get [32]: $\mathrm{Re}[\varepsilon_s(\omega)]/\varepsilon_b \simeq -2 - 12x^2/5$. This formula tells us that the plasmon resonance frequency is red-shifted when the size of the particle increases. The counterpart for dielectric nanoparticles considering electric *and* magnetic dipolar polarizabilities can be found in [29].

where the excitation field appearing in Eq. (2.28) is the one produced by the point electric dipole source of dipole moment $\mathbf{p}_0$ and located at $\mathbf{r}_0$, and reads:

$$\mathbf{E}_{\text{exc}}(\mathbf{r}_s, \omega_0) = \omega_0^2 \mu\mu_0 \hat{\mathbf{G}}_0(\mathbf{r}_s, \mathbf{r}_0, \omega_0) \cdot \mathbf{p}_0 \tag{2.32}$$

By plugging the obtained expression for $\mathbf{E}_s(\mathbf{r}_0, \omega_0)$ into Eq. (2.4), and using the expression of the free-space Green function [Eq. (2.8)], one gets the following decay rate for an emitter oriented perpendicular to the surface of the sphere (along the z direction, or "radially oriented") [30]:

$$\frac{\gamma^{\perp}}{\gamma_0} = 1 + \frac{3k_0^3}{2\pi} \text{Im}\left[\alpha(\omega_0) \text{e}^{2\text{i}k_0 z}\left(\frac{-1}{(k_0 z)^4} + \frac{2}{\text{i}(k_0 z)^5} + \frac{1}{(k_0 z)^6}\right)\right] \tag{2.33}$$

and for an emitter oriented parallel to the surface (dipole moment oriented perpendicular to the z direction) [30]:

$$\frac{\gamma^{\parallel}}{\gamma_0} = 1 + \frac{3k_0^3}{8\pi} \text{Im}\left[\alpha(\omega_0) \text{e}^{2\text{i}k_0 z}\left(\frac{1}{(k_0 z)^2} - \frac{2}{\text{i}(k_0 z)^3} - \frac{3}{(k_0 z)^4} + \frac{2}{\text{i}(k_0 z)^5} + \frac{1}{(k_0 z)^6}\right)\right] \tag{2.34}$$

Similarly, for the Lamb shift given by Eq. (2.3), ones get:

$$\frac{\Delta\omega^{\perp}}{\gamma_0} = -\frac{3k_0^3}{4\pi} \text{Re}\left[\alpha(\omega_0) \text{e}^{2\text{i}k_0 z}\left(\frac{-1}{(k_0 z)^4} + \frac{2}{\text{i}(k_0 z)^5} + \frac{1}{(k_0 z)^6}\right)\right] \tag{2.35}$$

and for an emitter oriented parallel to the surface:

$$\frac{\Delta\omega^{\parallel}}{\gamma_0} = -\frac{3k_0^3}{16\pi} \text{Re}\left[\alpha(\omega_0) \text{e}^{2\text{i}k_0 z}\left(\frac{1}{(k_0 z)^2} - \frac{2}{\text{i}(k_0 z)^3} - \frac{3}{(k_0 z)^4} + \frac{2}{\text{i}(k_0 z)^5} + \frac{1}{(k_0 z)^6}\right)\right] \tag{2.36}$$

Note: These equations for the decay rate and Lamb shift are exact (modelling the nanoparticle as an electric dipole), but one can get approximate expressions in the near-field region $k_0 z \ll 1$, by expanding the exponential term (this has been done for the decay rate expressions in [30]).

In order to illustrate the limitations of this electric dipole approximation, we compare in Fig. 2.2 the decay rate obtained within this approximation [Eq. (2.33)] (red curve) with the one computed with the exact Mie theory (black curve), as a function of the distance d emitter - surface of the sphere. For the calculations, we consider that the emitter is oriented perpendicular to the surface of a silver nanosphere of radius $a = 20\,\text{nm}$, and that the emission wavelength is $\lambda_0 = 2\pi c/\omega_0 = 335\text{nm}$. One can see that the electric dipole approximation describes well the decay rate for distances $d > 2a$ (see also Ref. [33]). However, for $d < 2a$ this approximation fails. The reason is the following: the excitation source, an oscillating dipole in the classical picture, radiates a field which is highly non-homogeneous in the near-field of the source. This problem was pointed out and discussed in Ref. [34]. Therefore, the field within the nanoparticle cannot be assumed to be uniform, even if $\lambda_0 \gg a$, and the particle response (the scattered field) cannot be modeled as the one radiated by a giant electric dipole. There is a need to go beyond the quais-static approximation to describe an emitter located at short distances from a resonator; this can

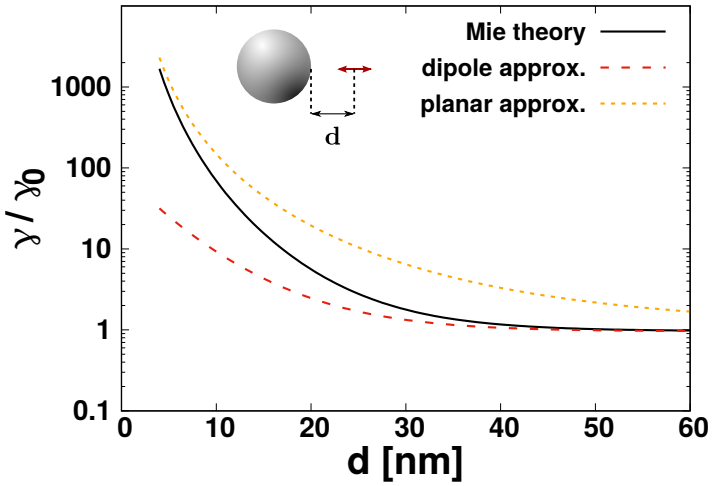

Figure 2.2 – Normalized decay rate γ/γ_0 (black curve) as a function of the distance d between a radially-oriented dipole emitter (red arrow) and the surface of a silver nanosphere of radius $a = 20\,\text{nm}$. The emission wavelength is at $\lambda_0 = 335\,\text{nm}$. The red dashed curve corresponds to a dipolar response of the nanoparticle (electric dipole approximation), and the orange dashed curve to the asymptotic case of a silver planar surface. Note that the vertical axis is in logscale. A Drude-Lorentz model for the silver permittivity is used according to [35].

be done by using a *multipolar description of the scattered field*, which is presented in the next Section.

Note that in Fig. 2.2, we also plotted the asymptotic case of a planar surface (orange dashed curve), where the decay rate is given by [7]:

$$\frac{\gamma^{\perp}}{\gamma_0} = 1 + \frac{3}{4k_0^3}\frac{\text{Im}[\varepsilon_s(\omega_0)]}{|\varepsilon_s(\omega_0)+\varepsilon_b|^2}\frac{1}{d^3} \tag{2.37}$$

We also give the analogous Lamb shift expression [7]:

$$\frac{\Delta\omega^{\perp}}{\gamma_0} = -\frac{3}{16k_0^3}\frac{|\varepsilon_s(\omega_0)|^2-\varepsilon_b}{|\varepsilon_s(\omega_0)+\varepsilon_b|^2}\frac{1}{d^3}\,, \tag{2.38}$$

These expressions are valid in the near-field region $k_0 z \ll 1$ (also called the non-retarded regime) and for an emitter oriented perpendicular to the surface (for the expressions for an emitter parallel to the surface, see Ref. [7]). In this case, the decay rate and frequency-shift have a resonant response when $\varepsilon_s \simeq -\varepsilon_b$. which is possible for metallic interfaces, due to the coupling to the surface plasmon polariton mode of the metal (which is essentially *non-radiative* and is referred to as *quenching* of the excited quantum emitter when it couples to this surface plasmon of the metal). For the case of a silver interface in air ($\varepsilon_b = 1$), it occurs around 340 nm.

2.4 Multipolar formulation of the scattering problem

2.4.1 Multipolar basis

In order to calculate the field scattered by the environment $\mathbf{E}_s$, we will use the *multipolar theory*, which is especially useful in describing EM scattering for particles with spherical symetries [18, 36], allowing an analytical formulation of the scattering problem (and avoid an integral formulation using the Green formalism). We will make use of the multipolar modes — also called Vector Partial Waves — which are a basis for EM fields, and that are by definition solutions of the vectorial Helmholtz equations in spherical coordinates. The construction of these modes and their explicit representations are given in Appendix 2.B. Importantly, each mode is specified by three discrete numbers: q accounts for the parity of the field, and $q = 1$ for a magnetic mode and $q = 2$ for an electric mode; $n = 1, 2, ..., \infty$ and will be called the "multipolar order"; and $m = -n, ..., n$ and will be called the "orbital number". In the following, we will denote these modes by $\mathbf{M}_{nm}(k\mathbf{r})$ for the magnetic modes ($q = 1$) and $\mathbf{N}_{nm}(k\mathbf{r})$ for the electric modes ($q = 2$), in the real space representation ($k = \omega/c$).

2.4.2 T-Matrix formulation

A very fruitful method to calculate the scattered field $\mathbf{E}_\mathrm{s}$ knowing the excitation field $\mathbf{E}_\mathrm{exc}$ is the T-Matrix method [28]. In *operator notation*, the T-Matrix denoted $\hat{\mathbf{T}}$ can be defined as:

$$\hat{\mathbf{E}}_\mathrm{s} = \hat{\mathbf{T}} \cdot \hat{\mathbf{E}}_\mathrm{exc} \tag{2.39}$$

The above expression traduces the fact that the scattered field $\mathbf{E}_\mathrm{s}$ has a *linear* relation with the excitation field $\mathbf{E}_\mathrm{exc}$, and this linear dependence is embodied by the T-Matrix. The T-Matrix is associated to a scatterer center and characterizes entirely its optical response to an arbitrary excitation. Considering the case of a single scatterer first, its coefficients can be defined from the following procedure:

1. One breaks the domain into two sub-domains separated by the surface of the scatterer, defining the internal field $\mathbf{E}_\mathrm{int}$ and outside field $\mathbf{E}_\mathrm{out} = \mathbf{E}_\mathrm{exc} + \mathbf{E}_\mathrm{s}$;

2. One then expands all the EM fields (excitation, internal and scattered) on the multipolar modes as (such expansions are particularly useful to describe the optical response of *spherical* objects):

$$\mathbf{E}_\mathrm{int}(k\mathbf{r}) = E_0 \sum_{n=1}^{\infty} \sum_{m=-n}^{n} s_{nm}^{(1)} \mathbf{M}_{nm}(k\mathbf{r}) + s_{nm}^{(2)} \mathbf{N}_{nm}(k\mathbf{r}) \tag{2.40}$$

$$\mathbf{E}_\mathrm{exc}(k\mathbf{r}) = E_0 \sum_{n=1}^{\infty} \sum_{m=-n}^{n} e_{nm}^{(1)} \mathbf{M}_{nm}(k\mathbf{r}) + e_{nm}^{(2)} \mathbf{N}_{nm}(k\mathbf{r}) \tag{2.41}$$

$$\mathbf{E}_\mathrm{s}(k\mathbf{r}) = E_0 \sum_{n=1}^{\infty} \sum_{m=-n}^{n} f_{nm}^{(1)} \mathbf{M}_{nm}^{(+)}(k\mathbf{r}) + f_{nm}^{(2)} \mathbf{N}_{nm}^{(+)}(k\mathbf{r}) \tag{2.42}$$

where E_0 is the amplitude of the field, $s_{nm}^{(i)}$, $e_{nm}^{(i)}$ and $f_{nm}^{(i)}$ are the coefficients of the magnetic ($i=1$) and electric ($i=2$) modes of the internal, excitation and scattered field, respectively.

3. Finally, one uses the continuity of the tangential components of the fields inside and outside the scatterer; as a consequence of the linearity of the Maxwell equations and of the continuity conditions, the coefficients of the scattered field are linearly related to those of the excitation field:

$$f_{nm}^{(2)} = -t_n^{(2)} e_{nm}^{(2)} \tag{2.43}$$

$$f_{nm}^{(1)} = -t_n^{(1)} e_{nm}^{(1)} \tag{2.44}$$

The T-Matrix coefficients are then defined as the coefficients of proportionnality between the coefficients $f_{nm}^{(i)}$ and $e_{nm}^{(i)}$. Note that this T-Matrix is infinite dimensional because the multipolar basis is infinite (the multipolar order $n=1,...,\infty$), but in practice it is rendered finite by truncating the multipolar order n to some finite dimension n_{cut} (the choice of n_{cut} for which the summation with respect to the multipolar order n converges will depend on particle size and interaction strengths).

Generalized Lorentz-Mie theory: In the case of a spherical Mie scatterer, T, is a diagonal matrix composed of the Mie coefficients of the sphere (multiplied by -1). We now give the expressions of the Mie coefficients in a slightly different way than in [28] (where they are called the scattering coefficients). By introducing ε_s [μ_s] and ε_b [μ_b] as the relative permittivity [permeability] of the sphere and the homogeneous background respectively, $k_s = \sqrt{\varepsilon_s(\omega)}\omega/c$ and $k = \sqrt{\varepsilon_b}\omega/c$, the Mie coefficients of a sphere of radius a take the form:

$$a_n = \frac{(\varepsilon_s/\varepsilon_b) j_n(k_s a)\psi_n'(ka) - \psi_n'(k_s a) j_n(ka)}{(\varepsilon_s/\varepsilon_b) j_n(k_s a)\xi_n'(ka) - \psi_n'(k_s a) h_n(ka)}\,, \tag{2.45}$$

for the electric Mie coefficient of order n, and

$$b_n = \frac{(\mu_s/\mu_b) j_n(k_s a)\psi_n'(ka) - \psi_n'(k_s a) j_n(ka)}{(\mu_s/\mu_b) j_n(k_s a)\xi_n'(ka) - \psi_n'(k_s a) h_n(ka)}\,, \tag{2.46}$$

for the magnetic Mie coefficient of order n, where $j_n(x)$ and $h_n(x)$ are respectively the spherical Bessel functions and the first-type (outgoing) spherical Hankel functions, and $\psi_n(x)$ and $\xi_n(x)$ are the Ricatti-Bessel functions defined as:

$$\psi_n(x) \equiv x j_n(x) \tag{2.47}$$

$$\xi_n(x) \equiv x h_n(x)\,. \tag{2.48}$$

2.4.3 Scattered field from a dipole source

We next apply this method to the scattering problem sketched in Fig. 2.1: we want to compute the expression of the electric field $\mathbf{E}_s(\mathbf{r}, \omega_0)$ scattered by a single scatterer

centered on $\mathbf{r}_s$ and excited by a ponctual electric dipole source of dipole moment $\mathbf{p}_0 = p_0\vec{u}_p$, frequency ω_0 and located at the position $\mathbf{r}_0$. Denoting by T the T-Matrix of the scatterer, the electric field scattered back at the position of the source reads [37]:

$$\mathbf{E}_s(\mathbf{r}_0,\omega_0) = \frac{\mathrm{i}p_0 k\omega_0^2}{\epsilon_0 c^2}\left[[\mathbf{M}(k\mathbf{r}_s),\mathbf{N}(k\mathbf{r}_s)]^t T H^{(1,0)} e\right], \tag{2.49}$$

where $[\mathbf{M},\mathbf{N}]$ is a column matrix composed of the $\mathbf{M}_{nm}$ and $\mathbf{N}_{nm}$ functions, e represents the coefficients of the dipole source written as a column matrix in the multipole space. $H^{(1,0)}$ is the irregular translation-addition matrix between the emitter position at $\mathbf{r}_0$ and the position of particle at $\mathbf{r}_s$, and comes from the translation-addition theorem [38] which allows the field to be written as a regular expansion around the center of the particle by using the translation-addition matrix [4].

Generalization to N scatterers: One of the powerful point of the T-Matrix is that it can also be used to describe the multiple-scattering from an ensemble of N scatterers, excited by a source. In the case of N scatterers, the above formula reads [37]:

$$\mathbf{E}_s(\mathbf{r}_0,\omega_0) = \frac{\mathrm{i}p_0 k\omega_0^2}{\epsilon_0 c^2}\sum_{i,j=1}^{N}\left[[\mathbf{M}(k\mathbf{r}_i),\mathbf{N}(k\mathbf{r}_i)]^t T^{(i,j)} H^{(j,0)} e\right], \tag{2.50}$$

where the $T^{(i,j)}$ matrices represent all multiple-scattering events from a multiple-scattering viewpoint [38]), with i and j being the particle labels. Several methods exist for calculating the $T^{(i,j)}$ matrices, and we use the analytical balancing techniques detailed in [39] and implemented in an in-house code used for the numerical simulations of this article.

2.4.4 Multipole formula for the Lamb shift

Finally, the expression of $\mathbf{E}_s(\mathbf{r},\omega_0)$ [Eq. (2.50)] can be utilized in Eq. (2.3) to obtain the multipole expression for the normalized Lamb shift induced by the presence of N scatterers [37]:

$$\frac{\Delta\omega}{\gamma_0} = 3\pi \times \mathrm{Im}\left(\sum_{i,j=1}^{N} e^t H^{(0,i)} T^{(i,j)} H^{(j,0)} e\right). \tag{2.51}$$

In the case of a single particle ($N = 1$), Eq. (2.51) takes the form:

$$\frac{\Delta\omega}{\gamma_0} = 3\pi \times \mathrm{Im}\left(e^t H^{(0,1)} T^{(1,1)} H^{(1,0)} e\right), \tag{2.52}$$

where $T^{(1,1)}$ is the single-particle T-Matrix. For the analogous expression of the decay rate, see Ref. [37].

[4] Remember that the multipolar fields depends on the origin, and the origin is chosen by us to be at the position of the source.

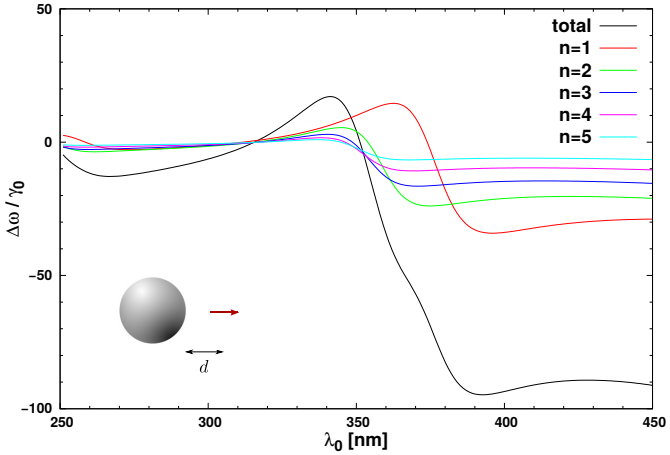

Figure 2.3 – Numerical simulations of the total Lamb shift $\Delta\omega$ (black curve) and its multipolar contributions $n = 1, 2, 3, 4, 5$ (colored curves) as a function of the transition wavelength $\lambda_0 = 2\pi c/\omega_0$ for a perfect electric dipole emitter with radial orientation and located at $d = 10\,\text{nm}$ from a silver nanosphere with $a = 20\,\text{nm}$ radius (red arrow). The Lamb shift is normalized to the dipole's decay rate in free space γ_0. The refractive index of the homogeneous background is $n_b = 1$. A Drude-Lorentz model for the silver permittivity is used according to [35]. The total Lamb shift is computed by taking $n_{\text{cut}} = 10$.

Case of a spherical Mie scatterer: In the case of a sphere, the T-Matrix appearing in Eq. (2.52) is diagonal, and its coefficients are the Mie coefficients given by Eqs. (2.45) and (2.46) (and multiplied by -1). Eq. (2.52) is then equivalent to expressions derived for a single sphere [13, 14], and for the decay rate see [40]. Exact analytical expressions of the first two multipolar contributions to the Lamb shift can be found in Appendix 2.C. For the case of the decay rate, see Ref. [41].

2.5 Multipolar analysis

2.5.1 Multipolar origin of the plasmon resonance enhanced Lamb shift

Let us first calculate the Lamb shift in the case of a silver nanosphere of radius $a = 20\,\text{nm}$ in vacuum ($n_b = 1$). Based on Eq. (2.52), we compute using an in-house code the Lamb shift of a quantum emitter radially oriented and located at a distance $d = 10\,\text{nm}$ from the nanoparticle, as a function of the bare transition wavelength $\lambda_0 = 2\pi c/\omega_0$ (black curve in Fig. 2.3). We analyze this Lamb shift spectrum by plotting separately the different multipolar contributions (plotted in colors in Fig. 2.3: $n = 1$ corresponds to the contribution of the dipolar mode, $n = 2$ to the contribution of the quadrupolar mode and so on). One can thus see that in the near-field of the nanoparticle, the total Lamb shift (black curve) is due to the contribution of several multipolar modes (colored curves). In other words, in the near-field region, the atom couples to several plasmon modes of the silver nanoparticle (see also [40]), which gives rise to the complex pattern of the Lamb shift spectrum, which cannot be grasped by the electric dipole approximation (which would correspond to the red curve in Fig. 2.3).

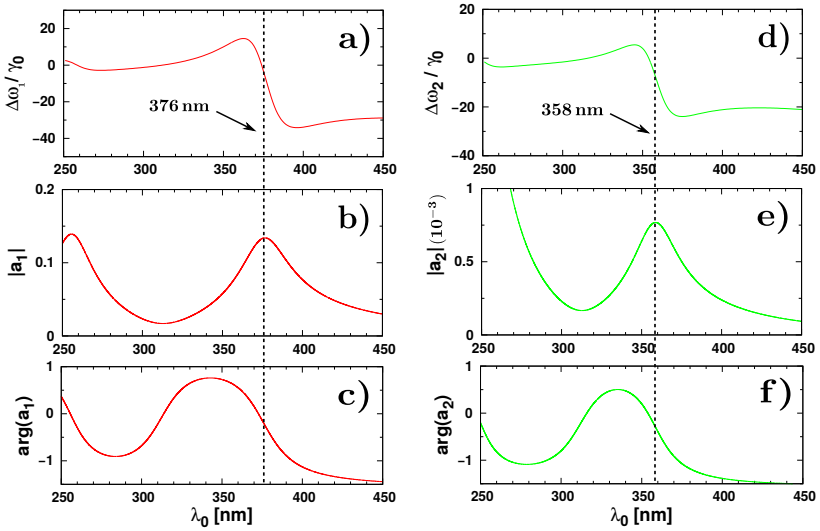

Figure 2.4 – (a) and (d): Lamb shift dipolar (red curve) and quadrupolar (green curve) contributions of Fig.2.3 (same color code) normalized by γ_0. (b) and (e): Modulus of the associated electric dipolar (red curve) and quadrupolar (green curve) Mie coefficients a_1 and a_2 as a function of the excitation wavelength λ_0. (c) and (f): Argument of the associated electric dipolar (red curve) and quadrupolar (green curve) Mie coefficients a_1 and a_2 as a function of λ_0. A Drude-Lorentz model for the silver permittivity is used according to [35].

In order to account for the Lamb shift spectral response, we will make use of the analytical expressions of the dipolar and quadrupolar contributions derived in Appendix 2.C, in the case of a radially oriented dipole. In the non-retarded regime $k_0 z \ll 1$ (which is fulfilled here), the analytical expression of the dipolar contribution ($n = 1$) reduces to,

$$\frac{\Delta\omega_1^{\perp}}{\gamma_0} = \frac{9}{2}\frac{1}{(k_0 z)^6}\mathrm{Im}[a_1] + O\left((k_0 z)^{-6}\right), \tag{2.53}$$

while the quadrupolar contribution ($n = 2$) reduces to,

$$\frac{\Delta\omega_2^{\perp}}{\gamma_0} = \frac{405}{2}\frac{1}{(k_0 z)^8}\mathrm{Im}[a_2] + O\left((k_0 z)^{-8}\right), \tag{2.54}$$

where the subscript $\perp$ indicates a dipole perpendicular to the particle surface (radially oriented), and a_1 (a_2) is the electric dipolar (quadrupolar) Mie coefficient whose expressions are given by Eq. (2.45). The explanation of the spectral behavior of the Lamb shift is thus found in the imaginary part of the Mie coefficient. In Fig. 2.4, we plot the modulus ((b) and (e)) and phase ((c) and (f)) of the electric dipolar and quadrupolar Mie coefficients a_1 and a_2 respectively as a function of the excitation wavelength, together with the first two multipolar contributions $n = 1$ and $n = 2$ of Fig. 2.3 ((a) and (d) in Fig. 2.4 plotted with the same color code). One can see that the inflection point of the Lamb shift spectrum (around 376 nm for $n = 1$ and 358 nm for $n = 2$) corresponds to a resonance maximum of the modulus of the associated Mie coefficient accompanied by a strong phase change (the resonance of the Mie coefficients around 250 nm is a spurious resonance peculiar to the model of permittivity used [42]). This clearly shows the multipolar origin of the plasmon resonance enhanced Lamb shift.

Finally, it is interesting to note that this resonant coupling induces a *positive* Lamb shift $\Delta\omega = \omega - \omega_0 > 0$ (around 340 nm in the configuration under study, see Fig. 2.3), which was first predicted in the case of silver [7] and sodium [25] surfaces (see also [13] where a similar effect was reported in the case of a dielectric microsphere). This positive Lamb shift leads to a *repulsive van der Waals potential* as long as the atom remains in its excited state, which was shown experimentally with *excited* cesium atoms in the presence of a sapphire surface [43, 44].

2.5.2 Blue-shift of the resonance

In this section, we show how the size of the nanoparticle affects the position of the Lamb shift resonance. We still consider the case of a silver nanosphere. We plot in Fig. 2.5 the normalized Lamb shift as a function of the transition wavelength for different particle radii (full lines). The asymptotic case of a planar surface is also plotted (dashed line) according to the expression given in Eq. (2.38), valid in the non-retarded regime and for an emitter oriented perpendicular to the surface. In this case, the dipole emitter couples to the surface plasmon mode which comes from the infinite density of states of the high order modes (around $\lambda_0 \simeq 340\,\text{nm}$ for a planar silver surface).

In sharp contrast with a nanosphere characterized by a purely dipolar response, we predict in the near-field of the nanosphere a *blue*-shift of the Lamb shift resonance as the radius of the nanosphere increases (see Fig. 2.5). To understand this feature, let us recall that as the radius increases, each plasmon resonance is red-shifted and the dipole emitter couples to higher-order multipoles [40]. The displacement (blue-shift) of the Lamb shift resonance then results from the *interference* between these different modes. Therefore, this effect will only exist if the dipole emitter is located in the near-field of the nanoparticle, so that it will be able to excite *several* modes and to get this interference effect, resulting then in a blue-shift of the resonance.

Thus, it can be observed in Fig. 2.5 that in the near-field of the nanoparticle, a precise engineering of this resonant coupling between the quantum emitter and the plasmon resonances is possible. For instance, the transition wavelength at which the Lamb shift is suppressed is $\lambda_0 = 363\,\text{nm} > \lambda_0 = 357\,\text{nm} > \lambda_0 = 350\,\text{nm} > \lambda_0 = 342\,\text{nm} > \lambda_0 = 339\,\text{nm}$ for the radii $a = 2.5\,\text{nm}$, $a = 5\,\text{nm}$, $a = 10\,\text{nm}$, $a = 50\,\text{nm}$ and the case of the planar silver surface respectively. The tuning of this interaction is of current interest [45], and we suggest that thanks to their highly tunable optical properties, metallic nanoparticles can also be used to tune and shape the Lamb shift of a nearby quantum emitter through a control of their geometry, but also spatial organization and environment, which can all be investigated through Eq. (2.51).

2.6 Calculation for a gold dimer nanoantenna

In order to make a realistic calculation of the Lamb shift, let us now consider a gold dimer with a dipole emitter located at the center of the nanogap. This configuration is now experimentally realizable using DNA templates [46, 47]. For the Lamb shift calculation,

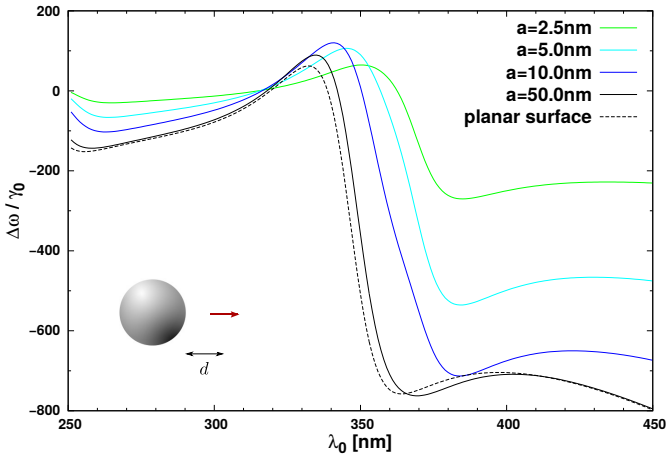

Figure 2.5 – Numerical simulations of the normalized Lamb shift $\Delta\omega/\gamma_0$ as a function of the transition wavelength λ_0 for a perfect electric dipole emitter with radial orientation and located at $d = 5\,\text{nm}$ from a silver nanosphere (red arrow), for different radii a (full lines). The asymptotic case of a planar silver surface (Eq. (2.38)) is also plotted (dashed line). The refractive index of the homogeneous background is $n_b = 1$. A Drude-Lorentz model for the silver permittivity is used according to [35]. The Lamb shift is computed by taking $n_{\text{cut}} = 10$ except for the case $a = 50\,\text{nm}$ where $n_{\text{cut}} = 50$ in order to converge.

we take the parameters corresponding to those adopted in Ref. [48]: the nanoparticles radius is 40 nm, the nanogap is 6 nm, and the effective refractive index surrounding the nanoparticles is $n_{\text{eff}} = 1.5$; the fluorescent molecule is an *Alexa Fluor 647* dye, which presents an emission peak around $\lambda_0 = 670\,\text{nm}$ with 40 nm width; its total decay rate in the homogeneous solution is measured at $\gamma_0 = 2.63\,\text{ns}^{-1}$ [49].

The Lamb shift spectrum of such a configuration with a dipole emitter of parallel orientation is shown in Fig. 2.6. At $\lambda_0 = 670\,\text{nm}$, the normalized Lamb shift computed with Eq. (2.51) is $\Delta\omega/\gamma_0 = -8200$. In order to find the Lamb shift of the dye, one needs to multiply the value given by the numerical simulations by the reference *quantum yield* $\phi_0 = 0.08$ in open solution (*i.e.* without the antenna): $\Delta\omega = \phi_0 \times (-8200) \times \gamma_0$. The corresponding shift in terms of wavelength is given by the following formula (valid if $\Delta\omega/\omega_0 \ll 1$): $\Delta\lambda/\lambda_0 = -\Delta\omega/\omega_0$ where $\Delta\lambda = \lambda - \lambda_0$ with λ the new wavelength of the emitted photon. Thus, for the Alexa Fluor 647 dye, the relative shift is $\Delta\lambda/\lambda_0 = 3.8\times10^{-3}$, corresponding to a shift $\Delta\lambda = 2.5\,\text{nm}$.

Such a shift could be detected at room temperature, by fitting the entire emission spectrum of the molecule (see for instance [50] where a shift of $\Delta\lambda \simeq 0.3\,\text{nm}$ has been detected — for the resonance spectrum of a gold nanorod — between neighboring Gaussian peaks with width of about 50 nm which is similar to our case here). One should also ensure that the spectral dependence of the Lamb shift, decay rate enhancement and quantum yield enhancement, do not vary appreciably in the range used for fluorescence detection (the decay rate enhancement and quantum yield enhancement spectra for the same configuration can be found in [48], Fig. 3).

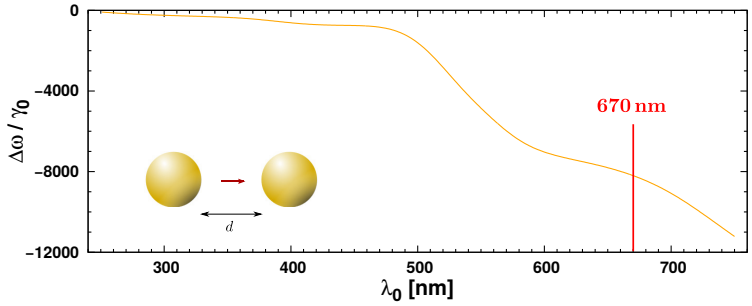

Figure 2.6 – Numerical simulations of the normalized Lamb shift $\Delta\omega/\gamma_0$ as a function of the transition wavelength λ_0 for a perfect electric dipole emitter with parallel orientation and located in the center of a gold dimer antenna of radius 40 nm and 6 nm gap (red arrow). The refractive index of the homogeneous background is $n_b = 1.5$. A Drude-Lorentz model for the gold permittivity is used according to [35]. The Lamb shift is computed by taking $n_{\text{cut}} = 40$.

2.7 Conclusion

In this Chapter, we firstly recalled in Section 2.2 the equivalence between a classical and a quantum description of a QE in the weak-coupling regime. The equivalence is established by expressing the Lamb shift and decay rate in terms of the Green tensor, which is straightforward in the classical description by expressing the electric field in terms of the Green tensor, and requires the use of the quantum version of the fluctuation-dissipation theorem in the quantum description.

We next derived in Section 2.5 an exact multipole formula, Eq. (2.51), to compute the Lamb shift induced by an arbitrary set of resonant scatterers on a nearby quantum emitter, based on the multipolar and the T-Matrix formalisms presented in Section 2.4. In the case of a single silver nanoparticle, our numerical simulations show that the electric dipole approximation fails to account for the total Lamb shift spectrum in the near-field region, and that one must include higher multipolar contributions. This formula also predicts a displacement of the Lamb shift resonance in the near-field to higher frequencies (blue-shift) when the size of the nanoparticle increases. Finally, in Section 2.6, a calculation of the Lamb shift in a physically realistic configuration is carried on. Our prediction of a shift of the emission wavelength of 2.5 nm for a fluorescent molecule embedded in a gold dimer nanogap indicates that a direct detection may be possible.

2.A Quantum derivation of the Lamb shift and decay rate

In this Appendix, we derive the quantum expressions of the decay rate and the energy shifts of a two-level atoms in terms of the Green tensor of Maxwell equations, following closely [8, 25].

System

One consider a two-level atom with ground state $|\mathrm{g}\rangle$ and excited state $|\mathrm{e}\rangle$ of eigenenergies E_g and E_e, respectively. When one introduces a coupling with the quantized electromagnetic field modeled by $\hat{H}_I$:

$$\hat{H}_I(\mathbf{r}_0) = -\hat{\mathbf{d}} \cdot \hat{\mathbf{E}}_v(\mathbf{r}_0) \tag{2.55}$$

where $\hat{\mathbf{d}}$ is the atomic electric dipole operator and $\hat{\mathbf{E}}_v(\mathbf{r}_0)$ is the transverse electric field operator evaluated at the position of the atom $\mathbf{r}_0$, the energy level of the atom E_g and E_e are shifted by a quantity ΔE_i.

Perturbation theory

By considering that the matrix elements of the interaction Hamiltonian are small compared to those of the non-interacting Hamiltonian (weak-coupling approximation in a quantum context), the energy-shifts $\Delta E_\mathrm{e} = E_\mathrm{e}^* - E_\mathrm{e}$ where E_e^* is the new energy can calculated using time-independent perturbation theory to second order in the perturbation $H_I(\mathbf{r}_0)$:

$$\Delta E_\mathrm{e} = E_\mathrm{e}^* - E_\mathrm{e} = \sum_{I,F} p(I) \frac{|\langle \mathrm{g}, F|\hat{H}_I(\mathbf{r}_0)|\mathrm{e}, I\rangle|^2}{\hbar(\omega_\mathrm{e} - \omega_g) - \hbar(\omega_F - \omega_I)} \tag{2.56}$$

where the capital letters I and F refer to the states of the EM field in the presence of the medium. We assume that the field is in thermodynamic equilibrium with the environment at temperature T such that the probability $p(I)$ that the field is in the state I with energy E_I is given by:

$$p(I) = \frac{\exp(-\beta E_I)}{\sum_k \exp(-\beta E_k)} \qquad \text{with} \quad \beta \equiv (k_B T)^{-1} \tag{2.57}$$

Such expression can be put in an integral form as:

$$\Delta E_\mathrm{e} = \mathcal{P}\left\{ \int_0^{+\infty} \mathrm{d}\omega \sum_{I,F} p(I) \frac{|\langle \mathrm{g}, F|\hat{H}_I(\mathbf{r}_0)|\mathrm{e}, I\rangle|^2}{\hbar(\omega_\mathrm{e} - \omega_g - \omega)} \delta(\omega_F - \omega_I - \omega) \right\} \tag{2.58}$$

where we introduce $\mathcal{P}$ as the "principal value" of the integral.

The decay rate is given by the Fermi golden rule, which is derived using time-dependent perturbation theory to first order in the perturbation $H_I(\mathbf{r}_0)$:

$$\gamma = \frac{2\pi}{\hbar^2} \sum_{I,F} p(I) |\langle \mathrm{g}, F|\hat{H}_I(\mathbf{r}_0)|\mathrm{e}, I\rangle|^2 \delta(\omega_F + \omega_g - \omega_I - \omega_\mathrm{e}) \tag{2.59}$$

Reservoir coupling spectrum

In these two expressions (2.58) and (2.59), we introduce the quantity called *reservoir coupling spectrum*:

$$R(\mathbf{r},\omega) \equiv \frac{1}{\hbar^2}\sum_{I,F} p(I)|\langle \mathrm{g},F|\hat{H}_I(\mathbf{r})|\mathrm{e},I\rangle|^2\delta(\omega_F-\omega_I-\omega) \tag{2.60}$$

so that these expressions are recast conveniently in terms of this function in the form:

$$\Delta E_\mathrm{e} = \mathcal{P}\left\{\int_0^{+\infty} \mathrm{d}\omega\,\hbar\frac{R(\mathbf{r}_0,\omega)}{(\omega_0-\omega)}\right\} \tag{2.61}$$

and

$$\gamma = 2\pi R(\mathbf{r}_0,\omega_0) \tag{2.62}$$

where we used the fact that $\omega_0 = \omega_\mathrm{e}-\omega_\mathrm{g}$.

Fluctuation-dissipation theorem

We now will use the fluctuation-dissipation theorem to show that the reservoir coupling spectrum $R(\mathbf{r},\omega)$ is related to the Green tensor $\hat{\mathbf{G}}(\mathbf{r},\mathbf{r}',\omega)$. We start from the expression of $R(\mathbf{r},\omega)$ given in Eq. (2.60) and we proceed by expressing the δ function in integral form [see Ref. [8] passage from Eq. (2.2) to (2.3) for instance[5]]:

$$\begin{aligned} R(\mathbf{r},\omega) &= \frac{1}{2\pi\hbar^2}\int_{-\infty}^{+\infty}\mathrm{d}t\sum_{I,F} p(I)|\langle \mathrm{g},F|\hat{H}_I(\mathbf{r})|\mathrm{e},I\rangle|^2\,\mathrm{e}^{-\mathrm{i}(\omega_F-\omega_I-\omega)t} \\ &= \frac{1}{2\pi\hbar^2}\int_{-\infty}^{+\infty}\mathrm{d}t\,\mathbf{d}^*\left\langle\hat{\mathbf{E}}_\nu(\mathbf{r},t)\hat{\mathbf{E}}_\nu(\mathbf{r},0)\right\rangle\mathbf{d}\,\mathrm{e}^{\mathrm{i}\omega t} \end{aligned} \tag{2.63}$$

where $\hat{\mathbf{E}}_\nu(\mathbf{r},t)$ is now in the interaction picture and the braket indicates an ensemble average:

$$\left\langle\hat{\mathbf{E}}_\nu(\mathbf{r},t)\hat{\mathbf{E}}_\nu(\mathbf{r},0)\right\rangle = \sum_{I,F} p(I)|\langle F|\hat{\mathbf{E}}_\nu(\mathbf{r})|I\rangle|^2\,\mathrm{e}^{-\mathrm{i}(\omega_F-\omega_I)t} \tag{2.64}$$

and $\mathbf{d} = \langle \mathrm{e}|\hat{\mathbf{d}}|\mathrm{g}\rangle$. By introducing the **correlation tensor** $\hat{\mathbf{C}}(\mathbf{r},\mathbf{r}',\omega)$:

$$\hat{\mathbf{C}}(\mathbf{r},\mathbf{r}',\omega) \equiv \int_{-\infty}^{+\infty}\mathrm{d}t\,\left\langle\hat{\mathbf{E}}_\nu(\mathbf{r},t)\hat{\mathbf{E}}_\nu(\mathbf{r}',0)\right\rangle\mathrm{e}^{\mathrm{i}\omega t} \tag{2.65}$$

the expression of $R(\mathbf{r},\omega)$ is recast in the form:

$$R(\mathbf{r},\omega) = \frac{1}{2\pi\hbar^2}\,\mathbf{d}^*\cdot\hat{\mathbf{C}}(\mathbf{r},\mathbf{r},\omega)\cdot\mathbf{d} \tag{2.66}$$

Therefore, the energy shift and decay rate given in Eqs. (2.61) and (2.62), respectively, can be written in terms of the correlation tensor $\hat{\mathbf{C}}(\mathbf{r},\mathbf{r},\omega)$:

$$\Delta E_\mathrm{e} = \frac{1}{2\pi\hbar}\mathcal{P}\left\{\int_0^{+\infty}\mathrm{d}\omega\,\frac{\mathbf{d}^*\cdot\hat{\mathbf{C}}(\mathbf{r}_0,\mathbf{r}_0,\omega)\cdot\mathbf{d})}{(\omega_0-\omega)}\right\} \tag{2.67}$$

[5] Do not be confused that the quantity 'R' used in Ref. [8] is the decay rate, not like us.

and

$$\gamma = \frac{1}{\hbar^2}\mathbf{d}^* \cdot \hat{\mathbf{C}}(\mathbf{r}_0, \mathbf{r}_0, \omega_0) \cdot \mathbf{d} \tag{2.68}$$

We next use the **linear-response theory** and the quantum form of the **fluctuation-dissipation theorem** to express the correlation tensor in terms of the Green tensor $\hat{\mathbf{G}}(\mathbf{r}, \mathbf{r}', \omega)$ [22–24]:

$$\boxed{\hat{\mathbf{C}}(\mathbf{r}, \mathbf{r}', \omega) = \left(1 - \mathrm{e}^{-\hbar\omega/k_B T}\right) \frac{2\hbar\omega^2}{\epsilon_0 c^2} \mathrm{Im}(\hat{\mathbf{G}}(\mathbf{r}, \mathbf{r}', \omega))} \tag{2.69}$$

where $\hat{\mathbf{G}}(\mathbf{r}, \mathbf{r}', \omega)$ is defined as the solution of Eq. (2.6) with the proper boundary conditions. One can see that the temperature dependence will only be important for $k_B T > \hbar\omega$. Since we are dealing with optical frequencies, one has $k_b T \ll \hbar\omega$ at room temperature, so that one can set it to zero $T = 0\,\mathrm{K}$.

Finally, employing expression (2.69) into Eq. (2.66) gives the following expression of $R(\mathbf{r}, \omega)$ in terms of the Green tensor at zero temperature:

$$\boxed{R(\mathbf{r}, \omega) = \frac{1}{\pi}\frac{1}{\hbar\epsilon_0}\frac{\omega^2}{c^2}\mathbf{d}^* \cdot \mathrm{Im}(\hat{\mathbf{G}}(\mathbf{r}, \mathbf{r}, \omega)) \cdot \mathbf{d}} \tag{2.70}$$

Expressions of energy shift and decay rate in terms of the Green tensor

Now, by plugging expression (2.70) of the reservoir into Eqs. (2.61) and (2.62), one gets:

$$\Delta E_\mathrm{e} = -\mathcal{P}\left\{\int_0^{+\infty} \mathrm{d}\omega \, \frac{1}{\pi}\frac{1}{\epsilon_0}\frac{\omega^2}{c^2} \frac{\mathbf{d}^* \cdot \mathrm{Im}(\hat{\mathbf{G}}(\mathbf{r}_0, \mathbf{r}_0, \omega)) \cdot \mathbf{d}}{(\omega - \omega_0)}\right\} \tag{2.71}$$

One get the expression for the shift of the energy of the ground state ΔE_g by inverting ω_e and ω_g in the above equation, which gives (we discard the principal value $\mathcal{P}$ which is not needed anymore):

$$\Delta E_g = -\int_0^{+\infty} \mathrm{d}\omega \, \frac{1}{\pi}\frac{1}{\epsilon_0}\frac{\omega^2}{c^2} \frac{\mathbf{d}^* \cdot \mathrm{Im}(\hat{\mathbf{G}}(\mathbf{r}_0, \mathbf{r}_0, \omega)) \cdot \mathbf{d}}{(\omega + \omega_0)} \tag{2.72}$$

The decay rate reads:

$$\gamma = \frac{2\omega_0^2}{\hbar\epsilon_0 c^2}\mathbf{d}^* \cdot \mathrm{Im}(\hat{\mathbf{G}}(\mathbf{r}_0, \mathbf{r}_0, \omega_0)) \cdot \mathbf{d} \tag{2.73}$$

2.B The multipolar basis

In this Appendix, we present a particular basis of electromagnetic mode of the Maxwell equations without source particularly suitable to describe problems with spherical symmetry: the multipolar modes, also called Vector Partial Waves, following the notations of Ref. [18] Chapter 3. The multipolar modes are a set of solutions of the Helmholtz equation in spherical coordinates:

$$\begin{aligned} \nabla \cdot (\nabla \mathbf{E}) + \left(\frac{\omega}{c}\right)^2 \varepsilon(\mathbf{r},\omega)\mathbf{E} = 0 \\ \nabla \cdot (\nabla \mathbf{H}) + \left(\frac{\omega}{c}\right)^2 \varepsilon(\mathbf{r},\omega)\mathbf{H} = 0 \end{aligned} \tag{2.74}$$

They can be constructed from the solution of the *scalar* Helmholtz equation in spherical coordinates denoted by φ [18]:

$$\mathbf{M} = \frac{\nabla \times (\vec{r}\varphi)}{\sqrt{n(n+1)}}, \tag{2.75}$$

$$\mathbf{N} = \frac{\nabla \times \mathbf{M}}{k} \tag{2.76}$$

The scalar Helmholtz equation is:

$$\nabla^2 \varphi + k^2 \varphi = 0 \tag{2.77}$$

One can construct the following sets of solution of this equation in spherical $\varphi(r,\theta,\phi)$:

$$\begin{aligned} \varphi_{nm}(k\mathbf{r}) &= j_n(kr)Y_{nm}(\theta,\phi) \\ \varphi^{(+)}_{nm}(k\mathbf{r}) &= h_n(kr)Y_{nm}(\theta,\phi) \end{aligned} \tag{2.78}$$

where $j_n(kr)$ and $h_n(x)$ are respectively the spherical Bessel functions and the first-type (outgoing) spherical Hankel functions.

$$Y_{nm}(\theta,\phi) = \left[\frac{2n+1}{4\pi}\frac{(n-m)!}{(n+m)!}\right] e^{im\phi} P_n^m(cos(\theta)) \tag{2.79}$$

where the functions P_n^m are the Legendre polynomials for $n = 0,1,2.....\infty$ and $m = -n,...,n$. n is called the "multipolar order", and m the "orbital number". From these two sets of solution of the scalar Helmholtz equation, two sets of solution for the **M** and **N** can be deduced.

However, it is more useful to express them in terms of the Vector Spherical Harmonics (VSH), defined as:

$$\begin{aligned} \mathbf{Y}_{nm}(\theta,\phi) &= Y_{nm}(\theta,\phi)\vec{r} \\ \mathbf{Z}_{nm}(\theta,\phi) &= \frac{r\nabla \mathbf{Y}_{nm}(\theta,\phi)}{\sqrt{n(n+1)}} \\ \mathbf{X}_{nm}(\theta,\phi) &= \mathbf{Z}_{nm}(\theta,\phi) \times \vec{r} \end{aligned} \tag{2.80}$$

which form a complete basis permitting to describe the angular variations of any vector fields.

The first set of basis is:

$$\begin{aligned}\mathbf{M}_{nm}(k\mathbf{r}) &= j_n(kr)\mathbf{X}_{nm}(\theta,\phi)\\ \mathbf{N}_{nm}(k\mathbf{r}) &= \frac{1}{kr}\left[\sqrt{n(n+1)}j_n(kr)\mathbf{Y}_{nm}(\theta,\phi)+[krj_n(kr)]'\mathbf{Z}_{nm}(\theta,\phi)\right]\end{aligned} \tag{2.81}$$

and the second set is:

$$\begin{aligned}\mathbf{M}^{(+)}_{nm}(k\mathbf{r}) &= h_n(kr)\mathbf{X}_{nm}(\theta,\phi)\\ \mathbf{N}^{(+)}_{nm}(k\mathbf{r}) &= \frac{1}{kr}\left[\sqrt{n(n+1)}h_n(kr)\mathbf{Y}_{nm}(\theta,\phi)+[krh_n(kr)]'\mathbf{Z}_{nm}(\theta,\phi)\right]\end{aligned} \tag{2.82}$$

2.C Analytical expressions of dipolar/quadrupolar Lamb shift

In this Appendix, we derive from Eq. (2.52) analytical expressions for the Lamb shift dipolar and quadrupolar contributions for a sphere. We consider the sphere placed at the position $\mathbf{r}_s = (0,0,+z)$ and an electric dipole emitter at the position $\mathbf{r}_0 = (0,0,0)$ and oriented either perpendicular to the surface of the sphere (orbital number $m = 0$, dipole moment oriented along the z direction) or parallel to the surface ($m = 1$, dipole moment oriented perpendicularly to the z direction). Due to spherical symmetry, the T-Matrix of the single sphere is a diagonal matrix t composed of the Mie coefficients of the sphere multiplied by -1. With a quadrupolar assumption [41]:

$$t = -\mathrm{Diag}(a_1, a_2, b_1, b_2)\,, \tag{2.83}$$

with a_1 (a_2) the electric dipolar (quadrupolar) Mie coefficient and b_1 (b_2) the magnetic dipolar (quadrupolar) Mie coefficient defined in Eqs. (2.45) and (2.46),

$$e = [e_1, 0, 0, 0]^t\,, \tag{2.84}$$

with e_1 the incident electric dipole coefficient, and

$$H^{(0,1)} = \begin{bmatrix} A_{1,m,1,m} & A_{1,m,2,m} & B_{1,m,1,m} & B_{1,m,2,m} \\ A_{1,m,2,m} & A_{2,m,2,m} & B_{1,m,2,m} & B_{2,m,2,m} \\ B_{1,m,1,m} & B_{1,m,2,m} & A_{1,m,1,m} & A_{1,m,2,m} \\ B_{1,m,2,m} & B_{2,m,2,m} & A_{1,m,2,m} & A_{2,m,2,m} \end{bmatrix}\,, \tag{2.85}$$

where $A_{n,m,n',m'}$ ($B_{n,m,n',m'}$) the coupling coefficient from the electric (magnetic) multipole order n with orbital number m, to the multipole order n' with orbital number m'. Note that $H^{(1,0)}$ is the same as $H^{(0,1)}$ with all the B coefficients multiplied by -1. Employing the expressions of the coefficients A and B calculated in [41] in Eq. (2.52), one gets for an electric dipole oriented perpendicular to the particle surface ($m = 0$):

$$\frac{\Delta\omega_1^{\perp}}{\gamma_0} = \frac{9}{2}\mathrm{Im}\left[a_1 \frac{e^{2\mathrm{i}k_0 z}}{(k_0 z)^6}(1 - \mathrm{i}k_0 z)^2\right] \tag{2.86}$$

for the dipolar contribution and

$$\frac{\Delta\omega_2^{\perp}}{\gamma_0} = -\frac{9}{10}\mathrm{Im}\left[a_2 \frac{e^{2\mathrm{i}k_0 z}}{(k_0 z)^8}\left(-15\mathrm{i} - 15(k_0 z) - 25(k_0 z)^2\right)^2\right] \tag{2.87}$$

for the quadrupolar contribution. In the case of an electric dipole emitter oriented parallel to the particle surface ($m = 1$), the dipolar and quadrupolar contributions to the Lamb shift read:

$$\begin{aligned} \frac{\Delta\omega_1^{\parallel}}{\gamma_0} =& \frac{9}{8}\mathrm{Im}\left[a_1 \frac{e^{2\mathrm{i}k_0 z}}{(k_0 z)^6}\left(1 - 2\mathrm{i}(k_0 z) - 3(k_0 z)^2 + 2\mathrm{i}(k_0 z)^3 + (k_0 z)^4\right)\right] \\ & - \frac{9}{8}\mathrm{Im}\left[b_1 \frac{e^{2\mathrm{i}k_0 z}}{(k_0 z)^4}\left(\mathrm{i} + (k_0 z)\right)^2\right] \end{aligned} \tag{2.88}$$

$$\begin{aligned}\frac{\Delta\omega_2^{\parallel}}{\gamma_0} =& -\frac{15}{8}\mathrm{Im}\left[a_2\frac{e^{2ik_0z}}{(k_0z)^8}\left(6\mathrm{i}+6(k_0z)-3\mathrm{i}(k_0z)^2-(k_0z)^3\right)^2\right]\\ &+\frac{15}{8}\mathrm{Im}\left[b_2\frac{e^{2ik_0z}}{(k_0z)^6}\left(3-3\mathrm{i}(k_0z)-(k_0z)^2\right)^2\right]\end{aligned} \tag{2.89}$$

Note that the Eq. (2.86) is the same as Eq. (2.35) using the fact that $\alpha = \mathrm{i}(6\pi/k_0^3)a_1$, and Eq. (2.88) gives the same expression as Eq. (2.36) provided one sets $b_1 = 0$. For plasmonic nanoparticles, the magnetic resonances can be neglected compared to the electric ones, and one can set all the $b_n = 0$ in Eqs. (2.88) and (2.89). However, dielectric nanoparticle support magnetic resonances (see *e.g.* Ref. [41]), and one cannot set all the $b_n = 0$. For dielectric nanoparticles, in the case of a dipole emitter with parallel orientation [Eqs. (2.88) and (2.89)], the presence of the magnetic Mie coefficients b_1 and b_2 traduces the coupling between the electric dipole emitter and the *magnetic* resonances. Note that it is not the case for a dipole perpendicularly oriented [whose multipolar Lamb shift contributions only depends on the electric Mie coefficients, see Eqs. (2.86) and (2.87)] because the magnetic field produced by an electric dipole is null along the dipole axis, and therefore for this specific orientation the emitter only couples to *electric* resonances.

Bibliography

[1] A. F. Koenderink, ACS Photonics **4**, 710 (2017).

[2] E. M. Purcell, Physical Review **69**, 681 (1946).

[3] R. G. Hulet, E. S. Hilfer, and D. Kleppner, Physical Review Letters **55**, 2137 (1985).

[4] W. E. Lamb and R. C. Retherford, Physcial Review **72**, 241 (1947).

[5] H. A. Bethe, Physical Review **72**, 339 (1947).

[6] G. Barton, Journal of Physics B: Atomic and Molecular Physics **7**, 2134 (1974).

[7] R. R. Chance, A. Prock, and R. Silbey, Physical Review A **12**, 1448 (1975).

[8] J. M. Wylie and J. Sipe, Physical Review A **30**, 1185 (1984).

[9] A. Kofman, G. Kurizki, and B. Sherman, Journal of Modern Optics **41**, 353 (1994).

[10] S.-Y. Zhu, Y. Yang, H. Chen, H. Zheng, and M. S. Zubairy, Physical Review Letters **84**, 2136 (2000).

[11] X.-H. Wang, Y. S. Kivshar, and B.-Y. Gu, Physical Review Letters **93**, 073901 (2004).

[12] S. C. Ching, H. M. Lai, and K. Young, Journal of the Optical Society of America B **4**, 2004 (1987).

[13] V. V. Klimov, M. Ducloy, and V. S. Letokhov, Journal of Modern Optics **43**, 2251 (1996).

[14] H. T. Dung, L. Knöll, and D.-G. Welsch, Physical Review A **64**, 013804 (2001).

[15] V. Klimov, M. Ducloy, and V. Letokhov, The European Physical Journal D-Atomic, Molecular, Optical and Plasma Physics **20**, 133 (2002).

[16] A. Asatryan, L. Botten, N. Nicorovici, R. McPhedran, and C. M. de Sterke, Waves in Random and Complex Media **16**, 151 (2006).

[17] W. Zhu, R. Esteban, A. G. Borisov, J. J. Baumberg, P. Nordlander, H. J. Lezec, J. Aizpurua, and K. B. Crozier, Nature Communications **7** (2016).

[18] R. Colom, *Etude théorique et expérimentale des résonances optiques des résonateurs de Mie diélectriques pour exalter les interactions lumière-matière*, Ph.D. thesis, Aix-Marseille Université (2018).

[19] F. Marquier, C. Sauvan, and J.-J. Greffet, ACS Photonics **4**, 2091 (2017).

[20] L. Novotny and B. Hecht, *Principles of nano-optics* (Cambridge University Press, 2012).

[21] J. D. Jackson, *Classical electrodynamics* (AAPT, 1999).

[22] R. Kubo and K. Tomita, Journal of the Physical Society of Japan **9**, 888 (1954).

[23] A. McLachlan, Proceedings of the Royal Society of London A **271**, 387 (1963).

[24] G. Agarwal, Physical Review A **11**, 230 (1975).

[25] J. Wylie and J. Sipe, Physical Review A **32**, 2030 (1985).

[26] D. Dzsotjan, J. Kästel, and M. Fleischhauer, Physical Review B **84**, 075419 (2011).

[27] E. Hinds and V. Sandoghdar, Physical Review A **43**, 398 (1991).

[28] C. F. Bohren and D. R. Huffman, *Absorption and scattering of light by small particles* (John Wiley & Sons, 2008).

[29] R. Colom, A. Devilez, N. Bonod, and B. Stout, Physical Review B **93**, 045427 (2016).

[30] R. Carminati, J.-J. Greffet, C. Henkel, and J. Vigoureux, Optics Communications **261**, 368 (2006).

[31] S. Albaladejo, M. I. Marqués, M. Laroche, and J. J. Sáenz, Physical Review Letters **102**, 113602 (2009).

[32] A. Moroz, Journal of the Optical Society of America B **26**, 517 (2009).

[33] E. Castanié, M. Boffety, and R. Carminati, Optics Letters **35**, 291 (2010).

[34] P. C. Chaumet, A. Rahmani, F. de Fornel, and J.-P. Dufour, Physical Review B **58**, 2310 (1998).

[35] A. D. Rakić, A. B. Djurišić, J. M. Elazar, and M. L. Majewski, Applied Optics **37**, 5271 (1998).

[36] X. Zambrana-Puyalto, *Control and characterization of nano-structures with the symmetries of light*, Ph.D. thesis, Macquarie University (2014).

[37] B. Stout, A. Devilez, B. Rolly, and N. Bonod, Journal of the Optical Society of America B **28**, 1213 (2011).

[38] B. Stout, J.-C. Auger, and J. Lafait, Journal of Modern Optics **49**, 2129 (2002).

[39] B. Stout, J.-C. Auger, and A. Devilez, Journal of the Optical Society of America A **25**, 2549 (2008).

[40] G. C. des Francs, A. Bouhelier, E. Finot, J. C. Weeber, A. Dereux, C. Girard, and E. Dujardin, Optics Express **16**, 17654 (2008).

[41] B. Rolly, B. Bebey, S. Bidault, B. Stout, and N. Bonod, Physical Review B **85**, 245432 (2012).

[42] F. Hao and P. Nordlander, Chemical Physics Letters **446**, 115 (2007).

[43] M. Fichet, F. Schuller, D. Bloch, and M. Ducloy, Physical Review A **51**, 1553 (1995).

[44] H. Failache, S. Saltiel, M. Fichet, D. Bloch, and M. Ducloy, Physical Review Letters **83**, 5467 (1999).

[45] S. A. Aljunid, E. A. Chan, G. Adamo, M. Ducloy, D. Wilkowski, and N. I. Zheludev, Nano Letters **16**, 3137 (2016).

[46] M. P. Busson, B. Rolly, B. Stout, N. Bonod, and S. Bidault, Nature Communications **3**, 962 (2012).

[47] S. Bidault, A. Devilez, V. Maillard, L. Lermusiaux, J.-M. Guigner, N. Bonod, and J. Wenger, ACS Nano **10**, 4806 (2016).

[48] D. Punj, R. Regmi, A. Devilez, R. Plauchu, S. B. Moparthi, B. Stout, N. Bonod, H. Rigneault, and J. Wenger, ACS Photonics **2**, 1099 (2015).

[49] R. Regmi, A. A. Al Balushi, H. Rigneault, R. Gordon, and J. Wenger, Scientific Reports **5** (2015).

[50] I. Ament, J. Prasad, A. Henkel, S. Schmachtel, and C. Sönnichsen, Nano Letters **12**, 1092 (2012).

CHAPTER 3

Quasi-Normal Mode analysis of the decay rate and Lamb shift

3.1 Introduction

The multipolar formulation of the T-Matrix to describe the scattering problem that we presented in the precedent Section appeared to be very useful and powerful to describe the (multiple-)scattering of an arbitrary set of optical resonators, particularly for objects with a spherical symmetry. However, despite its exact predictions in this case, the physics is somewhat obscured in the complicated mathematical formulas. Now, we are going to present another analytical approach, based on the natural modes of the resonator, called Quasi-Normal Modes (QNMs) [1–3], or Resonant States [4] which has the advantage to make the physics appears clearly. Of particular interest for us, is that their use to study the interaction between a quantum emitter (QE) and a resonant nanostructure allows to generalize the figures-of-merit of cavity Quantum ElectroDynamics (cQED), such as the Purcell factor or the mode volume to the case of open and/or absorbing systems (and also taking into account material dispersion) that are almost always found in nanophotonics [5–7], and for which the figures-of-merit of cQED are ill-defined [8] (this will be explained in Chapter 4).

We first present and define the QNMs in Section 3.2, and we then apply them to express the Lamb shift and decay rate in Section 3.3. We illustrate the derived expressions of the Lamb shift and decay rate in terms of the QNMs on the canonical systems of a dielectric and a plasmonic nanoparticles in Section 3.4. Thanks to the great analyticity provided by this tool, we will provide in Section 3.5 an answer to the following question: "Can the Lamb shift, which can be observed as a shift of the emission spectrum, exceed the linewidth (equal to the decay rate)?" We will see that the answer depends on the nature of the system coupled to the QE: closed or open/absorbing.

Let us emphasize here that when we refer to "closed systems", we mean conservative (Hermitian) systems in the sense of the (photon) energy. By contrast, when we refer to "open and/or absorbing systems", we mean dissipative (non-Hermitian) systems in the sense that: (i) in open systems there are *radiative losses* and (ii) in absorbing systems, there are absorption losses of the photons. For instance, in the examples considered in this Chapter in Section 3.4, the dielectric sphere is an open system (radiative losses) and

the plasmonic sphere is an open *and* absorbing system (absorption by the free electrons of the metal, also called Ohmic losses); on the other hand, a cavity made of perfect mirrors is considered as a closed system.

3.2 Definition of the Quasi-Normal Modes

3.2.1 Definition and normalization

The QNMs can be defined either as an eigenvalue problem, or as poles in Green's tensor or other related matrices (*e.g.* the S-Matrix or the T-Matrix) [2, 3]. Here, we present them as an eigenvalue problem, and consider only the electric field which we only need in the future study. The QNMs of the photonic system denoted $\mathbf{E}_\alpha(\mathbf{r})$ are defined as the solutions of the Maxwell equations in the absence of source [3]

$$\nabla \times (\nabla \times \mathbf{E}_\alpha(\mathbf{r})) = \left(\frac{\omega_\alpha}{c}\right)^2 \varepsilon(\mathbf{r},\omega)\mathbf{E}_\alpha(\mathbf{r}) \tag{3.1}$$

where $\varepsilon(\mathbf{r},\omega)$ is the relative permittivity of the resonator and where a constant relative permeability $\mu = 1$ is assumed. Moreover, these eigenmodes satisfy outgoing wave boundary conditions (also known as the Sommerfeld radiation condition as $|\mathbf{r}| \to +\infty$) [5, 6, 9]. Because of the boundary conditions and the possible absorption of the system [characterized by a complex part in the permittivity $\varepsilon(\mathbf{r},\omega)$], the eigenfrequencies ω_α associated to the eigenmodes $\mathbf{E}_\alpha(\mathbf{r})$ are complex: $\omega_\alpha \equiv \omega'_\alpha + \mathrm{i}\,\omega''_\alpha$, where $\omega''_\alpha < 0$ due to the convention "$e^{-\mathrm{i}\omega t}$" used for the time-harmonic fields. As a consequence, the QNM fields decay in time in the time-domain (which indeed models the dissipative nature of the system) but a *seemingly pathological behavior* occurs: the QNM fields *diverge* exponentially as $|\mathbf{r}| \to +\infty$. In Ref. [2], the authors say: "QNMs should be thought of as *quasistationary* states which cannot have existed for all times: they decay exponentially with time and are excited only at a particular instant in time." Such a statement has been formalized recently in Ref. [10], where they derive a QNM expansion of the scattered field in the *time domain*, and show that the causality principle prevents the scattered field from diverging far from the scatterer. Thus, the divergence of the QNMs is not a fundamental problem in time domain.

However, the divergence still makes the definition of the QNM norm difficult, since it is not possible to define it as an integral of the QNM field over the whole space, as commonly done with the eigenmodes of Hermitian systems; that is, a normalization condition of the kind

$$\int_V \varepsilon(\mathbf{r},\omega)|\mathbf{E}_\alpha(\mathbf{r})|^2 \,\mathrm{d}V = 1 \tag{3.2}$$

where V denotes the volume of the whole space cannot be applied [5, 6, 9]. Obviously, an efficient and accurate modal formalism requires the use of properly normalized QNMs. The problem of the normalization of the QNMs is mathematically quite involved: a different inner product needs to be defined, because the QNMs are not orthogonal in the sense of the energy. We will not discuss the problem in detail, but to summarize, one can list at

least four different normalization procedures in the nanophotonics litterature:
One procedure (I) presented in Refs. [6, 11] where the divergence is handled with perfectly matched layers (PML), and three other procedures where the divergence is handled with a surface integral, presented in: (II) Refs. [5, 12, 13], (III) Refs. [7, 9], and (IV) Ref. [14]. Note that only (I) and (IV) are valid for magnetic materials ($\mu \neq 1$). In Ref. [15], the authors compare the normalizations (I), (II) and (III), and show numerically that they are equivalent, providing the same results. Here we consider only non-magnetic materials ($\mu = 1$), and we follow the normalization condition (III) where the QNMs are normalized according to:

$$1 = \frac{1}{2}\int_V \mathbf{E}_\alpha \cdot \left[\frac{\partial(\omega\varepsilon)}{\partial(\omega)} + \varepsilon\right]\mathbf{E}_\alpha \,\mathrm{d}\mathbf{r} + \frac{c^2}{2\omega_\alpha^2}\oint_{\partial V}\left[\mathbf{E}_\alpha \cdot \frac{\partial}{\partial s}(\mathbf{r}\cdot\nabla)\mathbf{E}_\alpha - (\mathbf{r}\cdot\nabla)\mathbf{E}_\alpha \cdot \frac{\partial \mathbf{E}_\alpha}{\partial s}\right]\mathrm{d}S\,. \quad (3.3)$$

where all the quantities that depend on ω are taken at $\omega = \omega_\alpha$. The first integral is taken over a volume V enclosing the photonic system, and the second integral is taken over a closed surface ∂V of the volume V, with the normal derivative $\partial/\partial s = \mathbf{n}\cdot\nabla$, $\mathbf{n}$ being the outward unit vector normal to the surface. Note that this normalization sets the unit of the QNM electric fields as: $[\mathbf{E}_\alpha] = \mathrm{m}^{-3/2}$.

3.2.2 QNMs expansion of the Green tensor

Once the QNMs have been defined and properly normalized, the next question to address is the *completeness* of the QNMs. As said by Leung *et al.* in [1]: "Completeness of the QNMs relates two issues. First of all, can any function [...] be expanded [in terms of] the QNMs. More importantly, do the resonances represent the dynamics exactly [...] for all $t \geq 0$ and [everywhere]? One would wish to establish conditions under which these expansions are valid and, in circumstances where they are not, to characterize the remainder." The "remainder" is later called "non-resonant contribution" in [1], and we will employ the same vocabulary here.

While the completeness of the QNMs inside the resonator seems established (at least in 1D or for spherical objects since the work of [16] in the 1990s), they are certainly not complete outside the resonator and a *non-resonant contribution* must appear in order to satisfy the continuity conditions of the tranverse fields at the resonator boundaries [10]. This has been demonstrated in 3D for the S-Matrix and T-Matrix expansions in terms of the QNMs in [10] (for the S-Matrix, see also Eq. (4) in [17] and Eq. (16) in [18]). Physically, one can see this non-resonant contribution as the part of the field that is reflected by the resonator interface.

In this Chapter, we assume nevertheless that the scattered part of the Green tensor $\hat{\mathbf{G}}_s$ can expanded in terms of the QNMs of the photonic system, using the spectral representation given in [7, 9, 19]:

$$\hat{\mathbf{G}}_s(\mathbf{r},\mathbf{r}',\omega) \simeq c^2 \sum_\alpha \frac{\mathbf{E}_\alpha(\mathbf{r}) \otimes \mathbf{E}_\alpha(\mathbf{r}')}{2\omega(\omega_\alpha - \omega)} \quad (3.4)$$

where $\otimes$ denotes the tensor product such that for any vectors $\mathbf{a}$, $\mathbf{b}$, $\mathbf{c}$ and $\mathbf{d}$, $\mathbf{c}(\mathbf{a}\otimes\mathbf{b})\mathbf{d} = (\mathbf{c}\cdot\mathbf{a})(\mathbf{b}\cdot\mathbf{d})$. We will test the validity of the approximation in Section 3.4.

3.3 Lamb shift and decay rate expansions in terms of QNM

In this Section, we start from the expressions of the Lamb shift and decay rate given in terms of the scattered part of the Green tensor $\hat{\mathbf{G}}_s$ [Eqs. (2.9) and (2.10)]. Plugging Eq. (4.95) in Eqs. (2.10) and (2.9), one immediately gets

$$\frac{\gamma}{\gamma_0} = 1 + \frac{3\pi c^3}{\omega_0^2} \sum_\alpha \mathrm{Im}\left(\frac{1}{V_\alpha(\omega_\alpha - \omega_0)}\right) \tag{3.5}$$

$$\frac{\Delta\omega}{\gamma_0} = -\frac{3\pi c^3}{2\omega_0^2} \sum_\alpha \mathrm{Re}\left(\frac{1}{V_\alpha(\omega_\alpha - \omega_0)}\right) \tag{3.6}$$

where V_α is the mode volume of the QNM α defined as

$$V_\alpha \equiv \frac{1}{(\mathbf{u_p}\cdot\mathbf{E}_\alpha(\mathbf{r}_0))^2} \tag{3.7}$$

in which the QNM field $\mathbf{E}_\alpha$ is taken at the QE position $\mathbf{r}_0$. This figure of merit characterizes the coupling between the QE and the resonance α through the real part (the larger $\mathrm{Re}(1/V_\alpha)$, the better is the coupling) [20], and also energy dissipations through the presence of an imaginary part (a large $\mathrm{Im}(1/V_\alpha)$ indicates important energy dissipations) [6]. We next introduce the Purcell factor F_α, which corresponds to the enhancement of the total decay rate γ with respect to γ_0 due the the resonance α and for a perfect spectral match ($\omega_0 = \omega'_\alpha$),

$$F_\alpha \equiv \frac{6\pi c^3}{\omega'^3_\alpha} Q_\alpha \mathrm{Re}\,(1/V_\alpha)\ , \tag{3.8}$$

with the usual quality factor Q_α defined as $Q_\alpha \equiv -\omega'_\alpha/(2\omega''_\alpha)$ ($\omega''_\alpha < 0$ due to the convention used for the Fourier transform "$e^{-\mathrm{i}\omega t}$"). Expressions (3.5) and (3.6) can then be recast in a form revealing an interplay between Lamb shift and decay rate (see derivation in Appendix 3.A)

$$\frac{\gamma}{\gamma_0} = 1 + \sum_\alpha \left\{ \frac{\gamma^H_\alpha}{\gamma_0} - 2\frac{\Delta\omega^H_\alpha}{\gamma_0}\frac{\mathrm{Im}(1/V_\alpha)}{\mathrm{Re}(1/V_\alpha)} \right\} \tag{3.9}$$

$$\frac{\Delta\omega}{\gamma_0} = \sum_\alpha \left\{ \frac{\Delta\omega^H_\alpha}{\gamma_0} + \frac{1}{2}\frac{\gamma^H_\alpha}{\gamma_0}\frac{\mathrm{Im}(1/V_\alpha)}{\mathrm{Re}(1/V_\alpha)} \right\} \tag{3.10}$$

where the expressions of γ^H_α/γ_0 and $\Delta\omega^H_\alpha/\gamma_0$ are

$$\frac{\gamma^H_\alpha}{\gamma_0} = F_\alpha \left(\frac{\omega'_\alpha}{\omega_0}\right)^2 \frac{\omega''^2_\alpha}{(\omega'_\alpha - \omega_0)^2 + \omega''^2_\alpha} \tag{3.11}$$

$$\frac{\Delta\omega^H_\alpha}{\gamma_0} = F_\alpha \left(\frac{\omega'_\alpha}{\omega_0}\right)^2 \frac{\omega''_\alpha}{2} \frac{\omega'_\alpha - \omega_0}{(\omega'_\alpha - \omega_0)^2 + \omega''^2_\alpha}\ . \tag{3.12}$$

The superscript H indicates "Hermitian", because for conservative systems, and more realistically for systems with small losses, $\mathrm{Im}(V_\alpha) \simeq 0$ and one recovers the sum of Lorentzians which is phenomenologically used for high-Q cavities [6]: $\gamma/\gamma_0 = 1 + \sum_\alpha \gamma^H_\alpha/\gamma_0$. In contrast, for dissipative systems characterized by $\mathrm{Im}(V_\alpha) \neq 0$ [6], Eqs. (3.9) and (3.10) reveal

an interplay between the "Hermitian" decay rates γ_α^H and Lamb shifts $\Delta\omega_\alpha^H$. This constitues the first result of this Section.

To find the equivalent expressions in terms of wavelengths, one needs to extend the relation between ω and λ to complex numbers. By choosing $\lambda_\alpha \equiv 2\pi c/\omega_\alpha$, where $\lambda_\alpha = \lambda'_\alpha + \mathrm{i}\,\lambda''_\alpha$ is the complex wavelength associated to the complex frequency $\omega_\alpha = \omega'_\alpha + \mathrm{i}\,\omega''_\alpha$, we obtain the following relationships between the real and imaginary parts:

$$\omega'_\alpha = 2\pi c \frac{\lambda'_\alpha}{|\lambda_\alpha|^2} \tag{3.13}$$

$$\omega''_\alpha = -2\pi c \frac{\lambda''_\alpha}{|\lambda_\alpha|^2} \tag{3.14}$$

By replacing in Eqs. (3.11) and (3.12) the above expressions of ω'_α and ω''_α, we find:

$$\left.\frac{\gamma_\alpha^H}{\gamma_0}\right|_{\lambda_0} = F_\alpha \left(\frac{\lambda'_\alpha}{\widetilde{\lambda}_0}\right)^2 \frac{\lambda''^2_\alpha}{(\lambda'_\alpha - \widetilde{\lambda}_0)^2 + \lambda''^2_\alpha} \tag{3.15}$$

$$\left.\frac{\Delta\omega_\alpha^H}{\gamma_0}\right|_{\lambda_0} = -F_\alpha \left(\frac{\lambda'_\alpha}{\widetilde{\lambda}_0}\right)^2 \frac{\lambda''_\alpha}{2} \frac{\lambda'_\alpha - \widetilde{\lambda}_0}{(\lambda'_\alpha - \widetilde{\lambda}_0)^2 + \lambda''^2_\alpha} \tag{3.16}$$

where $\widetilde{\lambda}_0 \equiv |\lambda_\alpha|^2/\lambda_0$ and where the Purcell factor in terms of λ_α reads:

$$F_\alpha = \frac{3}{4\pi^2}\left(\frac{|\lambda_\alpha|^2}{\lambda'_\alpha}\right)^3 Q_\alpha \mathrm{Re}(1/V_\alpha) \tag{3.17}$$

with $Q_\alpha = \lambda'_\alpha/(2\lambda''_\alpha)$.

3.4 Examples

As an example, let us apply Eqs. (3.9) and (3.10) to two situations of a QE coupled to an open photonic system: (i) dielectric silicon (Si) nanosphere with no absorption (and no dispersion) and (ii) plasmonic silver (Ag) nanosphere with absorption (and dispersion) [see insets in Fig. 3.1 (a-c)]. For spherical resonators, the QNM fields are the multipolar fields introduced in Chapter 2 Section 2.4, labeled by four numbers $\{q,n,m,l\}$. q labels a magnetic ($q=1$) or an electric ($q=2$) mode, $n=1,2,...,\infty$ is the multipolar order, and $m=-n,...,n$ is the orbital (or azimutal) number. The number l numerates the different QNM complex frequencies $\omega_{q,n,m,l}$ found for a fixed combination of $\{q,n,m\}$, which are the poles of the Mie coefficients [20, 21]. Therefore, for spherical resonators the sums over α in Eqs. (3.9) and (3.10) become: $\sum_\alpha \to \sum_{q,n,m,l}$. Moreover, for a given set of $\{q,n,l\}$, the QNMs with a different number m are degenerate (*i.e.* have the same complex frequency $\omega_{q,n,m,l}$), and the sum can be recast in the form $\sum_{q,n,l}$ with "effective" mode volumes defined as $1/V_{q,n,l} \equiv \sum_m 1/V_{q,n,m,l}$ (see also Appendix E in [7]).

To compute the QNM fields $\mathbf{E}_\alpha$ necessary to calculate the mode volumes [Eq. (4.97)] which appears in the QNM formulas Eqs. (3.9) and (3.10), we use the analytical expressions of $\mathbf{E}_\alpha$ given in Ref. [9] for non-dispersive materials (*i.e.* with a constant permittivity)

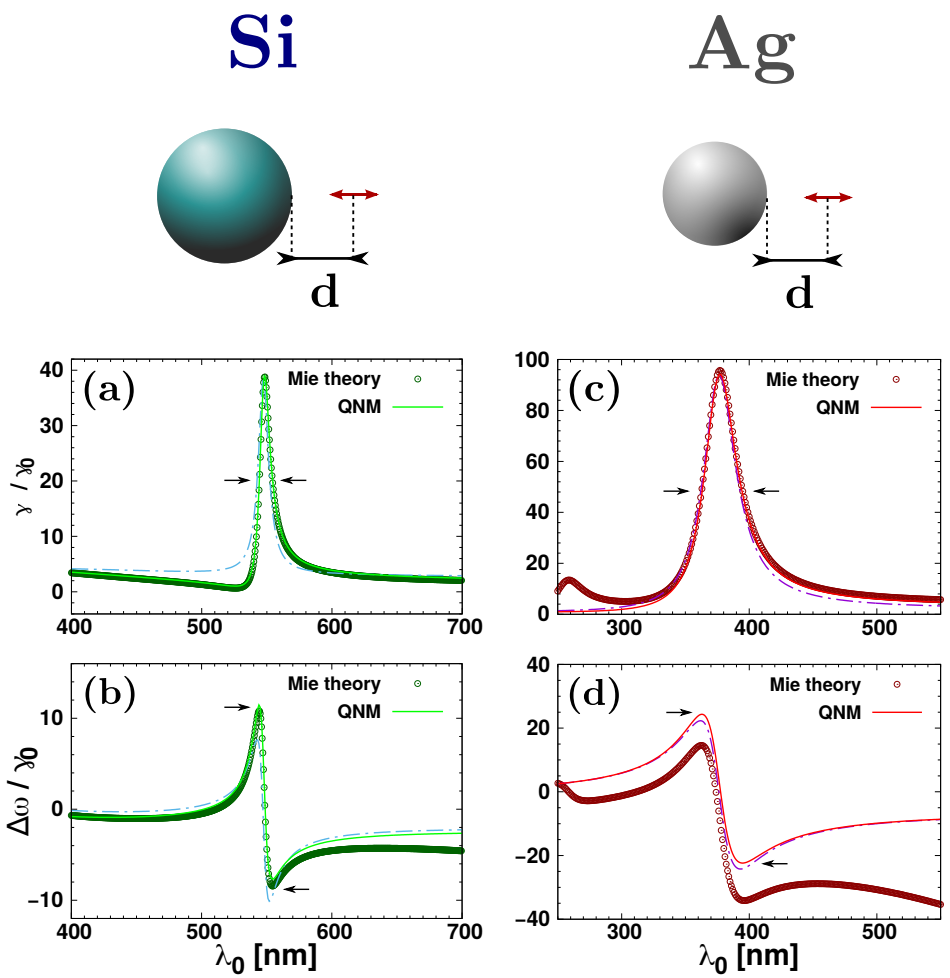

Figure 3.1 – Comparison between QNM calculations using Eqs. (3.9) and (3.10) (lines) and exact calculations using Mie theory (circles) of the decay rate γ and Lamb shift $\Delta\omega$ (normalized by γ_0) as a function of the emitter transition wavelength $\lambda_0 = 2\pi c/\omega_0$, for two configurations: (a-b) silicon (Si) and (c-d) silver (Ag) nanospheres of radii $a = 120\,\text{nm}$ and $a = 20\,\text{nm}$, respectively. In all cases, the emitter (red arrow) is radially oriented and located at a distance $d = 10\,\text{nm}$ from the sphere. For Si [Ag], only the electric quadrupolar [dipolar] contribution to the decay rate (a) [(c)] and Lamb shift (b) [(d)] is shown.

and in Ref. [7] for dispersive materials (*i.e.* with a permittivity that depends on the frequency ω), which are normalized according to Eq. (3.3). The QNM complex frequencies are found by solving a transcendental equation (giving the poles of the Mie coefficients) with the FindRoot function of Mathematica, and where we use an analytic continuation of the permittivity in the complex plane in the case of dispersive materials.

For the calculations, we consider an electric dipole emitter radially oriented (and therefore only coupled to the electric modes $q = 2$, see [22] and discussion at the end of Appendix 2.C) and located at a distance $d = 10\,\text{nm}$ from the sphere. The Si nanosphere (dielectric permittivity $\varepsilon = 16$) has a radius of $a = 120\,\text{nm}$, exhibiting a dominant electric quadrupolar resonance at 547 nm, and the Ag nanosphere (Drude-Lorentz model for the dielectric permittivity taken from [23]) has a radius of $a = 20\,\text{nm}$, exhibiting a dominant electric dipolar resonance at 375 nm. For the Si configuration, we show in Figs. 3.1 (a-b) the electric quadrupolar contribution ($n = 2$) to the decay rate γ and Lamb shift $\Delta\omega$ as

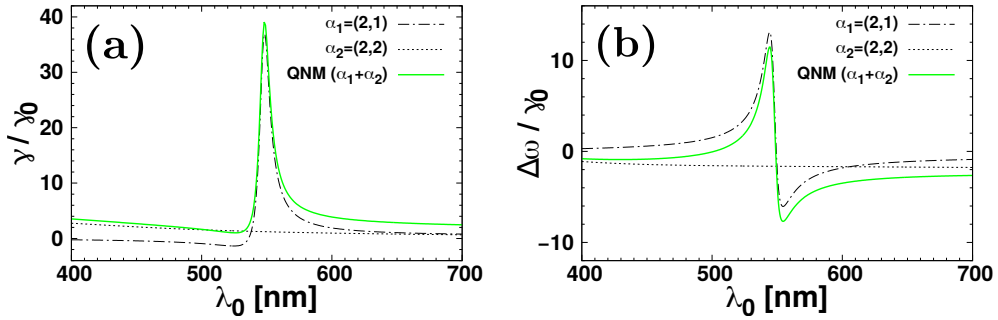

Figure 3.2 – Contributions of the QNMs $\alpha_1 = (2,1)$ and $\alpha_2 = (2,2)$ (dashed black lines) to the QNM decay rate (a) and Lamb shift (b) appearing in Fig. 3.1 (a) and (b) in green lines, respectively, and reproduced also here.

a function of the emitter transition wavelength $\lambda_0 = 2\pi c/\omega_0$, calculated from the QNM formulas (3.9) and (3.10) (solid green line), and compared with the exact Mie theory (green dots). We find several QNMs associated with this quadrupolar resonance, and by using the two dominant QNMs (whose mode volumes and complex wavelengths defined as $\lambda_\alpha \equiv 2\pi c/\omega_\alpha$ are given in Table 3.1), the QNM formulas work very well, with a better result for the decay rate than for the Lamb shift for which one can see a certain discrepancy at high wavelengths. The two individual contributions of the QNMs used in the expansion are also shown in Fig. 3.2 (dashed black lines).

For the Ag configuration we show in Figs. 3.1 (c-d) the dominant dipolar contribution ($n = 1$) to the decay rate γ and Lamb shift $\Delta\omega$ as a function of the emitter transition wavelength λ_0, calculated from Eqs. (3.9) and (3.10) (solid red lines) and compared with the Mie theory (red dots). We only find a single QNM associated with this dipolar resonance (whose mode volume and complex wavelength are given in Table 3.1).

On both examples, agreements are almost perfect for the decay rate (not considering the spurious resonance around 250 nm in the metallic case which is peculiar to the model of permittivity used [24]), but one can see certain discrepancies for the Lamb shift. These discrepancies (more important in the metallic case) appear to be related to omitted non-resonant contribution discussed in Section 3.2.2 which as we can see impacts more the Lamb shift than the decay rate in the near field.

Finally, let us emphasize the presence of an imaginary part in the mode volumes displayed in Table 3.1. In the dielectric case, the imaginary part characterizes the radiative losses and in the plasmonic case, it characterizes both radiative and absorption losses. To highlight the effect of this imaginary part, the same calculations but setting $\mathrm{Im}(1/V_\alpha) = 0$

	$\alpha = (n,l)$	λ_α (nm)	V_α (nm^3)
Si	(2,1)	$547.3 + i4.7$	$(17.573 - i6.974)\cdot 10^6$
	(2,2)	$329.7 + i106.3$	$(1.222 + i1.063)\cdot 10^6$
Ag	(1,1)	$375.6 + i15.5$	$(0.525 - i0.023)\cdot 10^6$

Table 3.1 – QNMs complex wavelengths λ_α and mode volumes V_α appearing in Eqs. (3.9) and (3.10) and used to obtain the results of Fig. 3.1.

in Eqs. (3.9) and (3.10) are also shown (dashed blue/purple lines in Fig. 3.1).

3.5 Maximum Lamb shift in the single-resonance case

From here on, we work under the assumption that the QE couples to a single resonance α. First, we revisit the case of conservative or low-loss systems for which $\mathrm{Im}(V_\alpha) \simeq 0$. In this case, Eqs. (3.9) and (3.10) become $\gamma/\gamma_0 = 1 + \gamma_\alpha^H/\gamma_0$ and $\Delta\omega/\gamma_0 = \Delta\omega_\alpha^H/\gamma_0$, and we can see that the decay rate γ_α^H and the Lamb shift $\Delta\omega_\alpha^H$ are dissociated and there is no interplay. We want to assess the maximum frequency shift $\Delta\omega_{\max}$, that occurs when the QE natural frequency ω_0 is detuned by $\pm\omega_\alpha''$ compared to the QNM resonance frequency ω_α'. At these particular frequencies $\omega_0 = \omega_\alpha' \mp \omega_\alpha''$, the decay rate and Lamb shift (pointed out with arrows in Fig. 3.1) are (see Appendix 3.B for derivation)

$$\frac{\gamma}{\gamma_0} = 1 + \frac{1}{2}F_\alpha + O(Q_\alpha^{-1}) \tag{3.18}$$

$$\frac{\Delta\omega_{\max}}{\gamma_0} = \pm\frac{1}{4}F_\alpha + O(Q_\alpha^{-1}) \tag{3.19}$$

($\Delta\omega_{\max} \simeq +1/4F_\alpha$ when $\omega_0 = \omega_\alpha' - \omega_\alpha''$ and $\Delta\omega_{\max} \simeq -1/4F_\alpha$ when $\omega_0 = \omega_\alpha' + \omega_\alpha''$). We retrieve in this ideal case the expressions for the maximum frequency shift that were derived in [25], Eq. (35), where they considered a two-level atom inside a cavity whose resonance was phenomenologically described by a Lorentzian. For large decay rate enhancements $\gamma \gg \gamma_0$, the first term in the right hand side of Eq. (3.18) can be omitted and we finally end up with the following relations for the maximum photonic Lamb shift

$$\Delta\omega_{\max} = \pm\frac{\gamma}{2}\,. \tag{3.20}$$

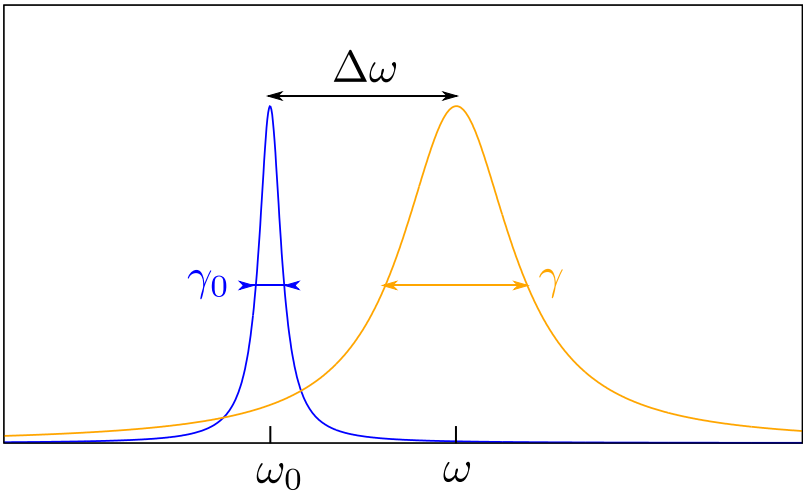

Figure 3.3 – Lorentzian emitted-light spectrum (arbitrary units) of a quantum emitter with resonance frequency ω_0 and decay rate γ_0 in free space (blue line) and modified by his photonic environment (orange line) where ω indicates the new resonance frequency and γ the new decay rate. The photonic Lamb shift $\Delta\omega = \omega - \omega_0$ is also indicated as the separation distance between the two Lorentzian.

Before commenting this result, let us first recall that in the weak-coupling regime, the emitted-light spectrum of the QE has a Lorentzian line shape (as we will see in the next Chapter), and one usually takes the full width at half maximum (FWHM) $\hbar\gamma$ as a measure of the energy spread δE, called energy level width or emission linewidth. This leads to the relation between the energy level width and the lifetime of the excited state (defined as $\tau \equiv 1/\gamma$): $\delta E\,\tau = \hbar$, which can be seen as a time-energy uncertainty relation (see *e.g.* [26]). Thus — and this is the second result of this Section — for conservative systems, or systems with weak energy dissipations, and in the single-resonance case, Eq. (3.20) shows that the photonic Lamb shift always lies within the emission linewidth. As already pointed out in [25], this makes it difficult to observe as a shift of the spectral line. Indeed, the induced frequency shift will be clearly visible only if the separation between the emitted-light spectrum (centered on $\omega = \omega_0 + \Delta\omega$) and the spectrum in free space (centered on ω_0) is bigger than half the FWHM of the two Lorentzians γ and γ_0 respectively (see Fig. 3.3), which gives the condition:$|\Delta\omega| > \gamma_0/2 + \gamma/2$, that simplifies to $|\Delta\omega| > \gamma/2$ for $\gamma \gg \gamma_0$. Note however that this is not a strict condition and it must be seen more as an order of magnitude condition (this condition is similar to the one used to observe the energy splitting in the strong coupling regime, see *e.g.* [27]).

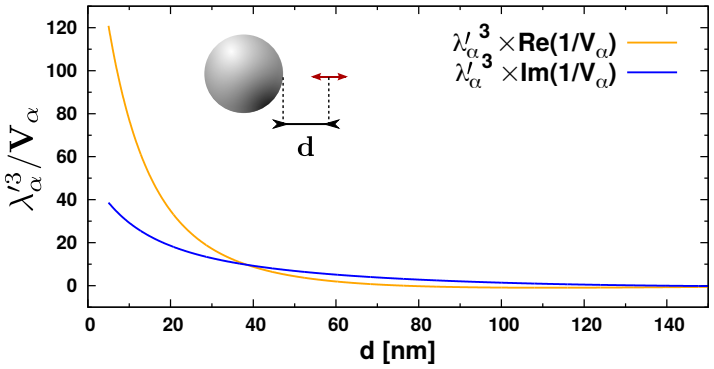

Figure 3.4 – Inverse of the mode volume $1/V_\alpha$ of the dipolar QNM of a silver nanosphere (radius $a = 50$ nm), as a function of the distance d (real part in orange and imaginary part in blue), for an emitter radially oriented (red arrow). Note that $1/V_\alpha$ has been multiplied by the cube of the QNM resonance wavelength $\lambda'_\alpha = 411.6$ nm.

Let us now turn to the case of dissipative systems, for which $\mathrm{Im}(V_\alpha) \neq 0$. In this case, the decay rate and Lamb shift are described by Eqs. (3.9) and (3.10), respectively. At the frequencies $\omega_0 = \omega'_\alpha \mp \omega''_\alpha$, these expressions reduce to (see Appendix 3.B)

$$\frac{\gamma}{\gamma_0} = 1 + \frac{1}{2}F_\alpha\left[1 \mp \frac{\mathrm{Im}(1/V_\alpha)}{\mathrm{Re}(1/V_\alpha)}\right] + O(Q_\alpha^{-1}) \tag{3.21}$$

$$\frac{\Delta\omega_{\max}}{\gamma_0} = \pm\frac{1}{4}F_\alpha\left[1 \pm \frac{\mathrm{Im}(1/V_\alpha)}{\mathrm{Re}(1/V_\alpha)}\right] + O(Q_\alpha^{-1}) \tag{3.22}$$

(when $\omega_0 = \omega'_\alpha - \omega''_\alpha$ one must take the upper sign and when $\omega_0 = \omega'_\alpha + \omega''_\alpha$ one must take the lower sign). For large decay rate enhancements $\gamma \gg \gamma_0$, the first term in the right hand side of (3.21) can be neglected and we get the following relation between the maximum

Lamb shift and decay rate

$$\Delta\omega_{\max} = \pm \frac{[\mathrm{Re}(1/V_\alpha) \pm \mathrm{Im}(1/V_\alpha)]}{[\mathrm{Re}(1/V_\alpha) \mp \mathrm{Im}(1/V_\alpha)]} \frac{\gamma}{2} \,. \tag{3.23}$$

In sharp contrast with Eq. (3.20) valid for conservative or high-Q systems, Eq. (3.23) shows that for dissipative systems, the Lamb shift is not bounded by the emission linewidth, and can go beyond this limit. This is the third result of this Section.

To illustrate this fundamental distinction in the behavior of conservative and dissipative systems, we consider in the following a QE radially oriented and coupled to the plasmonic dipolar resonance of a silver nanoparticle of radius $a = 50\,\mathrm{nm}$ (see inset in Fig. 3.4). The complex wavelength $\lambda_\alpha = \lambda'_\alpha + \mathrm{i}\lambda''_\alpha$ of the dipolar QNM is calculated to be $\lambda_\alpha = 411.6 + \mathrm{i}50.8$ nm, which gives a quality factor $Q_\alpha = \lambda'_\alpha/(2\lambda''_\alpha) = 4$. The QE transition wavelength $\lambda_0 = 2\pi c/\omega_0$ is assumed to be $\lambda_0 = 372$ nm. This corresponds to the case $\omega_0 = \omega'_\alpha - \omega''_\alpha$ for which the Lamb shift $\Delta\omega_{\max}$ is maximum and positive and given by Eq. (3.22) (taking the positive sign), and the decay rate γ is the one given by Eq. (3.21) (taking the negative sign). First, we plot in Fig. 3.4 (the inverse of) the mode volume V_α of the dipolar QNM as a function of the distance d between the QE and the nanoparticle. One can see that $\mathrm{Re}(1/V_\alpha)$, which characterizes the coupling between the QE and the nanoparticle, increases as d decreases (orange curve), which is in accordance with the expectation that the coupling increases as the QE gets closer to the resonator. Moreover, one can see the presence of energy dissipations through a non-negligible $\mathrm{Im}(1/V_\alpha)$ (blue curve), which is expected when considering the low quality factor of the resonance $Q_\alpha = 4$.

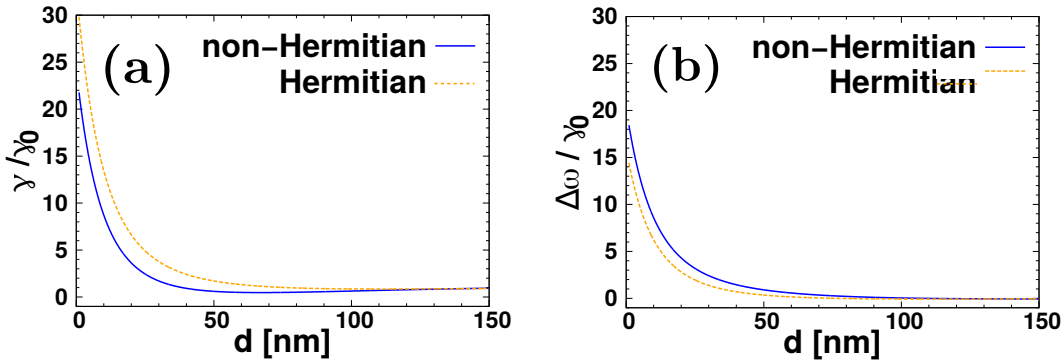

Figure 3.5 – (a) Normalized decay rate γ/γ_0 and (b) Lamb shift $\Delta\omega_{\max}/\gamma_0$ as a function of the distance d, calculated from Eqs. (3.21) and (3.22) (in blue), and from Eq. (3.18) (in orange), for the same configuration as in Fig. 3.4.

Accordingly, the decay rate γ [Eq. (3.21)] and maximum Lamb shift $\Delta\omega_{\max}$ [Eq. (3.22)] will increase as d decreases in a similar way as $\mathrm{Re}(1/V_\alpha)$ in Fig. 3.4 (because the Purcell factor appearing in their expression is $F_\alpha \propto \mathrm{Re}(1/V_\alpha)$ [see Eq. (3.8)]). More importantly, dissipations, through the presence of $\mathrm{Im}(1/V_\alpha)$ in Eqs. (3.21) and (3.22), will weaken the decay rate (due to the negative sign in Eq. (3.21)) and increase the Lamb shift (due to the positive sign in Eq. (3.22)), compared to the conservative case where $\mathrm{Im}(1/V_\alpha) = 0$. This is shown in Fig. 3.5 (a-b) where the (normalized) decay rate γ and Lamb shift $\Delta\omega_{\max}$ of the QE are calculated as a function of the distance d, from Eqs. (3.21) and (3.22)

(blue curves), and compared with the ideal conservative case given by Eq. (3.18) (orange curves).

Finally, we plot in Fig. 3.6 the ratio $\Delta\omega_{\max}/\gamma$ as a function of the distance d, for the dissipative case (blue curve) and the ideal conservative case (orange curve). The limit $\Delta\omega = \gamma/2$ is also shown (dashed black line). One can see that contrary to the conservative case where the Lamb shift is bounded by $\gamma/2$, dissipations allow to fulfill the condition $\Delta\omega > \gamma/2$. We compare this result with the Mie calculations taking into account only the electric dipolar ($n = 1$) response of the nanoparticle (red curve). Despite a decrease of the magnitude (that might be explained by the non-resonant contributions discussed previously), the Mie calculations still show a Lamb shift that exceeds the limit of conservative systems under a dipolar approximation.

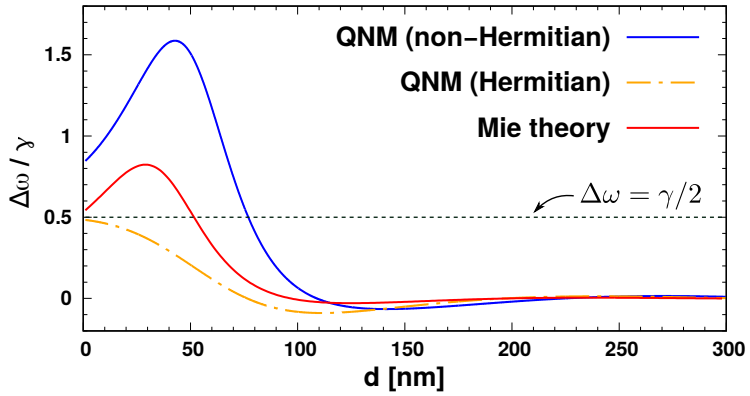

Figure 3.6 – Ratio between the Lamb shift $\Delta\omega_{\max}$ and the decay rate γ as a function of the distance d, calculated from Eqs. (3.21) and (3.22) (in blue), from Eqs. (3.18) and (3.19) (in orange), and from the Mie theory (in red), for the same configuration as in Fig. 3.4. A guide-to-the-eye shows the limit $\Delta\omega = \gamma/2$.

3.6 Conclusion

Using a quasi-normal mode description, we derive in Section 3.3 general expressions for the environment-modified decay rate and photonic Lamb shift, valid for open (dissipative) resonators, and tested on the canonical cases of dielectric and a plasmonic spheres in Section 3.4. In Section 3.5, considering the coupling to a single resonance, we consider the maximum level shift that can be expected, and we show a remarkable difference between closed (conservative) and open/absorbing (dissipative) systems: while for conservative systems, the Lamb shift remains inferior to the emission linewidth, it can surpass this limit for dissipative systems.

3.A Derivation of Eqs. (3.9), (3.10), (3.11) and (3.12)

Here we derive the interplay relations between the decay rate and Lamb shift [Eqs. (3.9), (3.10), (3.11) and (3.12)] obtained in Section 3.3. For Hermitian systems, $\mathrm{Im}(1/V_\alpha)=0$. In this case, Eqs. (3.5) and (3.6) (main text) can be written as

$$\frac{\gamma}{\gamma_0}=1+\frac{3\pi c^3}{\omega_0^2}\sum_\alpha \mathrm{Re}\left(\frac{1}{V_\alpha}\right)\mathrm{Im}\left(\frac{1}{\omega_\alpha-\omega_0}\right) \tag{3.24}$$

$$\frac{\Delta\omega}{\gamma_0}=-\frac{3\pi c^3}{2\omega_0^2}\sum_\alpha \mathrm{Re}\left(\frac{1}{V_\alpha}\right)\mathrm{Re}\left(\frac{1}{\omega_\alpha-\omega_0}\right). \tag{3.25}$$

We then define the Hermitian decay rate and Lamb shift associated to the resonance α as

$$\frac{\gamma_\alpha^H}{\gamma_0}\equiv\frac{3\pi c^3}{\omega_0^2}\mathrm{Re}\left(\frac{1}{V_\alpha}\right)\mathrm{Im}\left(\frac{1}{\omega_\alpha-\omega_0}\right) \tag{3.26}$$

$$\frac{\Delta\omega_\alpha^H}{\gamma_0}\equiv-\frac{3\pi c^3}{2\omega_0^2}\mathrm{Re}\left(\frac{1}{V_\alpha}\right)\mathrm{Re}\left(\frac{1}{\omega_\alpha-\omega_0}\right), \tag{3.27}$$

so that the total decay rate and Lamb shift read $\gamma^*=\gamma_0+\sum_\alpha\gamma_\alpha^H$ and $\Delta\omega=\sum_\alpha\Delta\omega_\alpha^H$ respectively.

For non-Hermitian systems, $\mathrm{Im}(1/V_\alpha)\neq 0$. In this case, Eqs. (3.5) and (3.6) present an extra term compared to the Hermitian case

$$\frac{\gamma}{\gamma_0}=1+\frac{3\pi c^3}{\omega_0^2}\sum_\alpha \mathrm{Re}\left(\frac{1}{V_\alpha}\right)\mathrm{Im}\left(\frac{1}{\omega_\alpha-\omega_0}\right)+\frac{3\pi c^3}{\omega_0^2}\sum_\alpha \mathrm{Im}\left(\frac{1}{V_\alpha}\right)\mathrm{Re}\left(\frac{1}{\omega_\alpha-\omega_0}\right) \tag{3.28}$$

$$\frac{\Delta\omega}{\gamma_0}=-\frac{3\pi c^3}{2\omega_0^2}\sum_\alpha \mathrm{Re}\left(\frac{1}{V_\alpha}\right)\mathrm{Re}\left(\frac{1}{\omega_\alpha-\omega_0}\right)+\frac{3\pi c^3}{2\omega_0^2}\sum_\alpha \mathrm{Im}\left(\frac{1}{V_\alpha}\right)\mathrm{Im}\left(\frac{1}{\omega_\alpha-\omega_0}\right). \tag{3.29}$$

By making use of (3.26) and (3.27), these expressions can be recast in the form

$$\frac{\gamma}{\gamma_0}=1+\sum_\alpha\left\{\frac{\gamma_\alpha^H}{\gamma_0}-2\frac{\Delta\omega_\alpha^H}{\gamma_0}\frac{\mathrm{Im}(1/V_\alpha)}{\mathrm{Re}(1/V_\alpha)}\right\} \tag{3.30}$$

$$\frac{\Delta\omega}{\gamma_0}=\sum_\alpha\left\{\frac{\Delta\omega_\alpha^H}{\gamma_0}+\frac{1}{2}\frac{\gamma_\alpha^H}{\gamma_0}\frac{\mathrm{Im}(1/V_\alpha)}{\mathrm{Re}(1/V_\alpha)}\right\} \tag{3.31}$$

which are the expressions (3.9) and (3.10) of the main text.

Now, we show how the expressions (3.26) and (3.27) for γ_α^H and $\Delta\omega_\alpha^H$ respectively can be rewritten in the form of Eqs. (3.11) and (3.12) (main text). First, by multiplying by the complex conjugate, we can explicitely write (we recall that we defined $\omega_\alpha\equiv\omega'_\alpha+\mathrm{i}\,\omega''_\alpha$)

$$\mathrm{Re}\left(\frac{1}{\omega_\alpha-\omega_0}\right)=\frac{\omega'_\alpha-\omega_0}{|\omega_\alpha-\omega_0|^2}=\frac{\omega'_\alpha-\omega_0}{(\omega'_\alpha-\omega_0)^2+\omega''^2_\alpha} \tag{3.32}$$

$$\mathrm{Im}\left(\frac{1}{\omega_\alpha-\omega_0}\right)=\frac{-\omega''_\alpha}{|\omega_\alpha-\omega_0|^2}=\frac{-\omega''_\alpha}{(\omega'_\alpha-\omega_0)^2+\omega''^2_\alpha} \tag{3.33}$$

By reporting these expressions into Eqs. (3.26) and (3.27), we get

$$\frac{\gamma_\alpha^H}{\gamma_0} = \frac{3\pi c^3}{\omega_0^2}\,\mathrm{Re}\left(\frac{1}{V_\alpha}\right)\frac{-\omega_\alpha''}{(\omega_\alpha'-\omega_0)^2+\omega_\alpha''^2} \tag{3.34}$$

$$\frac{\Delta\omega_\alpha^H}{\gamma_0} = -\frac{3\pi c^3}{2\omega_0^2}\,\mathrm{Re}\left(\frac{1}{V_\alpha}\right)\frac{\omega_\alpha'-\omega_0}{(\omega_\alpha'-\omega_0)^2+\omega_\alpha''^2} \tag{3.35}$$

Finally, by introducing the Purcell factor defined in Eq. (3.8) (main text), we end up with the Eqs. (3.11) and (3.12) of the main text, that is

$$\frac{\gamma_\alpha^H}{\gamma_0} = F_\alpha\left(\frac{\omega_\alpha'}{\omega_0}\right)^2\frac{\omega_\alpha''^2}{(\omega_\alpha'-\omega_0)^2+\omega_\alpha''^2} \tag{3.36}$$

$$\frac{\Delta\omega_\alpha^H}{\gamma_0} = F_\alpha\left(\frac{\omega_\alpha'}{\omega_0}\right)^2\frac{\omega_\alpha''}{2}\frac{\omega_\alpha'-\omega_0}{(\omega_\alpha'-\omega_0)^2+\omega_\alpha''^2}\,. \tag{3.37}$$

3.B Derivation of Eqs. (3.18), (3.19), (3.21) and (3.22)

Here we derive the expressions of the decay rate and Lamb shift obtained in Section 3.5 in the single-resonance case [Eqs. (3.18), (3.19), (3.21) and (3.22)].

We consider for that two particular detunings of the natural QE frequency ω_0 compared to the QNM resonance frequency ω'_α: $\omega_0 = \omega'_\alpha \mp \omega''_\alpha$, for which the Lamb shift presents an extremum (indicated by arrows in Fig. 3.1 (b) and (d) in the main text). We start with the detuning $\omega_0 = \omega'_\alpha + \omega''_\alpha$. By replacing ω_0 by $\omega'_\alpha + \omega''_\alpha$ in Eqs. (3.11) and (3.12), one gets

$$\frac{\gamma_\alpha^H}{\gamma_0} = \frac{1}{2} F_\alpha \left(\frac{\omega'_\alpha}{\omega'_\alpha + \omega''_\alpha} \right)^2 = \frac{1}{2} F_\alpha \left(\frac{1}{1 - \frac{1}{2Q_\alpha}} \right)^2 \tag{3.38}$$

$$\frac{\Delta\omega_\alpha^H}{\gamma_0} = -\frac{1}{4} F_\alpha \left(\frac{\omega'_\alpha}{\omega'_\alpha + \omega''_\alpha} \right)^2 = -\frac{1}{4} F_\alpha \left(\frac{1}{1 - \frac{1}{2Q_\alpha}} \right)^2 \tag{3.39}$$

where we used the fact that $Q_\alpha = -\omega'_\alpha/(2\omega''_\alpha)$. In the single-resonance case, Eqs. (3.9) and (3.10) thus reduce to

$$\frac{\gamma}{\gamma_0} = 1 + \frac{\gamma_\alpha^H}{\gamma_0} - 2\frac{\Delta\omega_\alpha^H}{\gamma_0} \frac{\mathrm{Im}(1/V_\alpha)}{\mathrm{Re}(1/V_\alpha)} \tag{3.40}$$

$$\frac{\Delta\omega}{\gamma_0} = \frac{\Delta\omega_\alpha^H}{\gamma_0} + \frac{1}{2}\frac{\gamma_\alpha^H}{\gamma_0} \frac{\mathrm{Im}(1/V_\alpha)}{\mathrm{Re}(1/V_\alpha)}, \tag{3.41}$$

and by employing the previous expressions of γ_α^H and $\Delta\omega_\alpha^H$, one gets

$$\frac{\gamma}{\gamma_0} = 1 + \frac{1}{2} F_\alpha \left(\frac{1}{1 - \frac{1}{2Q_\alpha}} \right)^2 \left[1 + \frac{\mathrm{Im}(1/V_\alpha)}{\mathrm{Re}(1/V_\alpha)} \right] \tag{3.42}$$

$$\frac{\Delta\omega^-}{\gamma_0} = -\frac{1}{4} F_\alpha \left(\frac{1}{1 - \frac{1}{2Q_\alpha}} \right)^2 \left[1 - \frac{\mathrm{Im}(1/V_\alpha)}{\mathrm{Re}(1/V_\alpha)} \right]. \tag{3.43}$$

Similarly, for the detuning $\omega_0 = \omega'_\alpha - \omega''_\alpha$, replacing ω_0 in Eqs. (3.11) and (3.12) yields

$$\frac{\gamma_\alpha^H}{\gamma_0} = \frac{1}{2} F_\alpha \left(\frac{\omega'_\alpha}{\omega'_\alpha - \omega''_\alpha} \right)^2 = \frac{1}{2} F_\alpha \left(\frac{1}{1 + \frac{1}{2Q_\alpha}} \right)^2 \tag{3.44}$$

$$\frac{\Delta\omega_\alpha^H}{\gamma_0} = \frac{1}{4} F_\alpha \left(\frac{\omega'_\alpha}{\omega'_\alpha - \omega''_\alpha} \right)^2 = \frac{1}{4} F_\alpha \left(\frac{1}{1 + \frac{1}{2Q_\alpha}} \right)^2. \tag{3.45}$$

Then, by plugging these equations in the expressions of the decay rate and Lamb shift in the single-resonance case as previously, one gets

$$\frac{\gamma}{\gamma_0} = 1 + \frac{1}{2} F_\alpha \left(\frac{1}{1 + \frac{1}{2Q_\alpha}} \right)^2 \left[1 - \frac{\mathrm{Im}(1/V_\alpha)}{\mathrm{Re}(1/V_\alpha)} \right] \tag{3.46}$$

$$\frac{\Delta\omega^{+}}{\gamma_0} = \frac{1}{4} F_\alpha \left(\frac{1}{1+\frac{1}{2Q_\alpha}} \right)^2 \left[1 + \frac{\mathrm{Im}(1/V_\alpha)}{\mathrm{Re}(1/V_\alpha)} \right] . \tag{3.47}$$

Note that for the Hermitian systems, the decay rate and Lamb shift for these two particular detunings are given by Eqs. (3.42), (3.43), (3.46) and (3.47) with $\mathrm{Im}(1/V_\alpha) = 0$, and one ends up with the Eqs. (3.18) and (3.19) of the main text.

Bibliography

[1] E. Ching, P. Leung, A. M. van den Brink, W. Suen, S. Tong, and K. Young, Reviews of Modern Physics **70**, 1545 (1998).

[2] E. Berti, V. Cardoso, and A. O. Starinets, Classical and Quantum Gravity **26**, 163001 (2009).

[3] P. Lalanne, W. Yan, K. Vynck, C. Sauvan, and J.-P. Hugonin, Laser & Photonics Reviews **12**, 1700113 (2018).

[4] G. García-Calderón, in *Unstable States in the Continuous Spectra, Part I: Analysis, Concepts, Methods, and Results*, Advances in Quantum Chemistry, Vol. 60, edited by C. A. Nicolaides and E. Brändas (Academic Press, 2010) pp. 407 – 455.

[5] P. T. Kristensen, C. Van Vlack, and S. Hughes, Optics Letters **37**, 1649 (2012).

[6] C. Sauvan, J.-P. Hugonin, I. Maksymov, and P. Lalanne, Physical Review Letters **110**, 237401 (2013).

[7] E. Muljarov and W. Langbein, Physical Review B **94**, 235438 (2016).

[8] A. F. Koenderink, Optics Letters **35**, 4208 (2010).

[9] M. Doost, W. Langbein, and E. A. Muljarov, Physical Review A **90**, 013834 (2014).

[10] R. Colom, R. McPhedran, B. Stout, and N. Bonod, Physical Review B **98**, 085418 (2018).

[11] B. Vial, F. Zolla, A. Nicolet, and M. Commandré, Physical Review A **89**, 023829 (2014).

[12] H. M. Lai, P. T. Leung, K. Young, P. W. Barber, and S. C. Hill, Physical Review A **41**, 5187 (1990).

[13] P. T. Kristensen and S. Hughes, ACS Photonics **1**, 2 (2013).

[14] B. Stout, R. Colom, N. Bonod, and R. McPhedran, arXiv:1903.07183 [physics] (2019).

[15] P. T. Kristensen, R.-C. Ge, and S. Hughes, Physical Review A **92**, 053810 (2015).

[16] P. Leung, S. Liu, and K. Young, Physical Review A **49**, 3057 (1994).

[17] V. Grigoriev, A. Tahri, S. Varault, B. Rolly, B. Stout, J. Wenger, and N. Bonod, Physical Review A **88**, 011803 (2013).

[18] T. Zhan and S. Chui, Physical Review A **90**, 023802 (2014).

[19] C. Sauvan, J.-P. Hugonin, R. Carminati, and P. Lalanne, Physical Review A **89**, 043825 (2014).

[20] X. Zambrana-Puyalto and N. Bonod, Physical Review B **91**, 195422 (2015).

[21] B. Stout, A. Devilez, B. Rolly, and N. Bonod, Journal of the Optical Society of America B **28**, 1213 (2011).

[22] B. Rolly, B. Bebey, S. Bidault, B. Stout, and N. Bonod, Physical Review B **85**, 245432 (2012).

[23] A. D. Rakić, A. B. Djurišić, J. M. Elazar, and M. L. Majewski, Applied Optics **37**, 5271 (1998).

[24] F. Hao and P. Nordlander, Chemical Physics Letters **446**, 115 (2007).

[25] S. C. Ching, H. M. Lai, and K. Young, Journal of the Optical Society of America B **4**, 2004 (1987).

[26] V. Dodonov and A. Dodonov, Physica Scripta **90**, 074049 (2015).

[27] P. Törmä and W. L. Barnes, Reports on Progress in Physics **78**, 013901 (2014).

CHAPTER 4

Quantum descriptions of the weak and strong coupling regimes

4.1 Introduction

In Chapters 2 and 3, we mostly talked about the *weak-coupling regime* of interaction between a quantum emitter (QE) and photonic/plasmonic resonators. In this regime, the decay rate of the QE and the emitted frequency are modified compared to their values in free space, and such modifications can be calculated by perturbative treatments as presented in Section 2.2. In this introduction, we therefore focus on the *strong-coupling regime*, and we do a short review of the experimental work carried in relation with strong-coupling.

In the 1980s, Serge Haroche popularized the picture of atoms coupled to a single (resonant) mode in a cavity, known as cavity-quantum electrodynamics (cQED) [1]. The quality factor of the cavity was so high that he was even able to explore the *strong-coupling regime* in which the atom exchanges several times a single photon with the mode of the cavity [2, 3]. These experiments were carried out in the microwave frequency range and involved several Rydberg atoms. However, similar experiments were also realized at the level of a single Rydberg atom by another group [4, 5]. A bit later, the strong-coupling was realized at *optical frequencies* [6–8], and achieved with a single atom [9, 10]. The realization of an efficient coupling between the quantum emitter (QE) and the cavity relies on the high cavity quality factor obtained at low temperature, spectrally sharp QEs and a fine tuning of the cavity resonance.

Due to the progress in micro and nanotechnologies, strong-coupling was observed in the 1990s at optical frequencies with solid-state quantum emitters (semiconductor quantum dots) in integrated microcavities cooled at cryogenic temperatures, and was achieved with single solid-state QEs in 2004 [11, 12]. A review concerning single solid-state QEs can be found in [13].

The generic term “cavity” has evolved and taken different forms over the years, and in general refers to a resonant system. In the nanophotonics community for instance, optically resonant nanostructures take the role of open cavities. In such systems, important coupling can be achieved at room temperature with QEs with broader linewidths. In 2004, the strong-coupling regime was clearly observed with J-aggregates in the group of

J. Bellessa [14, 15] and in the group of T. Ebbesen [16, 17], and later with other various types of QEs like dye molecules and quantum dots (for more references, see the recent review [18] and references therein). Note however that signatures of strong-coupling were already observed with dye molecules in 1982 [19]. More exhaustive overviews on the strong-coupling between QEs and photonic/plasmonic resonators are presented in three recent reviews on the topic [18, 20, 21]. Very recently, some groups claimed the realization of strong-coupling in plasmonic structures at room temperatures at the single emitter level [22–26]. These papers are compared and discussed in [20].

In the present Chapter, we aim at first summarizing the *quantum* theoretical approaches and models which were developed to deal with the problem of the spontaneous emission of a two-level atom interacting with a resonant system. In a quantum treatment, the quantity which is chosen to investigate the temporal behavior of the system is the probability of the atom to remain in its excited state, called the *survival probability* and denoted $P_{\text{surv}}(t)$ hereafter. We aim at understanding the transition between the weak and strong-coupling regimes. In the weak-coupling regime, $P_{\text{surv}}(t)$ decays monotically in time to zero, but with a decay rate modified compared to the free-space decay rate. On the other hand, in the strong-coupling regime, $P_{\text{surv}}(t)$ undergoes oscillations, called *vacuum Rabi oscillations*, before decaying to zero. These oscillations represent a coherent and reversible exchange of energy (photon) between the quantum emitter and the photonic system.

There is also an other *facet* of the interaction between an atom and the resonator when one looks at the emission spectrum. In the weak-coupling regime, the distribution in frequency of the emitted photons is essentially one peak whereas in the strong-coupling one can distinguish two distinct peaks: this is called the *vacuum Rabi splitting*, and the separation between the peaks depends on the strength of the coupling. Note that the theories presented here are not suitable as such to investigate the ultra-strong-coupling regime, because we systematically make the rotating-wave approximation when writing the interaction Hamiltonian, which is valid unless the atom-cavity coupling rate becomes comparable to the atomic resonance frequency. In this case, one enters the *ultra strong-coupling regime* which can be found in [27–32].

We first present in Section 4.2 a powerful model to describe an atom in a closed cavity extensively used in cQED. It is based on the Jaynes-Cummings Hamiltonian [33], with the figures-of-merit such as the coupling constant g characterizing the coupling between the QE and the mode, or the effective volume V, which is essentially the volume of the cavity and characterizes the confinement of the field, and the cavity losses are introduced either phenomenologically by a cavity decay rate γ_α, or more rigorously by coupling the mode of the cavity to a continuum of modes outside of the cavity, which leads to a master equation (see *e.g.* [34] chapter 5 or [35] chapter 6). Such a description is part of a larger paradigm developed to deal with dissipative quantum systems (see *e.g.* [36]), but is valid only in the limit of small leakages, which is most often verified for closed cavities with high quality factors Q, and has been very successful to describe cQED experiments, and later in optical microcavities in the 1990s.

An equivalent model is then presented in Section 4.3 but providing a different physical interpretation of the interaction, where the atom is this time coupled to a continuum of modes with a Lorentzian density of states of linewidth γ_α — the full width at half maximum (FWHM).

Such models were very successful in cQED where the systems considered usually suffer from small losses. However, these models are not a priori valid in nanophotonics where open, strongly absorbing and dispersive systems are usually considered (for example plasmonics in the visible).

Therefore, we present in Sections 4.4 and 4.5 two approaches to transpose the cQED formalism in nanophotonics. These approaches are based on a Green tensor description of the electromagnetic environment, and on the natural modes of the photonic or plasmonic resonator, which are the resonant states [or quasi-normal modes (QNMs)] presented in the Chapter 3. Such an approach based on the natural modes of the system was already pointed out in [37], where they wrote: "A more natural way of stating these ideas is to use the QNMs of the open system alone, rather than the modes of the universe — in other words, to eliminate the bath degrees of freedom. This would be possible as an exact statement only if the QNMs are complete."

In the approach presented in Section 4.4, we show how the QNM framework allows us to generalize the usual cQED figure-of-merit characterizing the interaction between dipole sources and a resonance of a cavity, such as the mode volume V. Moreover, it allows to revisit notions such as the density of states and the coupling constants in the case of nanophotonics.

In the approach presented in Section 4.5 and based on [38, 39], we derive a non-Hermitian "effective" Hamiltonian for the subsystem {atom + QNMs of the resonator}. However, the Lorentzian density of states of the resonant modes is introduced in a more phenomenologically way than in Section 4.4.

Finally, in conclusion we compare the figures-of-merit derived within the QNM framework in Section 4.4 with the cQED ones presented in Section 4.2.

4.2 cQED approach

One of the pioneering studies on the behaviour of open quantum systems (non-Hermitian) was that of George Gamow on alpha decay [40] in 1928, where he showed that a particle may escape the nucleus via tunnelling at a rate that can be effectively described through a complex energy eigenvalue. In doing so, he found that the real and imaginary parts of these eigenvalues are related to the experimentally observed energy levels and widths of the corresponding nuclear resonances. This was to a great extent phenomenological. In subsequent works, more rigorous appraoches were developped, giving some justification and background to the phenomelogical "non-Hermitian" descriptions. One can mention the Friedrichs' model [41], or the Lindblad master equation formalism ([34] chapter 5), in which the system interacts with a very large environment (in terms of the dimension of the environmental Hilbert space). These more rigorous approaches indicate that when a quantum system couples to a surrounding environment or bath, the dynamics of the subsystem itself becomes non-Hermitian. These approaches are discussed in [42], chapter 5, and one can also refer to the review article [43]. Here, we treat the spontaneous emission of an atom coupled to a single electromagnetic mode of a lossy (dissipative) cavity as depicted in Fig .4.1 (a). The losses are introduced either phenomenologically with a non-Hermitian Hamiltonian, or more rigorously by coupling the cavity mode to a large reservoir (bath) of quantized harmonic oscillators (see e.g. *[34] chapter 5 or [35] chapter 6 for an alternative but equivalent method), leading to a master (Lindblad) equation for the reduced density matrix of the system.*

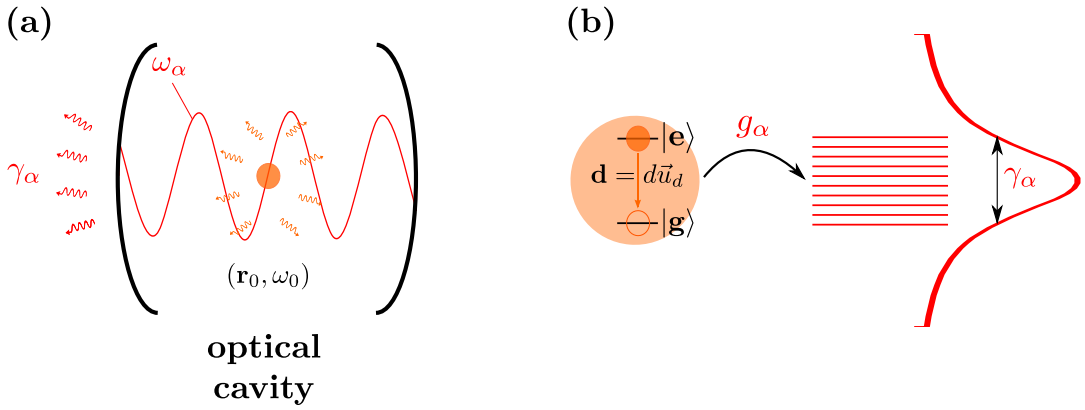

Figure 4.1 – Schemes of the systems under study: (a) A two-level atom initially excited coupled to a single mode of a cavity of frequency ω_α, where the cavity loses energy at a rate γ_α; (b) A two-level atom initially excited coupled to a continuum of modes, described by a density of states with a Lorentzian distribution centered on ω_α and of bandwidth γ_α.

4.2.1 Phenomenological approach (non-Hermitian Hamiltonian description)

The cQED approach treats the spontaneous emission of an atom coupled to a single electromagnetic mode of a lossy (dissipative) cavity. The atom is modeled as a two-level system with a transition frequency ω_0, and the cavity mode is modeled as a quantized harmonic oscillator of frequency ω_α.

The total Hamiltonian of the system {two-level atom + single cavity mode} (not taking into account the losses) obtained within the electric dipole and rotating wave approximations is given by (for a derivation, see Appendix 4.A, where the rotating-wave approximation is also clarified):

$$\hat{H}_{\mathrm{JC}} = \hbar\omega_0 \hat{\sigma}^\dagger \hat{\sigma} + \hbar\omega_\alpha \hat{a}^\dagger \hat{a} + \hbar g \left(\hat{\sigma}\hat{a}^\dagger + \hat{\sigma}^\dagger \hat{a}\right) \tag{4.1}$$

where we give the expression of the coupling constant g (for an atom dipole moment $\mathbf{d} = d\vec{u}_d$ and a perfect polarization and position matching with the mode, see Appendix 4.A):

$$\hbar g = d\sqrt{\frac{\hbar\omega_\alpha}{2\epsilon_0 V}} \tag{4.2}$$

with V the volume of the cavity. g is a real quantity with the dimensions of frequency. All the other notations are introduced in Appendix 4.A. The parameters of this Hamiltonian are the atomic transition frequency ω_0, the cavity mode frequency ω_α, and the coupling constant g. Such Hamiltonian is known as the Jaynes-Cummings Hamiltonian [33], hence the subscript "JC". It is worth noting that it is Hermitian.

This system {two-level atom + single cavity mode} can exchange energy with its environment, and therefore the dynamics becomes non-Hermitian. Such a dynamics can be describe by the *non-Hermitian* evolution of a *pure state* of the type:

$$|\psi(t)\rangle = \alpha(t)\,|\mathrm{e},0\rangle + \beta(t)\,|\mathrm{g},1\rangle \tag{4.3}$$

where the state $|\mathrm{e},0\rangle$ stands for atom in the excited state and no photon in the cavity and $|\mathrm{g},1\rangle$ stands for atom in the ground state and one photon in the cavity, which obeys the Schrödinger equation with the non-Hermitian "effective" Hamiltonian $\hat{H} = \hat{H}_{\mathrm{JC}} + \hat{H}_{\mathrm{loss}}$ where $\hat{H}_{\mathrm{loss}}$ is phenomenologically introduced and reads in the basis $\{|\mathrm{e},0\rangle, |\mathrm{g},1\rangle\}$:

$$\hat{H}_{\mathrm{loss}} = \hbar \begin{bmatrix} 0 & 0 \\ 0 & -\mathrm{i}\frac{\gamma_\alpha}{2} \end{bmatrix} \tag{4.4}$$

where the parameter γ_α is called the cavity decay rate.

The coefficients $\alpha(t)$ and $\beta(t)$ are obtained by solving the Schrödinger equation with the non-Hermitian Hamiltonian $\hat{H} = \hat{H}_{\mathrm{JC}} + \hat{H}_{\mathrm{loss}}$:

$$\mathrm{i}\hbar\frac{\partial}{\partial t}\begin{bmatrix}\alpha(t)\\ \beta(t)\end{bmatrix} = \hbar\begin{bmatrix}\omega_0 & g\\ g & \omega_\alpha - \mathrm{i}\frac{\gamma_\alpha}{2}\end{bmatrix}\begin{bmatrix}\alpha(t)\\ \beta(t)\end{bmatrix} \tag{4.5}$$

One way to solve the dynamics of such a system is to diagonalize the above matrix. Upon diagonalization, one gets the following eigenvalues:

$$\omega_\pm = \frac{\omega_0 + \omega_\alpha}{2} - \mathrm{i}\frac{\gamma_\alpha}{4} \pm \frac{\Omega}{2} \tag{4.6}$$

where we defined the quantity:

$$\Omega \equiv \sqrt{4g^2 + \left(\delta + \mathrm{i}\frac{\gamma_\alpha}{2}\right)^2} \tag{4.7}$$

and where $\delta \equiv \omega_0 - \omega_\alpha$ is the detuning. We are first of all interested in the probability to find the atom in the excited state, the *survival probability* defined as $P_{\text{surv}}(t) \equiv |\alpha(t)|^2$, so we want to find the expression of $\alpha(t)$. Its general expression reads:

$$\alpha(t) = A_+ e^{-i\omega_+ t} + A_- e^{-i\omega_- t} \tag{4.8}$$

where the constants A_+ and A_- are determined by the initial conditions $\alpha(0) = 1$ and $\dot{\alpha}(0) = -i\omega_0$ (coming from the fact that $\beta(0) = 0$ in Eq. (4.5)):

$$A_\pm = \frac{1}{2} \pm \frac{\delta + i\gamma_\alpha/2}{2\Omega} \tag{4.9}$$

Weak and strong coupling regimes in the resonant case $\omega_0 = \omega_\alpha$:

In the *resonant case* $\omega_0 = \omega_\alpha$, the eigen-frequencies in Eq. (4.6) become:

$$\omega_\pm = \omega_\alpha - i\frac{\gamma_\alpha}{4} \pm \frac{\Omega}{2} \tag{4.10}$$

where Ω now reads:

$$\Omega = \sqrt{4g^2 - \left(\frac{\gamma_\alpha}{2}\right)^2} \tag{4.11}$$

One can clearly see that two different regimes in the time-domain are possible depending on the values of g and γ_α:
(i) for small coupling constant $g < \frac{1}{4}\gamma_\alpha$, Ω becomes purely imaginary, and the eigen-frequencies $\omega_\pm$ [Eq. (4.10)] are now complex, leading to a monotonic decay of the amplitude $\alpha(t)$ in time [Eq. (4.8)], known as the **weak-coupling regime**;
(ii) for large coupling constant $g > \frac{1}{4}\gamma_\alpha$, Ω is real, and the eigen-frequencies $\omega_\pm$ [Eq. (4.10)] show a different real part, leading to *oscillations* of the amplitude $\alpha(t)$ in the time-domain, known as the **strong-coupling regime**. The oscillations, known as *vacuum Rabi oscillations*, can be seen physically as a *coherent* and *reversible* exchange of energy between the quantum emitter and the photonic system.

The general solution will not be derived explicitely. Only the two following limiting cases will be studied: the (very) weak-coupling regime, *i.e.* when $g \ll \gamma_\alpha$, and the (very) strong-coupling regime, *i.e.* when $g \gg \gamma_\alpha$. In fact, a very good approximate of the solution may be derived in these two cases by means of power series expansion. These two regimes are separated by the *critical regime*, *i.e.* when $g = \gamma_\alpha/4$.

Critical regime: $g = \gamma_\alpha/4$

Exactly at the transition between the two regimes, when $g = \gamma_\alpha/4$, one has $\Omega = 0$. At this sometimes called "exceptional point" [43], the eigenfrequencies in Eq. (4.10) coalesce and the eigenvectors become completely parallel giving for the amplitude $\alpha(t)$:

$$\alpha(t) = \left[1 + \frac{\gamma_\alpha}{2}\frac{t}{2}\right] e^{-\frac{\gamma_\alpha}{2}\frac{t}{2}} \tag{4.12}$$

Very weak-coupling regime: $g \ll \gamma_\alpha$

To get more insight about what is going on in this regime, we will derive an analytical solution in the case of huge losses due to the photonic system $g \ll \gamma_\alpha$. We can then do the following power series expansion:

$$\Omega \simeq \mathrm{i}\frac{\gamma_\alpha}{2} - \mathrm{i}\frac{4g^2}{\gamma_\alpha} \tag{4.13}$$

Then, from Eq. (4.11), the eigen-frequencies become:

$$\omega_+ \simeq \omega_\alpha - \mathrm{i}\frac{2g^2}{\gamma_\alpha} \tag{4.14}$$

$$\omega_- \simeq \omega_\alpha - \mathrm{i}\frac{\gamma_\alpha}{2} + \mathrm{i}\frac{2g^2}{\gamma_\alpha} \tag{4.15}$$

and the constants $A_\pm$ [Eq. (4.9)] become:

$$A_+ \simeq 1 + \frac{4g^2}{\gamma_\alpha^2} \tag{4.16}$$

$$A_- \simeq -\frac{4g^2}{\gamma_\alpha^2} \tag{4.17}$$

By defining the decay rate γ as:

$$\gamma \equiv \frac{4g^2}{\gamma_\alpha} \tag{4.18}$$

the expression of $\alpha(t)$ becomes:

$$\alpha(t) \simeq \left(1 + \frac{\gamma}{\gamma_\alpha}\right)\mathrm{e}^{-\mathrm{i}\omega_\alpha t}\mathrm{e}^{-\gamma\frac{t}{2}} - \frac{\gamma}{\gamma_\alpha}\mathrm{e}^{-\mathrm{i}\omega_\alpha t}\mathrm{e}^{-\gamma_\alpha\frac{t}{2}}\mathrm{e}^{\gamma\frac{t}{2}} \tag{4.19}$$

Very quickly when $t \gg 1/\gamma_\alpha$, and considering that $\gamma \ll \gamma_\alpha$, one gets the asymptotic result:

$$\alpha(t) \simeq \mathrm{e}^{-\frac{\gamma}{2}t} \tag{4.20}$$

which gives a survival probability

$$\boxed{P_{\mathrm{surv}}(t) = |\alpha(t)|^2 \simeq \mathrm{e}^{-\gamma t}} \tag{4.21}$$

This behavior is the one expected in the case of weak-coupling [35].

Purcell factor: We now introduce the Purcell factor F_p, which is a figure-of-merit commonly used when studying the weak-coupling between a QE and a resonance, defined by the equation $F_p \equiv \gamma/\gamma_0$ [where γ_0 is the atomic decay rate in free-space whose expression has been given in Chapter 2, Eq. (2.27)]:

$$F_p = \frac{4g^2}{\gamma_0\gamma_\alpha} \tag{4.22}$$

By using the expression of the coupling constant g given by Eq. (4.2) and the expression of the free-space decay rate given in Chapter 2, Eq. (2.27), one recovers the usual forms of the Purcell factor [44]:

$$F_p = \frac{6\pi c^3}{\omega_\alpha^3}\frac{Q}{V} \quad \Leftrightarrow \quad F_p = \frac{3}{4\pi^2}\lambda_\alpha^3\frac{Q}{V} \tag{4.23}$$

where $\lambda_\alpha = 2\pi c/\omega_\alpha$ and we introduced the quality factor of the resonance as: $Q \equiv \omega_\alpha/\gamma_\alpha$.

Very strong-coupling regime: $g \gg \gamma_\alpha$

We now consider the strong-coupling regime $g \gg \gamma_\alpha$. In this case, we can make the following expansion

$$\Omega \simeq 2g - \frac{\gamma_\alpha^2}{16g} \tag{4.24}$$

$$\omega_\pm \simeq -\mathrm{i}\frac{\gamma_\alpha}{4} \pm g \tag{4.25}$$

$$\begin{aligned} A_\pm &\simeq \frac{1}{2} \pm \mathrm{i}\frac{\gamma_\alpha}{8g}\left(1 + \frac{\gamma_\alpha^2}{32g^2}\right) \\ &\simeq \frac{1}{2} \end{aligned} \tag{4.26}$$

Then, $\alpha(t)$ becomes

$$\alpha(t) \simeq \mathrm{e}^{-\frac{\gamma_\alpha}{2}\frac{t}{2}}\cos(gt) \tag{4.27}$$

which gives a survival probability $P_{\mathrm{surv}}(t) = |\alpha(t)|^2$

$$\boxed{P_{\mathrm{surv}}(t) = \mathrm{e}^{-\frac{\gamma_\alpha}{2}t}\cos^2(gt) = \frac{1}{2}\mathrm{e}^{-\frac{\gamma_\alpha}{2}t}\left[1 + \cos(2gt)\right]} \tag{4.28}$$

One can see in this equation that $P_{\mathrm{surv}}(t) = |\alpha(t)|^2$ oscillates at the frequency $\Omega = 2g$. These oscillations, also called "vacuum Rabi oscillations", are characteristic of the strong-coupling [35].

4.2.2 Density matrix approach (master equation formalism)

We now treat the previous system within the master equation framework (closely following Ref. [35] chapter 6, especially section 6.2, entitled "Spontaneous emission: From irreversible decay to Rabi oscillations"). For that, the cavity is coupled to a bath of harmonic oscillators giving rise to the cavity decay rate γ_α. We present this approach for the resonant case where $\omega_0 = \omega_\alpha$.

The evolution of the reduced density matrix of the system {two-level atom + single cavity mode} is given by the following master equation [35]:

$$\frac{\partial\rho(t)}{\partial t} = \frac{1}{\mathrm{i}\hbar}[\hat{H}_{\mathrm{JC}}, \rho(t)] - \frac{\gamma_\alpha}{2}\{\hat{a}^\dagger\hat{a}, \rho(t)\} + \gamma_\alpha\hat{a}\rho(t)\hat{a}^\dagger \tag{4.29}$$

where in this equation [...] denotes the commutator and {...} the anti-commutator, and the new parameter γ_α is the linewidth of the cavity (FWHM), also called cavity decay rate in [35], taking into account the cavity losses.

Note: In the case of an ideal lossless cavity ($\gamma_\alpha = 0$), the dynamics is described by the equation:

$$\frac{\partial \rho(t)}{\partial t} = \frac{1}{i\hbar}[\hat{H}_{JC}, \rho(t)] \tag{4.30}$$

which is equivalent to the Jaynes-Cummings model [33].

We will solve the master equation (4.29) for the reduced density matrix of the system {two-level atom + single cavity mode} when the system is initially prepared in the pure state $|\psi(0)\rangle = |e,0\rangle$, standing for the atom in the excited state and no photon in the cavity field. Because of these initial conditions, the dynamics remains confined in the Hilbert-space spanned by the following three states:

$$|1\rangle \equiv |e,0\rangle \tag{4.31}$$

$$|2\rangle \equiv |g,1\rangle \tag{4.32}$$

$$|3\rangle \equiv |g,0\rangle \tag{4.33}$$

Therefore, we write the density matrix in the basis of these three states, and we get from Eq. (4.29):

$$\frac{\partial \rho_{11}}{\partial t} = ig(\rho_{12} - \rho_{21}) \tag{4.34}$$

$$\frac{\partial \rho_{22}}{\partial t} = -\gamma_\alpha \rho_{22} - ig(\rho_{12} - \rho_{21}) \tag{4.35}$$

$$\frac{\partial (\rho_{12} - \rho_{21})}{\partial t} = -\frac{\gamma_\alpha}{2}(\rho_{12} - \rho_{21}) + i2g(\rho_{11} - \rho_{22}) \tag{4.36}$$

$$\frac{\partial \rho_{33}}{\partial t} = \gamma_\alpha \rho_{22} \tag{4.37}$$

ρ_{ii} is the probability for the system to be in state $|i\rangle$, and ρ_{ij} $\forall i \neq j$ is the coherence between the states $|i\rangle$ and $|j\rangle$, for the states defined by Eqs. (4.31)-(4.33). Note that the above equations are not completely independent because $\rho_{11} + \rho_{22} + \rho_{33} = 1$. This set of four equations can be recast as a system of three independent equations:

$$\frac{\partial}{\partial t}\begin{bmatrix} \rho_{11} \\ \rho_{22} \\ \rho_{12} - \rho_{21} \end{bmatrix} = \begin{bmatrix} 0 & 0 & ig \\ 0 & -\gamma_\alpha & -ig \\ i2g & -i2g & -\gamma_\alpha/2 \end{bmatrix} \begin{bmatrix} \rho_{11} \\ \rho_{22} \\ \rho_{12} - \rho_{21} \end{bmatrix} \tag{4.38}$$

This linear system can be solved by finding the eigenvalues of the above matrix; one finds three eigenvalues:

$$\omega = -\frac{\gamma_\alpha}{2} \quad \text{and} \quad \omega_\pm = -\frac{\gamma_\alpha}{2} \pm \frac{\gamma_\alpha}{2}\sqrt{1 - \frac{16g^2}{\gamma_\alpha^2}} \tag{4.39}$$

Here, we are firstly interested in the survival probability to find the atom in the excited state $P_{surv}(t) \equiv \rho_{11}(t)$. The general solution is:

$$P_{surv}(t) = \rho_{11}(t) = Ae^{\omega t} + A_+ e^{\omega_+ t} + A_- e^{\omega_- t} \tag{4.40}$$

where the constants A, A_+ and A_- are determined by the initial conditions $\rho_{11}(0) = 1$, $\rho_{22}(0) = \rho_{33}(0) = 0$, and $\rho_{ij}(0) = 0$ $\forall i \neq j$, that give from Eqs. (4.34) and (4.36): $\rho_{11}(0) = 1$, $\frac{\partial}{\partial t}\rho_{11}(0) = 0$ and $\frac{\partial^2}{\partial t^2}\rho_{11}(0) = -2g^2$.

Weak and strong coupling regimes:

Again, one can clearly see that two different regimes in the time-domain are possible depending on the ratio between the parameters g and γ_α:
(i) For small coupling strength $g < \frac{\gamma_\alpha}{4}$, the eigen-frequencies $\omega_\pm$ [Eq. (4.39)] become all real and negative, leading to a monotonic decay of the survival probability $P_{\text{surv}}(t)$ in time [Eq. (4.40)], known as the **weak-coupling regime**; in this regime, spontaneous emission is an *irreversible* process.
(ii) For large coupling strength $g > \frac{\gamma_\alpha}{4}$, the eigen-frequencies $\omega_\pm$ [Eq. (4.39)] are now imaginary, leading to *oscillations* of the survival probability $P_{\text{surv}}(t)$ in the time-domain [Eq. (4.40)], known as the **strong-coupling regime**. The oscillations, known as *vacuum Rabi oscillations*, can be seen physically as a *coherent* exchange of energy between the quantum emitter and the photonic system. Physically, this means that the atom emits a photon, can reabsorb it, reemits it again etc... until the photon leaks out of the cavity. Spontaneous emission becomes *reversible* in a sense in the strong-coupling regime. An other signature of the strong-coupling regime is the *vacuum Rabi splitting* in the frequency-domain, which is observable under a more stringent condition than simply $g > \frac{\gamma_\alpha}{4}$ as we will see later in this chapter.

We will not explicitly derive the general solution here but will give the asymptotical behavior in two extreme cases: the very weak and very strong coupling regimes, where, respectively, the cavity decay rate is much larger than the coupling between the atom and the cavity mode $\gamma_\alpha \gg g$, and where the coupling is much larger than the cavity decay rate $g \gg \gamma_\alpha$.

Very weak-coupling regime: $g \ll \gamma_\alpha$

In the very weak-coupling regime where $g \ll \gamma_\alpha$, one can approximate the eigenvalues in Eq. (4.39) by:

$$\omega_\pm \approx -\frac{\gamma_\alpha}{2} \pm \frac{\gamma_\alpha}{2}\left(1 - \frac{8g^2}{\gamma_\alpha^2}\right) \tag{4.41}$$

and the solution for the survival probability $P_{\text{surv}}(t)$ in Eq. (4.40) is the *sum of three exponentials*:

$$P_{\text{surv}}(t) = A\mathrm{e}^{-\frac{\gamma_\alpha}{2}t} + A_+\mathrm{e}^{-\gamma t} + A_-\mathrm{e}^{-\gamma_\alpha t}\mathrm{e}^{+\gamma t} \tag{4.42}$$

where we introduced the decay rate:

$$\gamma \equiv \frac{4g^2}{\gamma_\alpha} \tag{4.43}$$

Very quickly for $t \gg 1/\gamma_\alpha$, one gets after using the initial conditions in Eq. (4.42):

$$\boxed{P_{\text{surv}}(t) \approx \mathrm{e}^{-\gamma t}} \tag{4.44}$$

One can see that the decay rate γ given in Eq. (4.43) is modified by the cavity compared to the decay in free space, as in Eq. (4.21).

Very strong-coupling regime: $g \gg \gamma_\alpha$

In the very strong-coupling regime where $g \gg \gamma_\alpha$, one can approximate the eigenvalues in Eq. (4.39) by:

$$\omega_\pm \approx -\frac{\gamma_\alpha}{2} \pm \mathrm{i}2g \tag{4.45}$$

and the solution for the survival probability $P_{\mathrm{surv}}(t)$ becomes, after using the initial conditions in Eq. (4.40) (one will have $A_- = A_+^*$):

$$\boxed{P_{\mathrm{surv}}(t) \approx \frac{1}{2}\mathrm{e}^{-\gamma_\alpha t/2}\left[1+\cos(2gt)\right]} \tag{4.46}$$

One can see in this case that $P_{\mathrm{surv}}(t)$ undergoes *vacuum Rabi oscillations* at the Rabi frequency $\Omega \equiv 2g$, which are damped at the cavity decay rate γ_α, as in Eq. (4.28).

4.2.3 Validity of the phenomenological approach

We note the following remarkable fact: the dynamics of this Lindblad system is equivalent to the *non-Hermitian* evolution of the *pure state* presented in section 4.2.1: for the initial condition $|\psi(0)\rangle = |\mathrm{e},0\rangle$, there is a perfect correspondance between $|\alpha(t)|^2$, $|\beta(t)|^2$ and $\alpha(t)\beta^*(t)$ in Eq. (4.5), and, respectively, $\rho_{11}(t)$, $\rho_{22}(t)$ and $\rho_{12}(t)$ in Eq. (4.38), provided one sets $\gamma_0 = 0$ and $\omega_0 = \omega_\alpha$ in Eq. (4.5). Indeed, in that case, one can check that a pure state that satisfies Eq. (4.5) also satisfies Eq. (4.29). Note however that for more than one excitation (photon), this equivalence is lost; the phenomenological approach can not be used and a rigorous dissipative approach with master equation is required instead.

4.2.4 Conclusion and generalization to N quantum emitters

This model allows to study the temporal evolution of the system, by providing analytical expression of the survival probability $P_{\mathrm{surv}}(t)$ of the atom to remain in the excited state. It gives an interpretation for the transition between the monotically decreasing regime of $P_{\mathrm{surv}}(t)$, known as the weak-coupling regime, and the so-called vacuum Rabi oscillations of $P_{\mathrm{surv}}(t)$, known as the strong-coupling regime in the resonant case $\omega_0 = \omega_\alpha$: when the losses quantified by the cavity decay rate γ_α are higher than (four times) the coupling constant $\gamma_\alpha > 4g$, this is the weak-coupling regime, and when $\gamma_\alpha < 4g$, this is the strong-coupling regime.

Such a model can be generalized to treat N quantum emitters coupled to the same electromagnetic mode, by replacing by replacing the JC Hamiltonian of Eq. (4.1) by the Tavis-Cummings Hamiltonian which reads (under the rotating-wave approximation) [45, 46]:

$$\hat{H}_{TC} = \sum_{j=1}^{N} \hbar\omega_0 \hat{\sigma}_j^\dagger \hat{\sigma}_j + \hbar\omega_\alpha\left(\hat{a}^\dagger\hat{a} + \frac{1}{2}\right) + \sum_{j=1}^{N} \hbar g_j\left(\hat{\sigma}_j\hat{a}^\dagger + \hat{\sigma}_j^\dagger\hat{a}\right) \tag{4.47}$$

One of the most striking results is that, under some approximations (identical coupling $g_j \equiv g$, N large but weak excitations of the QEs), the ensemble of N QEs behaves like a

giant harmonic oscillator coupled to the EM mode by a coupling constant $\sqrt{N}g$ [18, 20]. From this scaling, one can conclude that one way to enter the strong-coupling regime is simply to increases the number of QEs N as one has a favorable scaling of the coupling constant $\propto \sqrt{N}$.

4.3 "Continuum" approach

We now present a model which is conceptually quite different from the ones presented in the previous section. This model treats the spontaneous emission of an atom coupled to a bounded continuum of electromagnetic modes, with a bandwidth γ_α. As previously, the atom is modeled as a two-level system with transition frequency ω_0, and the continuum is assumed to have a "Lorentzian" density of states (modes) centered on a frequency ω_α and with a bandwidth γ_α (FWHM) as depicted in Fig. 4.1 (b). In particular, while conceptually very different, this model predicts the same temporal behavior as the previous ones. This rather simple approach will allow us to introduce different concepts that we will use in the following chapter, where we will give foundation and improve this phenomenological approach. Also, this model provides a different interpretation of the transition between the weak and strong coupling regimes in the resonant case $\omega_0 = \omega_\alpha$: the transition occurs when the bandwidth of the continuum is equal to γ, where γ is the modified atomic decay rate given by the Fermi golden rule. When $\gamma < \gamma_\alpha/4$, $P_{surv}(t)$ has a monotically decreasing behavior, and when $\gamma > \gamma_\alpha/4$, $P_{surv}(t)$ shows an oscillatory behavior (the vacuum Rabi oscillations). Finally, the interest of this model is that it predicts the distribution in energy of the emitted photons in the continuum which is an observable that one can measure in practice: the so-called vacuum Rabi splitting. We present here this model, following and readapting [47], chapter 1, Complement 1A.

4.3.1 Description of the model

We consider a two-level atom of transition frequency ω_0 and a *discrete*[1] continuum of electromagnetic states labeled by j and of frequency ω_j. This corresponds to the state:

$$|\psi(t)\rangle = \alpha(t)\,e^{-i\omega_0 t}\,|e,0\rangle + \sum_j \beta_j(t)\,e^{-i\omega_j t}\,|g,1_j\rangle \tag{4.48}$$

where $|g,1_j\rangle \equiv |g\rangle \otimes |1_j\rangle$ is the tensor product between the atomic ground state $|g\rangle$ and the state of the EM field $|1_j\rangle$ containing one photon in the mode j and $|e,0\rangle \equiv |e\rangle \otimes |0\rangle$ is the tensor product between the atomic excited state $|e\rangle$ and the vacuum state of the EM field $|0\rangle$. Note that by writing the state like this, we do not consider states like $|e,1_j\rangle$ (atom in the excited state and one photon in the mode j) or $|g,0\rangle$ (atom in the ground state and no photon), in the spirit of the rotating-wave approximation (which neglects in the interaction Hamiltonian the terms that couple the states $|e,1_j\rangle$ and $|g,0\rangle$).

[1] The *discretization* of the continuum in j distinct states of frequency ω_j is for pure mathematical convenience, and one recovers a real continuum in the limit where the separation in the frequencies ω_j tends to be null.

The total Hamiltonian of the system is written in the general form:

$$\hat{H} = \hat{H}_0 + \hat{H}_I(\mathbf{r}_0) \tag{4.49}$$

where $\hat{H}_0$ is the Hamiltonian of the non-interacting system {atom + EM field} with eigenstates $\{|g,1_j\rangle\,;|e,0\rangle\}$ and associated eigenenergies $\{\hbar\omega_j;\hbar\omega_0\}$, and $\hat{H}_I(\mathbf{r}_0)$ is the interaction Hamiltonian taken here in the **electric dipole approximation** form:

$$\hat{H}_I(\mathbf{r}_0) = -\hat{\mathbf{d}}\cdot\hat{\mathbf{E}}_\perp(\mathbf{r}_0) \tag{4.50}$$

where $\hat{\mathbf{d}}$ is the atomic electric dipole operator and $\hat{\mathbf{E}}_\perp(\mathbf{r}_0)$ is the transverse electric field operator evaluated at the position of the atom $\mathbf{r}_0$.

To know the dynamics of the spontaneous emission, one must get the coefficients $\alpha(t)$ and $\beta_j(t)$ by solving the Schrödinger equation with the initial condition $|\psi(0)\rangle = |e,0\rangle$ (*i.e.*, $\alpha(0) = 1$ and $\beta_j(0) = 0$) corresponding to the atom initially in the excited state and no photon in the electromagnetic field. One then obtains the following differential equations fullfilled by the coefficients $\alpha(t)$ and $\beta_j(t)$:

$$i\dot{\alpha}(t) = \sum_j g_j^*(\mathbf{r}_0)\beta_j(t)\,e^{i(\omega_0-\omega_j)t}, \tag{4.51}$$

$$i\dot{\beta}_j(t) = g_j(\mathbf{r}_0)\alpha(t)\,e^{-i(\omega_0-\omega_j)t}. \tag{4.52}$$

where we introduced the **coupling strength** $g_j(\mathbf{r})$ (also called coupling rate) defined by:

$$\hbar g_j(\mathbf{r}) \equiv \langle g,1_j|\,\hat{H}_I(\mathbf{r})\,|e,0\rangle \qquad \text{Unit:} \quad [g_j] = s^{-1} \tag{4.53}$$

By formally integrating Eq. (4.52) together with the initial condition $\beta_j(0) = 0$, one gets:

$$i\beta_j(t) = g_j(\mathbf{r}_0)\int_0^t dt'\,\alpha(t')e^{-i(\omega_0-\omega_j)t'} \tag{4.54}$$

and inserting this expression into Eq. (4.51) gives:

$$\dot{\alpha}(t) = -\sum_j |g_j(\mathbf{r}_0)|^2 \int_0^t dt'\,\alpha(t')e^{i(\omega_0-\omega_j)(t-t')} \tag{4.55}$$

that is conveniently recast in the form

$$\boxed{\dot{\alpha}(t) = -\int_0^t dt'\,\alpha(t')\int_0^\infty d\omega\,R(\mathbf{r}_0,\omega)e^{i(\omega_0-\omega)(t-t')}} \tag{4.56}$$

where we introduced the **reservoir coupling spectrum** $R(\mathbf{r},\omega)$ defined as:

$$R(\mathbf{r},\omega) = \sum_j |g_j(\mathbf{r})|^2\,\delta(\omega-\omega_j) \qquad \text{Unit:} \quad [R(\mathbf{r},\omega)] = s^{-1} \tag{4.57}$$

4.3.2 Fermi golden rule and density of states

We now introduce the *Fermi golden rule* that we will use in the following. It is obtained as a first-order perturbative solution of Eq. (4.56) with initial condition $\alpha(0) = 1$. To first order in $R(\mathbf{r}_0, \omega)$, one gets (see Appendix 4.B):

$$P_{\text{surv}}(t) = 1 - \gamma t \tag{4.58}$$

where γ is given by the following expression, known as the *Fermi golden rule* (FGR):

$$\gamma = 2\pi R(\mathbf{r}_0, \omega_0) \tag{4.59}$$

In reality, the one-photon states $|1_j\rangle$ form a continuum, and one can therefore write $R(\mathbf{r}, \omega)$ in terms of the density of states (DOS) $\rho(\omega)$ as:

$$R(\mathbf{r}, \omega) \longrightarrow |g(\mathbf{r}, \omega)|^2 \rho(\omega) \tag{4.60}$$

where $\hbar g(\mathbf{r}, \omega) \equiv \langle g, 1_\omega | \hat{H}_I(\mathbf{r}) | e, 0 \rangle$ with $|1_\omega\rangle$ representing the one-photon state with frequency ω, and the DOS $\rho(\omega)$ represents the number of electromagnetic modes per unit frequency. One then recovers a more common form of the FGR:

$$\gamma = 2\pi |g(\mathbf{r}, \omega_0)|^2 \rho(\omega_0) \tag{4.61}$$

in terms of the density of states[2].

4.3.3 Temporal evolution

The formalism presented so far is quite general, valid for any reservoir coupling spectrum $R(\mathbf{r}, \omega)$. We will develop further the analytical model by assuming a simple form for the reservoir. In this model, we first assume that the coupling strength $g(\mathbf{r}, \omega)$ is a constant of the position and frequency $g(\mathbf{r}, \omega) \equiv g$. On the other hand, we assume a "Lorentzian" distribution for the DOS $\rho(\omega)$ centered on the frequency ω_α and of FWHM $\Delta\omega = \gamma_\alpha$:

$$\rho(\omega) = \frac{1}{\pi} \frac{\gamma_\alpha/2}{(\omega_\alpha - \omega)^2 + (\gamma_\alpha/2)^2} \tag{4.62}$$

These assumptions lead to the following reservoir coupling spectrum:

$$R(\mathbf{r}, \omega) = g^2 \frac{1}{\pi} \frac{\gamma_\alpha/2}{(\omega_\alpha - \omega)^2 + (\gamma_\alpha/2)^2} \tag{4.63}$$

With the expression Eq. (4.63) of the reservoir coupling spectrum, the frequency integral in Eq. (4.56) can be calculated exactly (see [47], chapter 1, Complement 1A). By

[2] As already discussed in Chapter 1, Section 1.2.2, in the case of a *degenerate* continuum (*i.e.*, for a given frequency ω, there are many one-photon states $|1_k\rangle$ with $\omega_k = \omega$, differing for instance from the propagation direction and polarization, when these quantities are defined), $R(\mathbf{r}, \omega)$ must be written as: $R(\mathbf{r}, \omega) = \overline{|g(\mathbf{r}, \omega)|^2} \rho(\omega)$ where $\overline{|g(\mathbf{r}, \omega)|^2}$ denotes $|g(\mathbf{r}, \omega)|^2$ averaged over all one-photon states $|1_k\rangle$ with frequency $\omega_k = \omega$.

letting the lower limit of the integral tends to $-\infty$, one gets[3]:

$$\dot{\alpha}(t) = -\frac{\gamma\gamma_\alpha}{4}\int_0^t \mathrm{d}t'\,\alpha(t')\mathrm{e}^{(t-t')\left[\mathrm{i}(\omega_0-\omega_\alpha)-\frac{\gamma_\alpha}{2}\right]} \tag{4.64}$$

where one introduces the decay rate:

$$\gamma \equiv \frac{4g^2}{\gamma_\alpha} \tag{4.65}$$

Note: This decay rate is the one given by the Fermi golden rule (4.59): $\gamma = 2\pi R(\mathbf{r}_0, \omega_0) = 2\pi g^2 \rho(\omega_0)$, with $\rho(\omega_0) = 2/(\pi\gamma_\alpha)$ in the resonant case where $\omega_0 = \omega_\alpha$.

By differentiating this expression, one gets a second-order differential equation for the amplitude $\alpha(t)$ (see [47], chapter 1, Complement 1A):

$$\ddot{\alpha}(t) - \left[\mathrm{i}(\omega_0-\omega_\alpha) - \frac{\gamma_\alpha}{2}\right]\dot{\alpha}(t) + \frac{\gamma\gamma_\alpha}{4}\alpha(t) = 0 \tag{4.66}$$

One can then solve exactly this differential equation and get the general expression:

$$\boxed{\alpha(t) = \left[\left(\frac{\mathrm{e}^{-\mathrm{i}\Omega\frac{t}{2}} + \mathrm{e}^{\mathrm{i}\Omega\frac{t}{2}}}{2}\right) + \frac{(\omega_0-\omega_\alpha)+\mathrm{i}\frac{\gamma_\alpha}{2}}{\Omega}\left(\frac{\mathrm{e}^{-\mathrm{i}\Omega\frac{t}{2}} - \mathrm{e}^{\mathrm{i}\Omega\frac{t}{2}}}{2}\right)\right]\mathrm{e}^{\mathrm{i}(\omega_0-\omega_\alpha)\frac{t}{2}}\mathrm{e}^{-\frac{\gamma_\alpha}{2}\frac{t}{2}}} \tag{4.67}$$

where Ω reads:

$$\Omega = \sqrt{\gamma\gamma_\alpha + \left(\omega_0 - \omega_\alpha + \mathrm{i}\frac{\gamma_\alpha}{2}\right)^2} \tag{4.68}$$

Weak and strong coupling regimes in the resonant case $\omega_0 = \omega_\alpha$:

In the resonant case, Ω becomes:

$$\Omega = \sqrt{\gamma\gamma_\alpha - \left(\frac{\gamma_\alpha}{2}\right)^2} \tag{4.69}$$

Again, one can see two different regimes depending on the values of γ and γ_α:

- If $\gamma < \gamma_\alpha/4$, then Ω is purely imaginary and the exponentials in Eq. (4.67) do not oscillate, and one has a monotical behavior of $\alpha(t)$ which decreases with time. This is the *weak-coupling regime*.
- If $\gamma > \gamma_\alpha/4$, then Ω is real and the exponentials in Eq. (4.67) *do* oscillate, and one has an oscillating behavior of $\alpha(t)$, damped by the last exponential. This is the *strong-coupling regime*.

[3] Taking into account the truncation at 0 in the integral leads to some mathematical subtleties. The effects of such a truncation, also known as *threshold effects*, were studied in Ref. [48]. In letting the integral go from $-\infty$ to $+\infty$, we neglect these threshold effects (like in the Wigner-Weisskopf theory for instance [49]). This considerably simplifies the integral calculations, and one can check numerically that it is a good approximation when the width of the Lorentzian γ_α is much smaller than ω_α: $\gamma_\alpha \ll \omega_\alpha$ (in other words for a mode with a quality factor $Q = \omega_\alpha/\gamma_\alpha$ large compared to 1).

Note: The form of the reservoir coupling spectrum in Eq. (4.63) does not really matter as long as it has a width γ_α; for example, in Refs. [50] and [51] Appendix A, they consider a quasi-continuum, *i.e.* an ensemble of N *discrete* states j very close in frequency with a "door" distribution centered on the atomic frequency ω_0 and of variable bandwidth γ_α and of equal coupling constants: $g_j \equiv g$. They then get the expressions of $\alpha(t)$ and $\beta_j(t)$ by writing Eqs. (4.51) and (4.52) in a matrix form and by diagonalizing numerically the matrix (see Appendix 4.C). The authors then found that when $\gamma_\alpha \sim \gamma$ where γ is the atomic decay rate given by the Fermi's golden rule, there is a transition between a monotonic behavior (for $\gamma_\alpha > \gamma$) and an oscillatory behavior (for $\gamma_\alpha < \gamma$), which corroborate the present findings. In Appendix 4.C, we provide additionnal numerical simulations of the survival probability $P_{\text{surv}}(t) = |\alpha(t)|^2$ when the quasi-continuum bandwidth varies.

Very weak-coupling regime: $\gamma \ll \gamma_\alpha$

In the very weak-coupling regime, where $\gamma \ll \gamma_\alpha$, $\alpha(t)$ takes the form, to first order in γ/γ_α:

$$\alpha(t) = \left(1 + \frac{\gamma}{\gamma_\alpha}\right) e^{-\gamma \frac{t}{2}} - \frac{\gamma}{\gamma_\alpha} e^{-\gamma_\alpha \frac{t}{2}} e^{+\gamma \frac{t}{2}} \tag{4.70}$$

Zeno regime: Eq. (4.70) contains the *Zeno regime* with the characteristic dependence in t^2 [52–54]. Indeed, at short times $t \ll 1/\gamma_\alpha$ and to first order in γ/γ_α, one gets the following expression for the survival probability defined as $P_{\text{surv}}(t) = |\alpha(t)|^2$:

$$P_{\text{surv}}(t) \approx 1 - \frac{\gamma\gamma_\alpha}{4} t^2 \tag{4.71}$$

This development is valid as long as $t \ll \gamma_\alpha$, which means that by carefully designing a cavity with γ_α small enough for the measurement to be feasible, one can expect to observe experimentally the Zeno regime in a cavity, while in free space it is unattainable [54–56] (but be careful that if the cavity resonance is too narrow, *i.e.* γ_α too small, one is no longer in the weak-coupling but could enter the strong-coupling regime). The *Zeno time* defined as $P_{\text{surv}}(t) \approx 1 - (t/t_Z)^2$ [55] is by identification and by replacing γ by its expression (4.65) equal to $1/g$. This is in agreement with [57], where they observed such a regime, by coupling a discrete state to a continuum of a width verifying: $g \sim 0.1\gamma_\alpha$ (which is indeed the weak-coupling regime) [4].

Very quickly, for $t \gg \gamma_\alpha$, the contribution of the second exponential in Eq. (4.70) is negligible, and the expression (4.70) reduces to:

$$\alpha(t) \approx e^{-\gamma \frac{t}{2}} \tag{4.72}$$

leading to the survival probability $P_{\text{surv}} = |\alpha(t)|^2$:

$$P_{\text{surv}}(t) \approx e^{-\gamma t} \tag{4.73}$$

[4] In [57], the authors study the coupling of an optical mode (modeled by a single quantum state) to a chain of optical modes (modeled by a continuum of states of bandwidth $\gamma_\alpha = 4\kappa$). The coupling is characterized by a coupling constant $g = \kappa_0$. In the experiment, they have a ratio $\kappa_0/\kappa \simeq 0.37$, which corresponds indeed to a ratio $g/\gamma_\alpha \sim 0.1$.

Very strong-coupling regime: $\gamma \gg \gamma_\alpha$

In the very strong-coupling regime, where $g \gg \gamma_\alpha$, $\alpha(t)$ takes the form, to lowest order in γ_α/γ:

$$\alpha(t) \approx \mathrm{e}^{-\frac{\gamma_\alpha}{2}\frac{t}{2}} \cos(gt) \tag{4.74}$$

which gives for the survival probability $P_{\mathrm{surv}} = |\alpha(t)|^2$:

$$P_{\mathrm{surv}}(t) \approx \frac{1}{2}\mathrm{e}^{-\gamma_\alpha t/2}\left[1 + \cos(2gt)\right] \tag{4.75}$$

Discussion:

What is noteworthy is that this model, which considers the coupling of a two-level atom to a continuum of modes of width γ_α, predicts the same temporal behavior as the previous section [comparing *e.g.* Eq. (4.73) with Eqs. (4.21) and (4.42), or Eq. (4.75) with Eqs. (4.28) and (4.46)], which considered the coupling of the atom to a single lossy mode, where this mode is coupled to a reservoir.

4.3.4 Emission spectrum in the resonant-approximation

Moreover, this model allows us to predict the statistical distribution of energies of the photons, contrary to the previous one. We study the statistics in the two extreme cases in the resonance case $\omega_0 = \omega_\alpha$: the very weak and strong coupling regimes.

Emission spectrum in the very weak-coupling regime: $\gamma \ll \gamma_\alpha$

To know the population in the continuum, we insert Eq. (4.72) into Eq. (4.54) and get:

$$\begin{aligned} \mathrm{i}\beta_{\mathrm{j}}(t) &= g_{\mathrm{j}} \int_0^t \mathrm{d}t'\, \mathrm{e}^{-\frac{\gamma}{2}t'} \mathrm{e}^{-\mathrm{i}\left(\omega_0 - \omega_{\mathrm{j}}\right)t'} \\ &= g_{\mathrm{j}} \int_0^t \mathrm{d}t'\, \mathrm{e}^{\mathrm{i}\left[\left(\omega_{\mathrm{j}} - \omega_0\right) + \mathrm{i}\frac{\gamma}{2}\right]t'} \\ &= \mathrm{i}g_{\mathrm{j}} \frac{1 - \mathrm{e}^{\mathrm{i}\left[\left(\omega_{\mathrm{j}} - \omega_0\right) + \mathrm{i}\frac{\gamma}{2}\right]t}}{\left(\omega_{\mathrm{j}} - \omega_0\right) + \mathrm{i}\frac{\gamma}{2}} \end{aligned} \tag{4.76}$$

where we dropped the dependence in $\mathbf{r}_0$ in $g_{\mathrm{j}}(\mathbf{r}_0)$. In the limit $t \to +\infty$,

$$\beta_{\mathrm{j}}(t \to +\infty) = \frac{g_{\mathrm{j}}}{\left(\omega_{\mathrm{j}} - \omega_0\right) + \mathrm{i}\frac{\gamma}{2}} \tag{4.77}$$

Therefore, by defining the probability of emitting a photon in mode j by $P_{\mathrm{emit,j}}(t \to +\infty) \equiv |\beta_{\mathrm{j}}(t \to +\infty)|^2$, we get

$$P_{\mathrm{emit,j}}(t \to +\infty) = \frac{|g_{\mathrm{j}}|^2}{(\omega_{\mathrm{j}} - \omega_0)^2 + \left(\frac{\gamma}{2}\right)^2} \tag{4.78}$$

The total probability of emitting a photon is

$$\begin{aligned} P_{\text{emit}}(t\to+\infty) &= \sum_{\text{j}} P_{\text{emit,j}}(t) \\ &= \sum_{\text{j}} \frac{|g_{\text{j}}|^2}{(\omega_{\text{j}}-\omega_0)^2+\left(\frac{\Gamma}{2}\right)^2} \\ &= \int_0^\infty \text{d}\omega \sum_{\text{j}} \frac{|g_{\text{j}}|^2}{(\omega-\omega_0)^2+\left(\frac{\Gamma}{2}\right)^2}\delta(\omega-\omega_{\text{j}}) \\ &= \int_0^\infty \text{d}\omega \frac{R(\omega)}{(\omega-\omega_0)^2+\left(\frac{\Gamma}{2}\right)^2} \qquad \text{where} \qquad R(\omega)=\sum_{\text{j}}|g_{\text{j}}|^2\delta(\omega-\omega_{\text{j}}) \end{aligned} \tag{4.79}$$

The effective range of the integration is about γ, and at resonance one can consider the reservoir $R(\omega)$ of Eq. (4.63) as constant and equal to its maximum value in the very weak-coupling limit $\gamma \ll \gamma_\alpha$: $R(\omega) \simeq R(\omega_0) = \gamma/(2\pi)$. This then gives:

$$P_{\text{emit}}(t\to+\infty) \simeq \int_0^\infty \text{d}\omega \frac{\gamma/(2\pi)}{(\omega-\omega_0)^2+\left(\frac{\gamma}{2}\right)^2} \tag{4.80}$$

By letting the integral lower limit tend to $-\infty$ (which is a good approximation if $\gamma \ll \omega_0$), one finds that $P_{\text{emit}}(t\to+\infty) \simeq 1$, revealing the irreversibility of the emission. The important result is seen from Eq. (4.80): in the very strong-weak regime $\gamma \ll \gamma_\alpha$, the distribution of emitted photons is Lorentzian of linewidth γ (FWHM), also called radiative linewidth, which is equal to the decay rate. This can be seen as a time-energy uncertainty relation: by taking $\delta E = \hbar\gamma$ as a measure of the energy spread of the emitted photons, and defining $\tau = 1/\gamma$ the lifetime of the excited state, one has: $\delta E \tau = \hbar$.

Emission spectrum in the very strong-coupling regime: $\gamma \gg \gamma_\alpha$

Here, in order to get the populations in the continuum, we insert Eq. (4.74) into Eq. (4.54) and get:

$$\begin{aligned} \text{i}\beta_{\text{j}}(t) &= g_{\text{j}} \int_0^t \text{d}t'\, \text{e}^{-\frac{\gamma_\alpha}{2}\frac{t'}{2}} \cos(gt')\text{e}^{-\text{i}(\omega_0-\omega_{\text{j}})t'} \\ &= g_{\text{j}} \int_0^t \text{d}t'\, \text{e}^{-\frac{\gamma_\alpha}{2}\frac{t'}{2}} \frac{\text{e}^{\text{i}gt'}+\text{e}^{-\text{i}gt'}}{2}\text{e}^{-\text{i}(\omega_0-\omega_{\text{j}})t'} \\ &= \frac{g_{\text{j}}}{2}\int_0^t \text{d}t'\, \text{e}^{\text{i}(g-(\omega_0-\omega_{\text{j}}))t'-\frac{\gamma_\alpha}{2}\frac{t'}{2}} + \frac{g_{\text{j}}}{2}\int_0^t \text{d}t'\, \text{e}^{-\text{i}(g+(\omega_0-\omega_{\text{j}}))t'-\frac{\gamma_\alpha}{2}\frac{t'}{2}} \\ &= \text{i}\frac{g_{\text{j}}}{2}\frac{1-\text{e}^{\text{i}gt}\text{e}^{-\text{i}(\omega_0-\omega_{\text{j}})}\text{e}^{-\frac{\gamma_\alpha}{4}t}}{[(\omega_{\text{j}}-\omega_0)+g]+\text{i}\frac{\gamma_\alpha}{4}} + \text{i}\frac{g_{\text{j}}}{2}\frac{1-\text{e}^{-\text{i}gt}\text{e}^{-\text{i}(\omega_0-\omega_{\text{j}})}\text{e}^{-\frac{\gamma_\alpha}{4}t}}{[(\omega_{\text{j}}-\omega_0)-g]+\text{i}\frac{\gamma_\alpha}{4}} \end{aligned} \tag{4.81}$$

and in the limit $t \to +\infty$,

$$\beta_{\text{j}}(t\to+\infty) = \frac{1}{2}\frac{g_{\text{j}}}{[(\omega_{\text{j}}-\omega_0)+g]+\text{i}\frac{\gamma_\alpha}{4}} + \frac{1}{2}\frac{g_{\text{j}}}{[(\omega_{\text{j}}-\omega_0)-g]+\text{i}\frac{\gamma_\alpha}{4}} \tag{4.82}$$

As previously, by defining the probability of emitting a photon in mode j by $P_{\text{emit,j}}(t \to +\infty) \equiv |\beta_{\text{j}}(t \to +\infty)|^2$, we get

$$P_{\text{emit,j}}(t \to +\infty) = \frac{1}{4}\frac{|g_{\text{j}}|^2}{[(\omega_{\text{j}}-\omega_0)+g]^2+\left(\frac{\gamma_\alpha}{4}\right)^2} + \frac{1}{4}\frac{|g_{\text{j}}|^2}{[(\omega_{\text{j}}-\omega_0)-g]^2+\left(\frac{\gamma_\alpha}{4}\right)^2} + \text{C.T.} \quad (4.83)$$

where the cross-term C.T. is given by:

$$\text{C.T.} = \frac{|g_{\text{j}}|^2}{2}\frac{(\omega_{\text{j}}-\omega_0)^2 - g^2 + \left(\frac{\gamma_\alpha}{4}\right)^2}{\left[(\omega_{\text{j}}-\omega_0)^2 - g^2 + \left(\frac{\gamma_\alpha}{4}\right)^2\right]^2 + 4\left(\frac{\gamma_\alpha}{4}\right)^2 g^2} \quad (4.84)$$

As seen from Eq. (4.83), in the very strong-coupling regime $\gamma \gg \gamma_\alpha$, the distribution of emitted photons features two peaks separated by separated by $2g$, and of FWHM$= 2 \times \gamma_\alpha/4 = \gamma_\alpha/2$. Therefore, an "order of magnitude" condition to be able to distinguish the two peaks is:

$$2g > \frac{\gamma_\alpha}{2} \quad \Rightarrow \quad \boxed{g > \frac{\gamma_\alpha}{4}} \quad (4.85)$$

Comment: Note however that Eqs. (4.80) and (4.83) derived in this basic model do not allow us to quantify the number of photons which will be emitted in the far-field (and possibly detected by a detector) and the number of photon which will be absorbed by the environment (and therefore not coupled to the far-field).

4.4 Quasi-Normal Mode description

In the rest of this Chapter, we aim at studying the spontaneous emission of an atom in the presence of an arbitrary EM environment, which can be dissipative (open), dispersive and absorbing. A sketch of the problem is shown in Fig. 4.2. The atom is modeled by a two-level system with transition frequency ω_0, and the EM environment is fully characterized by the classical Green function of Maxwell equations. In the present Section, starting from the model presented in the Section 4.3.1, we show how the Green tensor can emerge in a fully quantum description by employing the powerful tools of the fluctuation-dissipation theorem encountered in Chapter 2 Section 2.2 (the quantization of the electromagnetic field is only implicitly used). We then use a Quasi-Normal Mode expansion of the Green tensor (which does not require the quantization of the QNMs), to derive the figure-of-merit characterizing the interaction between the two-level atom and the optical resonances of open/absorbing/dispersive systems, such as the coupling constant, the mode volume.

4.4.1 The fluctuation-dissipation theorem

We start from the model presented in the Section 4.3.1, that we briefly remind here the main results. In this simple model, we started from a state of the form [Eq. (4.48)]:

$$|\psi(t)\rangle = \alpha(t)\,\mathrm{e}^{-\mathrm{i}\omega_0 t}\,|\mathrm{e},0\rangle + \sum_{\text{j}} \beta_{\text{j}}(t)\,\mathrm{e}^{-\mathrm{i}\omega_{\text{j}} t}\,|\mathrm{g},1_{\text{j}}\rangle \quad (4.86)$$

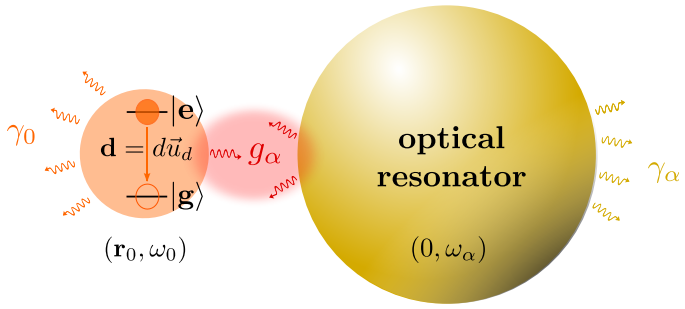

Figure 4.2 – Scheme of the system under study: a two-level atom initially excited and coupled to an optical resonator.

We next derived from the Scrödinger equation the following expression of the amplitude probability to be in the excited state [Eq. (4.56)]:

$$\dot{\alpha}(t) = -\int_0^t \mathrm{d}t'\, \alpha(t') \int_0^\infty \mathrm{d}\omega R(\mathbf{r}_0, \omega) \mathrm{e}^{\mathrm{i}(\omega_0 - \omega)(t-t')} \tag{4.87}$$

where we introduced the **reservoir coupling spectrum** $R(\mathbf{r}, \omega)$ defined as [Eq. (4.57) together with Eq. (4.53)]:

$$R(\mathbf{r}_0, \omega) = \frac{1}{\hbar^2} \sum_{\mathrm{j}} |\langle \mathrm{g}, 1_{\mathrm{j}}| \hat{H}_I(\mathbf{r}_0) |\mathrm{e}, 0\rangle|^2 \delta(\omega - \omega_{\mathrm{j}}) \quad \text{with} \quad \hat{H}_I(\mathbf{r}_0) = -\hat{\mathbf{d}} \cdot \hat{\mathbf{E}}_v(\mathbf{r}_0) \tag{4.88}$$

where the quantities appearing in the interaction Hamiltonian $\hat{H}_I$ are: $\hat{\mathbf{d}}$ is the atomic electric dipole operator and $\hat{\mathbf{E}}_v(\mathbf{r}_0)$ is the transverse electric field operator evaluated at the position of the atom $\mathbf{r}_0$. Note that the interaction Hamiltonian $\hat{H}_I$ is given within the electric dipole coupling approximation.

Now, we use the *linear-response theory* and the *fluctuation-dissipation theorem* presented in Chapter 2 Section 2.2 to express the reservoir coupling spectrum $R(\mathbf{r}_0, \omega)$ in terms of the Green tensor $\hat{\mathbf{G}}(\mathbf{r}_0, \mathbf{r}_0, \omega)$, at zero temperature [see Eq. (2.70) in Chapter 2 Appendix 2.A]:

$$\boxed{R(\mathbf{r}_0, \omega) = \frac{1}{\pi} \frac{1}{\hbar \epsilon_0} \frac{\omega^2}{c^2} \mathbf{d}^* \cdot \mathrm{Im}(\hat{\mathbf{G}}(\mathbf{r}_0, \mathbf{r}_0, \omega)) \cdot \mathbf{d}} \tag{4.89}$$

Then, the expression of $\alpha(t)$ in Eq. (4.87) can be cast in the form:

$$\dot{\alpha}(t) = -\int_0^t \mathrm{d}t'\, \alpha(t') K(t - t') \tag{4.90}$$

where the function $K(t-t')$ sometimes called the "kernel function" reads:

$$K(t - t') = \frac{1}{\pi} \frac{1}{\hbar \epsilon_0} \int_0^\infty \mathrm{d}\omega\, \frac{\omega^2}{c^2} \mathbf{d}^* \cdot \mathrm{Im}(\hat{\mathbf{G}}(\mathbf{r}_0, \mathbf{r}_0, \omega)) \cdot \mathbf{d}\, \mathrm{e}^{\mathrm{i}(\omega_0 - \omega)(t-t')} \tag{4.91}$$

Eq. (4.90) together with Eq. (4.91) is exact, and can be solved numerically once the Green's function is known.

4.4.2 Quasi-Normal Mode expansion of the Green tensor

We now present a description based on an expansion of the Green tensor. We first separate the Green tensor into an "unperturbed" part $\hat{\mathbf{G}}_0$ plus a "scattering" part $\hat{\mathbf{G}}_s$, where $\hat{\mathbf{G}}_0$ is the Green tensor in free space and $\hat{\mathbf{G}}_s$ describes the effect of the surrounding medium (this is due to the linearity of Maxwell's equations) [58]:

$$\hat{\mathbf{G}}(\mathbf{r},\mathbf{r}',\omega) = \hat{\mathbf{G}}_0(\mathbf{r},\mathbf{r}',\omega) + \hat{\mathbf{G}}_s(\mathbf{r},\mathbf{r}',\omega)\,, \tag{4.92}$$

Therefore, the function $R(\mathbf{r}_0,\omega)$ in Eq. (4.89) can be written in terms of a free space and a medium contributions:

$$R(\mathbf{r}_0,\omega) = \underbrace{\frac{1}{\pi}\frac{1}{\hbar\epsilon_0}\frac{\omega^2}{c^2}\mathbf{d}^*\cdot\mathrm{Im}(\hat{\mathbf{G}}_0(\mathbf{r}_0,\mathbf{r}_0,\omega))\cdot\mathbf{d}}_{\text{free space}} + \underbrace{\frac{1}{\pi}\frac{1}{\hbar\epsilon_0}\frac{\omega^2}{c^2}\mathbf{d}^*\cdot\mathrm{Im}(\hat{\mathbf{G}}_s(\mathbf{r}_0,\mathbf{r}_0,\omega))\cdot\mathbf{d}}_{\text{environment}} \tag{4.93}$$

From the expression of the Green tensor in free space $\hat{\mathbf{G}}_0$ ([59], chapter 8), one gets:

$$\vec{u}_\mathrm{d}\cdot\mathrm{Im}(\hat{\mathbf{G}}_0(\mathbf{r}_0,\mathbf{r}_0,\omega))\cdot\vec{u}_\mathrm{d} = \frac{\omega}{6\pi c} \tag{4.94}$$

where $\vec{u}_\mathrm{d}$ is a unit vector in the direction of the dipole moment: $\mathbf{d} = \mathrm{d}\vec{u}_\mathrm{d}$.

Next, we expand the scattered part of the Green tensor $\hat{\mathbf{G}}_s$ in terms of the resonant states of the photonic system as in Chapter 3 Section 3.2.2:

$$\hat{\mathbf{G}}_s(\mathbf{r},\mathbf{r}',\omega) \simeq c^2\sum_\alpha \frac{\mathbf{E}_\alpha(\mathbf{r})\otimes\mathbf{E}_\alpha(\mathbf{r}')}{2\omega(\tilde{\omega}_\alpha-\omega)} \tag{4.95}$$

Here, $\mathbf{E}_\alpha(\mathbf{r})$ are the QNM fields, $\tilde{\omega}_\alpha \equiv \omega_\alpha - \mathrm{i}\gamma_\alpha/2$ are the QNM complex frequencies, $\otimes$ denotes the tensor product. Note that the validity of Eq. (4.95) is directly related to the issue of the completeness of the QNM set, which is a critical issue and has been discussed in Chapter 3 Section 3.2.2. A similar expansion has been used in Ref. [58] in the case of a single resonance, where the authors investigate analytically the weak and strong coupling regime of a two-level atom.

One then gets:

$$\begin{aligned}&\vec{u}_\mathrm{d}\cdot\mathrm{Im}(\hat{\mathbf{G}}_s(\mathbf{r}_0,\mathbf{r}_0,\omega))\cdot\vec{u}_\mathrm{d} = \\ &\frac{c^2}{2\omega}\sum_\alpha\left\{\mathrm{Re}\left(\frac{1}{V_\alpha(\mathbf{r}_0)}\right)\frac{\gamma_\alpha/2}{(\omega_\alpha-\omega)^2+(\gamma_\alpha/2)^2} + \mathrm{Im}\left(\frac{1}{V_\alpha(\mathbf{r}_0)}\right)\frac{\omega_\alpha-\omega}{(\omega_\alpha-\omega)^2+(\gamma_\alpha/2)^2}\right\}\end{aligned} \tag{4.96}$$

where we defined the *mode volume* of the QNM α as:

$$V_\alpha(\mathbf{r}_0) \equiv \frac{1}{(\vec{u}_\mathrm{d}\cdot\mathbf{E}_\alpha(\mathbf{r}_0))^2} \tag{4.97}$$

in which the QNM field $\mathbf{E}_\alpha$ is taken at the QE position $\mathbf{r}_0$. $V_\alpha(\mathbf{r}_0)$ is a complex quantity in general, as the QNM fields $\mathbf{E}_\alpha$ are complex. It moreover depends on the orientation $\vec{u}_d$ of the QE with respect to the QNM polarization, and on the QE position $\mathbf{r}_0$, where the QNM field is evaluated in Eq. (4.97).

Employing Eqs. (4.94) and (4.96) into Eq. (4.93), one gets:

$$R(\mathbf{r}_0,\omega) = \frac{\omega^3}{6\pi^2\epsilon_0\hbar c^3}|\mathbf{d}|^2 + \frac{\omega}{2\pi\hbar\epsilon_0}|\mathbf{d}|^2\sum_\alpha \mathrm{Re}\left(\frac{1}{V_\alpha(\mathbf{r}_0)}\right)\frac{\gamma_\alpha/2}{(\omega_\alpha-\omega)^2+(\gamma_\alpha/2)^2} + \frac{\omega}{2\pi\hbar\epsilon_0}|\mathbf{d}|^2\sum_\alpha \mathrm{Im}\left(\frac{1}{V_\alpha(\mathbf{r}_0)}\right)\frac{\omega_\alpha-\omega}{(\omega_\alpha-\omega)^2+(\gamma_\alpha/2)^2} \tag{4.98}$$

4.4.3 Coupling rate and density of states: definitions

One can see that the reservoir in Eq. (4.98) contains three parts. To understand better the meaning of each part, one can introduce the concepts of *coupling strength* and *density of states*, by gathering the quantities (ω_0, d, $V_\alpha(\mathbf{r}_0)$) in a *coupling strentgh* $g_\alpha(\mathbf{r}_0,\omega)$ and the other parameters characterizing the environment (ω_α, γ_α) in the *density of states* $\rho_\alpha(\omega)$, such that the previous equation can be written as

$$R(\mathbf{r}_0,\omega) = \underbrace{\frac{\omega^3}{6\pi^2\epsilon_0\hbar c^3}|\mathbf{d}|^2}_{\text{free space}} + \sum_\alpha |g_\alpha(\mathbf{r}_0,\omega)|^2\underbrace{\rho_\alpha^{\mathrm{L}}(\omega)}_{\text{Lorentz}} + \sum_\alpha \frac{\mathrm{Im}(1/V_\alpha(\mathbf{r}_0))}{\mathrm{Re}(1/V_\alpha(\mathbf{r}_0))}|g_\alpha(\mathbf{r}_0,\omega)|^2\underbrace{\rho_\alpha^{\mathrm{NL}}(\omega)}_{\text{non-Lorentz}} \tag{4.99}$$

where

$$\hbar g_\alpha(\mathbf{r}_0,\omega) \equiv \sqrt{\frac{\hbar\omega}{2\epsilon_0}\mathrm{Re}\left(\frac{1}{V_\alpha(\mathbf{r}_0)}\right)}\times \mathrm{d} \quad \text{Unit:} \quad [g_\alpha(\mathbf{r}_0,\omega)] = \mathrm{s}^{-1} \tag{4.100}$$

$$\rho_\alpha^{\mathrm{L}}(\omega) \equiv \frac{1}{\pi}\frac{\gamma_\alpha/2}{(\omega_\alpha-\omega)^2+(\gamma_\alpha/2)^2} \quad \text{Unit:} \quad [\rho_\alpha^{\mathrm{L}}(\omega)] = \mathrm{s} \tag{4.101}$$

$$\rho_\alpha^{\mathrm{NL}}(\omega) \equiv \frac{1}{\pi}\frac{\omega_\alpha-\omega}{(\omega_\alpha-\omega)^2+(\gamma_\alpha/2)^2} = \frac{\omega_\alpha-\omega}{\gamma_\alpha/2}\rho_\alpha^{\mathrm{L}}(\omega) \quad \text{Unit:} \quad [\rho_\alpha^{\mathrm{NL}}(\omega)] = \mathrm{s} \tag{4.102}$$

We finally derive the expression of the reservoir coupling spectrum in terms of figures-of-merit

- The **mode volume** $V_\alpha(\mathbf{r}_0)$, discussed in Chapter 3 Section 3.3, whose real part characterizes the coupling between the QE and the resonance α (the larger $\mathrm{Re}(1/V_\alpha(\mathbf{r}_0))$ the better the coupling), and the appearance of $\mathrm{Im}(1/V_\alpha(\mathbf{r}_0))$, present in plasmonic systems due to energy dissipation, is often neglected, but gives rise to a non-Lorentzian term. It depends on the *location* and *orientation* of the QE through $V_\alpha(\mathbf{r}_0)$.

- The **coupling strength** $g_\alpha(\mathbf{r}_0,\omega)$, defined using the mode volume, which quantifies how much the QE is coupled to the electromagnetic modes with frequency ω, We will justify that it is legitimate to consider it as constant $g_\alpha(\mathbf{r}_0,\omega) \simeq g_\alpha(\mathbf{r}_0,\omega_\alpha)$, as it varies much more slowly than the density of states as a function of the frequency ω.

- The **density of states** $\rho_\alpha(\omega)$, which does *not* depend of the position or orientation of the QE, and strongly varies with the frequency ω.

Comments: In nanophotonics, it is commonly assumed that the coupling strength is constant: $g(\mathbf{r},\omega)\equiv g$, and that it is the density of states which is modified by the environment and depends on the position $\mathbf{r}$: is $\rho(\omega)=\rho_p(\mathbf{r},\omega)$. In this community, ρ_p is often called *(partial) local density of states* (see *e.g.* [59], Chapter 8.4), where "local" means that the DOS depends on the QE *position* $\mathbf{r}_0$, and "partial" means that the DOS depends on the QE *orientation* $\vec{u}_\mathrm{d}$.

Here, in contrast with this convention, we choose to keep the QE position and orientation dependence in the coupling strength [according to Eq. (4.100) together with Eq. (4.97)], and *not* in the density of states [Eq. (4.101)]. If we adopt the same vocabulary as in [59] Chapter 8.4, we should talk about "partial local coupling strentgh", and simply of "density of states". Furthermore, if the dipole moment orientation is not known, or random, one must average the coupling strength squared over the various orientations. Finally, an important difference is that the authors of [59] expand the Green function in terms of normal modes [see Eq. (8.111) in [59]], which fails when one has to deal with a dispersive and absorbing medium [60].

4.4.4 Integro-differential equation for $\alpha(t)$

Once the reservoir coupling spectrum is determined, the entire dynamics of $\alpha(t)$ can be deduced. Plugging its expression (4.99) into Eq. (4.87) gives:

$$\begin{aligned}\dot{\alpha}(t) = &-\int_0^t \mathrm{d}t'\,\alpha(t')\underbrace{\int_0^\infty \mathrm{d}\omega\,\frac{\omega^3}{6\pi^2\epsilon_0\hbar c^3}|\mathbf{d}|^2 \mathrm{e}^{\mathrm{i}(\omega_0-\omega)(t-t')}}_{K^{\text{free-space}}(t-t')}\\ &-\int_0^t \mathrm{d}t'\,\alpha(t')\sum_\alpha\underbrace{\int_0^\infty \mathrm{d}\omega\,|g_\alpha(\mathbf{r}_0,\omega)|^2\rho_\alpha^\mathrm{L}(\omega)\mathrm{e}^{\mathrm{i}(\omega_0-\omega)(t-t')}}_{K_\alpha^{\text{Lorentz}}(t-t')}\\ &-\int_0^t \mathrm{d}t'\,\alpha(t')\sum_\alpha\underbrace{\int_0^\infty \mathrm{d}\omega\,\frac{\mathrm{Im}(1/V_\alpha)}{\mathrm{Re}(1/V_\alpha)}|g_\alpha(\mathbf{r}_0,\omega)|^2\rho_\alpha^\mathrm{NL}(\omega)\mathrm{e}^{\mathrm{i}(\omega_0-\omega)(t-t')}}_{K_\alpha^{\text{non-Lorentz}}(t-t')}\end{aligned} \tag{4.103}$$

We first calculate the "free-space" kernel $K^{\text{free-space}}(t-t')$, the "Lorentzian" kernel $K_\alpha^{\text{Lorentz}}(t-t')$ and the "non-Lorentzian" kernel $K_\alpha^{\text{non-Lorentz}}(t-t')$ by letting the lower bound of the integrals tend to $-\infty$ (which results in neglecting threshold effects [48]).

Free-space kernel $K^{\text{free-space}}(t-t')$

We deal with the "free-space" kernel like in the Wigner-Weisskopf theory: we take ω^3 out of the integral and replace it by ω_0^3 (flat reservoir approximation, valid for the free-space reservoir which varies slowly with ω) (see [49] and [34], chapter 5.3). Using the result (ignoring the principal value term):

$$\int_{-\infty}^{+\infty}\mathrm{d}\omega\,\mathrm{e}^{\mathrm{i}(\omega_0-\omega)(t-t')}\approx 2\pi\,\delta(t-t') \tag{4.104}$$

one gets:

$$\begin{aligned} K^{\text{free-space}}(t-t') &\equiv \int_{-\infty}^{+\infty} \mathrm{d}\omega \, \frac{\omega^3}{6\pi^2\epsilon_0\hbar c^3}|\mathbf{d}|^2 \mathrm{e}^{\mathrm{i}(\omega_0-\omega)(t-t')} \\ &\simeq \frac{\omega_0^3}{6\pi^2\epsilon_0\hbar c^3}|\mathbf{d}|^2 \int_{-\infty}^{+\infty} \mathrm{d}\omega \, \mathrm{e}^{\mathrm{i}(\omega_0-\omega)(t-t')} \\ &\simeq \frac{\omega_0^3}{3\pi\epsilon_0\hbar c^3}|\mathbf{d}|^2 \delta(t-t') \\ &= \gamma_0 \, \delta(t-t') \end{aligned} \tag{4.105}$$

where

$$\gamma_0 \equiv \frac{\omega_0^3}{3\pi\epsilon_0\hbar c^3}|\mathbf{d}|^2 \tag{4.106}$$

which is the expression of the *free-space decay rate* γ_0.

Lorentzian kernel $K_\alpha^{\text{Lorentz}}(t-t')$

We now deal with the "Lorentzian" kernel. Similarly, to make the integration, we will consider that the quantity $g_\alpha(\mathbf{r}_0,\omega)$ is constant as a function of the frequency ω and we will take it out from the integral replacing it by $g_\alpha(\mathbf{r}_0,\omega_0)$. This is the equivalent in nanophotonics to assume that the coupling strength is constant and that only the density of states changes, but often said without justifications. Here we justify why it is legitimate to do that, as $|g_\alpha(\mathbf{r}_0,\omega)|^2 \propto \omega$ [Eq. (4.100)] slowly varies compared to the variation of the DOS $\rho_\alpha^{\text{L}}(\omega)$ [Eq. (4.101)]. Therefore, the only thing is to calculate the Fourier transform of a Lorentzian function, which can be determined analytically, and it is why the case of a Lorentzian reservoir is interesting.

We can then calculate the "Lorentzian" kernel analytically, by using the Fourier transform of a Lorentzian function (see Appendix 4.D):

$$\begin{aligned} K_\alpha^{\text{Lorentz}}(t-t') &\equiv \int_{-\infty}^{+\infty} \mathrm{d}\omega \, |g_\alpha(\mathbf{r}_0,\omega)|^2 \rho_\alpha^{\text{L}}(\omega) \mathrm{e}^{\mathrm{i}(\omega_0-\omega)(t-t')} \\ &\simeq |g_\alpha(\mathbf{r}_0,\omega_0)|^2 \int_{-\infty}^{+\infty} \mathrm{d}\omega \, \rho_\alpha^{\text{L}}(\omega) \mathrm{e}^{\mathrm{i}(\omega_0-\omega)(t-t')} \\ &= |g_\alpha(\mathbf{r}_0,\omega_0)|^2 \mathrm{e}^{\mathrm{i}(\omega_0-\omega_\alpha)(t-t')} \mathrm{e}^{-\frac{\gamma_\alpha}{2}|t-t'|} \end{aligned} \tag{4.107}$$

Non-Lorentzian kernel $K_\alpha^{\text{non-Lorentz}}(t-t')$

Similarly, we can then calculate the "non-Lorentzian" kernel analytically (see Appendix 4.D):

$$\begin{aligned} K_\alpha^{\text{non-Lorentz}}(t-t') &= \int_{-\infty}^{+\infty} \mathrm{d}\omega\, \frac{\mathrm{Im}(1/V_\alpha)}{\mathrm{Re}(1/V_\alpha)} |g_\alpha(\mathbf{r}_0,\omega)|^2\, \rho_\alpha^{\text{NL}}(\omega)\, \mathrm{e}^{\mathrm{i}(\omega_0-\omega)(t-t')} \\ &\simeq \frac{\mathrm{Im}(1/V_\alpha)}{\mathrm{Re}(1/V_\alpha)} |g_\alpha(\mathbf{r}_0,\omega_0)|^2 \int_{-\infty}^{+\infty} \mathrm{d}\omega\, \rho_\alpha^{\text{NL}}(\omega)\, \mathrm{e}^{\mathrm{i}(\omega_0-\omega)(t-t')} \\ &= \mathrm{i}\frac{\mathrm{Im}(1/V_\alpha)}{\mathrm{Re}(1/V_\alpha)} \underbrace{|g_\alpha(\mathbf{r}_0,\omega_0)|^2 \mathrm{e}^{\mathrm{i}(\omega_0-\omega_\alpha)(t-t')} \mathrm{e}^{-\frac{\gamma_\alpha}{2}|t-t'|}}_{K_\alpha^{\text{Lorentz}}(t-t')} \\ &= \mathrm{i}\frac{\mathrm{Im}(1/V_\alpha)}{\mathrm{Re}(1/V_\alpha)} K_\alpha^{\text{Lorentz}}(t-t') \end{aligned} \tag{4.108}$$

Finally, by plugging these previous expressions into Eq. (4.103), one gets:

$$\begin{aligned} \dot{\alpha}(t) = &-\gamma_0 \underbrace{\int_0^t \mathrm{d}t'\, \alpha(t')\delta(t-t')}_{=\alpha(t)/2} \\ &-\sum_\alpha |g_\alpha(\mathbf{r}_0,\omega_0)|^2 \left[1+\mathrm{i}\frac{\mathrm{Im}(1/V_\alpha)}{\mathrm{Re}(1/V_\alpha)}\right] \int_0^t \mathrm{d}t'\, \alpha(t') \mathrm{e}^{\mathrm{i}(\omega_0-\omega_\alpha)(t-t')} \mathrm{e}^{-\frac{\gamma_\alpha}{2}|t-t'|} \end{aligned} \tag{4.109}$$

which gives

$$\boxed{\dot{\alpha}(t) = -\frac{\gamma_0}{2}\alpha(t) - \sum_\alpha |g_\alpha(\mathbf{r}_0,\omega_0)|^2 \left[1+\mathrm{i}\frac{\mathrm{Im}(1/V_\alpha)}{\mathrm{Re}(1/V_\alpha)}\right] \int_0^t \mathrm{d}t'\, \alpha(t') \mathrm{e}^{\left[\mathrm{i}(\omega_0-\omega_\alpha)-\frac{\gamma_\alpha}{2}\right](t-t')}} \tag{4.110}$$

Note: From the integro-differential Eq. (4.87) for $\alpha(t)$, we end-up with this integro-differential Eq. (4.110), after using the fluctuation-dissipations theorem and the resonant state tools. It is necessary to employ numerical methods to solve and study this equation in the general case. An analytical treatment may however be carried out in the single-resonance case.

The weak-coupling regime: In the weak-coupling regime, one can do the following Markov approximations in the above integral: one replaces $\alpha(t')$ by $\alpha(t)$ and one makes tend to infinity the upper integral limit. Then, the above integro-differential equation can be calculated analytically. The solution becomes (see Appendix 4.E):

$$\alpha(t) = \exp\left(-\left[\frac{\gamma}{2} + \mathrm{i}\Delta\omega\right]t\right) \tag{4.111}$$

where

$$\gamma = \gamma_0 + \sum_\alpha |g_\alpha(\mathbf{r}_0,\omega_0)|^2 \frac{\gamma_\alpha}{(\omega_0-\omega_\alpha)^2 + \left(\frac{\gamma_\alpha}{2}\right)^2} - \sum_\alpha 2|g_\alpha(\mathbf{r}_0,\omega_0)|^2 \frac{\omega_0-\omega_\alpha}{(\omega_0-\omega_\alpha)^2 + \left(\frac{\gamma_\alpha}{2}\right)^2} \frac{\mathrm{Im}(1/V_\alpha)}{\mathrm{Re}(1/V_\alpha)} \tag{4.112}$$

$$\Delta\omega = \sum_\alpha |g_\alpha(\mathbf{r}_0,\omega_0)|^2 \frac{\omega_0-\omega_\alpha}{(\omega_0-\omega_\alpha)^2+\left(\frac{\gamma_\alpha}{2}\right)^2} + \sum_\alpha \frac{1}{2}|g_\alpha(\mathbf{r}_0,\omega_0)|^2 \frac{\gamma_\alpha}{(\omega_0-\omega_\alpha)^2+\left(\frac{\gamma_\alpha}{2}\right)^2} \frac{\mathrm{Im}(1/V_\alpha)}{\mathrm{Re}(1/V_\alpha)} \tag{4.113}$$

Note: The decay rate γ and the Lamb shift $\Delta\omega$ are exactly the same as the ones derived in Chapter 3 Section 3.3 once normalized by the decay rate in free space γ_0 (see Appendix 4.E).

4.4.5 Temporal evolution in the single-resonance case

We are going to derive an *exact* solution for the amplitude $\alpha(t)$ obeying Eq. (4.110) in the single-resonance case.

Single-resonance case: We consider the coupling between the atom and a *single* photonic or plasmonic resonance α. In this case, one can get a closed-form solution of the amplitude $\alpha(t)$. First, the integro-differential equation for $\alpha(t)$ reduces to:

$$\dot{\alpha}(t) = -\frac{\gamma_0}{2}\alpha(t) - g^2 \int_0^t \mathrm{d}t'\, \alpha(t') \mathrm{e}^{\left[\mathrm{i}(\omega_0-\omega_\alpha)-\frac{\gamma_\alpha}{2}\right](t-t')} \tag{4.114}$$

with

$$g^2 \equiv |g_\alpha(\mathbf{r}_0,\omega_0)|^2 \left[1+\mathrm{i}\frac{\mathrm{Im}(1/V_\alpha)}{\mathrm{Re}(1/V_\alpha)}\right] \tag{4.115}$$

which we will call the "generalized" coupling constant. By differentiating this equation, one gets the second order differential equation verified by $\alpha(t)$ (see Appendix 4.F):

$$\boxed{\ddot{\alpha}(t) - \left[\mathrm{i}(\omega_0-\omega_\alpha) - \frac{\gamma_0}{2} - \frac{\gamma_\alpha}{2}\right]\dot{\alpha}(t) + \left[g^2 - \mathrm{i}\frac{\gamma_0}{2}(\omega_0-\omega_\alpha) + \frac{\gamma_0}{2}\frac{\gamma_\alpha}{2}\right]\alpha(t) = 0} \tag{4.116}$$

Note: This equation is the same as Eq. (4.66) if we do not consider the emission of the atom in free space, *i.e.*, set $\gamma_0 = 0$ in Eq. (4.116), and if we neglect $\mathrm{Im}(1/V_\alpha(\mathbf{r}_0))$ in the expression of g in Eq. (4.116), provided g in Eq. (4.66) verifies $g = |g_\alpha(\mathbf{r}_0,\omega_0)|$.

This second order differential equation can be solved rigorously by writting the characteristic polynomial of this equation or equivalently by making the following *ansatz* for the solution:

$$\alpha(t) = \mathrm{e}^{-\mathrm{i}\omega t} \tag{4.117}$$

By plugging this expression of $\alpha(t)$, we get two eigen-frequencies:

$$\boxed{\omega_\pm = \frac{\omega_\alpha+\omega_0}{2} - \mathrm{i}\frac{\gamma_0}{4} - \mathrm{i}\frac{\gamma_\alpha}{4} \pm \frac{\Omega}{2}} \quad \text{with} \quad \boxed{\Omega = \sqrt{\left[\omega_0-\omega_\alpha+\mathrm{i}\left(\frac{\gamma_\alpha}{2}-\frac{\gamma_0}{2}\right)\right]^2 + 4g^2}} \tag{4.118}$$

Note: These are the eigen-frequencies as in Section 4.2.1, taking into account that in writing the state of the system [Eq. (4.86)], we add the phase factor "$e^{-i\omega_0 t}$", so the total amplitude in front of the state $|e,0\rangle$ gets an additional frequency ω_0, such that the frequency of the total amplitude is indeed:

$$\omega_\pm = \frac{\omega_\alpha + \omega_0}{2} - i\frac{\gamma_0}{4} - i\frac{\gamma_\alpha}{4} \pm \frac{\Omega}{2} \tag{4.119}$$

Therefore, $\alpha(t)$ can be written as:

$$\alpha(t) = A_+ e^{-i\omega_+ t} + A_- e^{-i\omega_- t} \tag{4.120}$$

where the constants $A_\pm$ are obtained with the initial conditions $\alpha(t=0)=1$ and $\dot{\alpha}(t=0)=0$ [as seen from Eq. (4.51) where $\beta_j(t=0)=0$]:

$$A_\pm = \frac{1}{2} \pm \frac{(\omega_0-\omega_\alpha) + i\left(\frac{\gamma_0}{2}+\frac{\gamma_\alpha}{2}\right)}{2\Omega} \tag{4.121}$$

The solution Eq. (4.120) together with the Eqs. (4.118) and (4.121) gives the exact solution for $\alpha(t)$:

$$\boxed{\alpha(t) = \left[\left(\frac{e^{-i\Omega\frac{t}{2}} + e^{i\Omega\frac{t}{2}}}{2}\right) + \frac{(\omega_0-\omega_\alpha) + i\left(\frac{\gamma_0}{2}+\frac{\gamma_\alpha}{2}\right)}{\Omega}\left(\frac{e^{-i\Omega\frac{t}{2}} - e^{i\Omega\frac{t}{2}}}{2}\right)\right] e^{i(\omega_0-\omega_\alpha)\frac{t}{2}} e^{-\left(\frac{\gamma_0}{2}+\frac{\gamma_\alpha}{2}\right)\frac{t}{2}}} \tag{4.122}$$

From this expression, one can numerically study the survival probability $P_{surv}(t) = |\alpha(t)|^2$ as a function of the time t, the detuning $\omega_0 - \omega_\alpha \neq 0$, the magnitude of the coupling strength g appearing in the expression of Ω [Eq. (4.118)], and the losses quantified by γ_0 and γ_α.

4.4.6 Emission spectrum in the resonant-approximation

We are going to give an "order-of-magnitude condition" for the vacuum Rabi splitting observation in the resonant case and in the strong-coupling regime.

Perfect Lorentzian case: To recover results found in the literature, we neglect the $\mathrm{Im}(1/V_\alpha(\mathbf{r}_0))$ (*i.e.* V_α is real) in the expression of g in Eq. (4.115), such that together with Eq. (4.100), g reads:

$$g = |g_\alpha(\omega_0)| = \sqrt{\frac{\omega_0}{2\hbar\epsilon_0 V_\alpha}}\,d \tag{4.123}$$

This is equivalent to consider only a DOS which is perfectly Lorentzian.

Resonant-approximation: We make the resonant-approximation $\omega_0 = \omega_\alpha$, to get:

$$\alpha(t) = A_+ e^{-i\omega_+ t} + A_- e^{-i\omega_- t} \tag{4.124}$$

with

$$A_\pm = \frac{1}{2} \pm i\frac{\gamma_0+\gamma_\alpha}{4\Omega} \tag{4.125}$$

$$\omega_\pm = \omega_\alpha - \mathrm{i}\frac{\gamma_0+\gamma_\alpha}{4} \pm \frac{\Omega}{2} \tag{4.126}$$

and

$$\Omega \equiv \omega_+(\omega_0=\omega_\alpha) - \omega_-(\omega_0=\omega_\alpha) = \sqrt{4g^2 - \left(\frac{\gamma_\alpha}{2}-\frac{\gamma_0}{2}\right)^2} \tag{4.127}$$

For our qualitative discussion, we consider the *strong-coupling regime* $g \gg \gamma_0, \gamma_\alpha$ so that $A_\pm$ in Eq. (4.125) can be approximated by $A_\pm \approx 1/2$. By plugging the expression of $\alpha(t)$ into the expression of $\beta(t)$ [from Eq. (4.86)], one gets:

$$\mathrm{i}\beta_\mathrm{j}(t) \approx \frac{g_\mathrm{j}}{2}\int_0^t \mathrm{d}t' \left(\mathrm{e}^{-\mathrm{i}\omega_+ t'} + \mathrm{e}^{-\mathrm{i}\omega_- t'}\right)\mathrm{e}^{-(\omega_0-\omega_\mathrm{j})t'} \tag{4.128}$$

which gives:

$$\begin{aligned}\beta(t\to+\infty) &= \frac{g_\mathrm{j}}{2}\frac{1}{(\omega_\mathrm{j}-\omega_0)-\omega_+} + \frac{g_\mathrm{j}}{2}\frac{1}{(\omega_\mathrm{j}-\omega_0)-\omega_-} \\ &= \frac{g_\mathrm{j}}{2}\frac{1}{(\omega_\mathrm{j}-\omega_0)-\frac{\Omega}{2}+\mathrm{i}\frac{\gamma_0+\gamma_\alpha}{4}} + \frac{g_\mathrm{j}}{2}\frac{1}{(\omega_\mathrm{j}-\omega_0)+\frac{\Omega}{2}+\mathrm{i}\frac{\gamma_0+\gamma_\alpha}{4}}\end{aligned} \tag{4.129}$$

and

$$P_{\mathrm{emit,j}}(t\to+\infty) = \frac{1}{4}\frac{|g_\mathrm{j}|^2}{[(\omega_\mathrm{j}-\omega_0)+\frac{\Omega}{2}]^2+\left(\frac{\gamma_0+\gamma_\alpha}{4}\right)^2} + \frac{1}{4}\frac{|g_\mathrm{j}|^2}{[(\omega_\mathrm{j}-\omega_0)-\frac{\Omega}{2}]^2+\left(\frac{\gamma_0+\gamma_\alpha}{4}\right)^2} + \text{C.T.} \tag{4.130}$$

In addition to a cross-term "C.T.", one gets two peaks separated by Ω, each one having a full width at half maximum (FWHM) of $(\gamma_0+\gamma_\alpha)/2$. This gives the following "order of magnitude" condition to observe the splitting:

$$\boxed{\Omega = \sqrt{4g^2 - \left(\frac{\gamma_\alpha}{2}-\frac{\gamma_0}{2}\right)^2} > \frac{\gamma_0+\gamma_\alpha}{2}} \tag{4.131}$$

The above condition can also be rewritten as

$$\boxed{4g^2 > \frac{\gamma_0^2+\gamma_\alpha^2}{2} \quad\Rightarrow\quad g > \frac{1}{2}\sqrt{\frac{\gamma_0^2+\gamma_\alpha^2}{2}}} \tag{4.132}$$

The quantity Ω is as before called the **vacuum Rabi splitting**, and in case of *equal loss* ($\gamma_0=\gamma_\alpha$), or very strong-coupling $g \gg |\gamma_\alpha-\gamma_0|$, corresponds to $2g$. In this case, the splitting reads:

$$2g > \frac{(\gamma_0+\gamma_\alpha)}{2} \quad\Rightarrow\quad \boxed{g > \frac{(\gamma_0+\gamma_\alpha)}{4}} \tag{4.133}$$

This condition above is the condition to observe the splitting in the frequency domain, in the limit case where $g \gg |\gamma_\alpha-\gamma_0|$ where we obtained an analytical solution accurate to first order in $g/|\gamma_\alpha-\gamma_0|$ only, and we got a splitting of $2g$. However, this is the *maximum* splitting one can get, and usually the splitting will be smaller than $2g$. It is the same condition as the one found in Section 4.3, Eq. (4.85), provided one sets $\gamma_0=0$ in Eq. (4.133).

Discussion: These equations (4.131), (4.132) and (4.133) are the same as the ones known in the literature [18, 20, 61]. What is particularly amazing is that this condition is identical as the one obtained with a completely classical treatment [18]. However, the presence of $\mathrm{Im}(1/V_\alpha(\mathbf{r}_0))$ appearing in the coupling constant g [Eq. (4.115)] complicates somewhat the discussion but has been discussed in the weak and strong coupling regimes in [62], showing that in the weak-coupling regime the decay rate is no longer Lorentzian, and that in the strong coupling regime it results in a blurring of the usual strong-coupling condition. Furthermore, it seems that the presence of $\mathrm{Im}(1/V_\alpha(\mathbf{r}_0))$ reduces the necessary coupling strength to observe the splitting [62].

4.5 Non-Hermitian Hamiltonian description

In this Section, we present a second quantization scheme for the EM field in the presence of a general medium — sometimes called "macroscopic QED", which was developped by a few groups [63–65] and [66, 67], and used to develop a formalism for the spontaneous emission problem of a two-level quantum emitter in terms of the Green tensor in [60] and [68], for instance. We briefly recall hereafter the quantization scheme, and we derive Hamiltonian allowing us to treat the problem of spontaneous emission, and we present an analytical approach developed in [69, 70] based on a phenomenological expansion of the Green tensor in terms of Lorentzians, each Lorentzian corresponding to a resonance.

4.5.1 Quantization scheme

The quantization procedure presented here is sometimes also called "macroscopic QED". The EM field in the presence of a general environment (dispersive and absorbing) is described by an electric-field operator $\hat{\mathbf{E}}(\mathbf{r},\omega)$, function of the spatial position $\mathbf{r}$ and the frequency ω. The environment is characterized by a relative permittivity: $\varepsilon(\mathbf{r}',\omega) = \varepsilon'(\mathbf{r}',\omega) + \mathrm{i}\,\varepsilon''(\mathbf{r}',\omega)$ and a constant relative permeability is assumed ($\mu = 1$). They show that this operator can be expressed in terms of the classical Green's function $\hat{\mathbf{G}}(\mathbf{r},\mathbf{r}',\omega)$ of the Maxwell's equations as:

$$\hat{\mathbf{E}}(\mathbf{r},\omega) = \mathrm{i}\sqrt{\frac{\hbar}{\pi\epsilon_0}}\frac{\omega^2}{c^2}\int \mathrm{d}\mathbf{r}'\,\sqrt{\varepsilon''(\mathbf{r}',\omega)}\,\hat{\mathbf{G}}(\mathbf{r},\mathbf{r}',\omega)\cdot\hat{\mathbf{f}}(\mathbf{r}',\omega) \tag{4.134}$$

where they introduced the bosonic field operators $\hat{\mathbf{f}}$ and $\hat{\mathbf{f}}^\dagger$ which are the equivalent of the annihilation and creation operators $\hat{a}$ and $\hat{a}^\dagger$ but for the EM field in the presence of the medium. $\hat{\mathbf{f}}$ and $\hat{\mathbf{f}}^\dagger$ depend on the position $\mathbf{r}$ and the frequency ω. Their cartesian components verify the following commutation relations:

$$\left[\hat{f}_i(\mathbf{r},\omega),\,\hat{f}_j(\mathbf{r}',\omega')\right] = 0 \tag{4.135}$$

$$\left[\hat{f}_i^\dagger(\mathbf{r},\omega),\,\hat{f}_j^\dagger(\mathbf{r}',\omega')\right] = 0 \tag{4.136}$$

$$\left[\hat{f}_i(\mathbf{r},\omega),\,\hat{f}_j^\dagger(\mathbf{r}',\omega')\right] = \delta_{ij}\delta(\mathbf{r}-\mathbf{r}')\delta(\omega-\omega') \tag{4.137}$$

The Hamiltonian of the radiation reads:

$$\hat{H}_R = \int \mathrm{d}\mathbf{r} \int_0^{+\infty} \mathrm{d}\omega\, \hbar\omega\, \hat{\mathbf{f}}^\dagger(\mathbf{r},\omega)\cdot\hat{\mathbf{f}}(\mathbf{r},\omega) \tag{4.138}$$

4.5.2 Temporal evolution

Employing this quantization scheme, one can study the dynamics of the excited two-level atom in terms of the Green tensor, which fully contains all the properties of the EM environment of the emitter.

The Hamiltonian of the two-level atom is:

$$\hat{H}_A = \hbar\omega_0 \hat{\sigma}^\dagger \hat{\sigma} \tag{4.139}$$

with ω_0 the transition frequency (defining the energy ground state as the zero of energy).

The interaction Hamiltonian reads, in the electric-dipole and rotating-wave approximations:

$$\hat{H}_I = -\left[\hat{\sigma}^\dagger \int_0^{+\infty} \mathrm{d}\omega\, \mathbf{d}\cdot\hat{\mathbf{E}}(\mathbf{r}_0,\omega) + \mathrm{H.c.}\right] \tag{4.140}$$

where $\mathbf{d}$ is the dipole moment and $\mathbf{r}_0$ is the position of the atom.

They then solve the Shrödinger equation with the total Hamiltonian $\hat{H} = \hat{H}_A + \hat{H}_R + \hat{H}_I$ considering that the system is described by the state:

$$|\psi(t)\rangle = \alpha(t)\mathrm{e}^{-\mathrm{i}\omega_0 t}\,|\mathrm{e},0\rangle + \int \mathrm{d}\mathbf{r} \int_0^{+\infty} \mathrm{d}\omega\, \beta_\omega(\mathbf{r},t)\mathrm{e}^{-\mathrm{i}\omega t}\,|\mathrm{g},1_\omega(\mathbf{r})\rangle \tag{4.141}$$

and get for the excited state amplitude $\alpha(t)$:

$$\dot{\alpha}(t) = \int_0^t \mathrm{d}t'\, K(t-t')\alpha(t') \tag{4.142}$$

where the function $K(t-t')$ called the "kernel function" in [60] reads:

$$K(t-t') = -\frac{1}{\pi}\frac{1}{\hbar\epsilon_0}\int_0^{+\infty} \mathrm{d}\omega\, \frac{\omega^2}{c^2}\mathbf{d}^*\cdot\mathrm{Im}(\hat{\mathbf{G}}(\mathbf{r}_0,\mathbf{r}_0,\omega))\cdot\mathbf{d}\,\mathrm{e}^{\mathrm{i}(\omega_0-\omega)(t-t')} \tag{4.143}$$

Comment: The Eqs. (4.142) and (4.143) are the same as the Eqs. (4.90) and (4.91) derived using the fluctuation-dissipation theorem.

Note: Note that these equations are exact, within the approximations made, and can be used to study both the weak and strong coupling. To further study the dynamics contained in Eqs. (4.142) and (4.143), one must know the Green tensor of the problem. We present next an analytical approach based on a phenomenological expansion of the Green tensor.

4.5.3 Derivation of an effective non-Hermitian Hamiltonian

Starting from this second quantization formalism, we briefly present here an analytical approach developed in [69, 70]. In these works, the authors study the problem of a two-level atom coupled to metallic nanoparticle, which is the archetype of a plasmonic resonator supporting plasmon resonances, refered to as localized surface plasmons resonances (LSP). The authors aimed at deriving an effective non-Hermitian Hamiltonian for the sub-system {QE + N LSP modes}, based on a phenomenological expansion of the Green tensor as a sum of Lorentzians, each Lorentzian corresponding to a plasmon resonance. Note that such an expansion is commonly used to go further analytically (see [71–73]), but one must be careful as it was shown not to be always accurate in nanophotonics [74]. In [69, 70], the authors start from the previous Hamiltonian $\hat{H} = \hat{H}_A + \hat{H}_R + \hat{H}_I$ [Eqs. (4.138), (4.139) and (4.140), where the emitter losses characterized by the rate γ_0 is introduced phenomenologically]:

$$\hat{H} = \hbar\omega_0 \hat{\sigma}^\dagger \hat{\sigma} - \mathrm{i}\hbar\frac{\gamma_0}{2}\hat{\sigma}^\dagger\hat{\sigma} + \int \mathrm{d}\mathbf{r} \int_0^{+\infty} \mathrm{d}\omega\, \hbar\omega\, \hat{\mathbf{f}}^\dagger(\mathbf{r},\omega)\cdot\hat{\mathbf{f}}(\mathbf{r},\omega) - \left[\hat{\sigma}^\dagger \int_0^{+\infty} \mathrm{d}\omega\, \mathbf{d}\cdot\hat{\mathbf{E}}(\mathbf{r}_0,\omega) + \mathrm{H.c.}\right] \tag{4.144}$$

Similarly to what has been done in Section 4.3 [Eq. (4.63)], they then express in a phenomenological way the Green tensor projection onto the dipole moment (that we called the reservoir coupling spectrum in Section 4.3) as a sum of Lorentzians through [5]:

$$R(\mathbf{r},\omega) = \frac{1}{\pi}\frac{\omega^2}{\hbar\epsilon_0 c^2}\mathbf{d}^*\cdot\mathrm{Im}\left(\hat{\mathbf{G}}(\mathbf{r},\mathbf{r}',\omega)\right)\cdot\mathbf{d} \approx \sum_{\alpha=1}^{N} |g_\alpha(\mathbf{r}_0)|^2 \frac{1}{\pi}\frac{\gamma_\alpha/2}{(\omega_\alpha-\omega)^2+(\gamma_\alpha/2)^2} \tag{4.145}$$

where ω_α and γ_α are the resonance frequency and width of the resonances labeled α, respectively, and $g_\alpha(\mathbf{r}_0)$ are the coupling constants. They are considered as free parameters and $g_\alpha(\mathbf{r}_0,\omega)$ as independent of ω and only dependent on $\mathbf{r}_0$. By integrating over all frequencies, or in other words, by tracing out the continuous degrees of freedom of the modes, they derive an effective Hamiltonian for the sub-system {QE + N LSP modes} [69, 70]:

$$\hat{H}_{\mathrm{eff}} = \hat{H}_A + \hat{H}_{R,\mathrm{eff}} + \hat{H}_{I,\mathrm{eff}} \tag{4.146}$$

which reads, in the new basis $\{|\mathrm{e},0\rangle, |\mathrm{g},1_\alpha\rangle\}$, with $|\mathrm{e}\rangle$ and $|\mathrm{g}\rangle$ the eigenstates of H_A, and $|0\rangle$ and $|1_\alpha\rangle$ eigenstates of $\hat{H}_{R,\mathrm{eff}}$:

$$\hat{H}_{\mathrm{eff}} = \hbar\begin{bmatrix} \omega_0 - \mathrm{i}\frac{\gamma_0}{2} & g_1 & g_2 & \dots & g_N \\ g_1 & \omega_1 - \mathrm{i}\frac{\gamma_1}{2} & 0 & \dots & 0 \\ g_2 & 0 & \omega_2 - \mathrm{i}\frac{\gamma_2}{2} & \dots & 0 \\ \dots & \dots & \dots & \dots & 0 \\ g_N & 0 & \dots & 0 & \omega_N - \mathrm{i}\frac{\gamma_N}{2} \end{bmatrix} \tag{4.147}$$

[5] In [69, 70] or [47] Chapter 1 Complement 1A, the authors talk about a Lorentzian coupling constant g which is misleading. The relevant quantity is actually the reservoir coupling spectrum $R(\mathbf{r},\omega)$ introduced here, which corresponds to the *density of states weighted by the coupling strength* (see Section 4.3.2). It is this reservoir that is Lorentzian. The confusion comes from the fact that $R(\mathbf{r},\omega)$ and g have the same unit.

The interest of this treatment is that it allows to deal with many resonances $\alpha = 1, ..., N$. Note that in the case of a single resonance, this Hamiltonian reduces to the one phenomenologically introduced before in Section 4.2.1 [see Eq. (4.5)]. The Schrödinger equation remains to be solve with the state:

$$|\psi(t)\rangle = \alpha(t)\,|\mathrm{e},0\rangle + \sum_{\alpha=1}^{N} \beta_\alpha(t)\,|\mathrm{g},1_\alpha\rangle \tag{4.148}$$

For some illustrations of the use of such an effective Hamiltonian $\hat{H}_{\mathrm{eff}}$, see Refs. [38, 39].

4.5.4 Emission spectrum in the far-field

Finally, from this formalism, one can express an important quantum optics quantities in terms of the Green tensor, the emitted-light spectrum defined as [60]:

$$S(\mathbf{r}_d,\omega) = \int_0^\infty \mathrm{d}t_2 \int_0^\infty \mathrm{d}t_1\, \mathrm{e}^{-\mathrm{i}\omega(t_2-t_1)} \left\langle \hat{\mathbf{E}}^{(-)}(\mathbf{r}_d,t_2)\hat{\mathbf{E}}^{(+)}(\mathbf{r}_d,t_1)\right\rangle \tag{4.149}$$

where $\hat{\mathbf{E}}^{(+)}(\mathbf{r})$ and $\hat{\mathbf{E}}^{(-)}(\mathbf{r})$ are defined as $\hat{\mathbf{E}}^{(+)}(\mathbf{r}) \equiv \int_0^\infty \mathrm{d}\omega\, \hat{\mathbf{E}}(\mathbf{r},\omega)$ and $\hat{\mathbf{E}}^{(-)}(\mathbf{r}) \equiv [\hat{\mathbf{E}}^{(+)}(\mathbf{r})]^\dagger$, and are written in the interaction picture in Eq. (4.149). This quantity is the emitted-light spectrum recorded by a detector located at the position $\mathbf{r}_d$.

This quantity can be recast in terms of the Green tensor as [71]:

$$S(\mathbf{r}_d,\omega) = \left| \frac{(\omega+\omega_0)\hat{\mathbf{G}}(\mathbf{r}_d,\mathbf{r}_0,\omega)\cdot\mathbf{d}/\epsilon_0}{\omega_0^2-\omega^2-2\omega_0\mathbf{d}\cdot\hat{\mathbf{G}}(\mathbf{r}_0,\mathbf{r}_0,\omega_0)\cdot\mathbf{d}/\hbar\epsilon_0} \right|^2 \tag{4.150}$$

This quantity is of particular importance to particularly investigate the strong-coupling regime, as in plasmonics, the mode splitting in the emission spectrum is the only signature of strong-coupling that one can observe. Compared to the previous models, this quantity takes into account the possible absorption of the light by the medium, while the distributions of the emitted photons derived previously in the limiting cases of the weak and strong coupling regimes [Eqs. (4.80), (4.83) and (4.130)] only give information about the near-field emission, and *not* the far-field emission. Numerical studies based on Eq. (4.150) can be found in [71] and [72, 73] for instance.

4.6 Conclusion

In this Chapter, we presented different models of the spontaneous emission of a two-level atom in the presence of an optical resonator. The models presented in Sections 4.2 and 4.3 are suitable for closed systems with low losses such as high-Q cavities, whereas the ones presented in Sections 4.4 and 4.5 were developed to deal with open/absorbing/dispersive systems, such as plasmonics resonators for example. Particularly, the approach presented in Section 4.4 based on the quasi-normal modes of the optical resonator allowed us to generalize the figures-of-merit of cQED (presented in Section 4.2) to the case where losses can be important (in open and absorbing systems).

In Table 4.1, we compare some parameters and the generalized figures-of-merit of the quasi-normal mode description with the ones of cQED: the detuning $\delta = \omega_0 - \omega_\alpha$ between the emitter transition frequency ω_0 and the resonator frequency ω_α; the natural decay rate of the atom γ_0 (in the absence of the resonator); the cavity decay rate or mode linewidth γ_α; the coupling constant $g_\alpha(\mathbf{r}_0, \omega)$ which characterizes the coupling between the atom and the resonance α (which involves the vector dipole moment of the two-level atom $\mathbf{d} = d\vec{u}_d$), and finally the mode volume V which quantifies the volume of interaction.

	δ	γ_0	γ_α	$\hbar g_\alpha(\mathbf{r}_0, \omega)$	$V_\alpha(\mathbf{r}_0)$
cQED	$\omega_0 - \omega_\alpha$	-	γ_α	$d\sqrt{\frac{\hbar\omega_\alpha}{2\epsilon_0 V}}$	cavity volume $V \in \mathbb{R}$
QNMs	$\omega_0 - \omega_\alpha$	$\frac{\omega_0^3}{3\pi\epsilon_0\hbar c^3}\lvert\mathbf{d}\rvert^2$	γ_α	$d\sqrt{\frac{\hbar\omega_\alpha}{2\epsilon_0}\mathrm{Re}\left(\frac{1}{V_\alpha(\mathbf{r}_0)}\right)}$	$V_\alpha(\mathbf{r}_0) = \frac{1}{(\vec{u}_\mathrm{d}\cdot\mathbf{E}_\alpha(\mathbf{r}_0))^2} \in \mathbb{C}$

Table 4.1 – Parameters of the cQED model (Section 4.2) and QNMs approach (Section 4.4).

The differences in the figures-of-merit give rise to discrepancies in the physical quantities which are expressed in terms of these parameters; In the weak-coupling, the decay rate γ, Lamb shift $\Delta\omega$ and Purcell factor F_α read (see Appendix 4.E):

$$\frac{\gamma}{\gamma_0} = 1 + \sum_\alpha \left\{ \frac{\gamma_\alpha^H}{\gamma_0} - 2\frac{\Delta\omega_\alpha^H}{\gamma_0}\frac{\mathrm{Im}(1/V_\alpha)}{\mathrm{Re}(1/V_\alpha)} \right\} \tag{4.151}$$

$$\frac{\Delta\omega}{\gamma_0} = \sum_\alpha \left\{ \frac{\Delta\omega_\alpha^H}{\gamma_0} + \frac{1}{2}\frac{\gamma_\alpha^H}{\gamma_0}\frac{\mathrm{Im}(1/V_\alpha)}{\mathrm{Re}(1/V_\alpha)} \right\} \tag{4.152}$$

with

$$\frac{\gamma_\alpha^H}{\gamma_0} = F_\alpha \left(\frac{\omega_\alpha}{\omega_0}\right)^2 \frac{(\gamma_\alpha/2)^2}{(\omega_0 - \omega_\alpha)^2 + \left(\frac{\gamma_\alpha}{2}\right)^2} \tag{4.153}$$

$$\frac{\Delta\omega_\alpha^H}{\gamma_0} = F_\alpha \left(\frac{\omega_\alpha}{\omega_0}\right)^2 \frac{\gamma_\alpha}{4} \frac{\omega_0 - \omega_\alpha}{(\omega_0 - \omega_\alpha)^2 + \left(\frac{\gamma_\alpha}{2}\right)^2} \tag{4.154}$$

where the generalized Purcell factor F_α is given by:

$$F_\alpha \equiv \frac{6\pi c^3}{\omega_\alpha^3} Q_\alpha \mathrm{Re}\left(1/V_\alpha(\mathbf{r}_0)\right) \tag{4.155}$$

and the quality factor Q_α by:

$$Q_\alpha \equiv \frac{\omega_\alpha}{\gamma_\alpha} \tag{4.156}$$

In the strong-coupling, the vacuum Rabi frequency Ω reads [using Eq. (4.115) into Eq. (4.118)]:

$$\Omega = \sqrt{\left[\omega_0 - \omega_\alpha + \mathrm{i}\left(\frac{\gamma_\alpha}{2} - \frac{\gamma_0}{2}\right)\right]^2 + 4|g_\alpha(\mathbf{r}_0, \omega_0)|^2 \left[1 + \mathrm{i}\frac{\mathrm{Im}(1/V_\alpha)}{\mathrm{Re}(1/V_\alpha)}\right]} \tag{4.157}$$

Indeed, in cQED, the mode volume $V_\alpha(\mathbf{r}_0)$ is real, and one can set $\mathrm{Im}(1/V_\alpha(\mathbf{r}_0)) = 0$ in these expressions to recover the cQED figures-of-merit for γ, $\Delta\omega$, F_α and Ω. However,

for systems with important losses, $V_\alpha(\mathbf{r}_0)$ is in general characterized by an imaginary part, which was illustrated in Chapter 3 Section 3.4 in the case of a dielectric (no absorption but radiation losses) and a plasmonic (absorption and radiation losses) spheres, which both constitute "open" cavities. Therefore, as pointed out by Koenderink in [75], the mode volume is a crucial parameter which has different meanings in closed or open cavities, and finds its proper definition in open cavities within the framework of the quasi-normal modes (see Chapter 3 and also [74, 76, 77]).

Moreover, while we discussed here only *quantum* formalisms, it is remarkable to point out that the Purcell factor F_α [Eq. (4.155)], the decay rate γ and Lamb shift $\Delta\omega$ *normalized by the free space decay rate* γ_0 [Eqs. (4.151), (4.152), (4.153) and (4.154)], as well as the vacuum Rabi splitting Ω [Eq. (4.157)], have the same expressions as the ones derived using a fully classical treatment. About the classical treatment, the interested reader could refer for instance to [18] when one does not consider $\mathrm{Im}[1/V_\alpha(\mathbf{r}_0)]$ and [62] in the general case.

4.A Jaynes-Cummings Hamiltonian

Atomic Hamiltonian: We consider a two-level atom with a ground state $|g\rangle$ of eigen-energy $\hbar\omega_g$ and an excited state $|e\rangle$ of eigen-energy $\hbar\omega_e$. If the zero of energy is taken at the level of the ground state ($\hbar\omega_g = 0$), the Hamiltonian of the two-level atom can be conveniently written as ([78] chapter 4.9):

$$\hat{H}_A = \hbar\omega_0 \hat{\sigma}^\dagger \hat{\sigma} \tag{4.158}$$

where ω_0 is the transition frequency defined as $\omega_0 \equiv \omega_e - \omega_g$, and σ and $\hat{\sigma}^\dagger$ are called the *transition* operators for the two-level atom, and are defined as $\hat{\sigma} \equiv |g\rangle\langle e|$ and $\hat{\sigma}^\dagger \equiv |e\rangle\langle g|$.

Electromagnetic (radiation) field Hamiltonian inside the cavity: The electromagnetic field inside the cavity is assumed to be made of a single mode, modeled as a *quantized harmonic oscillator* of frequency ω_α. Its Hamiltonian is ([78] chapter 4.3):

$$\hat{H}_R = \hbar\omega_\alpha \left(\hat{a}^\dagger \hat{a} + \frac{1}{2}\right) \quad \text{with} \quad \left[\hat{a}, \hat{a}^\dagger\right] = 1 \tag{4.159}$$

where $\hat{a}$ and $\hat{a}^\dagger$ are called, respectively, the *annihilation* and *creation* operators for the harmonic oscillator. In the following, we will systematically consider the energy associated to the one-photon state $\hbar\omega_\alpha$ by taking the energy of the vacuum $E_v \equiv \hbar\omega_\alpha/2$ as a reference (this is called *renormalization*). Therefore, $\hat{H}_R$ is recast in the form:

$$\hat{H}_R = \hbar\omega_\alpha \hat{a}^\dagger \hat{a} \tag{4.160}$$

Interaction Hamiltonian: The interaction Hamiltonian which describes the coupling between the atom and the single cavity mode in the *electric dipole approximation*, is given by ([78] chapter 4.8):

$$\hat{H}_I(\mathbf{r}_0) = -\hat{\mathbf{d}} \cdot \hat{\mathbf{E}}_\perp(\mathbf{r}_0) \tag{4.161}$$

In Eq. (4.161), $\hat{\mathbf{d}}$ is the electric dipole operator of the two-level atom written as ([78] chapter 4.9):

$$\hat{\mathbf{d}} = \mathbf{d}\left(\hat{\sigma} + \hat{\sigma}^\dagger\right) \tag{4.162}$$

with $\mathbf{d} \equiv \langle g|\,\hat{\mathbf{d}}\,|e\rangle$ is the electric dipole moment and was assumed to be a real vector in writing Eq. (4.162) without loss of generality.
In Eq. (4.161), $\hat{\mathbf{E}}_\perp(\mathbf{r}_0)$ denotes the tranverse electric field operator of the cavity mode evaluated at the atom position $\mathbf{r}_0$, which can be expressed in terms of the operators $\hat{a}$ and $\hat{a}^\dagger$ according to[6] ([78] chapter 4.7):

$$\hat{\mathbf{E}}_\perp(\mathbf{r}) = \vec{\varepsilon}_\alpha \sqrt{\frac{\hbar\omega_\alpha}{2\epsilon_0 V}} \left(\hat{a}\, e^{i\mathbf{k}_\alpha \cdot \mathbf{r}} + \hat{a}^\dagger e^{-i\mathbf{k}_\alpha \cdot \mathbf{r}}\right) \tag{4.163}$$

[6] In [78] ch. 4.7 or [47] ch. 6.2, the tranverse electric field operator is given by: $\hat{\mathbf{E}}_\perp(\mathbf{r}') = \vec{\varepsilon}_\alpha \sqrt{\frac{\hbar\omega_\alpha}{2\epsilon_0 V}} \left(i\hat{a}\, e^{i\mathbf{k}_\alpha \cdot \mathbf{r}'} - i\hat{a}^\dagger e^{-i\mathbf{k}_\alpha \cdot \mathbf{r}'}\right)$. This expression is completely equivalent to the one given in Eq. (4.163), as they only differ from the choice of origin: $\mathbf{r}' = \mathbf{r} - \frac{\pi}{2}\frac{\mathbf{k}_\alpha}{|\mathbf{k}_\alpha|^2}$.

where V denotes the physical volume of the cavity, $\mathbf{k}_\alpha$ is the wavevector of the mode verifying $|\mathbf{k}_\alpha| = \omega_\alpha/c$, and $\vec{\varepsilon}_\alpha$ is the polarization polarization vector of the mode such that $\vec{\varepsilon}_\alpha \cdot \mathbf{k}_\alpha = 0$.
By taking the origin such that the position of the atom is $\mathbf{r}_0 = 0$, and making use of Eqs. (4.162) and (4.163), the interaction Hamiltonian of Eq. (4.161) simplifies to:

$$\hat{H}_I = \hbar g \left(\hat{\sigma} + \hat{\sigma}^\dagger\right)\left(\hat{a} + \hat{a}^\dagger\right) \tag{4.164}$$

where we defined the coupling constant g as:

$$\hbar g \equiv -(\,\mathbf{d}\cdot\vec{\varepsilon}_\alpha\,)\sqrt{\frac{\hbar\omega_\alpha}{2\epsilon_0 V}} \tag{4.165}$$

g is a real quantity with the dimensions of frequency. Finally, we make the *rotating wave approximation* by dropping the terms "$\hat{\sigma}\hat{a}$" and "$\hat{\sigma}^\dagger\hat{a}^\dagger$" in Eq. (4.164) to get ([78] chapter 4.9):

$$\hat{H}_I = \hbar g \left(\hat{\sigma}^\dagger\hat{a} + \hat{a}^\dagger\hat{\sigma}\right) \tag{4.166}$$

Jaynes-Cummings Hamiltonian: The full Jaynes-Cummings Hamiltonian is the total Hamiltonian obtained within this model $\hat{H}_{\mathrm{JC}} = \hat{H}_A + \hat{H}_R + \hat{H}_I$:

$$\boxed{\hat{H}_{\mathrm{JC}} = \hbar\omega_0\hat{\sigma}^\dagger\hat{\sigma} + \hbar\omega_\alpha\hat{a}^\dagger\hat{a} + \hbar g\left(\hat{\sigma}^\dagger\hat{a} + \hat{a}^\dagger\hat{\sigma}\right)} \tag{4.167}$$

4.B Fermi golden rule

The Fermi golden rule is derived from time-dependent perturbation theory, which is valid (see [34], chapter 5.2):
(i) to describe short-time behavior (when $\alpha(t) \simeq \alpha(0) = 1$)
(ii) if the coupling between the two-level system and the reservoir is *weak* (*i.e.*, the coupling strengths g_j are *small*).

To get the first-order perturbative solution in g_j^2, we set $\alpha(t') = 1$ in the right-hand side of Eq. (4.56):

$$\dot{\alpha}(t) \simeq -\int_0^\infty \mathrm{d}\omega\, R(\mathbf{r}_0, \omega) \int_0^t \mathrm{d}t'\, \mathrm{e}^{\mathrm{i}(\omega_0-\omega)(t-t')} \tag{4.168}$$

One can first calculate the time integral:

$$\begin{aligned} \int_0^t \mathrm{d}t'\, \mathrm{e}^{\mathrm{i}(\omega_0-\omega)(t-t')} &= \frac{\mathrm{e}^{\mathrm{i}(\omega_0-\omega)t} - 1}{\mathrm{i}(\omega_0-\omega)} \\ &= h(\omega_0-\omega, t) \times t \end{aligned} \tag{4.169}$$

to get

$$\dot{\alpha}(t) \simeq -\int_0^\infty \mathrm{d}\omega\, R(\mathbf{r}_0, \omega) \times h(\omega_0-\omega, t) \times t \tag{4.170}$$

where we introduced the function $h(\omega, t)$ defined by:

$$h(\omega, t) \equiv \frac{\mathrm{e}^{\mathrm{i}\omega t} - 1}{\mathrm{i}\omega t} \tag{4.171}$$

We then proceed by formally integrating Eq. (4.169) together with the initial condition $\alpha(0) = 1$ to get

$$\begin{aligned} \alpha(t) &= 1 - \int_0^\infty \mathrm{d}\omega\, R(\mathbf{r}_0, \omega) \int_0^t \mathrm{d}t'\, h(\omega_0-\omega, t') \times t' \\ &= 1 - \int_0^\infty \mathrm{d}\omega\, R(\mathbf{r}_0, \omega)\, \mathrm{i} \left(\frac{1 - h(\omega_0-\omega, t)}{\omega_0-\omega} \right) t \end{aligned} \tag{4.172}$$

To compute the survival probability $P_{\mathrm{surv}}(t)$ defined as

$$\begin{aligned} P_{\mathrm{surv}}(t) &\equiv |\, \langle \mathrm{e}, 0 | \psi(t) \rangle\, |^2 \\ &= |\alpha(t)|^2 \end{aligned} \tag{4.173}$$

we will ignore the second-order contributions (*i.e.*, the term $\propto \left[\sum_j |g_j|^2\right]^2$) because we already neglected contributions of this order in obtaining Eq. (4.168) for $\alpha(t)$. Then the

first order perturbative solution for the probability $P_{\text{surv}}(t)$ is:

$$\begin{aligned} P_{\text{surv}}(t) &= |\alpha(t)|^2 \\ &\simeq 1 - 2 \times \text{Re}\left\{ \int_0^\infty \mathrm{d}\omega\, R(\mathbf{r}_0, \omega)\, \mathrm{i} \left(\frac{1 - h(\omega_0 - \omega, t)}{\omega_0 - \omega} \right) t \right\} \\ &= 1 - 2 \times \int_0^\infty \mathrm{d}\omega\, R(\mathbf{r}_0, \omega) \times \text{Re}\left\{ \mathrm{i} \times \frac{1 - h(\omega_0 - \omega, t)}{\omega_0 - \omega} \right\} \times t \\ &= 1 - 2 \times \int_0^\infty \mathrm{d}\omega\, R(\mathbf{r}_0, \omega) \times \text{Im}\left\{ \frac{h(\omega_0 - \omega, t)}{\omega_0 - \omega} \right\} \times t \end{aligned} \tag{4.174}$$

Moreover, one can easily show that

$$\text{Im}\left\{ \frac{h(\omega_0 - \omega, t)}{\omega_0 - \omega} \right\} = \frac{1}{2}\, t\, \text{sinc}^2\left(\frac{(\omega_0 - \omega)t}{2} \right) \tag{4.175}$$

with $\text{sinc}(x) \equiv \sin(x)/x$. Thus,

$$P_{\text{surv}}(t) = 1 - \int_0^\infty \mathrm{d}\omega\, R(\mathbf{r}_0, \omega) \times t\, \text{sinc}^2\left(\frac{(\omega_0 - \omega_\text{j})t}{2} \right) \times t \tag{4.176}$$

Finally, Eq. (4.176) can be recast in the form

$$\boxed{P_{\text{surv}}(t) = 1 - 2\pi \int_0^\infty \mathrm{d}\omega\, R(\mathbf{r}_0, \omega)\, F_t(\omega - \omega_0) \times t} \tag{4.177}$$

where

$$\boxed{R(\mathbf{r}_0, \omega) \equiv \sum_\text{j} |g_\text{j}(\mathbf{r}_0)|^2\, \delta(\omega - \omega_\text{j})} \qquad \text{Unit:} \quad [R(\omega)] = \text{s}^{-1} \tag{4.178}$$

and

$$\boxed{F_t(\omega - \omega_0) \equiv \frac{t}{2\pi} \text{sinc}^2\left(\frac{(\omega - \omega_0)\, t}{2} \right)} \qquad \text{Unit:} \quad [F_t(\omega - \omega_0)] = \text{s} \tag{4.179}$$

The *Fermi golden rule* is then obtained by noting that for $t \gg 1/\Delta\omega$ where $\Delta\omega$ is the width of the reservoir which determines the effective range of integration (but t sufficiently small for the perturbative solution to hold):

$$F_t(\omega - \omega_0) \to \delta(\omega - \omega_0) \tag{4.180}$$

and one therefore gets:

$$\boxed{P_{\text{surv}}(t) = 1 - \gamma \times t} \tag{4.181}$$

where γ is the decay rate given by the Fermi golden rule:

$$\boxed{\gamma \equiv 2\pi R(\mathbf{r}_0, \omega_0)} \tag{4.182}$$

4.C Discrete model

We recall here the discrete model from Refs. [50] and [51] Appendix A. In this model, one considers N states j with a "door" distribution centered on the atomic frequency ω_0 and of variable bandwidth γ_α. One can then write Eqs. (4.51) and (4.52) in a matrix form:

$$i\hbar\frac{\partial}{\partial t}\begin{pmatrix}\alpha(t)\\ \beta_1(t)\\ \vdots\\ \beta_N(t)\end{pmatrix} = \hbar\underbrace{\begin{pmatrix}\omega_0 & g_1^*(\mathbf{r}_0) & \cdots & g_N^*(\mathbf{r}_0)\\ g_1(\mathbf{r}_0) & \omega_1 & & \\ \vdots & & \ddots & 0\\ g_N(\mathbf{r}_0) & 0 & & \omega_N\end{pmatrix}}_{M}\cdot\begin{pmatrix}\alpha(t)\\ \beta_1(t)\\ \vdots\\ \beta_N(t)\end{pmatrix}, \tag{4.183}$$

Moreover, one assumes equal and real coupling constants: $g_j(\mathbf{r}_0)\equiv g$ for all modes j.

The square matrix M can be diagonalised using *Mathematica*. The program gives back the eigenvalues κ_n and eigenvectors $|\kappa_n\rangle$ of M, that can be used to solve for $\alpha(t)$ and $\beta_j(t)$ using the general expression of their solution

$$\begin{pmatrix}\alpha(t)\\ \beta_1(t)\\ \vdots\\ \beta_N(t)\end{pmatrix} = \sum_{n=1}^{N+1} c_n|\kappa_n\rangle e^{-i\kappa_n t}. \tag{4.184}$$

where the c_n are given by the initial conditions:

$$\alpha(t=0)=1 \tag{4.185}$$

$$\beta_j(t=0)=0 \tag{4.186}$$

In Figs. 4.3 and 4.4, we plot the survival probability $P_{\text{surv}}(t)=|\alpha(t)|^2$ obtained with this numerical method when the continuum bandwidth γ_α varies. As the value of the bandwidth decreases, one can see the transition from the weak (Fig. 4.3) to the strong (Fig. 4.4) coupling regime, where, respectively, $P_{\text{surv}}(t)$ decays monotically, and $P_{\text{surv}}(t)$ undergoes oscillations.

Note that the large "revival" peaks in the first two plots are an artefact peculiar to the discretization [51]. It is a manifestation of partial Poincaré recurrence due to the fact that when the Hilbert space of the quantum system is of finite dimension, the Poincaré recurrence time is finite (and its value is the smallest common multiple of all the eigenfrequencies of the Hamiltonian in Eq. (4.183)).

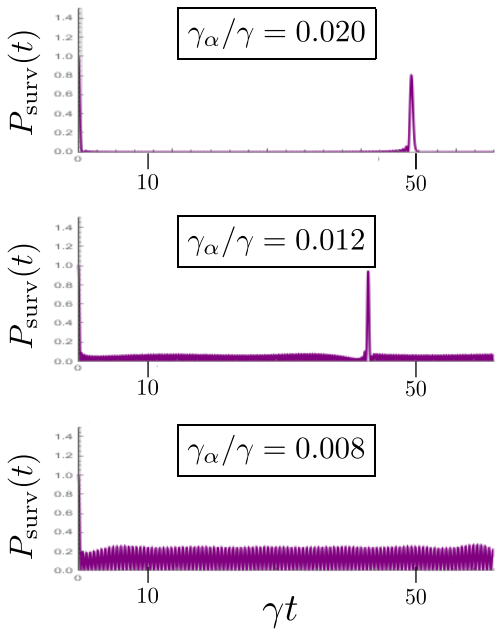

Figure 4.3 – Survival probability $P_{\rm surv}(t) = |\alpha(t)|^2$ for different continuum bandwidths γ_α: 0.020γ, 0.012γ and 0.008γ, where γ is the Fermi golden rule decay rate given by Eq. (4.61). For this discrete model, it reads $\gamma = 2\pi g^2 \rho(\omega_0)$ where the density of state of the discrete continuum considered here is calculated by $\rho(\omega_0) = N/\gamma_\alpha$.

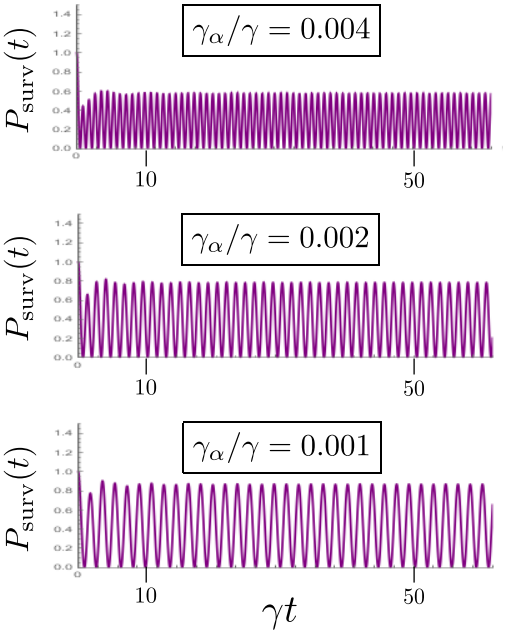

Figure 4.4 – Survival probability $P_{\rm surv}(t) = |\alpha(t)|^2$ for different continuum bandwidths γ_α: 0.004γ, 0.002γ and 0.001γ.

4.D Calculation of the kernels

Lorentzian kernel

We start from the expression [in Eq. (4.103)]

$$\begin{aligned} K^{\text{Lorentz}}(t-t') &\equiv \int_{-\infty}^{+\infty} \mathrm{d}\omega\, |g_\alpha(\mathbf{r}_0,\omega)|^2 \rho_\alpha^{\text{L}}(\omega) \mathrm{e}^{\mathrm{i}(\omega_0-\omega)(t-t')} \\ &\simeq |g_\alpha(\mathbf{r}_0,\omega_0)|^2 \int_{-\infty}^{+\infty} \mathrm{d}\omega\, \frac{1}{\pi} \frac{\gamma_\alpha/2}{(\omega_\alpha-\omega)^2+(\gamma_\alpha/2)^2} \mathrm{e}^{\mathrm{i}(\omega_0-\omega)(t-t')} \end{aligned} \tag{4.187}$$

and we rewrite it as:

$$K^{\text{Lorentz}}(t-t') = \frac{2}{\pi\gamma_\alpha} |g_\alpha(\mathbf{r}_0,\omega_0)|^2 \int_{-\infty}^{+\infty} \mathrm{d}\omega\, \frac{1}{1+\left(\frac{\omega_\alpha-\omega}{\gamma_\alpha/2}\right)^2} \mathrm{e}^{\mathrm{i}(\omega_0-\omega)(t-t')} \tag{4.188}$$

and we proceed by doing the change of variable $X = (\omega-\omega_\alpha)/(\gamma_\alpha/2)$, which gives:

$$\begin{aligned} K^{\text{Lorentz}}(t-t') &= \frac{1}{\pi} |g_\alpha(\mathbf{r}_0,\omega_0)|^2 \int_{-\infty}^{+\infty} \mathrm{d}X\, \frac{1}{1+X^2} \mathrm{e}^{\mathrm{i}\left(\omega_0-\omega_\alpha-\frac{\gamma_\alpha}{2}X\right)(t-t')} \\ &= \frac{1}{\pi} |g_\alpha(\mathbf{r}_0,\omega_0)|^2 \mathrm{e}^{\mathrm{i}(\omega_0-\omega_\alpha)(t-t')} \int_{-\infty}^{+\infty} \mathrm{d}X\, \frac{1}{1+X^2} \mathrm{e}^{-\mathrm{i}\frac{\gamma_\alpha}{2}(t-t')X} \end{aligned} \tag{4.189}$$

The Fourier transform gives:

$$\int_{-\infty}^{+\infty} \mathrm{d}X\, \frac{1}{1+X^2} \mathrm{e}^{-\mathrm{i}\xi X} = \pi \mathrm{e}^{-|\xi|} \tag{4.190}$$

and therefore we get:

$$\boxed{K^{\text{Lorentz}}(t-t') = |g_\alpha(\mathbf{r}_0,\omega_0)|^2 \mathrm{e}^{\mathrm{i}(\omega_0-\omega_\alpha)(t-t')} \mathrm{e}^{-\frac{\gamma_\alpha}{2}|t-t'|}} \tag{4.191}$$

Non-Lorentzian kernel

We start from the expression [in Eq. (4.103)]:

$$\begin{aligned} K^{\text{non-Lorentz}}(t-t') &= \int_{-\infty}^{+\infty} \mathrm{d}\omega\, \frac{\mathrm{Im}(1/V_\alpha)}{\mathrm{Re}(1/V_\alpha)} |g_\alpha(\mathbf{r}_0,\omega)|^2 \rho_\alpha^{\text{NL}}(\omega) \mathrm{e}^{\mathrm{i}(\omega_0-\omega)(t-t')} \\ &\simeq \frac{\mathrm{Im}(1/V_\alpha)}{\mathrm{Re}(1/V_\alpha)} |g_\alpha(\mathbf{r}_0,\omega_0)|^2 \int_{-\infty}^{+\infty} \mathrm{d}\omega\, \frac{\omega_\alpha-\omega}{\gamma_\alpha/2} \frac{1}{\pi} \frac{\gamma_\alpha/2}{(\omega_\alpha-\omega)^2+(\gamma_\alpha/2)^2} \mathrm{e}^{\mathrm{i}(\omega_0-\omega)(t-t')} \end{aligned} \tag{4.192}$$

and as previously we make the same change of variable to get:

$$\begin{aligned} K^{\text{non-Lorentz}}(t-t') &= -\frac{1}{\pi} \frac{\mathrm{Im}(1/V_\alpha)}{\mathrm{Re}(1/V_\alpha)} |g_\alpha(\mathbf{r}_0,\omega_0)|^2 \int_{-\infty}^{+\infty} \mathrm{d}X\, \frac{X}{1+X^2} \mathrm{e}^{\mathrm{i}\left(\omega_0-\omega_\alpha-\frac{\gamma_\alpha}{2}X\right)(t-t')} \\ &= -\frac{1}{\pi} \frac{\mathrm{Im}(1/V_\alpha)}{\mathrm{Re}(1/V_\alpha)} |g_\alpha(\mathbf{r}_0,\omega_0)|^2 \mathrm{e}^{\mathrm{i}(\omega_0-\omega_\alpha)(t-t')} \int_{-\infty}^{+\infty} \mathrm{d}X\, \frac{X}{1+X^2} \mathrm{e}^{-\mathrm{i}\frac{\gamma_\alpha}{2}(t-t')X} \end{aligned} \tag{4.193}$$

We know use the property of the Fourier transform:

$$\int_{-\infty}^{+\infty} \mathrm{d}X\, X f(X) \mathrm{e}^{-\mathrm{i}\xi X} = \mathrm{i}\hat{f}'(\xi) \tag{4.194}$$

with

$$f(X) = \frac{1}{1+X^2} \Rightarrow \hat{f}(\xi) = \pi \mathrm{e}^{-|\xi|} \Rightarrow \hat{f}'(\xi) = -\pi \mathrm{e}^{-|\xi|} \tag{4.195}$$

then one has

$$\boxed{K^{\text{non-Lorentz}}(t-t') = \mathrm{i}\frac{\mathrm{Im}(1/V_\alpha)}{\mathrm{Re}(1/V_\alpha)} |g_\alpha(\mathbf{r}_0, \omega_0)|^2 \mathrm{e}^{\mathrm{i}(\omega_0-\omega_\alpha)(t-t')} \mathrm{e}^{-\frac{\gamma_\alpha}{2}|t-t'|}} \tag{4.196}$$

4.E QNM expressions of the decay rate and Lamb shift

There is one situation in which the Eq. (4.110) can be solved analytically: in the weak-coupling regime, where the Markov approximations apply. Eq. (4.110) shows that the value of $\dot{\alpha}(t)$ depends, in general, on the values of $\alpha(t)$ at *all earlier times*; the *Markov approximation* consists in replacing $\alpha(t)$ in the integrand by its value at $t' = t$ (see [34] chapter 5.3); this converts the previous integro-differential equation into a differential equation for $\alpha(t)$:

$$\dot{\alpha}(t) = -\frac{\gamma_0}{2}\alpha(t) - \sum_\alpha |g_\alpha(\mathbf{r}_0,\omega_0)|^2 \left[1 + \mathrm{i}\frac{\mathrm{Im}(1/V_\alpha)}{\mathrm{Re}(1/V_\alpha)}\right]\alpha(t) \underbrace{\int_0^t \mathrm{d}t'\, \mathrm{e}^{[\mathrm{i}(\omega_0-\omega_\alpha)-\frac{\gamma_\alpha}{2}](t-t')}}_{I} \tag{4.197}$$

The integral I is reexpressed by doing the change of variable $\tau = t - t'$:

$$I = \int_0^t \mathrm{d}\tau\, \mathrm{e}^{[\mathrm{i}(\omega_0-\omega_\alpha)-\frac{\gamma_\alpha}{2}]\tau} \tag{4.198}$$

In order to evaluate the integral I, we make the *second Markov approximation*, which consists in allowing the upper limit of the integral to tend to infinity (see [34] chapter 5.3). Then, I is calculated straightforwardly:

$$I = \int_0^{+\infty} \mathrm{d}\tau\, \mathrm{e}^{[\mathrm{i}(\omega_0-\omega_\alpha)-\frac{\gamma_\alpha}{2}]\tau} \tag{4.199}$$

$$= \frac{\mathrm{i}}{(\omega_0-\omega_\alpha)+\mathrm{i}\frac{\gamma_\alpha}{2}} \tag{4.200}$$

Then the differential Eq. (4.197) becomes:

$$\dot{\alpha}(t) = -\frac{\gamma_0}{2}\alpha(t) - \sum_\alpha |g_\alpha(\mathbf{r}_0,\omega_0)|^2 \frac{\mathrm{i}}{(\omega_0-\omega_\alpha)+\mathrm{i}\frac{\gamma_\alpha}{2}}\left[1 + \mathrm{i}\frac{\mathrm{Im}(1/V_\alpha)}{\mathrm{Re}(1/V_\alpha)}\right]\alpha(t) \tag{4.201}$$

whose solution is of the form:

$$\alpha(t) = \exp\left(-\left[\frac{\gamma}{2} + \mathrm{i}\Delta\omega\right]t\right) \tag{4.202}$$

This means that the probability to stay in the excited state $P_{\mathrm{surv}}(t) = |\alpha(t)|^2$ decays exponentially at a γ, called the *decay rate*, and the amplitude oscillates at a frequency shifted by $\Delta\omega$, called the *Lamb shift*. One gets by identifying γ and $\Delta\omega$ with the real and imaginary terms in Eq. (4.201), respectively (after multiplying by the complex conjugate to have the denominator in a real form):

$$\gamma = \gamma_0 + \sum_\alpha \underbrace{|g_\alpha(\mathbf{r}_0,\omega_0)|^2 \frac{\gamma_\alpha}{(\omega_0-\omega_\alpha)^2 + \left(\frac{\gamma_\alpha}{2}\right)^2}}_{\gamma_\alpha^H} - \sum_\alpha 2 \underbrace{|g_\alpha(\mathbf{r}_0,\omega_0)|^2 \frac{\omega_0-\omega_\alpha}{(\omega_0-\omega_\alpha)^2 + \left(\frac{\gamma_\alpha}{2}\right)^2}}_{\Delta\omega_\alpha^H} \frac{\mathrm{Im}(1/V_\alpha)}{\mathrm{Re}(1/V_\alpha)} \tag{4.203}$$

$$\Delta\omega = \sum_\alpha \underbrace{|g_\alpha(\mathbf{r}_0,\omega_0)|^2 \frac{\omega_0-\omega_\alpha}{(\omega_0-\omega_\alpha)^2+\left(\frac{\gamma_\alpha}{2}\right)^2}}_{\Delta\omega_\alpha^H} + \sum_\alpha \frac{1}{2}\underbrace{|g_\alpha(\mathbf{r}_0,\omega_0)|^2 \frac{\gamma_\alpha}{(\omega_0-\omega_\alpha)^2+\left(\frac{\gamma_\alpha}{2}\right)^2}}_{\gamma_\alpha^H} \frac{\mathrm{Im}(1/V_\alpha)}{\mathrm{Re}(1/V_\alpha)} \tag{4.204}$$

By normalizing these quantities by the free space decay rate γ_0 given by Eq. (4.106) and using the expression of $g_\alpha(\mathbf{r}_0,\omega_0)$ given by Eq. (4.100), one gets:

$$\boxed{\frac{\gamma}{\gamma_0} = 1 + \sum_\alpha \left\{ \frac{\gamma_\alpha^H}{\gamma_0} - 2\frac{\Delta\omega_\alpha^H}{\gamma_0}\frac{\mathrm{Im}(1/V_\alpha)}{\mathrm{Re}(1/V_\alpha)} \right\}} \tag{4.205}$$

$$\boxed{\frac{\Delta\omega}{\gamma_0} = \sum_\alpha \left\{ \frac{\Delta\omega_\alpha^H}{\gamma_0} + \frac{1}{2}\frac{\gamma_\alpha^H}{\gamma_0}\frac{\mathrm{Im}(1/V_\alpha)}{\mathrm{Re}(1/V_\alpha)} \right\}} \tag{4.206}$$

with

$$\boxed{\frac{\gamma_\alpha^H}{\gamma_0} = F_\alpha \left(\frac{\omega_\alpha}{\omega_0}\right)^2 \frac{(\gamma_\alpha/2)^2}{(\omega_0-\omega_\alpha)^2+\left(\frac{\gamma_\alpha}{2}\right)^2}} \tag{4.207}$$

$$\boxed{\frac{\Delta\omega_\alpha^H}{\gamma_0} = F_\alpha \left(\frac{\omega_\alpha}{\omega_0}\right)^2 \frac{\gamma_\alpha}{4} \frac{\omega_0-\omega_\alpha}{(\omega_0-\omega_\alpha)^2+\left(\frac{\gamma_\alpha}{2}\right)^2}} \tag{4.208}$$

where we defined the generalized Purcell factor as:

$$\boxed{F_\alpha \equiv \frac{6\pi c^3}{\omega_\alpha^3} Q_\alpha \mathrm{Re}\left(1/V_\alpha(\mathbf{r}_0)\right)} \tag{4.209}$$

and the quality factor Q_α:

$$Q_\alpha \equiv \frac{\omega_\alpha}{\gamma_\alpha} \tag{4.210}$$

These expressions are exactly the ones derived in chapter 2, where we used the complex frequency notation $\omega_\alpha \equiv \omega'_\alpha + \mathrm{i}\omega''_\alpha$, where one has the correspondance $\omega'_\alpha \longleftrightarrow \omega_\alpha$ and $\omega''_\alpha \longleftrightarrow -\gamma_\alpha/2$.

4.F Second-order differential equation verified by $\alpha(t)$

We start from Eq. (4.115):

$$\begin{aligned}\dot{\alpha}(t) &= -\frac{\gamma_0}{2}\alpha(t) - g^2\int_0^t \mathrm{d}t'\,\alpha(t')\mathrm{e}^{[\mathrm{i}(\omega_0-\omega_\alpha)-\frac{\gamma_\alpha}{2}](t-t')} \\ &= -\frac{\gamma_0}{2}\alpha(t) - g^2\mathrm{e}^{[\mathrm{i}(\omega_0-\omega_\alpha)-\frac{\gamma_\alpha}{2}]t}\int_0^t \mathrm{d}t'\,\alpha(t')\mathrm{e}^{-[\mathrm{i}(\omega_0-\omega_\alpha)-\frac{\gamma_\alpha}{2}]t'}\end{aligned} \tag{4.211}$$

By calling

$$\begin{cases} I(t) = \int_0^t \mathrm{d}t'\,\alpha(t')\mathrm{e}^{-[\mathrm{i}(\omega_0-\omega_\alpha)-\frac{\gamma_\alpha}{2}]t'} \\ I'(t) = \alpha(t)\mathrm{e}^{-[\mathrm{i}(\omega_0-\omega_\alpha)-\frac{\gamma_\alpha}{2}]t} \end{cases} \tag{4.212}$$

we get by differentiating the previous equation:

$$\begin{aligned}\ddot{\alpha}(t) &= -\frac{\gamma_0}{2}\dot{\alpha}(t) - g^2[\mathrm{i}(\omega_0-\omega_\alpha)-\frac{\gamma_\alpha}{2}]\mathrm{e}^{[\mathrm{i}(\omega_0-\omega_\alpha)-\frac{\gamma_\alpha}{2}]t}\times I(t) - g^2\underbrace{\mathrm{e}^{[\mathrm{i}(\omega_0-\omega_\alpha)-\frac{\gamma_\alpha}{2}]t}\times I'(t)}_{\alpha(t)} \\ &= -\frac{\gamma_0}{2}\dot{\alpha}(t) - g^2[\mathrm{i}(\omega_0-\omega_\alpha)-\frac{\gamma_\alpha}{2}]\mathrm{e}^{[\mathrm{i}(\omega_0-\omega_\alpha)-\frac{\gamma_\alpha}{2}]t}\times I(t) - g^2\alpha(t)\end{aligned} \tag{4.213}$$

Moreover, by noticing from Eq. (4.211) that

$$-g^2\mathrm{e}^{[\mathrm{i}(\omega_0-\omega_\alpha)-\frac{\gamma_\alpha}{2}]t}\times I(t) = \dot{\alpha}(t) + \frac{\gamma_0}{2}\alpha(t) \tag{4.214}$$

one gets

$$\ddot{\alpha}(t) = -\frac{\gamma_0}{2}\dot{\alpha}(t) + [\mathrm{i}(\omega_0-\omega_\alpha)-\frac{\gamma_\alpha}{2}][\dot{\alpha}(t)+\frac{\gamma_0}{2}\alpha(t)] - g^2\alpha(t) \tag{4.215}$$

which is rearranged into the Eq. (4.116) in the main text:

$$\boxed{\ddot{\alpha}(t) - [\mathrm{i}(\omega_0-\omega_\alpha) - \frac{\gamma_0}{2} - \frac{\gamma_\alpha}{2}]\dot{\alpha}(t) + [g^2 - \mathrm{i}\frac{\gamma_0}{2}(\omega_0-\omega_\alpha) + \frac{\gamma_0}{2}\frac{\gamma_\alpha}{2}]\alpha(t) = 0} \tag{4.216}$$

Bibliography

[1] S. Haroche and D. Kleppner, Physics Today **42**, 24 (1989).

[2] Y. Kaluzny, P. Goy, M. Gross, J. M. Raimond, and S. Haroche, Physical Review Letters **51**, 1175 (1983).

[3] M. Brune, J. Raimond, P. Goy, L. Davidovich, and S. Haroche, Physical Review Letters **59**, 1899 (1987).

[4] D. Meschede, H. Walther, and G. Müller, Physical Review Letters **54**, 551 (1985).

[5] G. Rempe, H. Walther, and N. Klein, Physical Review Letters **58**, 353 (1987).

[6] M. Raizen, R. Thompson, R. Brecha, H. Kimble, and H. Carmichael, Physical Review Letters **63**, 240 (1989).

[7] Y. Zhu, D. J. Gauthier, S. Morin, Q. Wu, H. Carmichael, and T. Mossberg, Physical Review Letters **64**, 2499 (1990).

[8] G. Rempe, R. Thompson, R. Brecha, W. Lee, and H. Kimble, Physical Review Letters **67**, 1727 (1991).

[9] R. Thompson, G. Rempe, and H. Kimble, Physical Review Letters **68**, 1132 (1992).

[10] C. J. Hood, M. S. Chapman, T. W. Lynn, and H. J. Kimble, Physical Review Letters **80**, 4157 (1998).

[11] J. P. Reithmaier, G. Sęk, A. Löffler, C. Hofmann, S. Kuhn, S. Reitzenstein, L. Keldysh, V. Kulakovskii, T. Reinecke, and A. Forchel, Nature **432**, 197 (2004).

[12] T. Yoshie, A. Scherer, J. Hendrickson, G. Khitrova, H. Gibbs, G. Rupper, C. Ell, O. Shchekin, and D. Deppe, Nature **432**, 200 (2004).

[13] P. Lodahl, S. Mahmoodian, and S. Stobbe, Reviews of Modern Physics **87**, 347 (2015).

[14] J. Bellessa, C. Bonnand, J. Plenet, and J. Mugnier, Physical Review Letters **93**, 036404 (2004).

[15] J. Bellessa, C. Symonds, K. Vynck, A. Lemaitre, A. Brioude, L. Beaur, J. C. Plenet, P. Viste, D. Felbacq, E. Cambril, and P. Valvin, Physical Review B **80**, 033303 (2009).

[16] J. Dintinger, S. Klein, F. Bustos, W. L. Barnes, and T. W. Ebbesen, Physical Review B **71**, 035424 (2005).

[17] J. Dintinger, S. Klein, and T. W. Ebbesen, Advanced Materials **18**, 1267 (2006).

[18] P. Törmä and W. L. Barnes, Reports on Progress in Physics **78**, 013901 (2014).

[19] I. Pockrand, A. Brillante, and D. Möbius, The Journal of Chemical Physics **77**, 6289 (1982).

[20] D. G. Baranov, M. Wersall, J. Cuadra, T. J. Antosiewicz, and T. Shegai, ACS Photonics **5**, 24 (2017).

[21] F. Marquier, C. Sauvan, and J.-J. Greffet, ACS Photonics **4**, 2091 (2017).

[22] T. Itoh, Y. S. Yamamoto, H. Tamaru, V. Biju, S.-i. Wakida, and Y. Ozaki, Physical Review B **89**, 195436 (2014).

[23] T. Hartsfield, W.-S. Chang, S.-C. Yang, T. Ma, J. Shi, L. Sun, G. Shvets, S. Link, and X. Li, Proceedings of the National Academy of Sciences **112**, 12288 (2015).

[24] K. Santhosh, O. Bitton, L. Chuntonov, and G. Haran, Nature Communications **7**, 11823 (2016).

[25] R. Chikkaraddy, B. de Nijs, F. Benz, S. J. Barrow, O. A. Scherman, E. Rosta, A. Demetriadou, P. Fox, O. Hess, and J. J. Baumberg, Nature **535**, 127 (2016).

[26] R. Liu, Z.-K. Zhou, Y.-C. Yu, T. Zhang, H. Wang, G. Liu, Y. Wei, H. Chen, and X.-H. Wang, Physical Review Letters **118**, 237401 (2017).

[27] A. Ridolfo, M. Leib, S. Savasta, and M. J. Hartmann, Physical Review Letters **109**, 193602 (2012).

[28] A. Ridolfo, S. Savasta, and M. J. Hartmann, Physical Review Letters **110**, 163601 (2013).

[29] R. Stassi, A. Ridolfo, O. Di Stefano, M. J. Hartmann, and S. Savasta, Physical Review Letters **110**, 243601 (2013).

[30] S. De Liberato, Physical Review Letters **112**, 016401 (2014).

[31] A. Cacciola, O. Di Stefano, R. Stassi, R. Saija, and S. Savasta, ACS Nano **8**, 11483 (2014).

[32] F. Todisco, M. De Giorgi, M. Esposito, L. De Marco, A. Zizzari, M. Bianco, L. Dominici, D. Ballarini, V. Arima, G. Gigli, *et al.*, ACS Photonics **5**, 143 (2017).

[33] E. T. Jaynes and F. W. Cummings, Proceedings of the IEEE **51**, 89 (1963).

[34] S. M. Barnett and P. M. Radmore, *Methods in theoretical quantum optics*, Vol. 15 (Oxford University Press, 2002).

[35] S. M. Dutra, *Cavity quantum electrodynamics: the strange theory of light in a box* (John Wiley & Sons, 2005).

[36] R. P. Feynman and F. Vernon Jr, Annals of Physics **281**, 547 (2000).

[37] P. Leung, S. Liu, and K. Young, Physical Review A **49**, 3057 (1994).

[38] H. Varguet, B. Rousseaux, D. Dzsotjan, H. Jauslin, S. Guérin, and G. C. des Francs, Optics Letters **41**, 4480 (2016).

[39] H. Varguet, B. Rousseaux, D. Dzsotjan, H. R. Jauslin, S. Guérin, and G. C. des Francs, Journal of Physics B: Atomic, Molecular and Optical Physics **52**, 055404 (2019).

[40] G. Gamow, Zeitschrift für Physik **51**, 204 (1928).

[41] K. Friedrichs, Communications on Pure and Applied Mathematics **1**, 361 (1948).

[42] V. Debierre, *La fonction d'onde du photon en principe et en pratique*, Ph.D. thesis, Ecole Centrale Marseille (2015).

[43] R. El-Ganainy, K. G. Makris, M. Khajavikhan, Z. H. Musslimani, S. Rotter, and D. N. Christodoulides, Nature Physics **14**, 11 (2018).

[44] E. M. Purcell, Physical Review **69**, 681 (1946).

[45] M. Tavis and F. Cummings, Physics Letters A **25**, 714 (1967).

[46] B. M. Garraway, Philosophical Transactions of the Royal Society A: Mathematical, Physical and Engineering Sciences **369**, 1137 (2011).

[47] G. Grynberg, A. Aspect, and C. Fabre, *Introduction to quantum optics: from the semi-classical approach to quantized light* (Cambridge University Press, 2010).

[48] B. Piraux, R. Bhatt, and P. Knight, Physical Review A **41**, 6296 (1990).

[49] V. Weisskopf and E. Wigner, Zeitschrift für Physik **63**, 54 (1930).

[50] V. Debierre, I. Goessens, E. Brainis, and T. Durt, Physical Review A **92**, 023825 (2015).

[51] B. Kolaric, B. Maes, K. Clays, T. Durt, and Y. Caudano, Advanced Quantum Technologies **1**, 1800001 (2018).

[52] B. Misra and E. Sudarshan, Journal of Mathematical Physics **18**, 756 (1977).

[53] P. Facchi, H. Nakazato, and S. Pascazio, Physical Review Letters **86**, 2699 (2001).

[54] A. Kofman and G. Kurizki, Nature **405**, 546 (2000).

[55] P. Facchi and S. Pascazio, Physics Letters A **241**, 139 (1998).

[56] V. Debierre, T. Durt, A. Nicolet, and F. Zolla, Physics Letters A **379**, 2577 (2015).

[57] A. Crespi, F. V. Pepe, P. Facchi, F. Sciarrino, P. Mataloni, H. Nakazato, S. Pascazio, and R. Osellame, Physical Review Letters **122**, 130401 (2019).

[58] D. Bouchet and R. Carminati, Journal of the Optical Society of America A **36**, 186 (2019).

[59] L. Novotny and B. Hecht, *Principles of nano-optics* (Cambridge University Press, 2012).

[60] H. T. Dung, L. Knöll, and D.-G. Welsch, Physical Review A **62**, 053804 (2000).

[61] G. Khitrova, H. Gibbs, M. Kira, S. W. Koch, and A. Scherer, Nature Physics **2**, 81 (2006).

[62] P. Lalanne, W. Yan, K. Vynck, C. Sauvan, and J.-P. Hugonin, Laser & Photonics Reviews **12**, 1700113 (2018).

[63] T. Gruner and D.-G. Welsch, Physical Review A **53**, 1818 (1996).

[64] H. T. Dung, L. Knöll, and D.-G. Welsch, Physical Review A **57**, 3931 (1998).

[65] S. Scheel, L. Knöll, and D.-G. Welsch, Physical Review A **58**, 700 (1998).

[66] R. Matloob, R. Loudon, S. M. Barnett, and J. Jeffers, Physical Review A **52**, 4823 (1995).

[67] R. Matloob and R. Loudon, Physical Review A **53**, 4567 (1996).

[68] P. Yao, C. Van Vlack, A. Reza, M. Patterson, M. Dignam, and S. Hughes, Physical Review B **80**, 195106 (2009).

[69] B. Rousseaux, D. Dzsotjan, G. C. des Francs, H. Jauslin, C. Couteau, and S. Guérin, Physical Review B **93**, 045422 (2016).

[70] D. Dzsotjan, B. Rousseaux, H. Jauslin, G. C. des Francs, C. Couteau, and S. Guérin, Physical Review A **94**, 023818 (2016).

[71] C. Van Vlack, P. T. Kristensen, and S. Hughes, Physical Review B **85**, 075303 (2012).

[72] A. González-Tudela, P. Huidobro, L. Martín-Moreno, C. Tejedor, and F. García-Vidal, Physical Review Letters **110**, 126801 (2013).

[73] A. Delga, J. Feist, J. Bravo-Abad, and F. Garcia-Vidal, Physical Review Letters **112**, 253601 (2014).

[74] C. Sauvan, J.-P. Hugonin, I. Maksymov, and P. Lalanne, Physical Review Letters **110**, 237401 (2013).

[75] A. F. Koenderink, Optics Letters **35**, 4208 (2010).

[76] P. T. Kristensen, C. Van Vlack, and S. Hughes, Optics Letters **37**, 1649 (2012).

[77] E. Muljarov and W. Langbein, Physical Review B **94**, 235438 (2016).

[78] R. Loudon, *The quantum theory of light* (Oxford University Press, 2000).

Part III

Far-field interactions

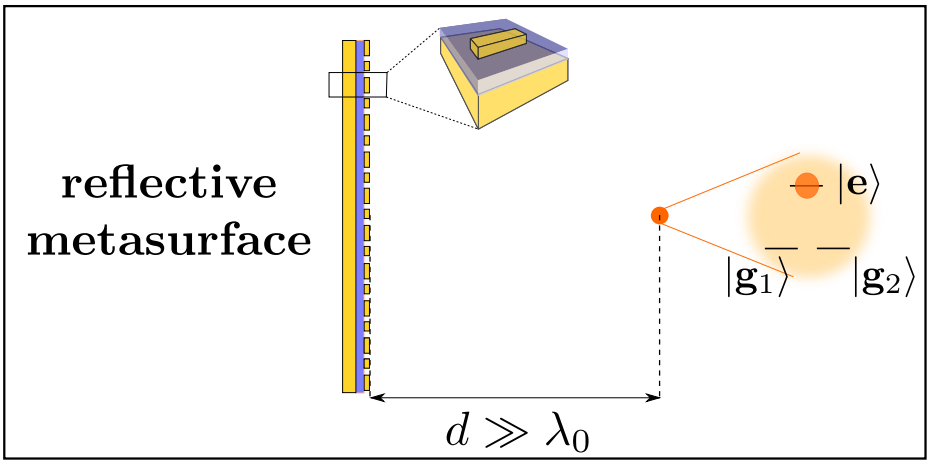

CHAPTER 5

Anisotropic quantum vacuum induced by a metasurface

5.1 Introduction

The control of the spontaneous emission of quantum emitters (QEs) has been investigated principally in confined space by the cavity-quantum electrodynamics (cQED) community [1], whose archetype is a cavity formed by perfect mirrors, and where the notion of "cavity" has been generalized to open resonators in nanophotonics [2]. In such systems, important coupling can be achieved but it however occurs only in the near-field of the photonic nanostructure and vanishes beyond a distance $d \sim \lambda_0$, where λ_0 is the emission wavelength of the QE in vacuum.

A few other optical systems can affect the spontaneous emission of QEs in the far-field ($d \gg \lambda_0$). For instance, by covering half of the QE emission solid angle with a *single spherical mirror*, the vacuum fluctuations can be fully suppressed within a volume λ_0^3 at remote distances, leading to a total inhibition of the decay of a two-level atom [3]. In a classical picture, the field reflected by the spherical mirror can fully interfere with the direct field emitted by the atom: if the atom is located at the focus of the spherical mirror such that $d = n\lambda_0/2$ with n an integer number, there is a complete suppression of the spontaneous emission, whereas if the atom is at the position $d = (n + 1/2)\lambda_0/2$, the spontaneous emission is enhanced by a factor of 2. One can expect such effects as long as the time it takes for the light field to go to the mirror and to be back to the atom is shorter than the atom decay time $1/\gamma_0$ (with γ_0 the decay rate in free space of the two-level atom), that is for distances d smaller than the *photonic coherence length* $d_{\mathrm{cl}} \equiv c/2\gamma_0$ [4, 5]. Such an alteration of the decay rate over many wavelengths was already reported in Ref. [6], where they measured a 1% change in the decay rate of an ion located at 30 cm from a mirror.

Recently, the use of reflecting metasurface acting as a spherical mirror but with a polarization-dependent response has been suggested to induce quantum interferences on a multilevel QE located at remote distances [7, 8]. This new paradigm brings together the quantum optics and the metasurface communities [9, 10], and relies on the fact that reflecting metasurfaces, made of nano-resonators also called meta-atoms, can modify the structure of the vacuum at macroscopic distances. It was predicted that such a metasur-

face with a polarization-dependent response can create an anisotropic quantum vacuum (AQV) [7], leading to quantum interferences in orthogonal levels of a multilevel QE [11]. However, the predicted effects, that is a population transfer between orthogonal states in a V-configuration of 1% [7], and an induced coherence between the two excited states of about 10% [8], only last as long as the atom remains in its excited state, which is a drastic constraint for an experimental confirmation [7, 8].

The present Chapter discusses about spontaneous emission properties of a QE with Λ-scheme, meaning one excited state and two nearly degenerate ground states, in an anisotropic quantum vacuum created by a metasurface. We predict the construction of a coherence between the two ground states, which survives after the photon emission, in contrast with the V-scheme proposed in earlier works [7, 8, 11]. The interest in the ground state coherence arises from its long lifetime, which allows high resolution experiments. Moreover, this coherence could be previously generated only with an external coherent laser field (see [12], chapter 3).

In Section 5.2, we derive the master equation for the Λ-scheme and we show how an anisotropic vacuum can induce coherence between the ground states. In Section 5.3, we propose two designs to realize the anisotropic vacuum using metasurfaces. Finally, in Section 5.4, we assess the value of the coherence predicted in Section 5.2 induced by the metasurfaces presented in Section 5.3, taking into account the finite size of the nano-resonators that compose the metasurfaces.

5.2 Theoretical predictions: long lifetime coherence

5.2.1 Interaction Hamiltonian and Master Equation

We consider a three-level system in a so-called Λ-scheme: one single excited state $|0\rangle$, which can decay into two ground states $|1\rangle$ and $|2\rangle$ *via* two orthogonal dipolar transitions by the emission of circularly polarized photons σ^+ and, respectively, σ^- (see the inset in Fig. 5.1). By orthogonal transitions, it means that the dipole matrix elements $\mathbf{d}_{01}$ and $\mathbf{d}_{02}$ corresponding to these transitions are orthogonal ($\mathbf{d}_{01}\cdot\mathbf{d}_{02}=0$). They are given by: $\mathbf{d}_{01} = +d_{01}\vec{\varepsilon}_+$ and $\mathbf{d}_{02} = -d_{02}\vec{\varepsilon}_-$ where $\vec{\varepsilon}_\pm = (\vec{x}\pm \mathrm{i}\vec{y})/\sqrt{2}$. We use the z-axis as the quantization axis. This scheme appears naturally in NV-centers in diamond, using the states $|E_0\rangle\otimes|\pm 1\rangle$ and $|A_1\rangle$ as the ground states and excited state, respectively [13]. It also can be founded in atoms, using Zeeman manifold with $|F, m=\pm 1\rangle$ for the ground states and $|F, m=0\rangle$ for the excited state [12]. Here, F is a strictly positive integer corresponding to the quantum number of the total angular moment.

The interaction between the atom (at position $\mathbf{r}_0$) and the vacuum is described by the interaction Hamiltonian in the *electric dipole approximation*:

$$\hat{H}_I = -\hat{\mathbf{d}}\cdot\hat{\mathbf{E}}_v(\mathbf{r}_0) \tag{5.1}$$

The electromagnetic field operator $\hat{\mathbf{E}}_v$ can be written as a sum of a complex field $\hat{\mathbf{E}}_v^{(+)}$ and its Hermitian conjugate $\hat{\mathbf{E}}_v^{(-)} = [\hat{\mathbf{E}}_v^{(+)}]^\dagger$: $\hat{\mathbf{E}}_v(\mathbf{r}_0) = \hat{\mathbf{E}}_v^{(+)}(\mathbf{r}_0) + \hat{\mathbf{E}}_v^{(-)}(\mathbf{r}_0)$. In the rotating wave

approximation and using the interaction picture, the interaction Hamiltonian reads:

$$\hat{H}_I(t) = -\left(\mathbf{d}_{01}\left|0\right\rangle\left\langle 1\right| e^{\mathrm{i}\omega_1 t} + \mathbf{d}_{02}\left|0\right\rangle\left\langle 2\right| e^{\mathrm{i}\omega_2 t}\right)\cdot\hat{\mathbf{E}}_v^{(+)}(\mathbf{r}_0,t) - \left(\mathbf{d}_{01}^*\left|1\right\rangle\left\langle 0\right| e^{-\mathrm{i}\omega_1 t} + \mathbf{d}_{02}^*\left|2\right\rangle\left\langle 0\right| e^{-\mathrm{i}\omega_2 t}\right)\cdot\hat{\mathbf{E}}_v^{(-)}(\mathbf{r}_0,t) \quad (5.2)$$

where ω_i is the transition frequency associated with the transition $|i\rangle \leftrightarrow |0\rangle$ $(i=1,2)$.

The total system {atom+environment} is characterized by the density matrix $\rho_T(t)$, which obeys the Schrödinger equation written in the *interaction picture* [14, 15]:

$$\frac{\partial\rho_T(t)}{\partial t} = \frac{1}{\mathrm{i}\hbar}[\hat{H}_I(t),\rho_T(t)] \quad (5.3)$$

with $\hat{H}_I(t)$ given by Eq. (5.2). We want to derive the Master Equation for the density matrix of the atom, denoted $\rho(t)$, obtained by taking the trace over the degrees of freedom of the environment: $\rho(t) = \mathrm{Tr}_e(\rho_T(t))$. By using the *Born and Markov* approximations we obtain, assuming closed-lying states $\omega_1 \simeq \omega_2 \equiv \omega_0$ (see Appendix 5.A for the details of the derivation):

$$\frac{\partial\rho(t)}{\partial t} = -\left[\mathrm{i}\omega_0 + \frac{\gamma_1}{2} + \frac{\gamma_2}{2}\right]\left|0\right\rangle\left\langle 0\right|\rho(t) + \rho_{00}(t)\left[\frac{\gamma_1}{2}\left|1\right\rangle\left\langle 1\right| + \frac{\gamma_2}{2}\left|2\right\rangle\left\langle 2\right| + \frac{\kappa_{21}}{2}\left|2\right\rangle\left\langle 1\right| + \frac{\kappa_{12}}{2}\left|1\right\rangle\left\langle 2\right|\right] + \mathrm{H.c.} \quad (5.4)$$

where $\rho_{00}(t) \equiv \langle 0|\rho(t)|0\rangle$. In Eq. (5.4), we have introduced the definitions of the coefficients:

$$\gamma_i \equiv \frac{1}{\hbar^2}\mathbf{d}_{0i}^*\cdot\hat{\mathbf{C}}(\mathbf{r}_0,\mathbf{r}_0,\omega_0)\cdot\mathbf{d}_{0i} \quad (5.5)$$

and

$$\kappa_{ij} \equiv \frac{1}{\hbar^2}\mathbf{d}_{0i}^*\cdot\hat{\mathbf{C}}(\mathbf{r}_0,\mathbf{r}_0,\omega_0)\cdot\mathbf{d}_{0j} \quad (5.6)$$

defined in terms of the *correlation tensor* $\hat{\mathbf{C}}$ that reads:

$$\hat{\mathbf{C}}(\mathbf{r},\mathbf{r}',\omega) \equiv \int_{-\infty}^{+\infty}\mathrm{d}\tau\,\left\langle\hat{\mathbf{E}}_v^{(+)}(\mathbf{r},\tau)\hat{\mathbf{E}}_v^{(-)}(\mathbf{r}',0)\right\rangle e^{\mathrm{i}\omega\tau} \quad (5.7)$$

where the braket indicates an ensemble average:

$$\left\langle\hat{\mathbf{E}}_v^{(+)}(\mathbf{r},\tau)\hat{\mathbf{E}}_v^{(-)}(\mathbf{r}',0)\right\rangle \equiv \mathrm{Tr}_e\left(\rho_e(0)\hat{\mathbf{E}}_v^{(+)}(\mathbf{r},\tau)\hat{\mathbf{E}}_v^{(-)}(\mathbf{r}',0)\right) \quad (5.8)$$

In Eq. (5.4), we have ignore the relaxation of the ground state coherence ρ_{12} which is suppose to be much smaller than the the coherences involving the excited state.

5.2.2 Solution of the Master Equation

From the Master Equation, given in Eq. (5.4), we obtain the following equations for the atomic populations $\rho_{ii}(t)$ and atomic coherences $\rho_{ij}(t)$ with $j \neq i$

$$\dot{\rho}_{ii}(t) = \gamma_i\rho_{00}(t) \quad \text{for} \quad i=1,2 \quad (5.9)$$

$$\dot{\rho}_{00}(t) = -(\gamma_1+\gamma_2)\rho_{00}(t) \quad (5.10)$$

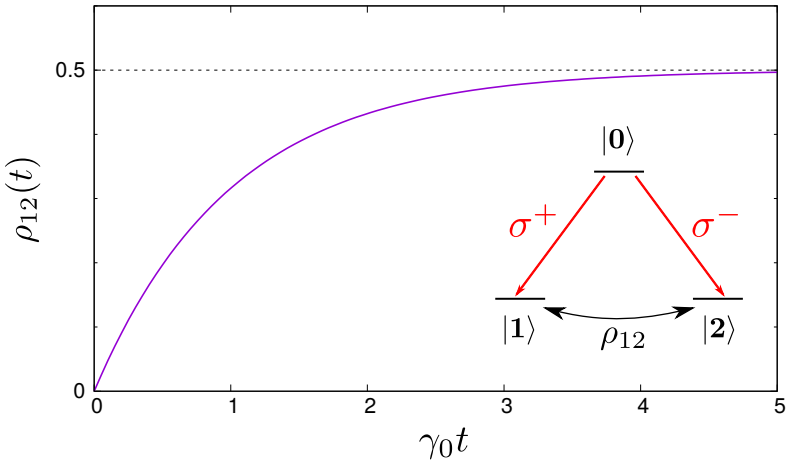

Figure 5.1 – Inset: three-level quantum emitter with a Λ configuration. The upper level $|0\rangle$ can decay via two transitions: either to the state $|1\rangle$ (transition energy $\hbar\omega_1$) with the emission of a right circularly polarized photon denoted σ^+ or to the state $|2\rangle$ (transition energy $\hbar\omega_2$) with the emission of a left circularly polarized photon denoted σ^-. Main figure: coherence ρ_{12} from Eq. (5.18) as a function of the (normalized) time $\gamma_0 t$, in the case $\kappa_{12} = \gamma_1 = \gamma_2 = \gamma_0/2$ with γ_0 the decay rate of the transitions in free space (considering same dipole moments $d_{01} = d_{02}$).

$$\dot{\rho}_{i0}(t) = -\left(\frac{\gamma_1+\gamma_2}{2} - i\omega_0\right)\rho_{i0}(t) \quad \text{for} \quad i = 1,2 \tag{5.11}$$

$$\dot{\rho}_{12}(t) = \kappa_{12}\rho_{00}(t) \tag{5.12}$$

where we used the fact that $\kappa_{21}^* = \kappa_{12}$. Note that these equations are also supplemented by their conjugates.

The atom is initially prepared in the excited state with the following initial conditions (at $t = 0$): $\rho_{00}(0) = 1$, $\rho_{11}(0) = \rho_{22}(0) = 0$ and $\rho_{ij}(0) = 0$ for $j \neq i$. Solving Eqs. (5.9) and (5.10) with the initial conditions above is straightforward. With the initial condition $\rho_{00}(0) = 1$, Eq. (5.10) gives

$$\rho_{00}(t) = e^{-(\gamma_1+\gamma_2)t} \Rightarrow \rho_{00}(\infty) = 0 \tag{5.13}$$

Substituting it in Eqs. (5.9) and carrying out the integration with the initial conditions $\rho_{11}(0) = \rho_{22}(0) = 0$ gives

$$\rho_{11}(t) = \frac{\gamma_1}{\gamma_1+\gamma_2}\left[1 - e^{-(\gamma_1+\gamma_2)t}\right] \Rightarrow \rho_{11}(\infty) = \frac{\gamma_1}{\gamma_1+\gamma_2} \tag{5.14}$$

$$\rho_{22}(t) = \frac{\gamma_2}{\gamma_1+\gamma_2}\left[1 - e^{-(\gamma_1+\gamma_2)t}\right] \Rightarrow \rho_{22}(\infty) = \frac{\gamma_2}{\gamma_1+\gamma_2} \tag{5.15}$$

Furthermore, integration of Eq. (5.11) together with the initial condition $\rho_{ij}(0) = 0$ for $j \neq i$ gives

$$\rho_{10}(t) = \rho_{20}(t) = 0 \quad \forall t \tag{5.16}$$

Finally, for the coherence $\rho_{12}(t)$ given by Eq. (5.12), substituting the expression of $\rho_{00}(t)$ [Eq. (5.13)] in Eq. (5.12) gives:

$$\dot{\rho}_{12}(t) = \kappa_{12} e^{-(\gamma_1+\gamma_2)t} \tag{5.17}$$

and after integration, together with the initial condition $\rho_{12}(0) = 0$, we find

$$\rho_{12}(t) = \frac{\kappa_{12}}{\gamma_1 + \gamma_2}\left[1 - e^{-(\gamma_1+\gamma_2)t}\right] \tag{5.18}$$

and for $t \to \infty$

$$\rho_{12}(\infty) = \frac{\kappa_{12}}{\gamma_1 + \gamma_2} \tag{5.19}$$

While the results in Eqs. (5.14) and (5.15) simply show that the populations in the final state are in a probabilistic distribution either in $|1\rangle$ or $|2\rangle$, the result for the coherence ρ_{12} in Eq. (5.19) is more surprising: to date, it was thought that such a coherence between the two ground states required an external coherent field such as a laser field (Ref. [12], chapter 3); our result reveals that a coherence between the two ground states can be induced by *spontaneous emission*, that is *without* external field.

In Fig. 5.1, we plot this coherence from Eq. (5.18) as a function of time in the case where $\kappa_{12} = \gamma_1 = \gamma_2 = \gamma_0/2$ where γ_0 is the decay rate of the transitions in free space (considering same dipole moments $d_{01} = d_{02}$). The upper bound of $1/2$ is derived in the next Section.

5.2.3 Anisotropic quantum vacuum

To compute the anisotropic quantum vacuum contribution, we apply the *fluctuation-dissipation theorem* at zero temperature to relate the *correlation function* to the Green tensor of the Maxwell equations, characterizing the electromagnetic environment [11]:

$$\hat{\mathbf{C}}(\mathbf{r}, \mathbf{r}', \omega) = \frac{2\hbar\omega^2}{\epsilon_0 c^2}\mathrm{Im}\left(\hat{\mathbf{G}}(\mathbf{r}, \mathbf{r}', \omega)\right) \tag{5.20}$$

so that the coefficients γ_i and κ_{12} read in term of the Green tensor:

$$\gamma_i = \frac{2\omega_0^2}{\hbar\epsilon_0 c^2}\,\mathbf{d}_{0i}^* \cdot \mathrm{Im}\left(\hat{\mathbf{G}}(\mathbf{r}_0, \mathbf{r}_0, \omega_0)\right) \cdot \mathbf{d}_{0i} \tag{5.21}$$

and

$$\kappa_{12} = \frac{2\omega_0^2}{\hbar\epsilon_0 c^2}\,\mathbf{d}_{01}^* \cdot \mathrm{Im}\left(\hat{\mathbf{G}}(\mathbf{r}_0, \mathbf{r}_0, \omega_0)\right) \cdot \mathbf{d}_{02} \tag{5.22}$$

We point out that in the usual isotropic vacuum, $\hat{\mathbf{G}}(\mathbf{r}_0, \mathbf{r}_0, \omega_0) \propto \mathbb{I}$ ($\mathbb{I}$ is the unit tensor). So, one can see from Eq. (5.22) that κ_{12} vanishes because the transitions are orthogonal (*i.e.* $\mathbf{d}_{01}^* \cdot \mathbf{d}_{02} = 0$), and therefore there is no coherence ρ_{12}. To built up a coherence, when the dipole matrix elements are orthogonal, the vacuum has to be anisotropic. This result was first put forward by Agarwal in Ref. [11], where he predicted coherent population transfer between the two (orthogonal) excited states of a system with a V-configuration (two excited states and one ground state), in an anisotropic quantum vacuum.

We will now find the conditions for which the coherence in Eq. (5.19) is not null. For this purpose, we firstly express all the vectorial quantities in the cartesian basis $(\vec{x}, \vec{y}, \vec{z})$ as:

$$\begin{cases} \mathbf{d}_{01} = d_{01}(\vec{x} + \mathrm{i}\vec{y})/\sqrt{2} \\ \mathbf{d}_{02} = -d_{02}(\vec{x} - \mathrm{i}\vec{y})/\sqrt{2} \end{cases}$$

and

$$\hat{\mathbf{G}} = \begin{bmatrix} G_{xx} & G_{xy} & G_{xz} \\ G_{yx} & G_{yy} & G_{yz} \\ G_{zx} & G_{zy} & G_{zz} \end{bmatrix}. \tag{5.23}$$

Using Eqs. (5.21)-(5.22), we obtain:

$$\gamma_i = \frac{\omega_0^2}{\hbar\epsilon_0 c^2} d_{0i}^2 \left[\mathrm{Im}\left(G_{xx} + G_{yy}\right)\right], \tag{5.24}$$

and, since $G_{yx} = G_{xy}$:

$$\kappa_{12} = \frac{\omega_0^2}{\hbar\epsilon_0 c^2} d_{01} d_{02} \left[\mathrm{Im}\left(G_{xx} - G_{yy}\right) - 2\mathrm{iIm}\left(G_{xy}\right)\right] \tag{5.25}$$

where the Green's function Cartesian components have to be evaluated at the position of the quantum emitter $\mathbf{r}_0$ and for the transition frequency ω_0. Inserting these two equations into (5.19), we find:

$$\rho_{12}(\infty) = \underbrace{\frac{d_{01} d_{02}}{d_{01}^2 + d_{02}^2}}_{R} \times \underbrace{\frac{\mathrm{Im}\left[G_{xx} - G_{yy}\right] - \mathrm{i}2\mathrm{Im}\left[G_{xy}\right]}{\mathrm{Im}\left[G_{xx} + G_{yy}\right]}}_{V} \tag{5.26}$$

From Eq. (5.26), we note that the coherence is a product of two terms: The coefficients R and V, characterizing the quantum emitter and the anisotropy of the EM environment, respectively. R reaches its maximum value of $1/2$ when the two dipole moments amplitudes are identical. The coefficient V, in its general form, is a complex quantity. Since the two metasurface design, discussed in Section 5.3 are made of nano-resonators that respect the mirror symmetry, $G_{xy} = 0$. From now, V will be considered as a real quantity and takes the form of a *visibility* with extremum value ± 1. Therefore the extremum values of the coherence are $\rho_{12}(\infty) = \pm 1/2$. In this situation the density matrix, after spontaneous emission, reads $\rho(\infty) = \frac{1}{2}\begin{bmatrix} 1 & \pm 1 \\ \pm 1 & 1 \end{bmatrix}$ which correspond to a pure state. In contrast, in an isotropic vacuum, we obtain a statistical mixture with a density matrix $\rho(\infty) = \frac{1}{2}\mathbb{I}$.

Anisotropy in vacuum appears naturally at the near-field of a material. For instance, suppression of spontaneous emission of atoms located between two close mirrors have been reported by W. Jhe and co-authors [16]. Anisotropy of Casimir-Polder interactions between atoms and planar surfaces have also been investigated [17] leading to atomic level mixing [18]. Resonant nano-structure are also known to show important discrepancies between $\mathrm{Im}(G_{xx})$ and $\mathrm{Im}(G_{yy})$ in near-field [19]. In far-field, metasurfaces acting as a spherical mirror for a particular polarization of the EM-field and as a planar mirror for the other polarizations, have been proposed to create anisotropic vacuum [7]. We are following this approach and we will characterized two designs in Section 5.3. In an idealized case, an infinite metasurface will perfectly reflected back to the QE half of its own emission at a particular polarization, let say the x-component, leading to a perfect destructive interference and $\mathrm{Im}(G_{xx}) = 0$. The other polarization component (the y-component) is not affected and $\mathrm{Im}(G_{yy}) = \gamma_0/2$, its value in vacuum. Thus, an idealized metasurface might leads to an optimum visibility of $V = \pm 1$ in far-field. Interestingly, we note that if

near-field interaction can enhance the QE emission rate because of large $\mathrm{Im}(G_{ii})$ values (see *e.g.* Ref. [20]), it does not seem to be a better alternative than far-field interaction to develop anisotropic vacuum environment.

Instead of expressing the quantities in Cartesian coordinates, one can also express the Green tensor and dipole moments in the spherical basis $(\vec{\varepsilon}_+, \vec{\varepsilon}_-, \vec{z})$ where $\vec{\varepsilon}_\pm = (\vec{x} \pm \mathrm{i}\vec{y})/\sqrt{2}$:

$$\begin{cases} \mathbf{d}_{01} = d_{01}\vec{\varepsilon}_+ \\ \mathbf{d}_{02} = -d_{02}\vec{\varepsilon}_- \end{cases}$$

and

$$\hat{\mathbf{G}} = \begin{bmatrix} G_{++} & G_{+-} & G_{+z} \\ G_{-+} & G_{--} & G_{-z} \\ G_{z+} & G_{z-} & G_{zz} \end{bmatrix} \tag{5.27}$$

where one has the relations (using the fact that $G_{yx} = G_{xy}$):

$$G_{+-} = \frac{1}{2}\left(G_{xx} - G_{yy} - \mathrm{i}2G_{xy}\right) \tag{5.28}$$

and

$$G_{++} = G_{--} = \frac{1}{2}(G_{xx} + G_{yy}) \tag{5.29}$$

Similarly, by expressing Eqs. (5.21) and (5.22) in this basis and plugging them into Eq. (5.19), one finds the following expression for the coherence:

$$\rho_{12}(\infty) = \underbrace{\frac{d_{01}d_{02}}{d_{01}^2 + d_{02}^2}}_{R} \times \underbrace{\frac{\mathrm{Im}(G_{+-})}{\mathrm{Im}(G_{++})}}_{V} \tag{5.30}$$

where the Green's function spherical components are evaluated at the position of the quantum emitter $\mathbf{r}_0$ and for the transition frequency ω_0. This expression is equivalent to Eq. (5.26), and the criteria for a non-zero coherence $\rho_{12}(\infty)$ now reads:

$$\mathrm{Im}(G_{+-})(\mathbf{r}_0, \mathbf{r}_0, \omega_0) \neq 0 \tag{5.31}$$

5.3 Metasurface designs

We consider here the problem of the interaction between a (meta)surface and an electric dipole source of emission wavelength λ_0 and located at a distance d above the surface. At remote distances (in the so-called far-field $d \gg \lambda_0$), the interaction will be efficient if the metasurface is able to reflect and focus back the light originating from the "point" source. This is the optical equivalent of a spherical mirror whose focal length is $f = d/2$, with the following spherical phase profile:

$$\varphi(\mathbf{r}) = \pi - 2k_0|\mathbf{r} - \mathbf{r}_0| \,(\mathrm{mod}\, 2\pi) \tag{5.32}$$

where $k_0 = 2\pi/\lambda_0$ and $\mathbf{r}_0 = (x_0, y_0, d)$ are the coordinates of the QE and $\mathbf{r} = (x, y, 0)$ the coordinates of the points of the metasurface which lies in the plan $z = 0$. In other words, the phase accumulated through propagation should be compensated in each point $\mathbf{r}$ of the

metasurface by a phase-shift corresponding to the phase profile given in Eq. (5.32). Using a flat surface with high numerical aperture, the interface is engraved with subwavelength nanoantennas [9, 10], which induce local phase-shifts and allow to mimic the spherical phase profile given by Eq. (5.32). This is also called the *phase-mapping approach*.

Such metasurfaces, whose role is to focus the light, are the equivalent in reflection of *metalenses* [9, 10]. They can be implemented using metallic subwavelength reflectarrays, made of a metallic mirror, a dielectric spacer and the subwavelength structures patterned on top (see Fig. 5.2). It was reported good reflectance efficiencies; about 80% for gold reflectarrays [7, 21–23] and up to 90% for silver reflectarrays [8, 24].

In the coming Subsections 5.3.1 and 5.3.2, we study in detail two designs for such a metasurface. We note that each design is specific for a couple of parameters $\{\lambda_0, d\}$, so a modification of one of these parameters leads to a new design. All the numerical simulations are done using the open-source code *Reticolo software for grating analysis* [25], developped by J.P. Hugonin and P. Lalanne, Institut d'Optique, Palaiseau, France (2005), which implements a frequency-domain modal method known as the Rigorous Coupled Wave Analysis (RCWA) (see Refs. [26–29]).

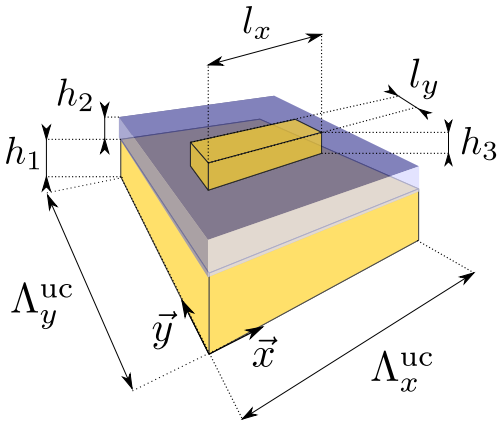

Figure 5.2 – Metasurface unit-cell sketch made of: a metallic mirror of thickness h_1, a dielectric spacer of thickness h_2, and a rectangular nanoantenna of dimmensions (l_x, l_y) and of thickness h_3. The dimensions of the unit-cell are: $\Lambda_x^{\mathrm{uc}} \times \Lambda_y^{\mathrm{uc}}$.

5.3.1 Design based on resonant-phase delays

In this Section, we present our first design of metasurface aiming at creating a coherence in a QE located at $\mathbf{r}_0$. As seen from Eq. (5.26), a way to reach the maximum value for the coherence ρ_{12} is to cancel one of the two components $\mathrm{Im}[G_{xx}(\mathbf{r}_0, \mathbf{r}_0, \omega_0)]$ or $\mathrm{Im}[G_{yy}(\mathbf{r}_0, \mathbf{r}_0, \omega_0)]$. This strategy was followed in [7], where the authors proposed a metasurface with the following optical properties:

- The metasurface acts as a spherical mirror *only* for a linearly-polarized light along the x-direction, so that it induces destructive interferences between the field emitted by the atom in the half space $z > 0$ and the field reflected by the metasurface, resulting in $G_{xx}(\mathbf{r}_0, \mathbf{r}_0, \omega_0) = 0$.

- The metasurface acts as a planar mirror for a linearly-polarized light along the y-direction, so $G_{yy}(\mathbf{r}_0, \mathbf{r}_0, \omega_0)$ is untouched.

Following the proposal in [7], our first design is made of anisotropic resonant nanoantennas with different lengths along x to induce different phase-shifts in order to mimic the spherical phase profile of Eq. (5.32) for the x-polarization, while about the same width along y in order to act as a planar mirror with a flat phase profile for the y-polarization [7, 21, 22]. In Fig 5.3 (a) we reproduced the desired ideal unwrapped (wrapped) phase profile φ_x for a x-polarized wave in purple (red) corresponding to Eq. (5.32), and the flat phase profile φ_y for a y-polarized wave in green. Fig 5.3 (b) is illustrated the so-called phase-mapping approach, where in each nanoantenna gives the expected phase-shift at its mean x-position.

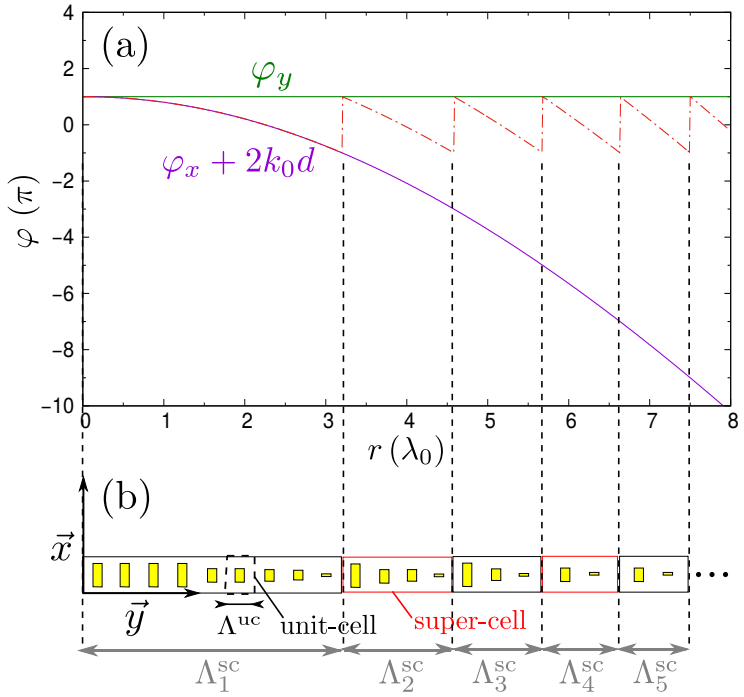

Figure 5.3 – Illustration of the phase-mapping approach in 1D: (a) Phase profiles to be encoded by the metasurface; the purple line is the unwrapped spherical phase profile φ_x corresponding to Eq. (5.32) desired for the x-polarization, the red dashed line is the same phase profile wrapped modulo 2π, and the green line is the flat phase profile φ_y desired for the y-polarization. (b) Corresponding nanoantennas to induced the desired phase-shifts φ_x and φ_y at the position r_m (starting from the center of the metasurface at $r_m = 0$). The unit-cells containing the nanoantennas are encompassed into super-cells of length Λ^{sc}, each super-cell spanning the phase-space of 2π.

In Fig. 5.4, we computed the phase-shift (green crosses) and the reflectance efficiency (purple dots) as a function of the length l_x of the nanoantenna for an incident x-polarized wave at normal incidence. Here, we considered a periodic arrangement of unit-cells of the type presented in Fig. 5.2, with gold metallic elements, SiO_2 as dielectric spacer, and a wavelength of $\lambda_0 = 852\,\text{nm}$ which corresponds to the D2 line of cesium atom. One can see in Fig. 5.4 that the phase-shift spans over $4\pi/5$. One can therefore choose five nanoantennas (see dimension in Table 5.1) with respective phase-shifts of 0, $\pi/5$, $2\pi/5$,

$3\pi/5$ and $4\pi/5$ to sample the entire phase space of 2π .

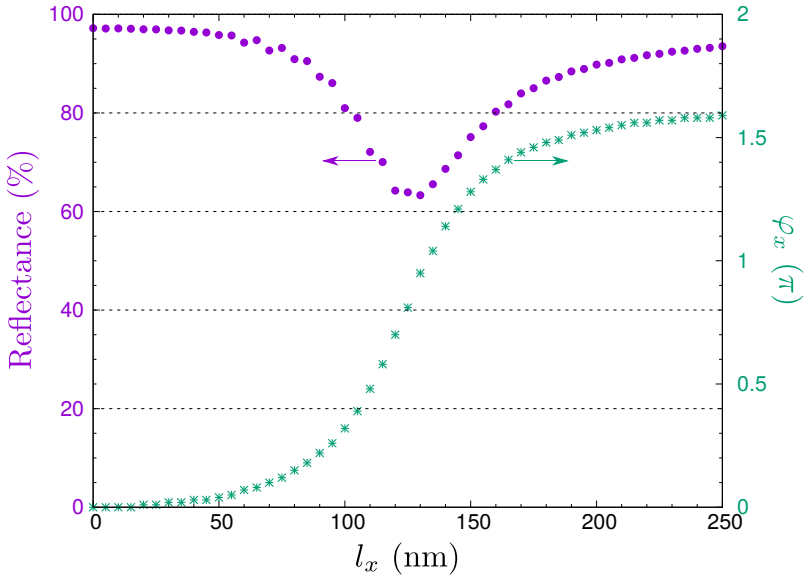

Figure 5.4 – Phase-shift in reflection of an incident x-polarized wave as a function of the length l_x of the nanoantennas of a periodic reflect-array metasurface. The metasurface consists in a periodic array of unit-cells of the type shown in Fig. 5.2 with the following dimensions: lateral dimensions of $\Lambda_x^{\text{uc}} \times \Lambda_y^{\text{uc}} = 300\,\text{nm} \times 150\,\text{nm}$, gold film of thickness $h_1 = 130\,\text{nm}$, dielectric film (SiO_2) of thickness $h_2 = 50\,\text{nm}$, and gold nanoantenna of thickness $h_3 = 30\,\text{nm}$, and width $l_y = 100\,\text{nm}$. The dotted purple lines are spaced by $\pi/5$ and correspond to the phase-shift of the five chosen nanoantennas. The wavelength is 852 nm. At this wavelength, the refractive indices are $n = 0.16 + i5.34$ for gold and $n = 1.45$ for SiO_2.

We now compute the reflectance of a super-cell with periodic boundary condition. This super-cell is composed by nanoantannas that mimic a constant linear-gradient of the phase (see inset in Fig. 5.5). More precisely, here the metasurface is designed to diffract light like a blazed grating in the order $m = -1$. We compute the reflectance in the diffracted order $m = -1$, and compare it with the other dominant orders in Fig. 5.5 (a). One can see that the reflectance in $m = -1$ is about 60% for incident angles θ_i up to 30°, and remains above 40% for incident angles up to 70°.

nanoantenna	l_x	l_y
#1	30 nm	100 nm
#2	105 nm	100 nm
#3	125 nm	100 nm
#4	145 nm	100 nm
#5	250 nm	100 nm

Table 5.1 – Nanoantennas sizes for sampling the phase from 0 to 2π.

We check [see Fig. 5.5 (b)] that we recover the generalized Snell's law of reflection

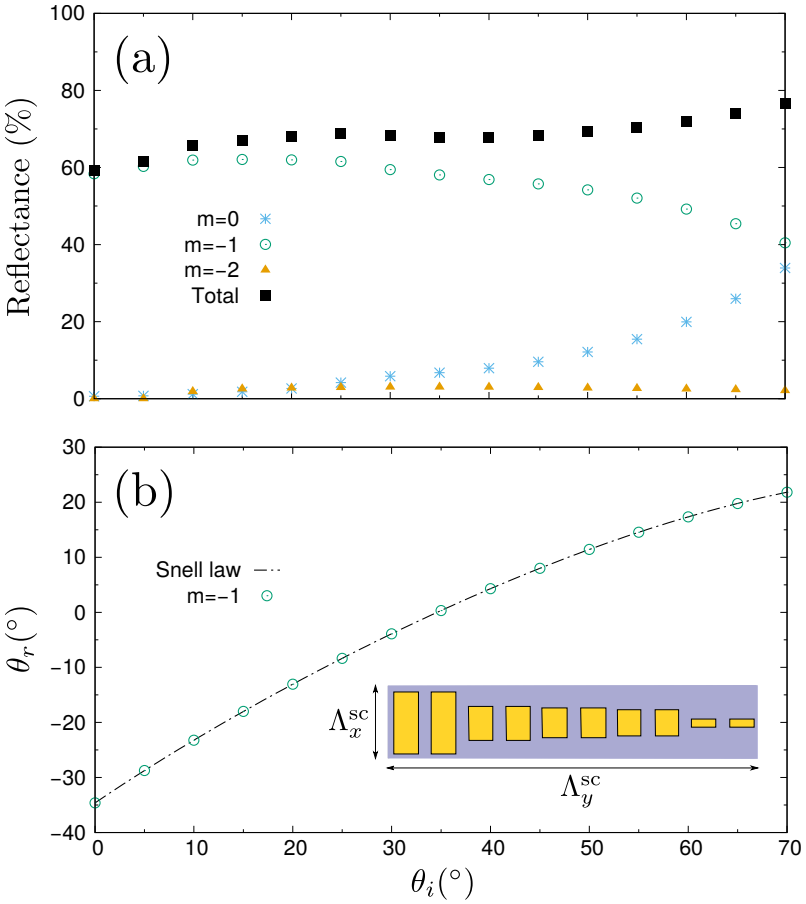

Figure 5.5 – (a) Reflection efficiency (in energy) in the diffracted orders $m = -2, -1, 0$ (dashed lines) and total reflection efficiency (black line) as a function of the incident angle θ_i of an incident plane wave polarized along x. (b) Reflection angle θ_r in the diffracted order $m = -1$ as a function of the incident angle θ_i of an incident plane wave polarized along x (points). The generalized Snell's law of reflection $\sin(\theta_r) = \sin(\theta_i) + (2\pi/\lambda_0)(\partial\varphi/\partial y)$ is also plotted where $\partial\varphi/\partial y = -2\pi/_y$ with $L_y = 1500\,\text{nm}$ (black line). The inset shows the super-cell of a linear-gradient metasurface made of pairs of nanoantennas whose sizes are given in Table 5.1. The dimensions of the super-cells are: $\Lambda_x^{sc} = 300\,\text{nm}$ and $\Lambda_y^{sc} = 1500\,\text{nm}$.

[10]

$$\sin(\theta_r) = \sin(\theta_i) + \frac{2\pi}{\lambda_0}\frac{\partial\varphi}{\partial y}, \tag{5.33}$$

where here $\partial\varphi/\partial y = -2\pi/L_y$ with $L_y = 1500\,\text{nm}$. The general Snell's law is perfectly recovered because the diffraction angles are the same either for a periodic blazed grating or for a smooth linear-gradient metasurface: the diffraction angle only depends on the period, and not on the underlying structure. However, the reflectance into a given order depends on the incident angle as illustrated in Fig. 5.5 (a) and also on the underlying structure.

In Fig. 5.5 (a), we show the reflectance properties as a metasurface mimicking a linear-gradient of the phase. The final metasurface is more complex since it should realize the spherical phase profile given by Eq. (5.32). So, when the distance $\mathbf{r}$ (or the incident angle) increases the phase variation increases as well and its sampling by the super-cell becomes more stringent resulting in stronger reduction of its efficiency compared to the

Super-cell	$\Lambda^{sc}(\lambda_0)$	N	Reflectance (%)
1	3.17	9	60
2	1.41	4	55
3	1.06	3	50
4	0.94	2	30
5	0.82	2	30
...	...	...	...
∞	0.5	1	10

Table 5.2 – Characteristics of the super-cells labelled by integer n starting from the center of the metasurface: length Λ^{sc} (in units of λ_0), number of unit-cells N per super-cell, diffraction efficiency in reflection into the order $m = -1$ of a periodic arrangement of the super-cell given at normal incidence.

linear-gradient metasurface. For example in a 1D configuration, the larger super-cell at the center of the metasurface (at $r_m = 0$) has a length equal to $\Lambda^{sc}_{max} = \sqrt{d\lambda_0}$, and the smallest super-cell has a length of $\Lambda^{sc}_{min} = \lambda_0/2$ (see Appendix 5.B for more detail). In Table 5.2, we give the length Λ^{sc} of the first five super-cells (labelled $n = 1, ..., 5$ starting from the center) for $\lambda_0 = 852\,\text{nm}$ and $d = 10\lambda_0$. We also put the number of unit-cells N per super-cell, considering a fixed unit-cell length $\Lambda^{uc} = 0.35\lambda_0$ (300 nm). For each super-cell, we computed the reflectance in the order $m = -1$ of a periodic arrangement, at normal incidence. One can see that the reflectance decreases as the number of nanoantennas per super-cell decreases.

In summary, we shown that the reflectance is reduced for two main reasons; the increasing of the incident angle θ_i which limit the numerical aperture (NA) of the metasurface, and the finite number of unit-cell to sample the phase.

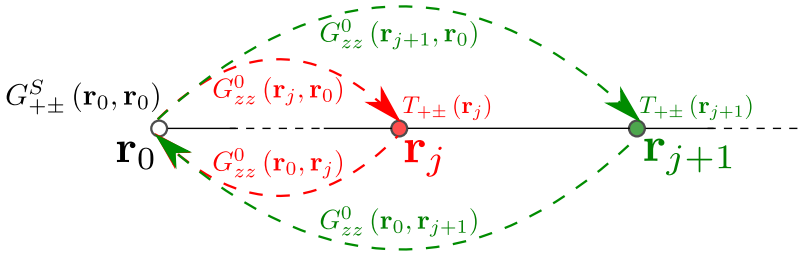

Figure 5.6 – Feynman diagram representing the interaction between the atom located at $\mathbf{r}_0$ and the meta-atoms of the metasurface located at $\mathbf{r}_j$, mediated by virtual photons depicted by oriented dashed lines. To each dashed line starting from point $\mathbf{r}$ and ending at point $\mathbf{r}'$ is associated a propagator $G^0_{zz}(\mathbf{r}', \mathbf{r})$ which describes the propagation of the photon in free-space. At each meta-atom position $\mathbf{r}_j$ are associated coupling factors $T_{++}(\mathbf{r}_j)$ and $T_{+-}(\mathbf{r}_j)$ which describe the coupling of the meta-atom with the photon. The total interaction, characterized by $G^S_{+\pm}(\mathbf{r}_0, \mathbf{r}_0)$, is the sum of all interactions with all the meta-atoms: $G^S_{+\pm}(\mathbf{r}_0, \mathbf{r}_0) = \sum_j G^0_{zz}(\mathbf{r}_0, \mathbf{r}_j)\, T_{+\pm}(\mathbf{r}_j)\, G^0_{zz}(\mathbf{r}_j, \mathbf{r}_0)$.

5.3.2 Design based on geometric-phases

The second design is based on a geometric Pancharatnam–Berry phase rotation as suggested in Ref. [8]. Here, the design is made of an unique nanoantenna with a position-dependent orientation.

The design should be such that Re[V] in Eq. (5.30) is maximum (in absolute value). We then write $\hat{G}$ as a free-space contribution $\hat{G}^0$ plus a "scattered" contribution $\hat{G}^S$ due to the metasurface so that the components G_{++} and G_{+-} in Eq. (5.30) can be written as:

$$G_{++} = G^0_{++} + G^S_{++} \tag{5.34}$$

$$G_{+-} = G^0_{+-} + G^S_{+-} = G^S_{+-} \tag{5.35}$$

Eq. (5.35) simplifies because the free-space components $G^0_{+-} = 0$. Moreover, $G^0_{++} = G^0_{--} = G^0_{zz}$ and in the following we replace G^0_{++} and G^0_{--} by G^0_{zz}. According to Eq. (5.30, Re[V] is maximal if the following criteria are fulfilled:

(i) $G^S_{++}(\mathbf{r}_0, \mathbf{r}_0, \omega_0) = 0$

(ii) $G^S_{+-}(\mathbf{r}_0, \mathbf{r}_0, \omega_0)$ is maximum.

Using a T-Matrix-like formalism [30], one can write $\hat{G}^S$ in the form [31, 32]:

$$\hat{G}^S = \hat{G}^0 \hat{T} \hat{G}^0 \tag{5.36}$$

where $\hat{T} \equiv \sum_j \hat{T}^{(j)}$ and $\hat{T}^{(j)}$ is the T-Matrix describing the field scattered by the nanoantenna j. Moreover, we suppose that the spacing between nanoantennas is large enough so that they are not coupled (single scattering approximation) [9]. In the position representation, $\hat{G}^S$ reads (dropping the variable ω_0 for concision):

$$\hat{G}^S(\mathbf{r}_0, \mathbf{r}_0) = \sum_j \hat{G}^0(\mathbf{r}_0, \mathbf{r}_j) \hat{T}(\mathbf{r}_j) \hat{G}^0(\mathbf{r}_j, \mathbf{r}_0) \tag{5.37}$$

In Fig. 5.6 we give a representation of Eq. (5.37) using a Feynman diagram. Such a representation allows us to reinterpret the conditions that will satisfy the criteria (i) and (ii). The criteria (i) is achieved when $T_{++}(\mathbf{r}_j)$ is null for each point $\mathbf{r}_j$:

$$|T_{++}(\mathbf{r}_j)| = 0 \quad \forall j \tag{5.38}$$

where T_{++} is the component ++ of the T-Matrix in the spherical basis. The criteria (ii) is achieved when the coupling $T_{+-}(\mathbf{r}_j)$ is maximum (that is $|T_{+-}(\mathbf{r}_j)|$ maximum). In addition, the following phase condition should be satisfied:

$$\arg[G^0_{zz}(\mathbf{r}_0, \mathbf{r}_j)] + \arg[T_{+-}(\mathbf{r}_j)] + \arg[G^0_{zz}(\mathbf{r}_j, \mathbf{r}_0)] = 2\pi, \tag{5.39}$$

so that the contributions of all nanoantennas add-on constructively. T_{+-} is the component +− of the T-Matrix in the spherical basis. In the far-field approximation, we expand the free-space Green function so that:

$$\arg\left[G^0_{zz}(\mathbf{r}_0, \mathbf{r}_j)\right] = \arg\left[G^0_{zz}(\mathbf{r}_j, \mathbf{r}_0)\right] \simeq k_0 |\mathbf{r}_0 - \mathbf{r}_j| \,. \tag{5.40}$$

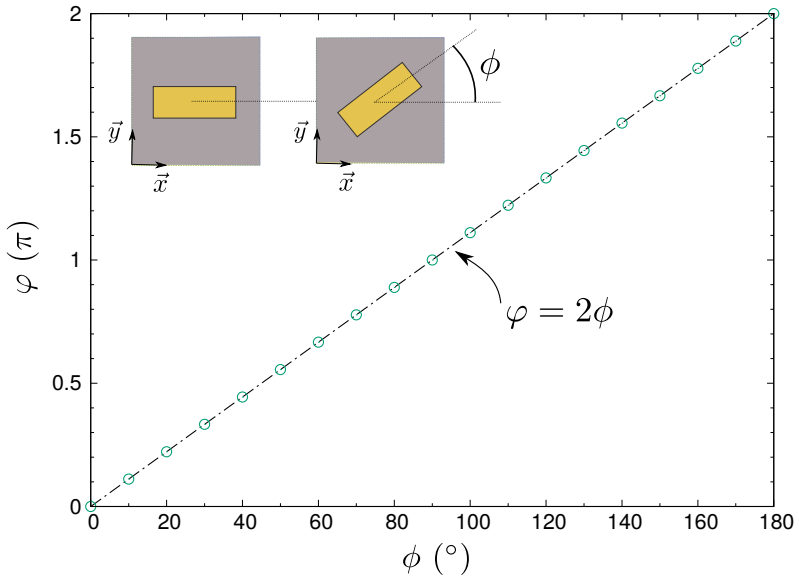

Figure 5.7 – Geometric phase $\varphi = \arg[R_{+-}]$ induced by a periodic array of unit-cells of the type of Fig. 5.2 as a function of the rotation angle θ of the nanorods in the plan $(\tilde{x}, \tilde{y})$ (see inset). In dotted purple line is the numerical simulations, and in full green line is the analytical expression $\varphi = 2\phi$. The metasurface characteristics are: lateral dimensions $\Lambda_x^{uc} \times \Lambda_y^{uc} = 300\,\text{nm} \times 300\,\text{nm}$, gold film of thickness $h_1 = 130\,\text{nm}$, dielectric (MgF_2) film of thickness $h_2 = 90\,\text{nm}$, and gold nanorod of thickness $h_3 = 30\,\text{nm}$ and dimensions $l_x = 200\,\text{nm}$ and $l_y = 80\,\text{nm}$. All these values are taken from Ref. [23]. At 852 nm, the refractive indices are $n = 0.16 + i5.34$ for gold and $n = 1.37$ for MgF_2.

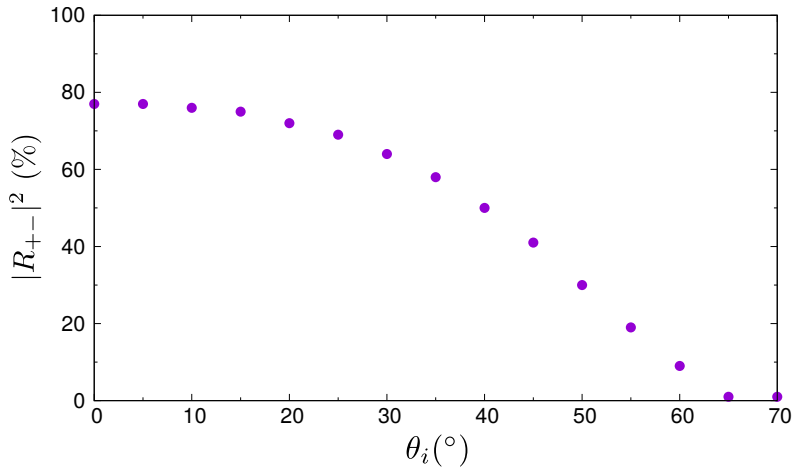

Figure 5.8 – Conversion efficiency $|R_{+-}|^2$ between a light circularly polarized σ^+ and a light circularly polarized σ^- of a periodic array of unit-cells of the type of Fig. 5.2 as a function of the incident angle θ_i. The metasurface consists in the same periodic array of unit-cells as described in the legend of Fig. 5.7.

In summary, the criteria (i) and (ii) are satisfied when:

(i) $|T_{++}(\mathbf{r}_j)| = 0 \quad \forall j$

(ii) $\arg[T_{+-}(\mathbf{r}_j)] = 2\pi - 2k_0|\mathbf{r}_0 - \mathbf{r}_j|$

and $|T_{+-}(\mathbf{r}_j)|$ is maximum $\quad \forall j$.

The next step is to design a metasurface with the $\hat{T}(\mathbf{r}_j)$ operator that satisfies these two criteria for each meta-atom j. In order to do so, we estimate the $\hat{T}(\mathbf{r}_j)$ operator using the following approximation: we consider that the meta-atom located at $\mathbf{r}_j$ "sees" an environment locally periodic around it, and behaves as in a periodic grating of this same meta-atom ("local periodicity approach"); therefore, one can deduce the T-Matrix components of the meta-atom j from the Jones Matrix R, which characterizes the reflection properties of a periodic grating of this same meta-atom, and which can be computed by using *Reticolo software for grating analysis* [25]. In short notations, we assume that:

$$\hat{T}(\mathbf{r}_j) \propto R \tag{5.41}$$

where R is the Jone's matrix in reflection of a periodic grating made of the same type of meta-atom as the one located in $\mathbf{r}_j$ in the metasurface.

Using the relation between spherical and Cartesian coordinates (see Ref. [33]), the criterion (i), which becomes $R_{++} = 0$, can be written as:

$$R_{xx} + R_{yy} = R_{xy} - R_{yx} = 0 \tag{5.42}$$

If the meta-atoms have a mirror symmetry in the reference frame (which will be the case here, see left inset in the Fig. 5.7), $R_{xy} = R_{yx} = 0$ and Eq. (5.42) reduces to

$$R_{xx} = -R_{yy} \tag{5.43}$$

Eq. (5.43) requires equality in the amplitude and phase of the two sides. The equality in amplitude is met if the metasurface is perfectly reflective (no losses due to absorption or transmission): $|R_{xx}| = |R_{yy}|$, and the equality in phase requires: $\varphi_{xx} - \varphi_{yy} = \pi$ where φ_{ii} denotes the argument of R_{ii}. Such a condition indicates that the desired system is a perfect half-wave plate working in reflection mode [23, 33]. For our nanoantennas, we use gold nanorods of dimensions $l_x = 200\,\text{nm}$ and $l_y = 80\,\text{nm}$ (see Fig. 5.2). At $\lambda_0 = 852\,\text{nm}$, we compute a periodic grating and find $\varphi_{xx} - \varphi_{yy} = \pi$ and $|R_{++}|^2 = 10\%$ at normal incidence [25], which is close to criterion (i).

To address criterion (ii), which becomes $\arg[R_{+-}(\mathbf{r}_j)] = 2\pi - 2k_0|\mathbf{r}_0 - \mathbf{r}_j|$, we shall tune the phase of R_{+-} from 0 to 2π. We then rotate the nanobar by an angle ϕ leading to a phase-shift $\arg[R_{+-}] = 2\phi$ [33]. This phase-shift is of geometric origin since it is solely due to the orientation of the nanoantenna and not to its resonance properties [34, 35]. In Fig. 5.7, we show that this behaviour is verified by our nanobars by simulating the phase-shift induced by a periodic grating of such nanoantennas all rotated by the same angle ϕ. We also compute the reflectance efficiency as a function of the incident angle

(see Fig. 5.8) and found $|R_{+-}|^2 > 40\%$ for $\theta_i < 45°$. Note that these performances are less than the design of Section 5.3.1, where from the simulation shown in Fig. 5.5 (a) we obtained a reflectance into the desired order $m = -1$ higher 40% up to $\theta_i = 70°$. These quantities, that is the reflectance and the conversion efficiency $|R_{+-}|^2$ between a light circularly polarized σ^+ and a light circularly polarized σ^-, are not the same (and one is computed for a grating of super-cells while the other one is computed for a grating of identical unit-cells) but they both characterizes the performance of the metasurface, and it is what we eventually want to compare.

To create the metasurface, we place, in each point $\mathbf{r}_j$ of the metasurface, a nanobar rotated by the appropriate angle to induce the expected phase-shift imposed by criterion (ii). In Fig. 5.9, we show a 3D drawing of a metasurface for the specific parameters $\lambda_0 = 852\,\text{nm}$ and $d = 10\lambda_0$. In this Figure, we also highlight a super-cell (white box) which samples the entire 2π-phase space.

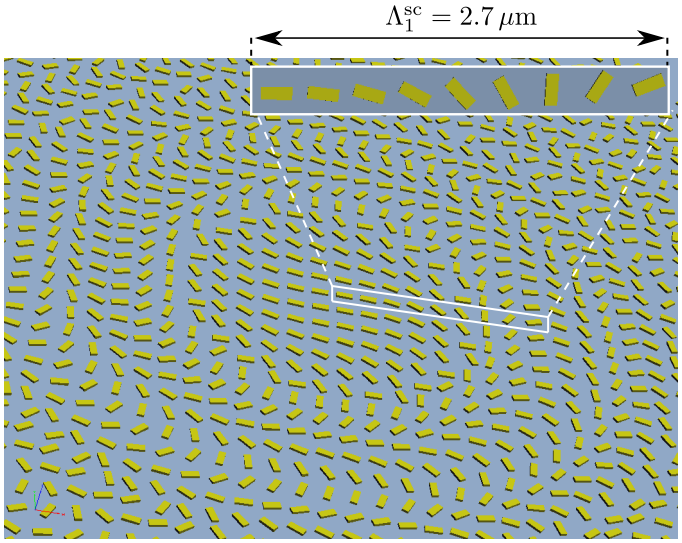

Figure 5.9 – 3D design of the geometric metasurface, *i.e* metallic reflectarray made of a gold nanofilm separated by a dielectric spacer from gold nanorods of different orientations which provides the desired phase-shift at each position following criterion (ii). The design is made for a distance of the dipole source $d = 10\lambda_0$ from the metasurface, and an emission wavelength of $\lambda_0 = 852\,\text{nm}$. The black box delimits the first (starting from the center), super-cell of size $\Lambda_1^{sc} = 2.7\,\mu\text{m}$ made of 9 nanorods, according to Table 5.2. This figure was drawn using the CAD software *SolidWorks*™ (developped by Dassault Systèmes®) .

5.4 Discussions on the coherence and limitations

We now assess the steady state value of the ground state coherence ρ_{12} [see Eq. (5.19)] based on the calculated performances of the design discussed in Section 5.3.1 as it presents better performance than the second design. If the dipole moments of the transition are equal ($d_{01} = d_{02}$), Eq. (5.26) [or equivalently Eq. (5.30)] becomes:

$$\rho_{12}(\infty) = \frac{1}{2} \times \frac{\text{Im}\left[G_{xx} - G_{yy}\right]}{\text{Im}\left[G_{xx} + G_{yy}\right]} \tag{5.44}$$

where the component $\mathrm{Im}\left[G_{xy}\right]=0$ since the nanoantennas have a mirror symmetry.

We note that the dipole moment $\mathbf{d}$ oriented along the i-axis has a decay rate given by:

$$\gamma_i = \frac{2\omega_0^2}{\hbar\epsilon_0 c^2}|\mathbf{d}|^2 \mathrm{Im}(G_{ii}), \tag{5.45}$$

which allows to recast Eq. (5.44) such as:

$$\rho_{12}(\infty) = \frac{1}{2}\times\frac{\gamma_x-\gamma_y}{\gamma_x+\gamma_y} \tag{5.46}$$

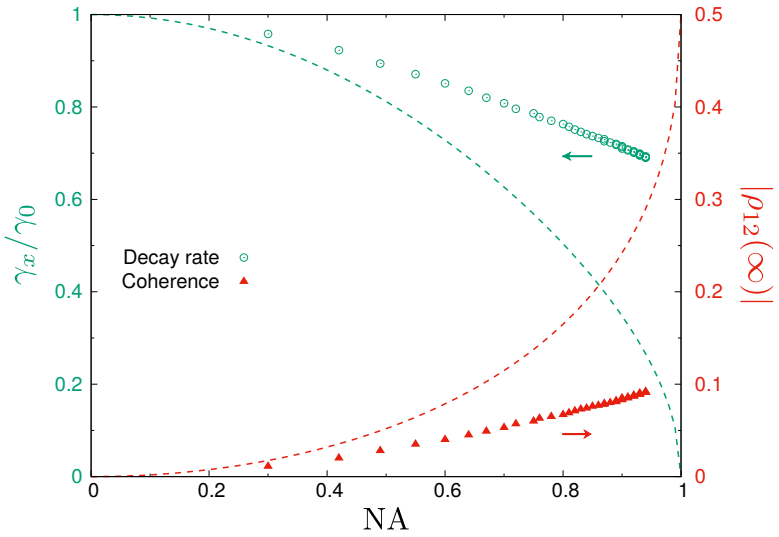

Figure 5.10 – Relative decay rate modification γ_x/γ_0 (green circles) and coherence $|\rho_{12}|$ (red triangles) as a function of NA, the numerical aperture of the metasurface. In dashed green (red) line is shown the relative decay rate (coherence) for an ideal reflector of reflectance $R_x = 1$.

The quantity γ_y is not affected by the metasurface presented in Section 5.3.1 so $\gamma_y = \gamma_0$. γ_x is now computed as function of the reflectance R_x for an optical field polarization along x and for a given NA of the metasurface. Following Ref. [3] and considering a dipole oriented along x, we get:

$$\frac{\gamma_x}{\gamma_0} = 3\int_{2\pi}\frac{\mathrm{d}\Omega}{4\pi}\left[1-\frac{|\mathbf{d}\cdot\vec{\Omega}|^2}{|\mathbf{d}|^2}\right]\times(1-R_x), \tag{5.47}$$

where $\vec{\Omega}$ is the vectorial solid angle and $\mathrm{d}\Omega = \sin\theta\mathrm{d}\theta\mathrm{d}\phi$. The value of R_x are given by Table 5.2 and Fig. 5.8 for the first and second design respectively, and $R_x = 0$ if $\sin\theta > \mathrm{NA}$. If one considers R_x as constant, one can perform the integration in Eq. (5.47), and by expressing in terms of the numerical aperture defined as $\mathrm{NA} \equiv \sin\theta$, one obtains: By using the reflectance values displayed in Table 5.2, we compute the relative decay rate modification γ_x/γ_0 from Eq. (5.47). Those data are shown in Fig. 5.10 as function of NA. Note that for comparison, we also show (green dashed line) the case of a perfect reflective mirror ($R_x = 1$), for which Eq. (5.47) can be calculated analytically and reads:

$$\frac{\gamma_x}{\gamma_0} = \sqrt{1-\mathrm{NA}^2}\times\left(1-\frac{\mathrm{NA}^2}{4}\right) \tag{5.48}$$

For a metasurface of NA = 0.7, we get a reduction of the decay rate γ_x of 20% compared to γ_0. We note that larger NA results in a very moderate improvement because of the rapid drop of the Reflectance. We finally plug the γ_x values into Eq. (5.46), and get a coherence ~ 0.05 at NA$= 0.7$ (see Fig. 5.10). Similarly, we show the ideal case (red dashed line) when plugging Eq. (5.48) into Eq. (5.46). This value is about one order of magnitude smaller that the 0.5 value expected for a ideal reflector with NA$= 1$. Nevertheless this coherence, which is a direct consequence of AQV, should be observable using the current state-of-art NV-center experimental platform [13].

5.5 Conclusion

In this work, we predicted the creation of a long-lifetime coherence between the two ground states of a quantum emitter with a Λ-configuration, induced by a quantum anisotropic vacuum. We proposed two metasurface designs, based on two different approaches, a *resonant phase-delay* approach and a *geometric phase* approach to create the anisotropic vacuum. We quantify the efficiency of such metasurfaces to redirect light on the quantum emitter, located at macroscopic distances taking into account the limitations on the numerical aperture due to the phase-mapping approach. Based on the exact results available for a perfect spherical mirror, we estimate an redirection of the light of about 20% at NA$= 0.7$, leading to a coherence of 0.05. Due to the in-principle infinite lifetime of the coherence, this system allows for high resolution experiments, which is necessary to detect the effect of the metasurface on the atom predicted here.

Detecting this coherence would be, to our knowledge, the first experimental demonstration of the effect of the anisotropy of vacuum at remote distances on quantum emitters. In addition this experiment will be a new test of quantum electrodynamics, in a counter-intuitive regime where coherence is driven by relaxation processes and vacuum fluctuation. Such an experimental demonstration will also pave the way for controlled interactions between several quantum emitters by the means of a metasurface [24, 36], which ultimately can be used to perform entanglement of the emitter for quantum technology applications in a new paradigm.

5.A Derivation of the Master Equation

In this Appendix, we present the Master Equation framework, closely following Refs. [14] Chapter 5.6 and [15] Chapter 1, that we used to derive the master equation [Eq. (5.4)] in Section 5.2.

Short notations: It will be convenient for the following calculations to rewrite $\hat{H}_I(t)$ of Eq. (5.2) in a more compact form:

$$\hat{H}_I(t) = \hat{\mathbf{d}}^\dagger(t)\cdot\hat{\mathbf{E}}_v^{(+)}(t) + \hat{\mathbf{d}}(t)\cdot\hat{\mathbf{E}}_v^{(-)}(t) \tag{5.49}$$

where $\hat{\mathbf{d}}(t)$ and $\hat{\mathbf{d}}^\dagger(t)$ are defined by:

$$\hat{\mathbf{d}}(t) \equiv -\left(\mathbf{d}_{01}^* |1\rangle\langle 0| e^{-i\omega_1 t} + \mathbf{d}_{02}^* |2\rangle\langle 0| e^{-i\omega_2 t}\right) \tag{5.50}$$

$$\hat{\mathbf{d}}^\dagger(t) \equiv -\left(\mathbf{d}_{01} |0\rangle\langle 1| e^{i\omega_1 t} + \mathbf{d}_{02} |0\rangle\langle 2| e^{i\omega_2 t}\right) \tag{5.51}$$

Note that for clarity we dropped the label $\mathbf{r}_0$ appearing in $\hat{\mathbf{E}}_v^{(+)}(\mathbf{r}_0,t)$ and $\hat{\mathbf{E}}_v^{(-)}(\mathbf{r}_0,t)$, but one must remember that the fields are evaluated at the position of the atom $\mathbf{r}_0$. Remember that this Hamiltonian is written in the electric dipole and rotating-wave approximations.

In the *interaction picture*, the density matrix $\rho_T(t)$ of the total system {atom+environment} obeys the Schrödinger equation [14, 15]:

$$\frac{\partial\rho_T(t)}{\partial t} = \frac{1}{i\hbar}[\hat{H}_I(t),\rho_T(t)] \tag{5.52}$$

The atomic density matrix $\rho(t)$ is obtained by taking the trace over the degrees of freedom of the environment: $\rho(t) = \mathrm{Tr}_e(\rho_T(t))$, and therefore obeys:

$$\frac{\partial\rho(t)}{\partial t} = \frac{1}{i\hbar}\mathrm{Tr}_e[\hat{H}_I(t),\rho_T(t)] \tag{5.53}$$

We formally integrate Eq. (5.52):

$$\rho_T(t) = \rho_T(0) + \frac{1}{i\hbar}\int_0^t dt'\,[\hat{H}_I(t'),\rho_T(t')] \tag{5.54}$$

and substitute this expression in Eq. (5.53):

$$\frac{\partial\rho(t)}{\partial t} = \frac{1}{i\hbar}\mathrm{Tr}_e[\hat{H}_I(t),\rho_T(0)] - \frac{1}{\hbar^2}\int_0^t dt'\,\mathrm{Tr}_e\left[\hat{H}_I(t),[\hat{H}_I(t'),\rho_T(t')]\right] \tag{5.55}$$

Approximations 1 and 2:

- We assume that the environment has a large number of degrees of freedom and therefore is little changed by the coupling with the atom: therefore we write $\rho_T(t) = \rho(t)\otimes\rho_e(0)$, where $\rho_e(t)$ is the reduced density matrix of the environment (this is called the *Born approximation*).
- Moreover, we assume that $\mathrm{Tr}_e([\hat{H}_I(t),\rho_T(0)]) = 0$, which is guaranteed since the electric field operators $\hat{\mathbf{E}}_v^{(+)}(\mathbf{r}_0,t)$ and $\hat{\mathbf{E}}_v^{(-)}(\mathbf{r}_0,t)$ have zero mean in the vacuum state.

Under these approximations, Eq. (5.55) reduces to:

$$\frac{\partial \rho(t)}{\partial t} = -\frac{1}{\hbar^2}\int_0^t \mathrm{d}t' \,\mathrm{Tr}_e\left[\hat{H}_I(t),[\hat{H}_I(t'),\rho_e(0)\otimes\rho(t')]\right] \tag{5.56}$$

Approximation 3: We make the *Markov approximation* and replace $\rho(t')$ by $\rho(t)$ in the integrand.

Therefore, we get a Master Equation for the atomic density matrix $\rho(t)$ in the *Born-Markov approximation*:

$$\frac{\partial \rho(t)}{\partial t} = -\frac{1}{\hbar^2}\int_0^t \mathrm{d}t' \,\mathrm{Tr}_e\left[\hat{H}_I(t),[\hat{H}_I(t'),\rho_e(0)\otimes\rho(t)]\right] \tag{5.57}$$

It is now time to write $\hat{H}_I(t)$ explicitely and to expand the commutators. Using the compact form Eq. (5.49) into Eq. (5.57) one gets:

$$\begin{aligned}&\frac{\partial \rho(t)}{\partial t} = \\ &-\frac{1}{\hbar^2}\int_0^t \mathrm{d}t' \,\mathrm{Tr}_e\left[\hat{\mathbf{d}}^\dagger(t)\cdot\hat{\mathbf{E}}_v^{(+)}(t)+\hat{\mathbf{d}}(t)\cdot\hat{\mathbf{E}}_v^{(-)}(t),[\hat{\mathbf{d}}^\dagger(t')\cdot\hat{\mathbf{E}}_v^{(+)}(t')+\hat{\mathbf{d}}(t')\cdot\hat{\mathbf{E}}_v^{(-)}(t'),\rho_e(0)\otimes\rho(t)]\right]\end{aligned} \tag{5.58}$$

Expanding the commutators in Eq. (5.58) gives 16 terms. Noting that the trace only acts on the field operators and on $\rho_e(0)$, and using the cyclic property of the trace operation and the fact that for instance $\mathrm{Tr}_e\left(\rho_e(0))\hat{\mathbf{E}}_v^{(+)}(t)\hat{\mathbf{E}}_v^{(-)}(t')\right) = \left\langle\hat{\mathbf{E}}_v^{(+)}(t)\hat{\mathbf{E}}_v^{(-)}(t')\right\rangle$, we get

$$\begin{aligned}\frac{\partial \rho(t)}{\partial t} = -\frac{1}{\hbar^2}\int_0^t \mathrm{d}t' \,&\left\langle\hat{\mathbf{E}}_v^{(+)}(t)\hat{\mathbf{E}}_v^{(-)}(t')\right\rangle\left(\hat{\mathbf{d}}^\dagger(t)\hat{\mathbf{d}}(t')\rho(t)-\hat{\mathbf{d}}(t')\rho(t)\hat{\mathbf{d}}^\dagger(t)\right)\\
&+\left\langle\hat{\mathbf{E}}_v^{(+)}(t')\hat{\mathbf{E}}_v^{(-)}(t)\right\rangle\left(\rho(t)\hat{\mathbf{d}}^\dagger(t')\hat{\mathbf{d}}(t)-\hat{\mathbf{d}}(t)\rho(t)\hat{\mathbf{d}}^\dagger(t')\right)\\
&+\left\langle\hat{\mathbf{E}}_v^{(-)}(t)\hat{\mathbf{E}}_v^{(+)}(t')\right\rangle\left(\hat{\mathbf{d}}(t)\hat{\mathbf{d}}^\dagger(t')\rho(t)-\hat{\mathbf{d}}^\dagger(t')\rho(t)\hat{\mathbf{d}}(t)\right)\\
&+\left\langle\hat{\mathbf{E}}_v^{(-)}(t')\hat{\mathbf{E}}_v^{(+)}(t)\right\rangle\left(\rho(t)\hat{\mathbf{d}}(t')\hat{\mathbf{d}}^\dagger(t)-\hat{\mathbf{d}}^\dagger(t)\rho(t)\hat{\mathbf{d}}(t')\right)\\
&+\left\langle\hat{\mathbf{E}}_v^{(+)}(t)\hat{\mathbf{E}}_v^{(+)}(t')\right\rangle\left(\hat{\mathbf{d}}^\dagger(t)\hat{\mathbf{d}}^\dagger(t')\rho(t)-\hat{\mathbf{d}}^\dagger(t')\rho(t)\hat{\mathbf{d}}^\dagger(t)\right)\\
&+\left\langle\hat{\mathbf{E}}_v^{(+)}(t')\hat{\mathbf{E}}_v^{(+)}(t)\right\rangle\left(\rho(t)\hat{\mathbf{d}}^\dagger(t')\hat{\mathbf{d}}^\dagger(t)-\hat{\mathbf{d}}^\dagger(t)\rho(t)\hat{\mathbf{d}}^\dagger(t')\right)\\
&+\left\langle\hat{\mathbf{E}}_v^{(-)}(t)\hat{\mathbf{E}}_v^{(-)}(t')\right\rangle\left(\hat{\mathbf{d}}(t)\hat{\mathbf{d}}(t')\rho(t)-\hat{\mathbf{d}}(t')\rho(t)\hat{\mathbf{d}}(t)\right)\\
&+\left\langle\hat{\mathbf{E}}_v^{(-)}(t')\hat{\mathbf{E}}_v^{(-)}(t)\right\rangle\left(\rho(t)\hat{\mathbf{d}}(t')\hat{\mathbf{d}}(t)-\hat{\mathbf{d}}(t)\rho(t)\hat{\mathbf{d}}(t')\right)\end{aligned} \tag{5.59}$$

Approximations 4 and 5:

- We assume that the correlation functions $\left\langle\hat{\mathbf{E}}_v^{(+)}(t)\hat{\mathbf{E}}_v^{(+)}(t')\right\rangle$, $\left\langle\hat{\mathbf{E}}_v^{(+)}(t')\hat{\mathbf{E}}_v^{(+)}(t)\right\rangle$, $\left\langle\hat{\mathbf{E}}_v^{(-)}(t)\hat{\mathbf{E}}_v^{(-)}(t')\right\rangle$ and $\left\langle\hat{\mathbf{E}}_v^{(-)}(t')\hat{\mathbf{E}}_v^{(-)}(t)\right\rangle$ are all null, which is justified if the electromagnetic environment is in thermodynamic equilibrium.
- We also neglect the correlation functions $\left\langle\hat{\mathbf{E}}_v^{(-)}(t)\hat{\mathbf{E}}_v^{(+)}(t')\right\rangle$ and $\left\langle\hat{\mathbf{E}}_v^{(-)}(t')\hat{\mathbf{E}}_v^{(+)}(t)\right\rangle$, which is justified is one considers an atom emitting at optical frequencies.

Thus, only the first 2 terms remain in Eq. (5.59) which reduces to

$$\frac{\partial\rho(t)}{\partial t} = -\frac{1}{\hbar^2}\int_0^t \mathrm{d}t' \left\langle \hat{\mathbf{E}}_\nu^{(+)}(t)\hat{\mathbf{E}}_\nu^{(-)}(t')\right\rangle \left(\hat{\mathbf{d}}^\dagger(t)\hat{\mathbf{d}}(t')\rho(t) - \hat{\mathbf{d}}(t')\rho(t)\hat{\mathbf{d}}^\dagger(t)\right) + \left\langle \hat{\mathbf{E}}_\nu^{(+)}(t')\hat{\mathbf{E}}_\nu^{(-)}(t)\right\rangle \left(\rho(t)\hat{\mathbf{d}}^\dagger(t')\hat{\mathbf{d}}(t) - \hat{\mathbf{d}}(t)\rho(t)\hat{\mathbf{d}}^\dagger(t')\right) \tag{5.60}$$

Note: By using the property of the correlation function $\left\langle \hat{\mathbf{E}}_\nu^{(+)}(t')\hat{\mathbf{E}}_\nu^{(-)}(t)\right\rangle = \left\langle \hat{\mathbf{E}}_\nu^{(+)}(t)\hat{\mathbf{E}}_\nu^{(-)}(t')\right\rangle^*$, and noting the fact that $\left(\rho(t)\hat{\mathbf{d}}^\dagger(t')\hat{\mathbf{d}}(t) - \hat{\mathbf{d}}(t)\rho(t)\hat{\mathbf{d}}^\dagger(t')\right) = \left(\hat{\mathbf{d}}^\dagger(t)\hat{\mathbf{d}}(t')\rho(t) - \hat{\mathbf{d}}(t')\rho(t)\hat{\mathbf{d}}^\dagger(t)\right)^\dagger$, one can see that the second term in Eq. (5.60) is actually the Hermitian conjugate (H.c.) of the first one. Therefore, we simply write Eq. (5.60) as

$$\frac{\partial\rho(t)}{\partial t} = -\frac{1}{\hbar^2}\int_0^t \mathrm{d}t' \left\langle \hat{\mathbf{E}}_\nu^{(+)}(t)\hat{\mathbf{E}}_\nu^{(-)}(t')\right\rangle \left(\hat{\mathbf{d}}^\dagger(t)\hat{\mathbf{d}}(t')\rho(t) - \hat{\mathbf{d}}(t')\rho(t)\hat{\mathbf{d}}^\dagger(t)\right) + \text{H.c.} \tag{5.61}$$

Eq. (5.61) is the starting point to calculate the dynamical evolution of any multilevel atom. Here, we proceed by writing explicitely the terms in the integrand using the expressions for $\hat{\mathbf{d}}(t)$ and $\hat{\mathbf{d}}^\dagger(t)$ from Eqs. (5.50) and (5.51), which corresponds to the Λ-configuration with orthogonal transitions:

$$\hat{\mathbf{d}}^\dagger(t)\hat{\mathbf{d}}(t')\rho(t) = e^{\mathrm{i}\omega_1(t-t')}\mathbf{d}_{01}\left|0\right\rangle\left\langle 0\right|\mathbf{d}_{01}^*\rho(t) + e^{\mathrm{i}\omega_2(t-t')}\mathbf{d}_{02}\left|0\right\rangle\left\langle 0\right|\mathbf{d}_{02}^*\rho(t) \tag{5.62}$$

and by defining $\rho_{00}(t) \equiv \left\langle 0\right|\rho(t)\left|0\right\rangle$ to simplify the expressions:

$$\begin{aligned}\hat{\mathbf{d}}(t')\rho(t)\hat{\mathbf{d}}^\dagger(t) = {} & +e^{\mathrm{i}\omega_1(t-t')}\rho_{00}(t)\mathbf{d}_{01}^*\left|1\right\rangle\left\langle 1\right|\mathbf{d}_{01} + e^{\mathrm{i}\omega_2(t-t')}\rho_{00}(t)\mathbf{d}_{02}^*\left|2\right\rangle\left\langle 2\right|\mathbf{d}_{02} \\ & + e^{\mathrm{i}\omega_1 t}e^{-\mathrm{i}\omega_2 t'}\rho_{00}(t)\mathbf{d}_{02}^*\left|2\right\rangle\left\langle 1\right|\mathbf{d}_{01} + e^{\mathrm{i}\omega_2 t}e^{-\mathrm{i}\omega_1 t'}\rho_{00}(t)\mathbf{d}_{01}^*\left|1\right\rangle\left\langle 2\right|\mathbf{d}_{02}\end{aligned} \tag{5.63}$$

Substituting these expressions in Eq. (5.61) and by factorizing the exponential terms, we get:

$$\begin{aligned}\frac{\partial\rho(t)}{\partial t} = -\frac{1}{\hbar^2}\int_0^t \mathrm{d}t' \left\langle \hat{\mathbf{E}}_\nu^{(+)}(t)\hat{\mathbf{E}}_\nu^{(-)}(t')\right\rangle \times [& e^{\mathrm{i}\omega_1(t-t')}\left(\mathbf{d}_{01}\left|0\right\rangle\left\langle 0\right|\mathbf{d}_{01}^*\rho(t) - \rho_{00}(t)\mathbf{d}_{01}^*\left|1\right\rangle\left\langle 1\right|\mathbf{d}_{01}\right) \\ & + e^{\mathrm{i}\omega_2(t-t')}\left(\mathbf{d}_{02}\left|0\right\rangle\left\langle 0\right|\mathbf{d}_{02}^*\rho(t) - \rho_{00}(t)\mathbf{d}_{02}^*\left|2\right\rangle\left\langle 2\right|\mathbf{d}_{02}\right) \\ & - e^{\mathrm{i}\omega_1 t}e^{-\mathrm{i}\omega_2 t'}\rho_{00}(t)\mathbf{d}_{02}^*\left|2\right\rangle\left\langle 1\right|\mathbf{d}_{01} - e^{\mathrm{i}\omega_2 t}e^{-\mathrm{i}\omega_1 t'}\rho_{00}(t)\mathbf{d}_{01}^*\left|1\right\rangle\left\langle 2\right|\mathbf{d}_{02}] \\ & + \text{H.c.}\end{aligned} \tag{5.64}$$

Change of variable: $\left\langle \hat{\mathbf{E}}_\nu^{(+)}(t)\hat{\mathbf{E}}_\nu^{(-)}(t')\right\rangle = \left\langle \hat{\mathbf{E}}_\nu^{(+)}(t-t')\hat{\mathbf{E}}_\nu^{(-)}(0)\right\rangle$ (the correlation function only depends on the time difference). Making the change of variable $\tau = t - t'$, and:

Approximation 6: We make the upper limit tend to infinity. Eq. (5.64) becomes

$$\begin{aligned}\frac{\partial\rho(t)}{\partial t} = -\frac{1}{\hbar^2}\int_0^\infty \mathrm{d}\tau \left\langle \hat{\mathbf{E}}_\nu^{(+)}(\tau)\hat{\mathbf{E}}_\nu^{(-)}(0)\right\rangle \times [& e^{\mathrm{i}\omega_1\tau}\left(\mathbf{d}_{01}\left|0\right\rangle\left\langle 0\right|\mathbf{d}_{01}^*\rho(t) - \rho_{00}(t)\mathbf{d}_{01}^*\left|1\right\rangle\left\langle 1\right|\mathbf{d}_{01}\right) \\ & + e^{\mathrm{i}\omega_2\tau}\left(\mathbf{d}_{02}\left|0\right\rangle\left\langle 0\right|\mathbf{d}_{02}^*\rho(t) - \rho_{00}(t)\mathbf{d}_{02}^*\left|2\right\rangle\left\langle 2\right|\mathbf{d}_{02}\right) \\ & - e^{\mathrm{i}(\omega_1-\omega_2)t}e^{\mathrm{i}\omega_2\tau}\rho_{00}(t)\mathbf{d}_{02}^*\left|2\right\rangle\left\langle 1\right|\mathbf{d}_{01} - e^{\mathrm{i}(\omega_2-\omega_1)t}e^{\mathrm{i}\omega_1\tau}\rho_{00}(t)\mathbf{d}_{01}^*\left|1\right\rangle\left\langle 2\right|\mathbf{d}_{02}] \\ & + \text{H.c.}\end{aligned} \tag{5.65}$$

We finally introduce the positive part of the correlation tensor as:

$$\hat{\mathbf{C}}^{(+)}(\omega) \equiv \int_0^\infty \mathrm{d}\tau \left\langle \hat{\mathbf{E}}_\nu^{(+)}(\tau)\hat{\mathbf{E}}_\nu^{(-)}(0)\right\rangle e^{\mathrm{i}\omega\tau} \tag{5.66}$$

to get:

$$\begin{aligned}\frac{\partial\rho(t)}{\partial t} = &-\Gamma_1\left(|0\rangle\langle 0|\rho(t) - \rho_{00}(t)|1\rangle\langle 1|\right) - \Gamma_2\left(|0\rangle\langle 0|\rho(t) - \rho_{00}(t)|2\rangle\langle 2|\right)\\ &+\Gamma_{21}e^{\mathrm{i}(\omega_1-\omega_2)t}\rho_{00}(t)|2\rangle\langle 1| + \Gamma_{12}e^{\mathrm{i}(\omega_2-\omega_1)t}\rho_{00}(t)|1\rangle\langle 2| + \mathrm{H.c.}\end{aligned} \tag{5.67}$$

with the following definitions of the coefficients:

$$\Gamma_i \equiv \frac{1}{\hbar^2}\mathbf{d}_{0i}^* \cdot \hat{\mathbf{C}}^{(+)}(\omega_1)\cdot\mathbf{d}_{0i} \tag{5.68}$$

and

$$\Gamma_{ij} \equiv \frac{1}{\hbar^2}\mathbf{d}_{0i}^* \cdot \hat{\mathbf{C}}^{(+)}(\omega_1)\cdot\mathbf{d}_{0j} \tag{5.69}$$

Remember that in the Master Equation above $\rho(t)$ is still in the interaction picture, and we come back to the *Schrödinger picture* assuming furthermore that the transition energies are about the same $\omega_1 \simeq \omega_2 \equiv \omega_0$

$$\begin{aligned}\frac{\partial\rho(t)}{\partial t} = &-\mathrm{i}\omega_0|0\rangle\langle 0|\rho(t) - \Gamma_1\left(|0\rangle\langle 0|\rho(t) - \rho_{00}(t)|1\rangle\langle 1|\right) - \Gamma_2\left(|0\rangle\langle 0|\rho(t) - \rho_{00}(t)|2\rangle\langle 2|\right)\\ &+\Gamma_{21}\rho_{00}(t)|2\rangle\langle 1| + \Gamma_{12}\rho_{00}(t)|1\rangle\langle 2| + \mathrm{H.c.}\end{aligned} \tag{5.70}$$

In Eq. (5.70), we have introduced the definitions of the coefficients:

$$\Gamma_i \equiv \frac{1}{\hbar^2}\mathbf{d}_{0i}^* \cdot \hat{\mathbf{C}}^{(+)}(\mathbf{r}_0,\mathbf{r}_0,\omega_0)\cdot\mathbf{d}_{0i} \tag{5.71}$$

and

$$\Gamma_{ij} \equiv \frac{1}{\hbar^2}\mathbf{d}_{0i}^* \cdot \hat{\mathbf{C}}^{(+)}(\mathbf{r}_0,\mathbf{r}_0,\omega_0)\cdot\mathbf{d}_{0j} \tag{5.72}$$

defined in terms of the *positive part of the correlation tensor* $\hat{\mathbf{C}}^{(+)}$ that reads:

$$\hat{\mathbf{C}}^{(+)}(\mathbf{r},\mathbf{r}',\omega) = \int_0^{+\infty} \mathrm{d}\tau \left\langle \hat{\mathbf{E}}_\nu^{(+)}(\mathbf{r},\tau)\hat{\mathbf{E}}_\nu^{(-)}(\mathbf{r}',0)\right\rangle e^{\mathrm{i}\omega\tau} \tag{5.73}$$

where the braket indicates an ensemble average:

$$\left\langle \hat{\mathbf{E}}_\nu^{(+)}(\mathbf{r},\tau)\hat{\mathbf{E}}_\nu^{(-)}(\mathbf{r}',0)\right\rangle \equiv \mathrm{Tr}_e\left(\rho_e(0)\hat{\mathbf{E}}_\nu^{(+)}(\mathbf{r},\tau)\hat{\mathbf{E}}_\nu^{(-)}(\mathbf{r}',0)\right) \tag{5.74}$$

Using the mathematical relation:

$$\mathcal{P}\left(\frac{1}{x}\right) = \frac{1}{x+\mathrm{i}\epsilon} + \mathrm{i}\pi\delta(x) \qquad \text{with} \quad \epsilon\to 0 \tag{5.75}$$

one can demonstrate that:

$$\hat{\mathbf{C}}^{(+)}(\mathbf{r},\mathbf{r}',\omega_0) = \frac{1}{2}\hat{\mathbf{C}}(\mathbf{r},\mathbf{r}',\omega_0) + \frac{\mathrm{i}}{2\pi}\mathcal{P}\left\{\int_0^{+\infty} \mathrm{d}\omega\, \frac{\hat{\mathbf{C}}(\mathbf{r},\mathbf{r}',\omega)}{\omega_0-\omega}\right\} \tag{5.76}$$

where $\hat{\mathbf{C}}$ is the correlation tensor defined as:

$$\hat{\mathbf{C}}(\mathbf{r},\mathbf{r}',\omega) \equiv \int_{-\infty}^{+\infty} \mathrm{d}\tau\, \left\langle \hat{\mathbf{E}}_v^{(+)}(\mathbf{r},\tau)\hat{\mathbf{E}}_v^{(-)}(\mathbf{r}',0)\right\rangle e^{\mathrm{i}\omega\tau} \tag{5.77}$$

Therefore, the coefficients Γ_i become:

$$\Gamma_i = \frac{\gamma_i}{2} + \mathrm{i}\Delta\omega_i \tag{5.78}$$

with

$$\gamma_i = \frac{1}{\hbar^2}\mathbf{d}_{0i}^* \cdot \hat{\mathbf{C}}(\mathbf{r}_0,\mathbf{r}_0,\omega_0)\cdot\mathbf{d}_{0i} \tag{5.79}$$

and

$$\Delta\omega_i = \frac{1}{2\pi\hbar^2}\mathcal{P}\left\{\int_0^{+\infty} \mathrm{d}\omega\, \frac{\mathbf{d}_{0i}^* \cdot \hat{\mathbf{C}}(\mathbf{r}_0,\mathbf{r}_0,\omega)\cdot\mathbf{d}_{0i}}{\omega_0-\omega}\right\} \tag{5.80}$$

where γ_i can be interpreted as the decay rate on the transition $|0\rangle \rightarrow |i\rangle$, and $\Delta\omega_i$ is the Lamb shift of the level $|i\rangle$.

In the following, we recast the Lamb shift into the transition frequency and reduce $\hat{\mathbf{C}}^{(+)}(\mathbf{r},\mathbf{r}',\omega_0)$ as:

$$\hat{\mathbf{C}}^{(+)}(\mathbf{r},\mathbf{r}',\omega_0) \equiv \frac{1}{2}\hat{\mathbf{C}}(\mathbf{r},\mathbf{r}',\omega_0) \tag{5.81}$$

Therefore, the coefficients become:

$$\Gamma_i \approx \frac{\gamma_i}{2} \qquad \text{with} \quad \gamma_i = \frac{1}{\hbar^2}\mathbf{d}_{0i}^* \cdot \hat{\mathbf{C}}(\mathbf{r}_0,\mathbf{r}_0,\omega_0)\cdot\mathbf{d}_{0i} \tag{5.82}$$

and

$$\Gamma_{ij} \approx \frac{\kappa_{ij}}{2} \qquad \text{with} \quad \kappa_{ij} = \frac{1}{\hbar^2}\mathbf{d}_{0i}^* \cdot \hat{\mathbf{C}}(\mathbf{r}_0,\mathbf{r}_0,\omega_0)\cdot\mathbf{d}_{0j}. \tag{5.83}$$

5.B Metasurface design: super-cells

Here, we answer the following questions:

- Is there a minimum size for a super-cell (other than the practical limitation coming from the nanoantennas which have a finite size in practice, which will constrain even more the minimum size of a super-cell that one can design, as we will see in the next section)?
- Is there a maximum size? For a given configuration (that is a point source at distance d from the metasurface), what super-cell sizes must be used to impart the desired phase-shift? Where to place them on the metasurface?

To answer these questions, we derive the expression of the **lengths of the super-cells** as a function of the parameters d and λ_0 in 1D. For that, let us first denote by r_n the position at which ends the super-cell labelled by n, starting from the center of the metasurface ($n = 1$ corresponds to the first super-cell, $n = 2$ corresponds to the second super-cell etc...). This corresponds to the positions of the phase discontinuities of the red dashed curve in Fig. 5.3 (a). The positions r_n are obtained by solving the following equation:

$$|\varphi_x(r_n) - \varphi_y(0)| = 2\pi n \tag{5.84}$$

with $\varphi_x(0) = \pi - 2k_0 d$ [see Eq. (5.32)]. A simple algebric calculation leads to the result:

$$r_n = \sqrt{n(\lambda_0 d) + n^2 \left(\frac{\lambda_0}{2}\right)^2} \tag{5.85}$$

One can now deduce the length Λ_n^{sc} of a super-cell n. It simply reads:

$$\Lambda_n^{\text{sc}} = r_n - r_{n-1} \tag{5.86}$$

In Fig. 5.11, we show the length Λ_n^{sc} for the first 50 super-cells (green dots). One can see that the length decreases monotically: the first super-cells have the larger sizes, and as n increases the length of the super-cells dimishes.

Maximum and minimum lengths: One can derive approximate expressions for Λ_n^{sc} for small n (that is for the first super-cells) and for large n (that is for the more distant super-cells). Indeed, in Eq. (5.85) one can see two terms: the first term is $(\lambda_0 d)$, weighted by n, and the second term is $(\lambda_0/2)^2$, weighted by n^2.

For small n, the second term can be neglected, because for the source distance d considered here, $(\lambda_0 d) \gg (\lambda_0/2)^2$ (d is several wavelengths, like $d \sim 10\lambda_0$). Then Eq. (5.85) can be approximated by:

$$r_n \simeq \sqrt{n(\lambda_0 d)} \tag{5.87}$$

which leads to the following approximated length:

$$\Lambda_n^{\text{sc}} \simeq (\sqrt{n} - \sqrt{n-1})\sqrt{\lambda_0 d} \tag{5.88}$$

This expression is shown in Fig. 5.11 (blue dashed line) and works well until $n = 3$ for this specific case where $d = 10\lambda_0$. Moreover, from this formula one can get the **maximum length** of a super-cell, which is the length of the super-cell $n = 1$:

$$\Lambda_{\text{max}}^{\text{sc}} = \sqrt{\lambda_0 d} \tag{5.89}$$

For n large enough, the first term can be neglected and Eq. (5.85) can be approximated by:

$$r_n \simeq n\frac{\lambda_0}{2} \tag{5.90}$$

which leads to the following approximated length:

$$\Lambda_n^{\text{sc}} \simeq \frac{\lambda_0}{2} \tag{5.91}$$

This limit is shown in Fig. 5.11 (black dashed line) and one can see that the convergence is fast. This formula therefore gives the **minimum length** of a super-cell

$$\Lambda_{\text{min}}^{\text{sc}} = \frac{\lambda_0}{2} \tag{5.92}$$

Note: It is noteworthy to point out that these 2 extreme quantities $\Lambda_{\text{min}}^{\text{sc}}$ and $\Lambda_{\text{max}}^{\text{sc}}$ can be deduced from the grating equation for a *Littrow configuration* (where $\theta_r = \theta_i$, θ_i incident angle, θ_r diffracted angle into the first order):

$$2\,\Lambda \sin\theta_i = \lambda_0 \tag{5.93}$$

with Λ the grating period. In the very limit of large incident angle $\theta_i = 90°$, one gets $\Lambda_{\text{min}} = \lambda_0/2$ for the grating period, and for the limit of very small incident angles, let's say when the light impinges on the edge of the *first* period of the grating $\theta_i \simeq (\Lambda/2)/d$. Note that $\Lambda/2$ is because the grating is symmetric in 0 and the first period extends from $[-\Lambda/2; +\Lambda/2]$; moreover, it does not really make sense to consider smaller angle than that as the light would not see any period and would be reflected specularly. One then gets $\Lambda_{\text{max}} = \sqrt{\lambda_0 d}$.

Example: Let us calculate the size of a metasurface we could fabricate. Let us consider we use 40 super-cells. The extremity of the metasurface from the origin is therefore r_{40}. For $d = 10\lambda_0$ and $\lambda_0 = 852\,\text{nm}$, this corresponds to $r_{40} \simeq 24\,\mu\text{m}$ (which gives a metasurface of cross-section $48\,\mu\text{m} \times 48\,\mu\text{m}$). This corresponds to a NA defined as $\text{NA} = \sin\theta_i \simeq 0.94$ (that is an incident angle $\theta_i = 70°$). So in summary, for the configuration $d = 10\lambda_0$ and $\lambda_0 = 852\,\text{nm}$, a metasurface with a $\text{NA} = 0.94$ will have a cross-section $48\,\mu\text{m} \times 48\,\mu\text{m}$, and will be made of 40 different super-cells (differing by their length Λ_n^{sc}), whose lengths vary from $\Lambda_{\text{min}}^{\text{sc}} < \Lambda_n^{\text{sc}} < \Lambda_{\text{max}}^{\text{sc}}$, with $\Lambda_{\text{max}}^{\text{sc}} = \sqrt{10}\lambda_0 \simeq 3.16\lambda_0 \simeq 2.694\,\mu\text{m}$, and $\Lambda_{\text{min}}^{\text{sc}} \simeq 0.426\,\mu\text{m}$.

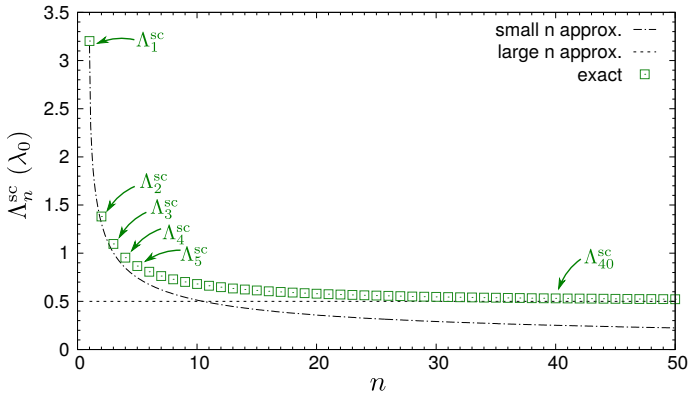

Figure 5.11 – Lengths of the super-cells of the metasurface. Green dots: Lengths Λ_n^{sc} of the super-cells, labelled by n starting from the center of the metasurface, obeying the relation: $\Lambda_n^{sc} = \sqrt{n\lambda_0 d + n^2(\lambda_0/2)^2} - \sqrt{(n-1)\lambda_0 d + (n-1)^2(\lambda_0/2)^2}$. Blue dashed line: asymptotic expression valid for small n: $\Lambda_n^{sc} \simeq (\sqrt{n} - \sqrt{n-1})\sqrt{\lambda_0 d}$, which gives the maximum length for a super-cell (for $n = 1$): $\Lambda_1^{sc} \simeq \sqrt{\lambda_0 d}$. Black dashed line: asymptotic expression valid for large n: $\Lambda_n^{sc} \to \lambda_0/2$, which gives the minimum length for a super-cell (for $n = \infty$): $\Lambda_\infty^{sc} = \lambda_0/2$. Here, the position of the atom d is taken to be $d = 10\lambda_0$.

5.C Metasurface design: unit-cells

The problem is that we want to span a *continuous* phase profile with *discrete* elements: this will definitely limit the *efficiency* of the metasurface, and to ensure the best efficiency, one has only a narrow working window and must follow several rules [9]:

- The first thing we desire is to use as much as possible nanoantennas of different sizes (*i.e.*, resonances) in order to sample the phase finely and ensure a good efficiency.
- However, if the elements are too closed, they are no longer independent and become coupled, resulting in a lost of control of the phase which is no-longer really monitored locally at the level of a single element.
- An other constraint will come from fabrication limits, for which a spacing of minimum 50 nm between two adjacent nanoantennas is necessary, as this is close to the resolution limit.

Reaching a good balance requires the use of metallic nanostructures which ensure a strong confinement of light, and to carefully set the size Λ^{uc} of a unit-cell (containing one nanoantenna). It seems that a good balance is reached by choosing a size $\lambda_0/7 \leq \Lambda^{\text{uc}} \leq \lambda_0/3$ (see Refs. [7, 21, 22, 24]). Note that this size also sets a upper-size limit for the nanoantenna dimensions.

Example: These considerations immediately limit the efficiency of the metasurface. Indeed, for the metasurface considered before made of 40 super-cells to reach a NA$\simeq$ 0.94, one can see from Fig. 5.11 that most of the super-cells have a length closed to the minimum size $\Lambda^{\text{sc}}_{\text{min}} = \lambda_0/2 = 426\,\text{nm}$. If one takes a unit-cell size of $\Lambda^{\text{uc}} = \lambda_0/5 \simeq 170\,\text{nm}$, one can see that these super-cells will contain at most 2 nanoantennas, which is way not sufficient to sample a phase range of 2π, and will eventually lead to a poor efficiency for these super-cells.

If one considers that at least 5 nanoantennas per super-cell are necessary to ensure a good efficiency, only the super-cells of length $\Lambda^{\text{sc}}_n \geq 5\Lambda^{\text{uc}} = \lambda_0$ must be retained. In the previous example, the super-cell $n = 3$ is the very limit with $\Lambda^{\text{sc}}_3 \simeq 915\,\text{nm}$.

So by saying that the metasurface will be efficient only with 3 types of super-cells, one can calculate the corresponding NA: with $r_3 \simeq 4.820\mu\text{m}$, NA$= r_3/\sqrt{r_3^2 + d^2} \simeq 0.49$ (maximum incident angle of 29°).

Generalization: We derived the limit value of NA$\simeq 0.5$ on a particular case, and our goal now is to show that, given a size of $\Lambda^{\text{uc}} = \lambda_0/5$ per unit cell, the NA is the same for any distance d of the point source. Let us define the critical length Λ_c beyond which the super-cell efficiency is considered as dropping as:

$$\Lambda_c \sim 5\Lambda^{\text{uc}} = \lambda_0 \tag{5.94}$$

We want to find the last super-cell n_c with a length $\Lambda^{\text{sc}}_{n_c} \geq \Lambda_c$. Considering that it happens for small n, we can use Eq. (5.88) (which must be checked a posteriori) to find the *largest* n satisfying the following transcendantal inequality:

$$\Lambda^{\text{sc}}_{n_c} \simeq (\sqrt{n_c} - \sqrt{n_c - 1})\sqrt{\lambda_0 d} \geq \lambda_0 \Rightarrow \sqrt{n_c} - \sqrt{n_c - 1} \geq \sqrt{\frac{\lambda_0}{d}} \tag{5.95}$$

From the above equation, one can see that as d increases, the number of super-cells n_c increases as well. We can then calculate the position r_{n_c} where the last super-cell ends using Eq. (5.87):

$$r_{n_c} \simeq \sqrt{n_c \lambda_0 d} \tag{5.96}$$

and calculate the NA of the metasurface as $\mathrm{NA} = r_{n_c}/\sqrt{r_{n_c}^2 + d^2}$ which gives:

$$\mathrm{NA} \simeq \sqrt{\frac{n_c \lambda_0}{n_c \lambda_0 + d}} \tag{5.97}$$

We show in Fig. 5.12 this NA as a function of d: it is found that the NA is invariant, and is about $\mathrm{NA} \simeq 0.5$ ($\theta_i \simeq 30°$). This is because when d increases, n_c increases as well [Eq. (5.95)], that is the last super-cell with length $\Lambda_n^{sc} \geq \Lambda_c$ is found to be further (see Fig. 5.13). The result is that the NA remains invariant [see Eq. (5.97)].

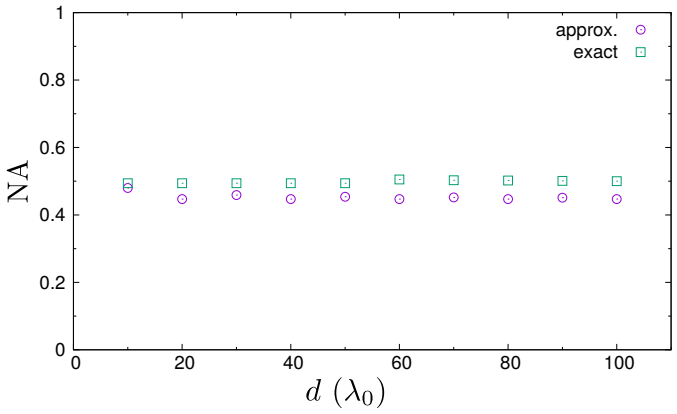

Figure 5.12 – Numerical aperture NA corresponding to the region of the metasurface considered as efficient. NA as a function of the distance d of the point source. Red dots: approximated calculations resulting from the use of Eqs. (5.87), (5.88) and (5.97). Green line: exact calculation resulting from the use of Eqs. (5.85) and (5.86).

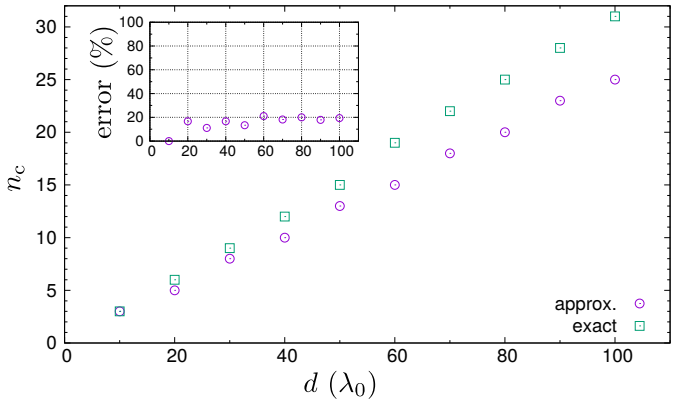

Figure 5.13 – Number of super-cells n_c considered as efficient. n_c as a function of the distance d of the point source. Red dots: approximated calculations resulting from the use of Eqs. (5.87), (5.88) and (5.95). Green line: exact calculation resulting from the use of Eqs. (5.85) and (5.86). The inset shows the relative error between the exact and approximated calculations.

Bibliography

[1] J.-M. Raimond and S. Haroche, *Exploring the quantum* (Oxford University Press, Oxford, 2006).

[2] D. G. Baranov, M. Wersall, J. Cuadra, T. J. Antosiewicz, and T. Shegai, ACS Photonics **5**, 24 (2017).

[3] G. Hétet, L. Slodička, A. Glätzle, M. Hennrich, and R. Blatt, Physical Review A **82**, 063812 (2010).

[4] U. Dorner and P. Zoller, Physical Review A **66**, 023816 (2002).

[5] J. Kästel and M. Fleischhauer, Physical Review A **71**, 011804 (2005).

[6] J. Eschner, C. Raab, F. Schmidt-Kaler, and R. Blatt, Nature **413**, 495 (2001).

[7] P. K. Jha, X. Ni, C. Wu, Y. Wang, and X. Zhang, Physical Review Letters **115**, 025501 (2015).

[8] P. K. Jha, N. Shitrit, X. Ren, Y. Wang, and X. Zhang, Physical Review Letters **121**, 116102 (2018).

[9] P. Lalanne and P. Chavel, Laser & Photonics Reviews **11**, 1600295 (2017).

[10] P. Genevet, F. Capasso, F. Aieta, M. Khorasaninejad, and R. Devlin, Optica **4**, 139 (2017).

[11] G. Agarwal, Physical Review Letters **84**, 5500 (2000).

[12] D. Suter, *The physics of laser-atom interactions*, Vol. 19 (Cambridge University Press, 1997).

[13] E. Togan, Y. Chu, A. Trifonov, L. Jiang, J. Maze, L. Childress, M. G. Dutt, A. S. Sørensen, P. Hemmer, A. S. Zibrov, *et al.*, Nature **466**, 730 (2010).

[14] S. M. Barnett and P. M. Radmore, *Methods in theoretical quantum optics*, Vol. 15 (Oxford University Press, 2002).

[15] H. J. Carmichael, *Statistical methods in quantum optics 1: master equations and Fokker-Planck equations* (Springer Science & Business Media, 2013).

[16] W. Jhe, A. Anderson, E. Hinds, D. Meschede, L. Moi, and S. Haroche, Physical Review Letters **58**, 666 (1987).

[17] T. Taillandier-Loize, J. Baudon, G. Dutier, F. Perales, M. Boustimi, and M. Ducloy, Physical Review A **89**, 052514 (2014).

[18] M. Boustimi, B. V. De Lesegno, J. Baudon, J. Robert, and M. Ducloy, Physical Review Letters **86**, 2766 (2001).

[19] G. C. Des Francs, A. Bouhelier, E. Finot, J.-C. Weeber, A. Dereux, C. Girard, and E. Dujardin, Optics Express **16**, 17654 (2008).

[20] E. Lassalle, N. Bonod, T. Durt, and B. Stout, Optics Letters **43**, 1950 (2018).

[21] S. Sun, K.-Y. Yang, C.-M. Wang, T.-K. Juan, W. T. Chen, C. Y. Liao, Q. He, S. Xiao, W.-T. Kung, G.-Y. Guo, *et al.*, Nano Letters **12**, 6223 (2012).

[22] A. Pors, O. Albrektsen, I. P. Radko, and S. I. Bozhevolnyi, Scientific Reports **3**, 2155 (2013).

[23] G. Zheng, H. Mühlenbernd, M. Kenney, G. Li, T. Zentgraf, and S. Zhang, Nature Nanotechnology **10**, 308 (2015).

[24] P. K. Jha, N. Shitrit, J. Kim, X. Ren, Y. Wang, and X. Zhang, ACS Photonics **5**, 971 (2017).

[25] J. Hugonin and P. Lalanne, *Reticolo software for grating analysis* (Institute d'Optique, Palaiseau, France, 2005).

[26] M. Moharam, E. B. Grann, D. A. Pommet, and T. Gaylord, Journal of the Optical Society of America A **12**, 1068 (1995).

[27] L. Li, Journal of the Optical Society of America A **14**, 2758 (1997).

[28] P. Lalanne and M. P. Jurek, Journal of Modern Optics **45**, 1357 (1998).

[29] E. Popov and M. Nevière, Journal of the Optical Society of America A **17**, 1773 (2000).

[30] B. Stout, J.-C. Auger, and J. Lafait, Journal of Modern Optics **49**, 2129 (2002).

[31] B. Stout, A. Devilez, B. Rolly, and N. Bonod, Journal of the Optical Society of America B **28**, 1213 (2011).

[32] E. Lassalle, A. Devilez, N. Bonod, T. Durt, and B. Stout, Journal of the Optical Society of America B **34**, 1348 (2017).

[33] W. Luo, S. Xiao, Q. He, S. Sun, and L. Zhou, Advanced Optical Materials **3**, 1102 (2015).

[34] S. Pancharatnam, in *Proceedings of the Indian Academy of Sciences-Section A*, Vol. 44 (Springer, 1956) pp. 398–417.

[35] M. V. Berry, Journal of Modern Optics **34**, 1401 (1987).

[36] S. Hughes and G. S. Agarwal, Physical Review Letters **118**, 063601 (2017).

CHAPTER 6

Cold atom experiment

6.1 Introduction

This Chapter is the only "experimental" Chapter of this thesis. It aims at presenting the experimental platform dedicated to observe the coherence induced by a metasurface, as predicted in the previous Chapter. The experiment is a *cold atom* experiment, with *cesium* atoms, which contain the three-level structure in Λ-configuration necessary to get a long-lifetime coherence, or more precisely a *tripod* structure with one excited state and three ground states.

The experimental project is threefold. Firstly, we want to start by cooling and trapping a cloud of cesium atoms, using a *magneto-optical trap* (MOT); this is a well-known technique in atomic physics [1], and the starting point of many quantum experiments with atoms. The ingredients of MOT are an ultra high vacuum cell, strong magnetic field gradients, and three pairs of orthogonal counter-propagating laser beams circularly polarized and overlapped at the trapping region, where the magnetic-field gradient is null.

The second objective is to build a *new* technique to trap a single atom, by using a *superoscillatory spot*, and to study it as a new tool to trap and cool a single atom. Its particularity is to be able to localize the light field below the diffraction limit, and therefore to trap an atom with subwavelength precision, which is one of the experimental constraints discussed in the previous Chapter (the coherence is induced only if the atom is in a well defined position). Such a *superoscillatory spot* can be generated by focusing a far red-detuned laser beam with a super-oscillatory lens (SOL), because a SOL allows to focus light on a spot of arbitrary size, below the diffraction limit. Such a technique was used recently to trap nanoparticles [2], and our goal here is to extend this technique to the trapping of single atoms. For a brief history about this promising technique, the discovery of super-oscillations was done in Ref. [3], and first observed in Refs. [4, 5]. Note that there are different techniques to create the super-oscillations [6]. Here, we want to use the technique developped recently and experimentally demonstrated in Ref. [7], where the spot is created by using two spatial light modulators (SLM), which presents the advantage that the spot can be created and imaged at remote distances; this is crucial for us to make the experiment easier since the SOL can now be located outside of the high vacuum cell which contain the atoms.

Eventually, the last step would be to interface the single atom trapped in the super-

oscillatory spot with the fabricated metasurface, and to observe the predicted coherence induced by spontaneous emission. The coherence can be measured by implementing a tomography technique, which consists in reading the atomic populations in different basis, in order to reconstruct the entire density matrix of the atom.

I participated to the first aspect of this project, that is the obtention and characterization of the MOT, and I present in this Chapter the results that we obtained. We first start in Section 6.2 by presenting the cesium atoms and giving some of its spectroscopic properties that will be used for cooling and trapping, and we then explain the principle of a MOT. In Section 6.3, we present the laser part of the MOT, in particular how we control its frequency with very high precision, which is absolutely necessary in order to trap and cool efficiently. At last, in Section 6.4, we present the first measurements of the temperature of the atoms in the MOT, which is one of the most important characteristics of a cold atomic cloud. For that we use the "time-of-flight" method, that we also explain briefly.

6.2 Description of the experimental set-up

The experimental set-up presented here is dedicated to cool down and trap cesium (Cs) atoms. We present first some physical and optical properties of the Cs atoms, and then we briefly explain the technique used to cool and trap the atoms.

6.2.1 Cesium atom

The cesium atom is an alkali-metal atom. It has 55 electrons (atomic number $Z = 55$), and only one in the outermost shell. Its electron configuration is:

$$[\mathrm{Xe}]\,6s^1 \tag{6.1}$$

where [Xe] denotes the electron configuration of the Xenon noble gas (atomic number $Z = 54$). The isotope considered here is ^{133}Cs, as it is the only stable isotope of cesium. Its mass is [8]:

$$m = 2.2 \times 10^{-25}\,\mathrm{kg} \tag{6.2}$$

The first excited state of Cs, labelled 6P-state, has a fine-structure doublet labelled $6P_{1/2}$ and $6P_{3/2}$, which results from the coupling between the orbital angular momentum of the outer electron (commonly denoted $\boldsymbol{L}$) and its spin angular momentum (commonly denoted $\boldsymbol{S}$). The total angular momentum of the electron is then denoted $\boldsymbol{J} = \boldsymbol{L} + \boldsymbol{S}$, and the corresponding quantum number J lies in the range $|L-S| \leq J \leq L+S$. For the ground state 6S, $S = 1/2$ and $L = 0$ so $J = 1/2$, and for the first excited state 6P, $S = 1/2$ and $L = 1$ so $J = 1/2$ or $J = 3/2$, resulting into two states of different energy (the energy level is shifted according to the value of J).

Nomenclature: The nomenclature of the energy levels now becomes obvious: the first number is the principal quantum number of the outer electron, the letter corresponds to the orbital angular quantum number L (with the following correspondance: $L = 0 \rightarrow$

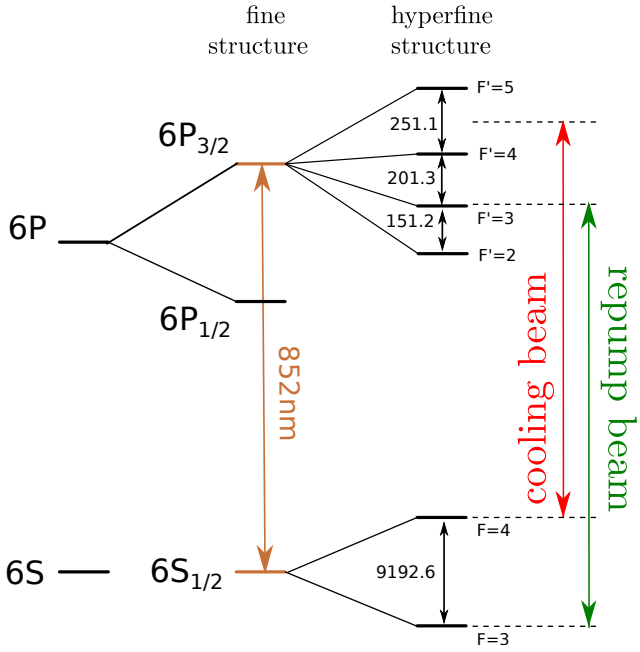

Figure 6.1 – Fine and hyperfine structure of the atomic cesium D_2-line. The cooling is made on the transition between the hyperfine ground state $6S_{1/2}$ $F = 4$ and the hyperfine state $6P_{3/2}$ $F' = 5$. The difference between the energy levels is given in MHz.

S, $L = 1 \rightarrow$ P, etc...), and the subscript gives the value of the total angular momentum quantum number J.

D_2 ($6S_{1/2} \rightarrow 6P_{3/2}$) transition: In what follows, we will only consider the electric dipole transition (called D_2-line) between the $6S_{1/2}$ and the $6P_{3/2}$ states as this transition will be used for the cooling and trapping because it is a cycling transition. Moreover, each of these transitions has an hyperfine-structure, resulting from the coupling between the total angular momentum of the outer electron $\boldsymbol{J}$ and the total angular momentum of the nucleus denoted $\boldsymbol{I}$. The total angular momentum of the atom is then denoted by $\boldsymbol{F} = \boldsymbol{J} + \boldsymbol{I}$, and the corresponding quantum number F lies in the range $|J - I| \leq F \leq J + I$. The nuclear spin of Cs is $I = 7/2$, therefore, for the ground state $6S_{1/2}$, $F = 3$ or $F = 4$, and for the excited state $6P_{3/2}$, F can be 2, 3, 4 or 5. Again, the atomic energy levels are shifted according to the value of F. The energy levels of interest are shown in Fig. 6.1. The frequency ω_0, the wavelength λ_0 (in vacuum), the lifetime τ and the natural decay rate/linewidth (FWHM) γ of this transition are shown in Table 6.1 (taken from [8]).

6.2.2 Magneto-optical trap

To cool down and trap the atoms, we implement a magneto-optical (MOT) trap. In such a trap, there are three ingredients:

- An ultra high vacuum chamber in order to eliminate collisions with other atoms present in air which contribute to heat and destroy the trap; in our vacuum chamber,

ω_0	$2\pi \times 351.7$ THz
λ_0	852.3 nm
τ	30.4 ns
γ	$2\pi \times 5.2$ MHz
I_s	2.7 mW/cm^2

Table 6.1 – Optical properties of the cesium D_2 transition ($6S_{1/2} \rightarrow 6P_{3/2}$) from [8]: transition frequency ω_0, transition wavelength λ_0, lifetime τ and linewidth γ of the state $F' = 5$, and saturation intensity I_s (specified for $F = 4 \rightarrow F' = 5$).

the vacuum pressure is $< 10^{-10}$ mbar.

- A cooling mechanism using pairs of counter-propagating laser beams, based on the radiative force of light: this is called the Doppler cooling.
- A trapping mechanism using pairs of coils to produce a strong magnetic field quadrupole, which will act on the atoms as a potential well and will confine them spatially.

Hereafter, we briefly describe the principle of the Doppler cooling and the principle of a MOT.

Radiation pressure: The Doppler cooling is based on the radiation pressure of light. If ones shines a laser on an atom with resonant photon with respect to a transition of the atom, the atom will scatter the photons, that is it will absorb and emit photons by spontaneous emission cyclically. For each process of absorption or emission, the momentum of the photon $\boldsymbol{p} = \hbar\boldsymbol{k}$ is transfered to the atom, retaining both its magnitude and direction. This momentum kick alters the velocity of the atom by the recoil velocity $\boldsymbol{v}_{rec} = \hbar\boldsymbol{k}/m$. As spontaneous emission is almost isotropic, the net change of momentum is null on average due to this process, and the overall change of the atomic momentum is solely due to absorption, along the direction of the laser beam, resulting in a net force $\boldsymbol{F} = \mathrm{d}\boldsymbol{p}/\mathrm{d}t$.

Doppler cooling: The Doppler cooling exploits the radiation pressure to slow down atoms. Considering a laser beam with wavevector $\boldsymbol{k}_L$ and frequency ω_L, an atom travelling with velocity $\boldsymbol{v}$ sees the Doppler shifted frequency $\omega = \omega_L - \boldsymbol{k}_L \cdot \boldsymbol{v}$. Considering a red-detuned laser compared to the atomic resonant frequency ω_0, *i.e.* $\omega_L < \omega_0$, if the atom propagates against the laser beam ($\boldsymbol{k}_L \cdot \boldsymbol{v} < 0$), then the frequency seen by the atom is higher than the laser frequency $\omega > \omega_L$, and therefore closer to atomic resonance ω_0. As a consequence, the probability of absorption will increase and the atom will slow down. On the contrary, if the atom co-propagates with the laser beam ($\boldsymbol{k}_L \cdot \boldsymbol{v} > 0$), the Doppler shifted frequency increases its distance from resonance and consequently the absorption probability is even further reduced. In that case of red-detuned laser ($\omega_L < \omega_0$), the deceleration force is therefore much stronger than the acceleration one. Note that in the case

of a blue-detuned laser ($\omega_L > \omega_0$), the contrary effect happens, and the acceleration is much stronger than the decceleration. Therefore, to cool down atoms, only a red-detuned laser is relevant.

Optical molasses: One can use appropriately this assymetry to cool down the atoms by using pairs of counter-propagating laser beams. In such a configuration, each atom moving in this field will be acted by a decceleration force much stronger than the acceleration one (both forces equalize only if the atom is not moving). Such an environment is called **optical molasse**.

Doppler limit: With this kind of cooling technique, one reaches a limit for the temperature. This limit is due to heating process arising from the scattering of photons (absorption and emission cycles). This heating can be seen as a Brownian motion in the momentum space. As well described in Ref. [9], "the temperature results from an equilibrium between laser cooling and the heating process arising from the random nature of both the absorption and emission of photons". At equilibrium, the effective temperature reads [1]:

$$T = \frac{\hbar\gamma^2}{8k_B\delta}\left(1 + 4\frac{\delta^2}{\gamma^2} + \frac{I}{I_s}\right) \tag{6.3}$$

where I is the intensity of the laser, I_s is the saturation intensity of the transition considered and reads: $I_s = \hbar\omega^3\gamma/12\pi c^2$, $\delta = \omega_L - \omega_0$ is the laser detuning, and we remind that γ^{-1} is the lifetime of the excited state used for the cooling. From this expression, one can see that the minimum temperature that can reach using this cooling technique, for a detuning $\delta = -\gamma/2$ and in the low-intensity limit, called the **Doppler limit**, is [1]:

$$T_D \simeq \frac{\hbar\gamma}{2k_B} \tag{6.4}$$

For us, we realize the cooling on the $6S_{1/2} \rightarrow 6P_{3/2}$ transition of cesium, which gives a Doppler limit of $T_D \simeq 125\,\mu$K.

Sub-Doppler cooling: As seen from Eq. (6.3), the minimum temperature one expects from the Doppler cooling is obtained for the parameters: $\delta = -\gamma/2$ and $I \rightarrow 0$. However, it is now well-known that one can reach much lower temperatures by taking into account the multilevel structure of the atom and the polarization gradient of the light in a MOT [10, 11]. These mechanisms are known as *polarization gradient cooling* mechanisms, and one of them is the *Sisyphus cooling*. In real 3D optical molasses, both mechanisms occur, and can produce ultra-low temperatures, closed to the recoil temperature given by:

$$T_{\text{rec}} = \frac{\hbar^2k^2}{2mk_B} \tag{6.5}$$

In principle, under some conditions, the temperature should be linear in I and $1/\delta$. The theory of sub-Doppler cooling tells us that for $|\delta| \gg \gamma$ and $\Omega \ll |\delta|$ [10]:

$$k_BT \propto \frac{\hbar\Omega^2}{|\delta|} \tag{6.6}$$

$$\propto \hbar\gamma \times \frac{\gamma}{|\delta|} \times \frac{I}{I_s} \tag{6.7}$$

where Ω is the Rabi frequency of the laser characterizing the coupling between the atomic dipole moment and the laser field.

Magneto-optical trap: The radiation pressure itself does not allow for spatial confinement of the atoms. Indeed, the atoms are still able to move slowly in any direction and eventually they can diffuse out of the overlap region between the laser beams. In order to both cool and confine the atoms, the force has to be additionally position-dependent. This dependence is provided by the MOT configuration. Operation of the MOT is based on manipulations of the external and internal degrees of freedom of atoms by means of carefully prepared optical and magnetic fields. The optical molasse is modified by selecting the proper circular polarizations for the beams and applying a weak quadrupole magnetic field.

To understand the functionment of a MOT, let's consider a 1D model as in Ref. [1]. The situation is the following. We consider the following simple level structure for the atom: hyperfine components $F = 0$ and $F' = 1$ for the ground and excited state respectively. The structure is shown on Fig. 6.2 (a). Then, we consider our atom moving in two laser beams counterpropagating along the z-axis, in a coaxial inhomogeneous magnetic field $\boldsymbol{B}$ of quadrupole symmetry [Fig. 6.2 (b)]. There are two things to note now:

- A first key point is that the two laser beam are of opposite circular polarization (right σ_+ and left σ_-), and are red-detuned from resonance. Therefore, by conservation of the angular momentum, we have some *selection rules* and the σ_+ [resp. σ_-] circularly polarized beam causes only transitions with $\Delta m_F = +1$ [resp. $\Delta m_F = -1$], as shown on figure 6.2.

- A second key point is that the magnetic field changes linearly with z, its sign altering in the trap center [Fig. 6.2 (c)]. The role of the magnefic field in to lift the degeneracy (Zeeman effect) of the upper states. Besides, since the inhomogeneous magnetic field has a constant gradient $\partial B/\partial z$, this splitting changes linearly with z [Fig. 6.2 (c)]. The Zeeman shift of these levels is proportional to the magnetic field $\boldsymbol{B}$ and to the magnetic quantum number m_F of the state:

$$\Delta E = g\mu_B m_F B \tag{6.8}$$

  where g is the Landé factor and μ_B the Bohr magneton.

Now, after having introduced the configuration, we can discuss how it allows us to effectively cool and trap the atoms. Let's for instance consider that the atom is situated to the left of the reference frame, where the magnetic field is negative. In that case, the σ_+ beam is significantly closer to resonance than the σ_- beam. Therefore, the momentum transfer induced by the σ_+ beam pushing the atom to the centre is higher than the one induced by the σ_- beam repelling the atom out of the trap centre. The opposite situation happens to the right of the trap. As a result, the atom is pushed towards the field free region $B = 0$, where the two forces cancel each other.

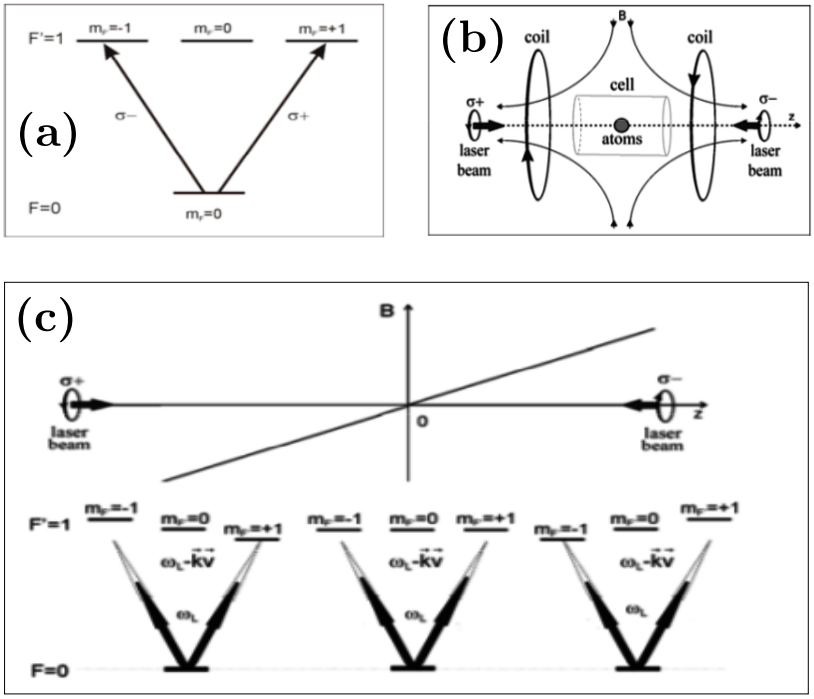

Figure 6.2 – (a) Selective absorption of the circularly polarized light. (b) Arrangement for a MOT in 1D. The atoms are in the field of two counterpropagating beams and of a magnetic field of quadrupole symmetry. (c) Atoms of a simple level structure ($F = 0$, $F' = 1$) in a 1D MOT. Zeeman shifts of the sublevels in the B-field of constant gradient $\partial B/\partial z$ are shown. The black arrows denote the laser frequency red-detuned from the resonance; the dotted arrows are for the Doppler modified frequency. Figures extracted from [1].

To trap the atoms in 2D or 3D, the generalization is rather natural, by irradiating respectively the atoms with two or three pairs of opposing laser beams, propagating along Cartesian axes (Fig. 6.3).

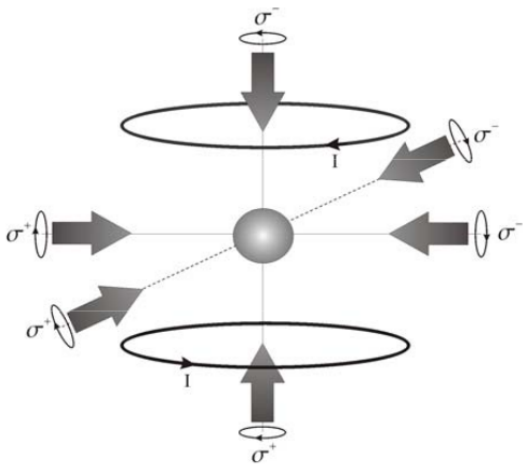

Figure 6.3 – Schematic of a 3D MOT. Figure extracted from [1].

6.3 Laser part

We want to realize the cooling on the transition between the hyperfine ground state $F = 4$ and the hyperfine excited state $F' = 5$ of cesium (Fig. 6.1) because it is the strongest hyperfine transition of the D_2 line, and the transition is closed. However, because the splitting between the hyperfine excited states is quite small, there is a non-negligible probability for atoms to be excited to the $F' = 4$ excited state (Fig. 6.1), which can then decay back to the ground state $F = 3$ (Fig. 6.1), which is no longer coupled to the cooling laser. This makes the cooling and trapping step less efficient. Therefore it is necessary to use a second laser addressing the transition between the ground state $F = 3$ to the excited state $F' = 4$ in order to "repump" the atoms back to the ground state $F = 4$. For that reason it will be called the *repumping* laser, and the laser used for the cooling the *cooling* beam.

For the repumping beam, we use a commercial diode laser operating in a continuous wave mode at the infrared wavelength 852 nm with a maximum output power of 80 mW (model *DL pro 850_11457* from *Toptica Photonics*). For the cooling beam, we use a tapered amplifier laser operating in a continuous wave mode at the infrared wavelength 852 nm with a maximum output power of 1 W (model *TA pro 850-2V0_13307* from *Toptica Photonics*). These lasers have narrow linewidths, about or less than 50 kHz. We measured the linewidth by doing an interference experiment between the two lasers. One has to frequency detuned both lasers, and observe the resulting *beating signal*. By processing this signal with a spectrum analyser, one can extract a linewidth, which corresponds to the mixing between the linewidths of the two lasers, as shown in Fig. 6.4. The actual linewidth of each laser is smaller than the measured linewidth. Therefore, with a linewidth of about 50 kHz for each laser, we are able to resolve the hyperfine structure of the cesium atoms (represented in Fig. 6.1 where we also give the energy separation between the hyperfine levels: the minimum separation is about 150 MHz).

6.3.1 Lock of the laser frequencies

In what follows, we explain the technique used to actively stabilize the frequency of the lasers. This is called to "lock" the lasers. Indeed, in addition to a linewidth narrow enough, it is very important to have a very accurate control of the frequency of the lasers in order to resolve the atomic energy levels . This is done by locking the laser frequency on an absolute frequency reference, which are the frequencies of the atomic transitions themselves. The technique, called *saturated absorption technique*, allows to lock the lasers with a precision of about 1 MHz.

Saturated absorption The saturated absorption technique is a spectroscopy technique that allows to resolve the hyperfine structure of an atomic gas *at room temperature* (in our case cesium atoms).

The principle is the following: The laser to be locked is separated into a pump beam (intense) and a probe beam (weak), which are sent through a cell containing the atomic

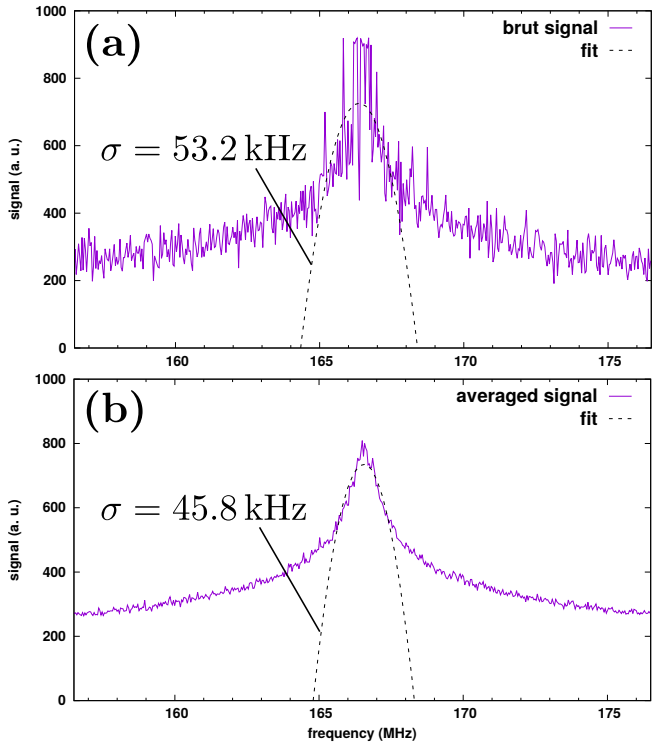

Figure 6.4 – Spectrum corresponding to the Fourier transform of the beating signal between the cooling laser and the repumping laser beams [brut signal in (a) and averaged signal in (b) to reduce the noise]. The "width" σ of the spectrum is extracted using a Gaussian fit.

gas, with a frequency close to a fine transition of the cesium atoms. The frequency of both beams is tuned in a range $[\omega_{\min};\omega_{\max}]$. The atoms in the cell can be classified into different velocity classes [when we talk about velocities we talk about the velocity component along the axis defined by the direction of the beams (1D)]: for some of the classes, the sum of the Doppler shift and the laser frequency will correspond to an hyperfine transition. However, as the range of velocities Δv is such that: $k\Delta v \gg \gamma, \Delta\nu_{\mathrm{HF}}$ (γ the natural linewidth given in Table 6.1 and $\Delta\nu_{\mathrm{HF}}$ the hyperfine splitting given in Fig. 6.1) many atoms belonging to different classes are excited to different hyperfine states. As a result, the absorption spectrum is broadened and the hyperfine structure can not be resolved. Moreover, as the pump beam has a high intensity, these atomic transitions are saturated. It is where the probe beam comes into play: to be able to resolve the sub-Doppler spectrum, the probe beam with a much weaker intensity is sent from the opposite direction. In most cases, the classes of atoms excited by the pump and the probe are different, and the probe beam is absorbed in the same way as the pump beam. However, there is one class of atoms that will be resonant for both beams, the class $v = 0$. In this case, the atoms are transparent for the probe beam, since the transition is saturated by the pump beam. Therefore, the transmission of the probe beam through the cell will exhibit a peak each time the frequency of the laser matches with the frequency of an hyperfine transition. By recording the spectrum of the transmitted light of the probe beam through the cell, one can resolve the hyperfine structure.

Note that in addition to the peaks corresponding to hyperfine transitions, the transmit-

ted spectrum will also features extra peaks, which corresponds to "cross-over" transitions. This happens when the laser frequency lies exactly in-between two transitions 1 and 2: $\omega_L = (\omega_1 + \omega_2)/2$. In this case, the atoms with a velocity v such that $kv = (\omega_2 - \omega_1)/2$ are resonant with both beams, and as the pump saturates the transition, one will see a peak in the transmission.

In our experiment, we use this technique to lock both the cooling beam and the repump beam (see the "locking part" in Fig 6.6). Each beam is split into two parts by using a polarizing beam splitter (PBS): one part is sent through the Cs cell (cooling beam in red, repump beam in green), and the other part, called the counter-propagating probe beam, is also sent through the Cs cell from the other side (dashed lines)[1]. The spectroscopic signal is recorded in transmission while scanning the frequency of the lasers accross the cell, and is shown in Fig. 6.5. The two main dips in the figure correspond to the absorption of the atoms in the $F = 4$ ground state (left dip), and to the absorption of the atoms in the $F = 3$ ground state (right dip). If one zoomes in, the hyperfine structure of the gas of cesium is revealed at room temperature (marked by red arrows in Fig. 6.5).

Locking points: We choose to lock the frequency of the cooling beam on the cross-over between the $F' = 4$ and $F' = 5$, and the repumping beam on the state $F' = 3$ (see Fig. 6.1). The lock is implemented by using a PDH technique (PDH for "Pound–Drever–Hall") and a simple PID controller (PID for "proportional–integral–derivative"). The stability of our lock was measured by doing a beating experiment between the two locked lasers at the level of the Cs cell. After a few hours (about 10 hours), the frequency drift is about 150 kHz, which is about three laser linewidth (see Appendix 6.A).

6.3.2 Control of the laser frequency

While the repumping beam has an importance, the most important laser is the cooling beam. The frequency of this laser is a very important parameter for the cooling and trapping of the atoms, and appearing for example in the expression of the temperature [through the detuning parameter $\delta/2\pi = f_L - f_0$ in Eqs. (6.3) and (6.7)]. We want to be able to control it. Once locked to an absolute reference as presented previously, the control can be done by using an acousto-optics modulator (AOM), which is a device which allows to diffract and shift the frequency of the beams. The functionment of an AOM is the following: a radio-frequency (RF) electric signal drives a piezoelectric transducer attached to a crystal. These vibrations create sound waves in the crystal. Then, the moving periodic waves change the refraction index of the crystal. Therefore, incoming light will be diffracted, similar to Bragg diffraction. The RF signal is provided by a RF source, the AOM driver, which gets a voltage as an input: the frequency is changed by applying a voltage to the AOM driver.

[1] Note that in practice the pump and probe beams shown in Fig 6.6 have to overlap, which is not the case on the drawing for clarity; moreover the colors red/green are fake colors used only to distinguish the two lasers.

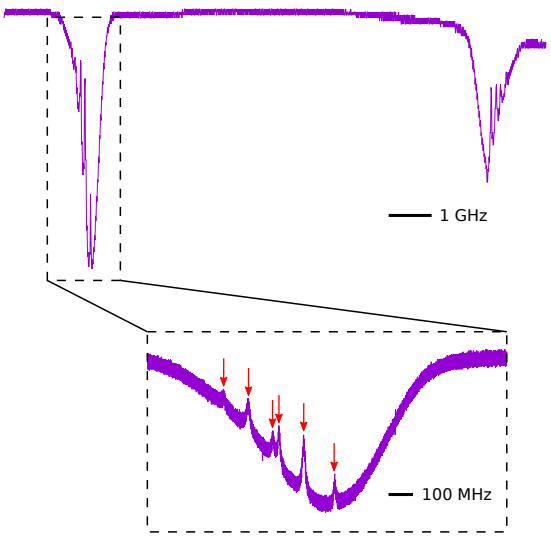

Figure 6.5 – Transmission spectrum. As the frequency of the laser scans the Cs cell, one can see on the main figure the left peak which corresponds to the absorption of the atoms in the $F = 4$ ground state, and the right peak which corresponds to the absorption of the atoms in the $F = 3$ ground state. They are separated by about 9.2 GHz (hyperfine structure of the ground state, see Fig. 6.1). If one zooms in, one can see on the inset the hyperfine structure of the excited state: the 6 peaks marked with red arrows correspond to the following transitions starting from the ground state $F = 4$ (from left to right): $F' = 3$, cross-over between $F' = 3$ and $F' = 4$, $F' = 4$, cross-over between $F' = 3$ and $F' = 5$, cross-over between $F' = 4$ and $F' = 5$, $F' = 5$ (the transition from the ground state $F = 4$ to the excited state $F' = 2$ is forbidden).

Double-pass AOM: The frequency of the cooling beam is controled by the AOM called "AOM_2" in Fig. 6.6, and the frequency of the repumping beam is controled by the "AOM_3". Both beam are then couple to a fiber by means of a fiber coupler (whose main characteristic is to have a focal lens which allows to focus the beam inside the fiber), denoted by "FC" in Fig. 6.6, and the output is split into six arms directly used for the MOT as shown in Fig. 6.3.

We want to *dynamically* be able to change the frequency of the cooling beam, in particular for the temperature measurements as will be seen in the next Section. For that, the AOM is connected to a *voltage controled oscillator* (VCO) that allows to drive the frequency of the AOM in real time. However, when a laser's frequency is scanned with an AOM, an effect to take into account is that the angle of the first-order diffracted beam shifts as well, because the beam diffraction angle is a function of modulation frequency. In our case, this beam shift will cause alignment problems and uncouple to the fiber shown in Fig. 6.6, which is connected to the MOT. Such an unwanted side effect can be nevertheless eliminated by using the AOM_2 in the *double-pass configuration* as explained in [12, 13]. In this configuration, the output of the $+1$ order of the AOM is retroreflected for a second pass through the AOM and with its polarization rotated by 90° (using a quarter wave plate denoted by $\lambda/4$ in Fig. 6.6) such that it counterpropagates the incident laser beam and it can be separated from the input beam with a polarizing beam splitter (PBS). In this

arrangement, in both pass the beams get shifted in opposite directions so that after the double-pass it is completely eliminated in the paraxial approximation. We measured 6% of power variations after the fiber when the frequency of the laser is scanned from $-2.6\,\mathrm{MHz}$ ($\gamma/2$) $< f_L - f_0 <$ $-26\,\mathrm{MHz}$ (5γ) due to the AOM (where f_0 denotes the transition frequency between the state $F = 4$ of $6S_{1/2}$ and the state $F' = 5$ of $6P_{3/2}$), which is considered as small. Note that for the double-pass configuration, we get 40% overall efficiency (defined as the optical power out of the double-pass divided by the optical power into the AOM), and that the coupling to the fiber is 50% for the repumping and the cooling beams.

Cooling beam frequency: One wants to know what is the final frequency of the cooling beam after passing through the double-pass AOM. Let us denote by f_L the frequency of the cooling beam, and by f_0 the transition frequency between the state $F = 4$ of $6S_{1/2}$ and the state $F' = 5$ of $6P_{3/2}$. As the cooling beam is passing from an AOM labeled "AOM_1" (of center frequency $110\,\mathrm{MHz}$) in the locking part[2] in Fig. 6.1, and we get the diffracted order $+1$, the frequency of the laser passing through the cell is: $f_{\mathrm{lock}} + 110\,\mathrm{MHz}$. As we saw above, this frequency is then locked on the cross-over transition between $F' = 4$ and $F' = 5$ at: $f_0 - 251.1/2\,\mathrm{MHz}$. By equaling the two, one gets the frequency f_{lock} of the laser: $f_{\mathrm{lock}} + 110\,\mathrm{MHz} = f_0 - 251.1/2\,\mathrm{MHz}$, that is:

$$f_{\mathrm{lock}} = f_0 - 235.55\,\mathrm{MHz} \tag{6.9}$$

This is the locking frequency. Now, at the output of the laser, the frequency is f_{lock}, which is going to change through the double-pass AOM. Let us express this new frequency f_L, which is the one that eventually the atoms will see, as a function of the frequency of the AOM_2 (variable through the VCO) denoted f_{AOM}. After the double-pass, the frequency f_L reads (as we take the order $+1$):

$$f_L = f_{\mathrm{lock}} + 2f_{\mathrm{AOM}} \qquad \text{with} \quad f_{\mathrm{lock}} = f_0 - 235.55\,\mathrm{MHz} \tag{6.10}$$

For example, in the experiment we need a minimum detuning $\delta_{\mathrm{min}} = 2\pi(f_L - f_0) = -\gamma/2$ and a maximum detuning $\delta_{\mathrm{max}} = 2\pi(f_L - f_0) = -5\gamma$. These conditions, together with Eq. (6.10), gives us the frequency of the AOM f_{AOM}, using the fact that $\gamma = 2\pi \times 5.2\,\mathrm{MHz}$:

- For a detuning $\delta_{\mathrm{min}} = -\gamma/2$, one needs $f_{\mathrm{AOM}} = 116.5\,\mathrm{MHz}$.
- For a detuning $\delta_{\mathrm{max}} = -5\gamma$, one needs $f_{\mathrm{AOM}} = 104.8\,\mathrm{MHz}$.

Note: at resonance, *i.e.* $\delta = 0$, one has $f_{\mathrm{AOM}} = 117.8\,\mathrm{MHz}$.

6.3.3 Control of the laser intensity

As for the detuning, the intensity of the cooling beam is a very important parameter for the cooling and trapping of the atoms, and appearing for example in the expression of the temperature [through the intensity parameter I in Eqs. (6.3) and (6.7)]. We want to

[2] This initial use of this AOM was to modulate the frequency for the locking, but we eventually modulate by changing the current of the diode laser.

be able to control it as well. This control can be done with the AOMs: by changing the RF power that is sent to the AOM, the laser beam is diffracted by the AOM and can gain energy or lose energy. This control is however not yet implemented in our experiment, but it will be implemented in the future using a variable RF attenuator.

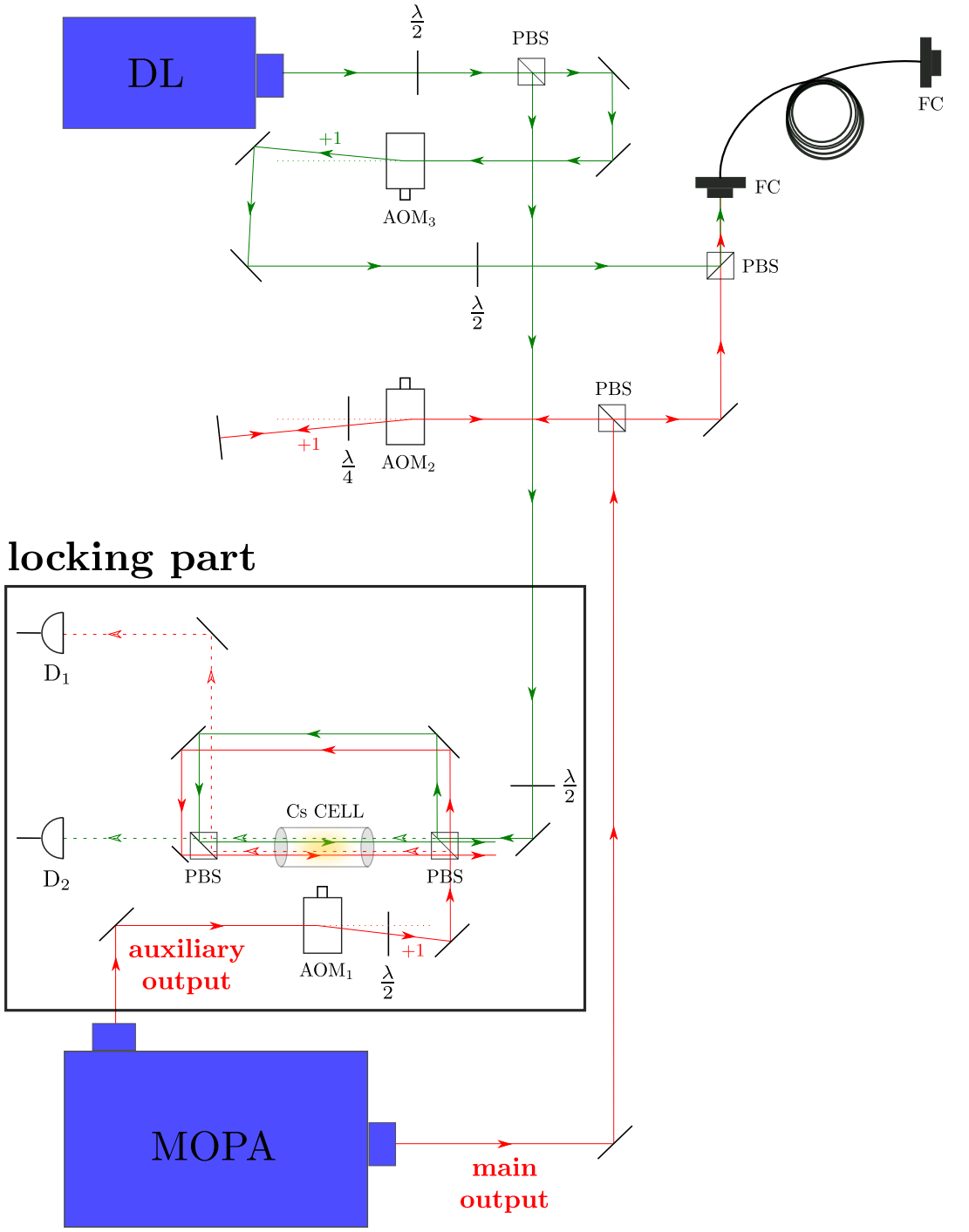

Figure 6.6 – Experimental setup: locking part and modulation part of the lasers. The MOPA (Master Oscillator Power Amplifier) laser corresponds to what we call the "cooling beam" in the text, and the DL (Diode Laser) laser corresponds to the repumping beam. The other symbols mean: D, detector; PBS, polarizing beam splitter; AOM, acousto-optic modulator; FC, fiber coupler; $\lambda/2$, half-wave plate; $\lambda/4$, quarter-wave plate.

6.4 Temperature measurements

The temperature of a cold atomic cloud is one of its most important characteristics. We present here our measurements of the temperature of the cloud of cold cesium atoms using the time-of-flight *(TOF) method. We did not implement the* shadow imaging *method to extract the atom number density, but roughly speaking the atom density in the MOT is about* $10^9 - 10^{10}$ *atoms/cm*^{3}.

6.4.1 Time-of-flight method

The time-of-flight method starts from a cold atomic cloud confined in a trap. At time t_0, one releases the atomic cloud from the trap, and lets it expands. At a later time t_1, one measures the fluorescence of the atoms using a resonant probe light to get an image of the expanded cloud using a CMOS camera (model *DCC3240N* from *Thorlabs*). By measuring the expansion of the cloud during the time $\Delta t = t_1 - t_0$, one can deduce its temperature. Note that this method is destructive: the cloud is destroyed after each measurement by the resonant probe which scatters the atoms away.

We now explain more quantitatively how to deduce the temperature of the cloud from its expansion. Taking z as the vertical direction, we consider only the plan (x,z) (as our CCD camera will image a section of this plan only), we start from an initial Gaussian position and velocity distributions of the atoms in the trap (assuming the classical behaviour of a gas), and assume that the cloud of cold atoms is initially spherically symmetric with a Gaussian radius σ_0. After a time t, the probability distribution of finding an atom at position (x,z) is given by [14]:

$$g(x,z,t) = \frac{1}{2\pi\sigma^2(t)} \exp\left(-\frac{x^2+z^2(t)}{2\sigma^2(t)}\right) \quad \text{with} \quad z(t) = z - \frac{1}{2} g\, t^2 \tag{6.11}$$

with

$$\sigma(t) = \sqrt{\sigma_0^2 + \frac{k_B T}{m} t^2} \tag{6.12}$$

Finally, considering a probe light with a section much larger than the atomic cloud size, one can consider the intensity seen by the atoms as constant and equal to I. Assuming that the fluorescence signal is directly proportionnal to the number of atoms in the beam, the fluorescence intensity distribution reads:

$$I_{\text{fluo}}(x,z,t) \propto I \times \frac{1}{2\pi\sigma^2(t)} \exp\left(-\frac{x^2+z^2(t)}{2\sigma^2(t)}\right) \tag{6.13}$$

with I the intensity of the resonant probe light. We get some fluorescence image in Fig. 6.7. The sequence is as following: all the lasers were switched off at time $t = 0$, and switched on again after various TOFs t for fluorescence imaging.

Fitting procedure: In order to extract the expanded Gaussian radius $\sigma(t)$ of the cloud, we fitted the fluorescence images obtained for different expansion times t (see Fig. 6.7)

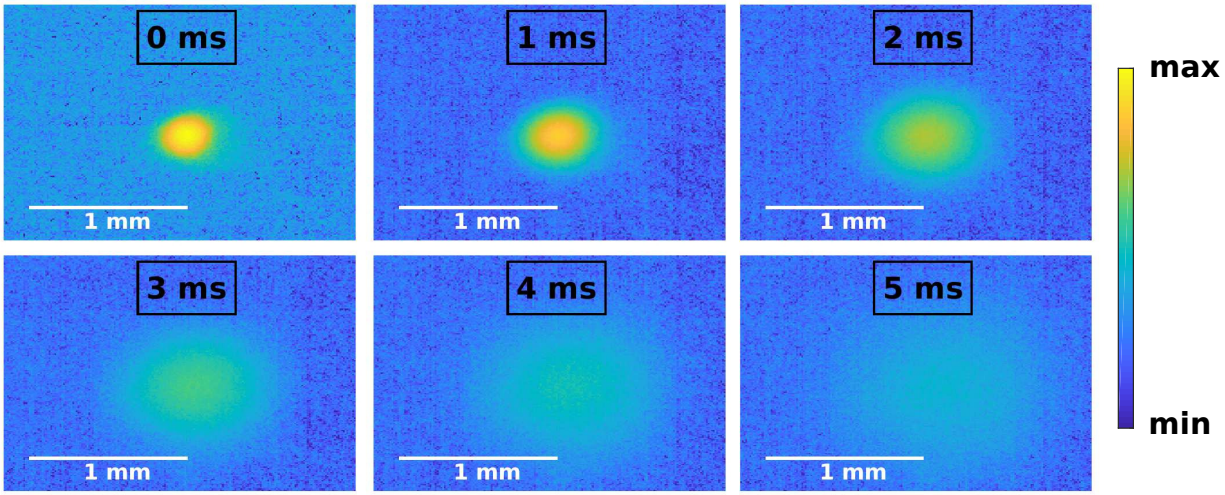

Figure 6.7 – Fluorescence of a thermally expanding cloud of cesium atoms, recorded by a CMOS camera at different time intervals (0, 1, …, 5 ms) after releasing the atoms from a MOT. Each image has been averaged over 10 realizations.

with a function of the form:

$$A \times \frac{1}{\sqrt{2\pi}\sigma_x^2} \exp\left(-\frac{x_c^2}{2\sigma_x^2}\right) \times \frac{1}{\sqrt{2\pi}\sigma_z^2} \exp\left(-\frac{z_c^2}{2\sigma_z^2}\right) + B \tag{6.14}$$

with A, B, x_c, y_c, σ_x and σ_z the free parameters. We reported in Fig. 6.8 the fitting parameters σ_x and σ_z for different times of flight. One can see that the expansion is isotropic $\sigma_x \simeq \sigma_z$, and quadratic in time in agreement with Eq. (6.12) (note that $\sqrt{\sigma_i^2 - \sigma_0^2}$ is plotted as a function of time t in Fig. 6.8). One can then deduce the temperature by fitting the points in Fig. 6.8 with the function given in Eq. (6.12), from which we extracted the following temperature:

$$T = 137\mu\text{K} \tag{6.15}$$

This temperature was obtained for the following experiment parameters: a detuning of the cooling beam frequency from resonance of $|\delta| = 2.75\gamma$, and a laser intensity per cooling beam of $I = 3.6 I_s$ (corresponding to a power after the fiber of about $P = 60\text{mW}$), where $I_s = 2.7\,\text{mW/cm}^2$ is the saturation intensity of the transition [8].

Note that the temperature obtained here is slightly above the Doppler limit given in Eq. (6.4), and that this is the same temperature as the one reported in the PhD dissertation of Guillem Sagué-Cassany [15] ($T = 135\,\mu\text{K}$, but without specifying the experimental parameters). This temperature corresponds to a root mean square (rms) atomic velocity, which is the square root of the mean square speed $\langle v^2 \rangle$, of:

$$v_{\text{rms}} = \sqrt{\frac{3k_B T}{m}} \simeq 16\,\text{cm/s} \tag{6.16}$$

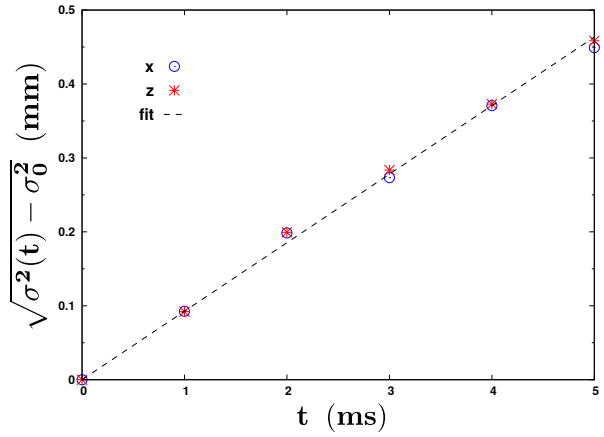

Figure 6.8 – Gaussian radius $\sigma(t)$ of the atomic cloud in thermal expansion as a function of the time-of-flight t. The blue (red) dots correspond the expansion σ_x (σ_z) along the x (z) direction extracted from the fitting procedure explained in the main text. The black dotted line corresponds to Eq. (6.12) with the temperature $T = 137\,\mu$K.

6.4.2 Temperature of the molasse: sub-Doppler cooling

As seen in Section 6.2.2, the temperature is function of two parameters: the laser detuning δ and the laser power or intensity I. We then proceeded with some systematic studies of the temperature as a function of these two parameters. We measured the temperature of the molasse for different detunings δ, and various intensities I. The time sequence of the measurements is the following (see Fig. 6.9):

1. loading the MOT during 3.5 s at the detuning $|\delta| = \gamma$ in order to have enough trapped atoms for a good fluorescence imaging;

2. switching off the magnetic fields and loading the molasse for 200 ms at the detuning δ desired for the temperature measurement;

3. switching off all the lasers during the time-of-flight;

4. switching on the lasers with a detuning $|\delta| = 0.5\gamma$ for fluorescence imaging for 0.5 ms.

We use the AOMs to switch on and off the lasers (equivalent to electrical shutters). This allows us to switch on and off the trap very quickly that is within some microseconds.

The results are shown on Fig. 6.10, where we plot the temperature T as a function of the inverse detuning $1/|\delta|$ ($|\delta| = 1,2,3,4,5\gamma$), and for different intensities I ($I = 0.9, 0.6, 0.3 I_s$). The full lines represent the average temperature of T_x and T_y (shown in dashed lines). The discrepancy between the two temperature comes from the fact that the magnetic field in the laboratory is not perfectly compensated by our compensation coils, leading to an slight anisotropic expansion of the could.

As one can see, there is some **sub-Doppler cooling** as the temperature goes below the Doppler temperature limit. The general behavior, that is the decrease of the temperature

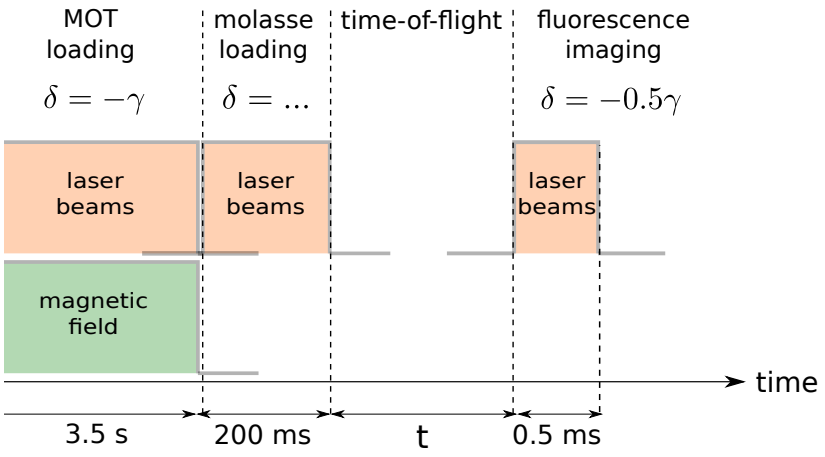

Figure 6.9 – Time-sequence of the temperature measurements.

as the detuning (intensity) increases (decreases), is in agreement with what is expected for a molasse [see Eq. (6.7)]. Note however that we are not really in the condition $|\delta| \gg \gamma$ yet, and in order to compare the law given in Eq. (6.7), we should decrease the detuning further.

Comparison Ref. [16]: In Fig. 6.10 we also compared our results with 4 points of Salomon *et al.* We have a very good agreement for $I/I_s = 0.3$, and good for $I/I_s = 0.6$ for one point.

Note that one must be careful that our definition of the Rabi frequencies are different: $\Omega \equiv -\mathbf{d}\cdot\mathbf{E}_0/\hbar$ for us and $\Omega^{\text{Sal}} \equiv 2\mathbf{d}\cdot\mathbf{E}_0/\hbar$ for Salomon *et al.* Moreover, from our definition of I_s it follows that [8]:

$$\frac{I}{I_s} \equiv 2\left(\frac{\Omega}{\gamma}\right)^2 \tag{6.17}$$

In Fig. 2 of [16], Salomon *et al.* show T as a function of the ratio $(\Omega^{\text{Sal}}/\gamma)^2$, and we have the equivalence: $(\Omega^{\text{Sal}}/\gamma)^2 \leftrightarrow 2I/I_s$. So for example, if I want T for $I/I_s = 0.3$, I must look for T at $(\Omega_s/\gamma)^2 = 0.6$ in Fig. 2 of [16].

We therefore managed to reach a temperature about $T \simeq 20\mu$K for the parameters $|\delta| = 5\gamma$ and $I/I_s = 0.3$ (see Fig. 6.10, blue curve), which gives a rms velocity of $v_{\text{rms}} = 6\,$cm/s. How can we decrease further the temperature? We have two options according to Salomon *et al.*:

1. We further decrease the detuning: for example, for $I/I_s = 0.3$, we can reach $T < 20\mu$K for $|\delta|/2\pi = 30\,$MHz ($\sim 6\gamma$) and $T < 10\,\mu$K for $|\delta|/2\pi = 40\,$MHz ($\sim 8\gamma$), and even lower by further increasing the detuning until $|\delta|/2\pi = 140$MHz ($\sim 27\gamma$), according to the data reported in Fig. 2 of [16].
   → The experimental limitation for us will be the change in power and probably in the coupling to the fiber for too large detunings...

2. We further decreases the intensity: for example, for $I/I_s = 0.1$, Salomon *et al.* got $T \simeq 10\,\mu$K and $T \simeq 5\,\mu$K for the detunings $|\delta|/2\pi = 10\,$MHz ($\sim 2\gamma$) and $|\delta|/2\pi =$

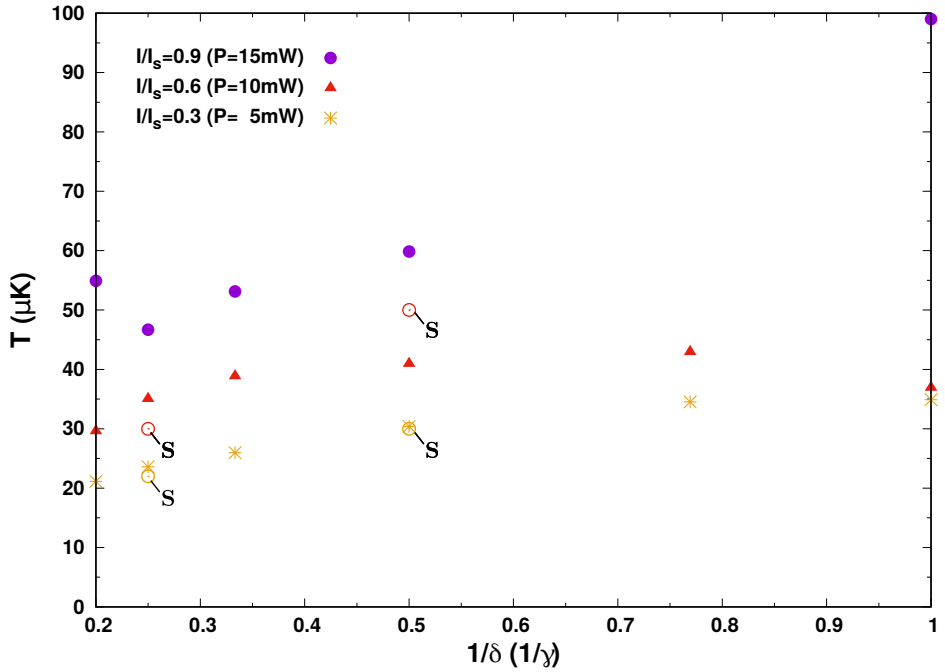

Figure 6.10 – Temperature T of the molasse as a function of the inverse detuning $1/|\delta|$ for various intensities: $I = 0.9I_s$ (purple circles), $I = 0.6I_s$ (red triangles) and $I = 0.3I_s$ (orange stars). The circles marked with "S" correspond to the data taken from Salomon *et al.* in [16] for $I/I_s = 0.6$ (red circles) and for $I/I_s = 0.3$ (orange circles).

20 MHz ($\sim 4\gamma$) respectively, and even lower temperatures until $T \simeq 3\,\mu$K for larger detunings and/or lower intensities. An important thing they reported, is that the lowest temperature is nearly independent of the detuning as long as $|\delta| > 2\gamma$.
The experimental limitation for now is that we cannot modulate the amplitude of the beam with the AOM yet, so we cannot go to such low intensities yet because the fluorescence signal would be too weak... We plan to buy the digital card to be able to control automatically the amplitude of the laser.

6.5 Conclusion

The temperature measurement of about $T \simeq 20\,\mu$K is a good starting point for the following work, because it is cool enough to proceed to the next step. The next step of the experiment will be to settle the imaging system to create the superoscillatory spot in the cloud of cold atoms. One will then have to study the transfer efficiency of a single atom in the superoscillatory spot and to perform some laser cooling of the atom in the spot. Ultimately, one would have to interface the atom with the fabricated metasurface, and try to measure the induced coherence.

6.A Lock drift with temperature

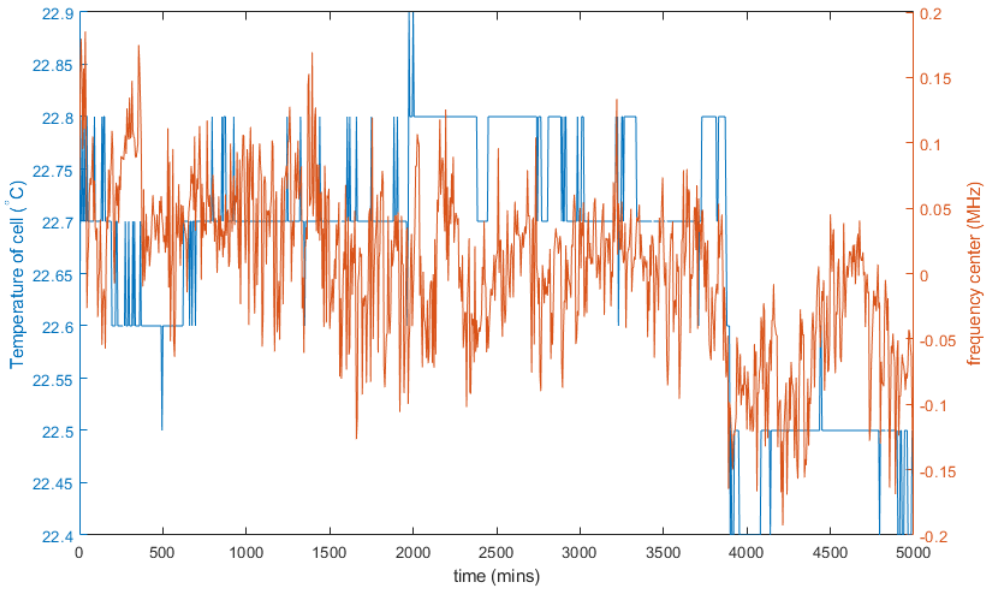

Figure 6.11 – Temperature (blue curve) and lock (red curve) drifts as a function of the time.

Bibliography

[1] K. Kowalski, V. Cao Long, K. Dinh Xuan, M. Głódź, B. Nguyen Huy, and J. Szonert, Computational Methods in Science and Technology **Special Issue (2)**, 115 (2010).

[2] B. K. Singh, H. Nagar, Y. Roichman, and A. Arie, Light: Science & Applications **6**, 17050 (2017).

[3] G. T. Di Francia, Il Nuovo Cimento (1943-1954) **9**, 426 (1952).

[4] F. M. Huang, Y. Chen, F. J. G. de Abajo, and N. I. Zheludev, Journal of Optics A: Pure and Applied Optics **9**, S285 (2007).

[5] F. M. Huang, N. Zheludev, Y. Chen, and F. Javier Garcia de Abajo, Applied Physics Letters **90**, 091119 (2007).

[6] E. T. Rogers and N. I. Zheludev, Journal of Optics **15**, 094008 (2013).

[7] J. Baumgartl, S. Kosmeier, M. Mazilu, E. T. Rogers, N. I. Zheludev, and K. Dholakia, Applied Physics Letters **98**, 181109 (2011).

[8] D. A. Steck, https://steck.us/alkalidata/cesiumnumbers.pdf (2007).

[9] W. D. Phillips, Reviews of Modern Physics **70**, 721 (1998).

[10] J. Dalibard and C. Cohen-Tannoudji, Journal of the Optical Society of America B **6**, 2023 (1989).

[11] P. J. Ungar, D. S. Weiss, E. Riis, and S. Chu, Journal of the Optical Society of America B **6**, 2058 (1989).

[12] E. A. Donley, T. P. Heavner, F. Levi, M. Tataw, and S. R. Jefferts, Review of Scientific Instruments **76**, 063112 (2005).

[13] D. McCarron, http://massey.dur.ac.uk/resources/slcornish/AOMGuide.pdf (2007).

[14] T. M. Brzozowski, M. Maczynska, M. Zawada, J. Zachorowski, and W. Gawlik, Journal of Optics B: Quantum and Semiclassical Optics **4**, 62 (2002).

[15] G. S. Cassany, *Cold atom physics using ultra-thin optical fibres*, Ph.D. thesis, Rheinischen Freidrich-Wilhelms-Universität Bonn (2008).

[16] C. Salomon, J. Dalibard, W. Phillips, A. Clairon, and S. Guellati, EPL (Europhysics Letters) **12**, 683 (1990).

General conclusion

In this thesis, we studied different facets of the spontaneous emission phenomenon. This requires interfacing the following scientific domains: quantum optics, nanophotonics (plasmonics, metasurfaces), and atomic physics. To investigate such a broad spectrum subject, I benefited from interactions and collaborations within the Institut Fresnel, with other French laboratories like the PIIM in Marseille or the LP2N in Bordeaux, as well as in the context of an international collaboration with the CDPT in Singapore. Thanks to this dynamic environment, I was able to carry out new theoretical predictions for each phenomenon studied in this thesis. Here is a brief summary of the main theoretical results of this thesis as well as some personal outlook.

Part I was devoted to the study of monitored spontaneous emission. Our main result is a theoretical prediction about the anti-Zeno effect (AZE) in hydrogen-like atoms in free-space. We show that the AZE is impossible for the most commonly studied electric-dipolar transitions, which drastically limits the candidates and explains why this effect has never been demonstrated experimentally for atoms in free space since its theoretical prediction about twenty years ago. We proposed an experimental test feasible with alkali-earth ions such as Ca^+ or Sr^+. This result has been published in: E. Lassalle, C. Champenois, B. Stout, V. Debierre, and T. Durt, *Conditions for anti-Zeno-effect observation in free-space atomic radiative decay*, Physical Review A **97**, 062122 (2018). This paves the way for a future experiment which would be the first experimental demonstration of the AZE in atoms in free-pace, and would be a further test of quantum optics predictions about the effect of measurement on quantum systems, which is one of the most striking quantum signatures compared to classical measurements.

Part II was dedicated to the study of the near-field interaction between a quantum emitter (QE) and optically resonant nanostructures. We particularly studied the frequency shift (Lamb shift) of the emitted photon induced by the resonances. Using the multipolar theory, we predicted a shift of the emission wavelength of $\Delta\lambda = 2.5\,\text{nm}$ for a molecule (Alexa fluor) located in the nanogap of a gold dimer (Chapter 2). The overall study has been published in: E. Lassalle, A. Devilez, N. Bonod, T. Durt, and B. Stout, *Lamb shift multipolar analysis*, Journal of the Optical Society of America B **34**, 1348 (2017).

The most important novelty in my eyes was the use of a quantum optics formalism based on a Quasi-Normal Mode description of the resonances of the resonator, which are the natural EM modes of the structure (Chapter 4). In particular, this description allowed us to demonstrate in the specific case of the photonic Lamb shift a fundamental distinction between closed and open systems in the presence of a single resonance. While for closed systems, the Lamb shift remains within the emission linewidth, it can go beyond this fundamental range for dissipative (open) systems (Chapter 3). This result has been

published in: E. Lassalle, N. Bonod, T. Durt, and B. Stout, *Interplay between spontaneous decay rates and Lamb shifts in open photonic systems*, Optics Letters **43**, 1950 (2018). I personally found the QNM formalism of great value for analytical analysis. In the future, I would like to investigate further the differences emphasized by this description with cQED-like descriptions. Moreover, I would like to see how this formalism generalizes to treat two QEs whose interactions are mediated by resonances.

In Part III, we addressed a new paradigm, which consists in the far-field interaction between QE and a metasurface. We predicted an effect on a quantum emitter by an anisotropic metasurface over a distance $d \sim 10\lambda$, far beyond the near-field region. Notably, we predicted the creation by spontaneous emission of a long-lifetime coherence between the two ground states of a Λ atom, and we conceived some metasurface designs, based on the phase-mapping approach, suitable for the creation of the anisotropic quantum vacuum (Chapter 5): E. Lassalle, P. Lalanne, S. Aljunid, B. Stout, T. Durt, and D. Wilkowski, *Long-lifetime coherence in a quantum emitter induced by a metasurface* (in preparation). The experimental set-up built to carry on such experiments with cesium atoms was also presented, along with our first characterization of the cold atomic cloud by the measurement of the temperature (Chapter 6). In the future, I hope that such an experiment would reveal the effect of the metasurface on a QE over macroscopic distances, opening the way towards the possibility of entangling atoms over remotes distances. Looking ahead, with the very dynamical field of metasurfaces, one could imagine a dynamically *reconfigurable* metasurface, and a regular array of atoms, to dynamically entangle atoms, and perform quantum processing.

Last but not least, in collaboration with B. Kolaric, M. Hatifi, B. Stout, and T. Durt, we are presently conceiving an experiment aimed at revealing the quantum signature of the dynamics underlying spontaneous emission of fluorophores put into a resonant cavity, through the temporal statistics of the emitted photons. Preliminary computations show that certain effects (like the Zeno regime) are intimately linked to the quantum nature of the process: B. Kolaric, E. Lassalle, M. Hatifi, B. Stout, T. Durt: *Quantum signature in the weak and strong coupling regimes revealed through temporal statistics of spontaneously emitted photons* (in preparation).

Physical constants

Speed of light (in vacuum)	$c = 2.997\,924\,58(1) \times 10^{8}$ m/s
Permeability of vacuum	$\mu_0 = 4\pi \times 10^{-7}$ N/A^2
Permittivity of vacuum	$\epsilon_0 = \frac{1}{\mu_0 c^2} = 8.854\,187\,812\,8(13) \times 10^{-12}$ C^2/N$\cdot$m^2
Planck's constant	$h = 6.626\,18(4) \times 10^{-34}$ J$\cdot$s
(Reduced) Planck's constant	$\hbar = \frac{h}{2\pi} = 1.054\,589(6) \times 10^{-34}$ J$\cdot$s
Electron charge	$e = -1.602\,189(5) \times 10^{-19}$ C
Electron mass	$m_e = 9.109\,53(5) \times 10^{-31}$ kg
Fine structure constant (dimensionless)	$\alpha = \frac{e^2}{4\pi\epsilon_0 \hbar c} = \frac{1}{137.036\,0(1)}$
Bohr radius	$a_0 = \frac{\hbar}{m_e c \alpha} = 0.529\,177\,1(5)$ Å
Rydberg's constant	$R_\infty = \frac{m_e e^4}{8\epsilon_0^2 h^3 c} = 10\,973\,731.568\,508\,(65)$ m^{-1}
Rydberg's constant (in unit of energy)	$R_\mathrm{y} = hcR_\infty = \frac{m_e e^4}{8\epsilon_0^2 h^2} = 13.605\,693\,009\,(84)$ eV
Boltzmann's constant	$k_B = 1.380\,66(4) \times 10^{-23}$ J/K